

Quantum Simulation of the Bilayer Hubbard Model Using Ultracold Atoms

Dissertation
zur
Erlangung des Doktorgrades (Dr. rer. nat.)
der
Mathematisch-Naturwissenschaftlichen Fakultät
der
Rheinischen Friedrich-Wilhelms-Universität Bonn

von
Marcell Wolfgang Gall
aus
Krumbach (Schwaben)

Bonn, 17.11.2020

Angefertigt mit Genehmigung der Mathematisch-Naturwissenschaftlichen Fakultät der Rheinischen Friedrich-Wilhelms-Universität Bonn

1. Gutachter: Prof. Dr. Michael Köhl
2. Gutachter: Prof. Dr. Simon Stellmer

Tag der Promotion: 19.07.2021
Erscheinungsjahr: 2021

Abstract

In this thesis, experiments performed in a quantum simulator for the two-dimensional and an extended Hubbard model are presented. The lowest two hyperfine states of fermionic potassium atoms are used to realise the model's spin-1/2 particles. They are probed in an optical lattice potential, located inside a vacuum chamber and observed using high-resolution imaging. We prepare a stack of either quasi-two-dimensional or bilayer lattice structures, which we then read out using radio-frequency tomography with single-plane resolution. We are able to perform localised magnetisation and density measurements by simultaneous detection of either singly-occupied sites of both spin states or the doubly-occupied sites relative to the singly-occupied ones.

We have experimentally verified a particle-hole symmetry of the Hubbard model, which maps density to spin degrees of freedom and also connects the attractive to the repulsive interaction side of the phase diagram. This mapping was achieved by performing measurements of density-doped and spin-imbalanced systems at both repulsive and attractive interaction strengths, which led to the observation of the equivalent of a Mott-insulating behaviour in a spin-imbalanced system with attractive on-site interactions.

Another result of this work was the first observation of competing magnetic orders in a bilayer Hubbard model. We prepared this bilayer through an entropy engineering scheme that created a highly filled two-dimensional band insulator and subsequently split it into two layers using a superlattice. Varying the tunnelling amplitude between both layers, we observed a crossover of the dominance of intra- to inter-layer spin correlations. Over different interaction strengths, we have identified two regimes with the same characteristic behaviour as expected for the low-temperature phase diagram of the bilayer Hubbard model.

Acknowledgements

This thesis is not only the result of a single project or timespan, but the culmination of a more than a decade long personal path in physics and life. Therefore, it is not easy to thank all people who took part in this journey individually, but nevertheless, I will try.

First, I would like to thank my supervisor Prof. Michael Köhl. For his trust in me, allowing me to work on an extremely complex and complicated machine, with even more challenging theory behind it. For his never-ending support for new ideas and new projects, even when he might not have been 100 per cent convinced of success. And for his immense knowledge, helping us out in dire phases of the project and putting the right ideas in our heads.

Most of this work was only possible in an extremely collaborative environment, formed by the team and the people around the *Fermi* experiment. A huge thanks goes out to my two colleagues and friends Jeffrey Chan and Nicola Wurz with whom I shared most of my time on the experiment. Both are unique and amazing in nearly everything they do, and I count myself lucky to have them around me. With his sharp mind and vast theory background, there was not a single tough nut Jeffrey could not crack or at least find out why it is irrelevant for our experiment. At the same time, I could not imagine a better and more understanding guiding hand to help me in my struggles for knowledge. And who would not want to have someone on the team who can, out of the blue, rewrite Fortran code to run on a super-cluster for numerical simulations? With a similar affinity for and an inspiring persistence to solve complex problems Nicola was able to push us through the dark valleys of no results, mysterious losses and “bad shots”. Focusing on the issues at hand, hard-working and more intelligent than she would ever admit to herself. I so much enjoyed the time we spent in the lab, still laughing after weeks of struggle and failure. I am glad that in the end, we succeeded.

We could build on a rock-solid basis in the experiment, set up by many generations of lab students and researchers. I want to thank our PhD predecessors Luke Miller, Eugenio Cocchi and Jan Drewes, for guiding my first steps in the experiment and leaving behind a vast toolset for lattice quantum simulation. A special thanks as well to our postdocs Daniel Pertot and Ferdinand Brennecke. My first contributions to the experiment would not have worked without the technical and advisory support of Daniel, allowing me to try out and do things he could have done way quicker and better. Meanwhile, Ferdinand’s empathic and kind ways gave me support during initial struggles and strong self-doubts. He always took the time to explain the physics and discuss ideas in lots of personal discussions. The idea of creating a Hubbard bilayer originated in one of these conversations. Without them, we could not have reached the point we are at now. And at the same time, I wish the new generation of PhD students, Jens Samland, Nick Klemmer and Janek Fleper all the best on their way. Thank you for your help and you sacrificing experiment time during the last paper crunch.

Of course, our team is but a part of a larger group from which I gained support and built up friendships. I want to thank Tina Naggert, who from day one helped me navigate the depths of administrative procedures and lent an open ear anytime needed. Akos Hoffmann supported my

experiments a lot with technical experience and skill, and I still hope he will forgive me one day that I could not test all the prototypes he made for me. Thanks to Martin Link whom I joined as a friend in the write-up office. We shared the stressful time of writing up and finishing a PhD [1], and together with Thorsten Langerfeld the good times and beers as well. Thorsten, I am sorry that I did not learn to recite rap lyrics better or improve my dance moves, you were a good teacher though. A shout out to all the other past and present members of the AQO group: Hendrik-Marten Meyer, Kuiyi Gao, Benjamin Rauf, Alexandra Behrle, Kilian Kluge, Tim Harrison, Tim Ballance, Pascal Kobel, Jonas Schmitz, Moritz Breyer, Steffen Gohlke, Felix Rönchen, Andreas Kell, Vidhya Nair, Daniel Eberz, Tobias Kree, Leon Reiffert, Santhosh Surendra, Andreas von Haaren, Ralf Berner, Max Zawierucha, Pia Fürtjes, Luisa Tolle, Moritz Scharfstädt, Anica Hamer and my bachelor students Benedikt Hartmann and Lukas Pache. I am thankful for the support we gave each other.

I do not want to forget to thank all my previous physics mentors and the groups I found friends in. From the group of Prof. Markus Oberthaler in Heidelberg or the JQI team of Prof. Ian Spielman in the USA, thank you for your joy and happiness! My thoughts to the time with you and Paco, Dina, Ana, Dalia, Alejandra, Ken, Lauren, Ben, Arno, Tobias, Helmut, Lisa, Zhongyi and so many more will always be pleasant.

Most importantly, I want to thank my whole family. I am only here at this point because you encouraged me to do what I thought was right, always reassuring me that you have my back when it counts.

Finally, I want to thank Sonja, for being “tyrannical” enough with me to overcome and perhaps also overlook my many issues and for always being a strong and supportive partner at my side. Thank you so much!

Contents

1	Introduction	1
2	The Hubbard model	5
2.1	Motivation and Hamiltonian	5
2.2	Single-site limit	8
2.3	The Hubbard double-well with two interacting fermions	9
2.4	The two-dimensional Hubbard model	15
2.5	The Hubbard model extended to a bilayer	20
3	Quantum simulation with ultracold atoms	23
3.1	Internal state control	24
3.2	From lattice potentials to localised wave functions	27
3.3	The local-density approximation	34
3.4	Tunable interactions through Feshbach resonances	36
4	Experimental setup	41
4.1	Cooling to quantum degeneracy	41
4.1.1	Laser cooling	41
4.1.2	Magnetic transport and forced evaporation	43
4.1.3	Dipole trap and initial spin preparation	44
4.2	Lattice loading and physics phase	47
4.2.1	Lattice geometries	47
4.2.2	Loading into two dimensions	51
4.3	Detection and data analysis	53
4.3.1	In-situ imaging	53
4.3.2	Double occupancy detection	55
4.3.3	Radio frequency tomography of a single plane	57
4.3.4	Singles-doubles and spin-spin detection sequences	59
4.3.5	Potential mapping with the local density approximation	61
4.4	Potential engineering with a spatial light modulator	64
5	Simulating a Mott insulator using attractive interaction	73
5.1	Symmetries of the Hubbard model	73
5.2	The simulation of the spin-imbalanced Hubbard model	80
5.3	Testing and validating the particle-hole symmetry	84

6	Creating and characterising a Hubbard bilayer quantum simulator	89
6.1	Tuning the superlattice phase with a 30 GHz frequency lock	89
6.1.1	Optical up-conversion and beat detection	90
6.1.2	High frequency signal processing	90
6.1.3	Regulation and characterisation of the lock performance	92
6.2	Characterisation of the superlattice	94
6.2.1	Parametric heating of the bi-chromatic lattice	95
6.2.2	Band mapping in a merged vertical lattice	96
6.2.3	Second plane removal and phase sweeps	99
6.2.4	Induced inter-layer Rabi-oscillations	102
6.2.5	Interaction strength calibration	105
6.3	From band insulator to bilayer	106
6.3.1	Preparing a repulsive single-layer band insulator	107
6.3.2	Phase sweep preparation	109
6.3.3	Splitting the band insulator	111
7	Magnetic correlations in a fermionic Hubbard bilayer	113
7.1	Intra-layer spin correlations in the bilayer	113
7.1.1	Magnetisation and spin correlations	113
7.1.2	Measuring the uniform magnetic structure factor	116
7.1.3	Spin-spiral technique and the staggered structure factor	119
7.1.4	Observation of intra-layer spin correlations in the bilayer	123
7.2	Detecting inter-layer singlet pairs	125
7.3	Competing magnetic orders in the bilayer Hubbard model	133
8	Conclusion and outlook	137
A	Linewidth broadening of the dipole trap laser	151
	List of Figures	157

Introduction

For a physicist, complexity can be a double-edged sword. On the one hand, complexity in a physical problem usually adds to its richness and increases the general interest its solution could gain. On the other hand, however, complexity can render the question hard or even impossible to solve. Dealing with this trade-off between complexity and possible understanding might be at the core of the work of any physicist. The equation of motion of two masses interacting through gravity can be solved analytically, however, it is a relatively simple system to begin with and is limited in describing, for example, the motion of the moon. Adding complexity by introducing another heavy mass, however, renders this general three-body problem already unsolvable by analytic means alone [2]. Numerical simulations still provide a suitable solution to most of these analytically unsolvable problems. This is not the case any more when dealing with quantum physics, where the exponential growth of the parameter space and computation time with system size critically limits the feasibility of numerical simulations. The complexity required to describe many-body physics on the smallest energy scales, therefore, restricts the access we have to its solutions. There have been some successful approaches to ease this issue.

In solid-state physics, the second quantisation formalism allowed for a simpler description of the Hamiltonian for quantum many-body problems. Here the Hubbard model [3–6] for a strongly interacting electron gas in an ionic lattice was successful in describing macroscopic conduction features in a solid [7]. This rather simple model, allowing electrons to move discretised from site to site with only on-site interactions, was early on predicted to enable the description of high-temperature superconductivity [8]. Still, issues like the fermion sign-problem for quantum Monte-Carlo simulations [9] render the numerical simulation of larger systems with long-range correlations nearly impossible. A way to reduce the complexity of this computational problem is the use of symmetries in the system. Luckily the Hubbard Hamiltonian is rich in these symmetries, which help ease or avoid the sign-problem and allow a simulation in some parameter ranges [10]. One part of this thesis is dedicated to the analysis of one particularly interesting symmetry of the Hubbard model.

Another road to investigate quantum many-body systems is to simulate or mimic their behaviour using platforms made out of quantum matter instead of digital computers. This *analogue quantum simulation* is at the core of this thesis. Starting with the Hamiltonian we would like to investigate, we are required to create a system that directly reproduces this Hamiltonian. With such a simulator, we are able to measure states and energies of a system acting and evolving under the laws of

quantum physics. It moves the complexity of a nearly impossible numerical calculation to the technical complexity of control and detection of the quantum matter making up the simulator. In this regard, it is not a competitor to numerical simulations, but one of two different approaches that can complement and cross-check each other.

Many different platforms have been shown to be suitable for quantum simulation like trapped ions, quantum dots, superconducting circuits and more [11]. The choice of a quantum platform depends heavily on its suitability to simulate the required Hamiltonian. For example, the two-dimensional Hubbard model has been successfully simulated with neutral atoms in optical lattices in various groups worldwide [12–17]. In this thesis, I present new results obtained from a setup using fermionic potassium atoms, that has been built and improved over the last decade [18–24].

While the two-dimensional Hubbard model is fascinating and challenging, it might be missing crucial ingredients to explain the mechanisms of high-temperature superconductivity [25, 26]. By extending the Hubbard model with additional terms, we increase the complexity of the physical problem but might gain insights into the superconducting pairing mechanism. One interesting extension to the two-dimensional Hubbard model is the introduction of a bilayer structure, where two lattice layers are coupled with each other. It is assumed to enrich the phase diagram of the Hubbard model even more, while still maintaining its symmetries. The magnetic correlations between the spins of two fermions are believed to play an elementary role in the formation of superconducting pairs [27], so measuring the magnetic correlations in such systems is crucial to foster our understanding of the underlying physics. In this thesis, I discuss the required experimental modifications and calibrations to create a quantum simulator for a Hubbard bilayer model and present the, to our knowledge, first magnetic correlation measurement in a quantum simulator of a cold Hubbard bilayer.

Following this introduction, the Hubbard model is presented in chapter 2. After starting with the limit of a single-site connected to a grand-canonical bath and the half-filled two-site system, the phase diagram of the two-dimensional Hubbard model is discussed. Finally, we extend the Hubbard model to a bilayer system with distinct new low-temperature phases.

Chapter 3 explores the requirements and tools necessary for a quantum simulator with ultracold potassium atoms in optical lattices. The experimental setup including the most relevant electro-optical systems is then described in chapter 4, as well as the tomographic detection of a single two-dimensional lattice layer.

The aforementioned symmetries of the Hubbard model are the topic of chapter 5. One particularly intriguing particle-exchange symmetry allows the connection of systems with attractive and repulsive on-site interactions and at the same time between density-doped and spin-imbalanced systems. By experimentally mapping results of these parameter spaces, we prove the validity of our quantum simulation of the Hubbard Hamiltonian.

Chapter 6 discusses how we create a Hubbard bilayer system in our experiment and how the bilayer parameters like inter-layer tunnelling and on-site interaction are characterised. Using these results, chapter 7 then presents the detection of magnetic correlations in the bilayer in a wide parameter space and illustrates the two distinct methods for intra- and inter-layer correlation measurements.

An outlook to possible future work on the topics of this thesis is presented in chapter 8.

The following journal articles were published during the course of this work and are listed here chronologically:

- [28] J. H. Drewes, L. A. Miller, E. Cocchi, C. F. Chan, N. Wurz, **M. Gall**, D. Pertot, F. Brennecke and M. Köhl, “Antiferromagnetic Correlations in Two-Dimensional Fermionic Mott-Insulating and Metallic Phases”, *Phys. Rev. Lett.* 118, 170401 (2017).
- [29] N. Wurz, C. F. Chan, **M. Gall**, J. H. Drewes, E. Cocchi, L. A. Miller, D. Pertot, F. Brennecke and M. Köhl, “Coherent manipulation of spin correlations in the Hubbard model”, *Phys. Rev. A* 97, 051602 (2018).
- [30] **M. Gall**, C. F. Chan, N. Wurz and M. Köhl, “Simulating a Mott Insulator Using Attractive Interaction”, *Phys. Rev. Lett.* 124, 010403 (2020).
- [31] C. F. Chan, **M. Gall**, N. Wurz and M. Köhl, “Pair correlations in the attractive Hubbard model”, *Phys. Rev. Research* 2, 023210 (2020).
- [32] **M. Gall**, N. Wurz, J. Samland, C. F. Chan and M. Köhl, “Competing magnetic orders in a bilayer Hubbard model with ultra-cold atoms”, *Nature* (accepted, soon to be published).

The Hubbard model

The Hubbard model has been used successfully throughout the years to simulate and help understand the physics of condensed matter systems. It is, therefore, not surprising that this simple-to-describe but hard-to-solve problem would be an ideal candidate for quantum simulation. This chapter will introduce the Hubbard model and discuss the approximations and assumptions that are used to obtain it. Furthermore, we will discuss solvable limiting cases, like the single-site and two-site limit including potential tilts. The insights gained there will be used in the description of the phase diagram of the two-dimensional Hubbard model. This basic model is then extended to describe two interconnected two-dimensional Hubbard planes: the Hubbard bilayer.

2.1 Motivation and Hamiltonian

The Hubbard model presents a simple system which describes the interplay of kinetic energy and interactions between fermionic particles, leading to insulating and magnetically ordered states [33, 34]. It is also predicted to feature a superconducting phase at low temperature, with the same underlying mechanisms as in high-temperature superconductors like the cuprates [8]. Since its first form was written down in 1963 and 1964 [3–6] it has been studied with a variety of computational methods, from dynamical mean field approaches [35, 36] to tools like numerical linked cluster expansion (*NLCE*) [37] and quantum Monte-Carlo (*QMC*) simulations [38, 39]. A special version of the latter, the determinant quantum Monte-Carlo (*DQMC*) method was implemented in a toolset provided by the group of R.T. Scalettar [40] which was then used in our group to compare and evaluate experimental output. This is described in detail in [24].

Nevertheless, most of these numerical methods have shortcomings, for example, working only at zero temperature, at finite size or only giving approximate solutions. Famously, the fermion sign problem [9] makes it impossible to solve large *QMC* simulations on classical computers. Here, quantum simulation with ultracold atoms provides an alternative route, which is described in detail in the later chapter 3. First, we will explore the Hubbard model itself. A very good reference to start with is provided in [33, 34], from which some of the following content is adapted and modified.

The Hubbard model describes spin-1/2 particles in a lattice structure, by using creation $\hat{c}_{i,\sigma}^\dagger$ and annihilation operators $\hat{c}_{i,\sigma}$ similar to those in a harmonic oscillator [33, 34]. Here, however, the index i indicates a discrete position on a lattice with σ indicating the spin of the created or annihilated

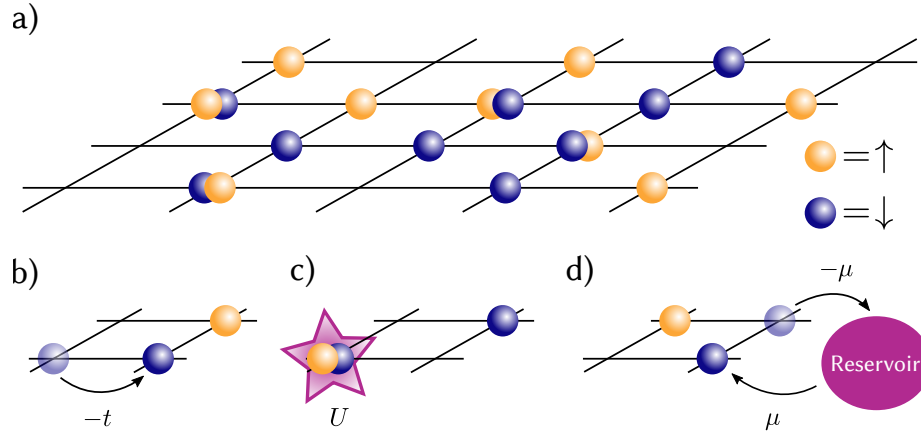


Figure 2.1: The Hubbard model in two dimensions. a) Orange (blue) circles represent spin-up (-down) fermionic particles, occupying sites on a discretised lattice structure. b) These particles can move or tunnel from one site to another, thereby lowering their kinetic energy by $-t$. We restrict ourselves to the discussion of nearest-neighbour tunnelling only. c) The maximal occupation number per site is 2, one spin-up and one spin-down particle, due to the Pauli exclusion principle. These doubly occupied sites, called *doubles*, experience an on-site interaction energy U , which is repulsive for $U > 0$ and attractive for $U < 0$. d) In the grand-canonical description used in this thesis, the atom number is not fixed, but determined by the chemical potential μ , which is the energy increase of adding one additional particle from a reservoir to the system.

particle. These are fermion operators, and therefore they obey anti-commutation relations:

$$\{\hat{c}_{i,\sigma}, \hat{c}_{j,\sigma'}^\dagger\} = \delta_{i,j} \delta_{\sigma,\sigma'} \quad (2.1)$$

$$\{\hat{c}_{i,\sigma}^\dagger, \hat{c}_{j,\sigma'}^\dagger\} = 0 \quad (2.2)$$

$$\{\hat{c}_{i,\sigma}, \hat{c}_{j,\sigma'}\} = 0 \quad (2.3)$$

With this, we define the number operator, that counts the number of particles with spin σ on site i :

$$\hat{n}_{i,\sigma} = \hat{c}_{i,\sigma}^\dagger \hat{c}_{i,\sigma}. \quad (2.4)$$

We will employ the *single-band approximation* which combined with the Pauli-exclusion principle means that we can only have one particle for each spin on a single lattice site i . We will discuss this and other approximations in more detail in section 3.2. With these operators we can start to describe a model which should have three ingredients: a kinetic part \hat{H}_{kin} describing movement in the lattice, an interaction term \hat{H}_{int} which includes that energy can be raised or lowered if particles interact with each other, and one that determines the overall particle number in the system $\hat{H}_{\text{chem-pot}}$. Figure 2.1 illustrates the model with the three terms which we will discuss in the following.

Kinetic term and tunnelling

We first describe the motion of a spin up (\uparrow) particle sitting on lattice site i , going to another site j . This we can do by first applying the annihilation operator $\hat{c}_{i,\uparrow}$ on our initial state, and afterwards

create a particle with the same spin on the other site with the operator $\hat{c}_{j,\uparrow}^\dagger$. The connected kinetic energy with this event is described by $-t_{ij}$, the tunnelling amplitude. It has a negative value, since the spatial delocalisation of the particle allows for a reduction in kinetic energy. This tunnelling from site i can theoretically go to any given site j and might have a position dependent amplitude. We will, however, limit ourselves to allow only a movement from adjacent sites with a fixed amplitude, the nearest-neighbour tunnelling t . The full kinetic term now is described by

$$\hat{H}_{\text{kin}} = -t \sum_{\langle i,j \rangle, \sigma} \left(\hat{c}_{i,\sigma}^\dagger \hat{c}_{j,\sigma} + \hat{c}_{j,\sigma}^\dagger \hat{c}_{i,\sigma} \right) \quad (2.5)$$

where $\langle i, j \rangle$ indicates that only combinations of i and j are considered with j neighbouring i .

On-site interaction

As a next step we would like to add interactions between the particles of our model. First, one has to determine the type of interaction combined with a length scale or range. For the Hubbard model the simplest interaction was chosen, a strictly local interaction, where particles only interact if both are at the same location, in our case the same lattice site. Since Pauli blocking in combination with the single band approximation prohibits two particles with equal spin to occupy the same site, this interaction can only happen between particles with different spin. For attractive (repulsive) on-site interaction the energy of the state gets lowered (raised) by $|U|$ for each double site-occupancy. This means that $U > 0$ describes repulsive interactions, whereas $U < 0$ leads to attractively interacting particles. Therefore, the interaction term is written as

$$\hat{H}_{\text{int}} = U \sum_i \hat{n}_{i,\uparrow} \hat{n}_{i,\downarrow}. \quad (2.6)$$

Particle filling and chemical potential

What is now missing is a way to describe how many particles are on the lattice we are investigating. An elegant way to do this is to use the description of a grand canonical ensemble. In it we look at a system with a given volume, i.e. the number of lattice sites and let the system be in contact with a particle reservoir with a certain chemical potential μ_σ . Note that this chemical potential can be different for each spin. Removing a particle from the system now has an energy cost of μ_σ , while the insertion of it releases this energy. The chemical potential term now will be written as

$$\hat{H}_{\text{chem-pot}} = - \sum_{i,\sigma} \mu_\sigma \hat{n}_{i,\sigma}. \quad (2.7)$$

The Hubbard Hamiltonian

Combining all of these terms we obtain the Hubbard Hamiltonian, which fully describes the model:

$$\hat{H} = -t \sum_{\langle i,j \rangle, \sigma} \left(\hat{c}_{i,\sigma}^\dagger \hat{c}_{j,\sigma} + \hat{c}_{j,\sigma}^\dagger \hat{c}_{i,\sigma} \right) + U \sum_i \hat{n}_{i,\uparrow} \hat{n}_{i,\downarrow} - \sum_{i,\sigma} \mu_\sigma \hat{n}_{i,\sigma} \quad (2.8)$$

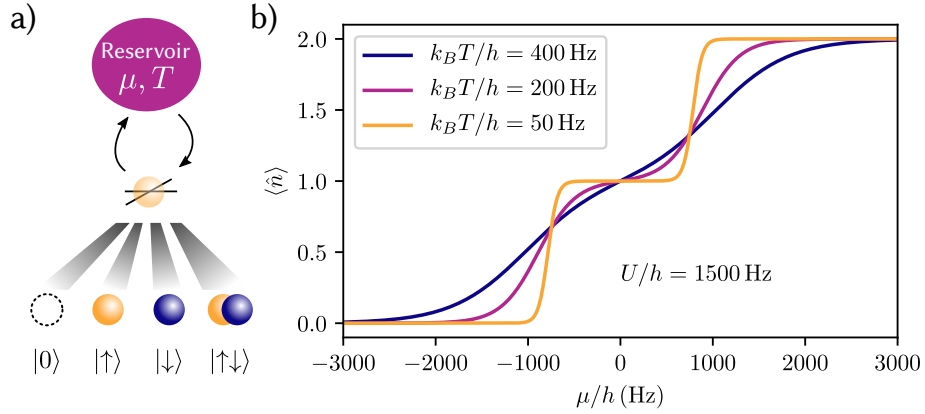


Figure 2.2: Single-site limit. a) A single site is connected to a particle reservoir (μ) and a thermal bath (T). The measurement basis consists of four states: an empty site $|0\rangle$, a singly occupied site of spin-up (down) $|\uparrow\rangle$ ($|\downarrow\rangle$), called *single*, or a doubly occupied site $|\uparrow\downarrow\rangle$ called *double*. b) This model can be solved analytically even with interactions. The total particle occupation number of this site $n(\mu)$ is shown for three different temperatures and repulsive interactions ($U > 0$). For low temperatures a feature similar to the so called *Mott-plateau* appears, where the density stays constant $n \approx 1$ around $\mu = 0$. The figure is inspired by [33].

Adding constant energy terms does not influence the dynamics of the evolution or the solution in general. For a fixed number of lattice sites the grand canonical description allows us to rewrite the Hamiltonian in a way which will later become more handy, especially considering certain symmetries of the Hubbard model, which we will discuss in detail in chapter 5.

$$\hat{H} = -t \sum_{\langle i,j \rangle, \sigma} \left(\hat{c}_{i,\sigma}^\dagger \hat{c}_{j,\sigma} + \hat{c}_{j,\sigma}^\dagger \hat{c}_{i,\sigma} \right) + U \sum_i (\hat{n}_{i,\uparrow} - 1/2) (\hat{n}_{i,\downarrow} - 1/2) - \sum_{i,\sigma} \mu_\sigma (\hat{n}_{i,\sigma} - 1/2) \quad (2.9)$$

This Hamiltonian can be used for one-, two- or three-dimensional systems. We continue with discussing several configurations in the next sections, but for the majority of this thesis the two-dimensional Hubbard Hamiltonian will be used. Most of the time we will investigate systems where the chemical potential for both spins is equal, resulting in an even ratio of spin-up to spin-down particles, the *spin-balanced* case. There we simplify further and assign a general chemical potential without index $\mu = \mu_\uparrow = \mu_\downarrow$.

In the following, two toy models are presented, the single-site limit and the half-filled double-well, forming the basic building blocks of the Hubbard model and giving insights into the properties of the many-site models.

2.2 Single-site limit

In order to avoid the computational complexity of large systems and by choosing the minimal size representation in the grand canonical description, we can start with a volume/site number of just one site. Alternatively we can set $t = 0$, such that the only operators in the Hamiltonian in equation 2.9 are the number operators $\hat{n}_{i,\sigma}$, which commute with all terms in the Hamiltonian itself

$[\hat{H}, \hat{n}_{i,\sigma}] = 0$. This means we can treat each site individually, again reaching the single-site limit. The following discussion was mostly adapted from [33].

All four possible site occupations shown in figure 2.2 are eigenstates to this Hamiltonian, with the following eigenenergies:

$$\begin{aligned}\hat{H} |0\rangle &= (U/4 - \mu) |0\rangle \\ \hat{H} |\uparrow\rangle &= -U/4 |\uparrow\rangle \\ \hat{H} |\downarrow\rangle &= -U/4 |\downarrow\rangle \\ \hat{H} |\uparrow\downarrow\rangle &= (U/4 + \mu) |\uparrow\downarrow\rangle\end{aligned}$$

With this diagonal form of the Hamiltonian and including a temperature with $\beta = 1/k_B T$ we can calculate the partition function directly:

$$Z = \text{Tr} \left[e^{-\beta \hat{H}} \right] = e^{-\beta(U/4 - \mu)} + 2e^{-\beta(-U/4)} + e^{-\beta(U/4 + \mu)} \quad (2.10)$$

Similarly, expectation values of operators like the total number operator $\hat{n} = \hat{n}_\uparrow + \hat{n}_\downarrow$ can be computed:

$$\langle \hat{n} \rangle = \langle \hat{n}_\uparrow + \hat{n}_\downarrow \rangle = \text{Tr} \left[(\hat{n}_\uparrow + \hat{n}_\downarrow) e^{-\beta \hat{H}} \right] Z^{-1} = \left(2e^{-\beta(-U/4)} + 2e^{-\beta(U/4 - \mu)} \right) Z^{-1} \quad (2.11)$$

With it we can investigate the changes of the site occupation while varying the reservoir properties μ and T and also the interaction U . For repulsive interactions of $U/h = 1500$ Hz the results of the simulations with different temperatures are shown in figure 2.2 b). This $n(\mu, T) = \langle \hat{n}(\mu, T) \rangle$ is the *equation of state*, that provides access to all thermodynamic variables of the system in equilibrium. At $\mu = 0$ we observe that on average we have one atom per site, half of the maximum of two atoms. This fix point is the so-called *half-filling*, which is also present in the many-site Hubbard Hamiltonian. Even in the single-site limit, we already observe the emergence of density ordering, since for temperatures T much lower than the interaction strength $U > 0$, any double occupancy is an excitation that is energetically unfavourable. Close to half-filling, we get a density plateau, which has the size of $\Delta\mu \approx U$. This is the so called *Mott* regime. As we have focused now on the density, i.e. the average filling, we investigate how spin ordering arises in the following section.

2.3 The Hubbard double-well with two interacting fermions

The double-well is a model describing two sites, coupled by a tunnelling term t and with on-site interaction U . Even though this is the bare minimal size for the Hubbard description with particle hopping, it nevertheless encapsulates many of its aspects, since the tunnelling allows for a delocalisation of the states, therefore, lowering their kinetic energy.

We start to investigate the upcoming competition of kinetic energy, interactions and later in this section potential energy differences. In the following we will fix the filling to $n = 1$ and focus on the case of a double-well filled with two fermions of opposite spin. There both particles are free to move on either site, albeit with potential energy cost of U when being on the same one. With the notation of |occupation left well, occupation right well>, we can define a complete basis with $|\uparrow\downarrow, 0\rangle, |\uparrow, \downarrow\rangle, |\downarrow, \uparrow\rangle, |0, \uparrow\downarrow\rangle$. Using this basis and allowing a transition between the states through

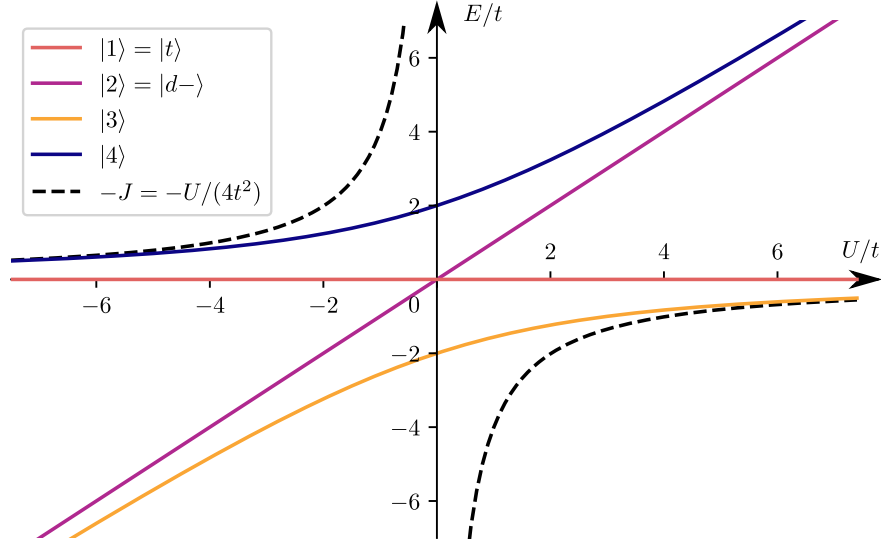


Figure 2.3: Eigenenergies of the balanced double-well. Plotted are the solutions to the Hamiltonian described in equation 2.12. The energy of eigenstates consisting mostly of a superposition of doubly occupied, i.e. $|d+\rangle$, $|d-\rangle$ sites is close to linear in U for $|U| \gg t$. The ground state $|3\rangle$ is dominated by contributions of doubles for large attractive interactions $U < -t$. However, this changes for repulsive interactions $U \gg t$, where the ground state is close to a pure singlet state $|s\rangle$ and the difference to the triplet state $|t\rangle$ is determined by the superexchange energy J .

tunnelling we are able to write the Hamiltonian as:

$$\hat{H} = \begin{pmatrix} U & -t & t & 0 \\ -t & 0 & 0 & -t \\ t & 0 & 0 & t \\ 0 & -t & t & U \end{pmatrix} \quad (2.12)$$

Diagonalising this matrix, we get the eigenenergies of the Hamiltonian:

$$\lambda_1 = 0 \quad (2.13)$$

$$\lambda_2 = U \quad (2.14)$$

$$\lambda_3 = U/2 - \sqrt{4t^2 + U^2/4} \quad (2.15)$$

$$\lambda_4 = U/2 + \sqrt{4t^2 + U^2/4}. \quad (2.16)$$

These eigenenergies are plotted in figure 2.3 as a function of U . For large values of U we can observe a clear separation of two pairs of states with energy difference of approximately U , which arises from contributions of the doubly occupied states. Additionally we see that while for repulsive interactions $U > 0$ the low energy eigenstates are mostly dominated by the singly occupied sites without the interaction energy shift U , doubly occupied state contributions are preferred on the attractive interaction side $U < 0$. We now introduce the notation of calling these doubly occupied

sites *doubles* in contrast to the singly occupied sites, the *singles* or the empty ones, the *holes*. We start with an initial guess for a new basis of states, with two states consisting of doubles and two of singles only:

$$|d-\rangle = (|\uparrow\downarrow, 0\rangle - |0, \uparrow\downarrow\rangle)/\sqrt{2} \quad (2.17)$$

$$|d+\rangle = (|\uparrow\downarrow, 0\rangle + |0, \uparrow\downarrow\rangle)/\sqrt{2} \quad (2.18)$$

$$|s\rangle = (|\uparrow, \downarrow\rangle - |\downarrow, \uparrow\rangle)/\sqrt{2} \quad (2.19)$$

$$|t\rangle = (|\uparrow, \downarrow\rangle + |\downarrow, \uparrow\rangle)/\sqrt{2}. \quad (2.20)$$

Because of their spin symmetry $|s\rangle$ is usually called the *singlet* and $|t\rangle$ the *triplet* state. Solving for the exact eigenstates of the double-well Hamiltonian we get:

$$|1\rangle = |t\rangle \quad (2.21)$$

$$|2\rangle = |d-\rangle \quad (2.22)$$

$$|3\rangle = \frac{|s\rangle - \frac{\lambda_3}{2t} |d+\rangle}{\sqrt{1 + \left(\frac{\lambda_3}{2t}\right)^2}} \quad (2.23)$$

$$|4\rangle = \frac{|s\rangle - \frac{\lambda_4}{2t} |d+\rangle}{\sqrt{1 + \left(\frac{\lambda_4}{2t}\right)^2}}. \quad (2.24)$$

We can see that our initial guess already was correct for two eigenstates $|1\rangle, |2\rangle$, which are also the ones with the simplest eigenenergies of $\lambda_1 = 0, \lambda_2 = U$. The other two, $|3\rangle, |4\rangle$ are mixtures of states with singles and states with doubles, with the mixing ratio determined by U/t .

For our discussion about spin-spin correlations, we will focus on $U \gg t$. Here it is easy to see that $|3\rangle \approx |s\rangle$ and $|4\rangle \approx |d+\rangle$. Additionally we can discard states with energy $\approx U$ in the following as high energy excitations. In this limit we approximate the ground state energy to

$$\lambda_3 = \frac{U}{2} - \sqrt{4t^2 + \frac{U^2}{4}} = \frac{U}{2} - \frac{U}{2} \sqrt{\frac{16t^2}{U^2} + 1} \approx \frac{U}{2} - \frac{U}{2} \left(\frac{8t^2}{U^2} + 1 \right) = -\frac{4t^2}{U}. \quad (2.25)$$

This lowering of the energy by $J = 4t^2/U$ can be understood as a second order perturbation to the singlet state, called *superexchange*. As shown in figure 2.4, even though a double occupancy is energetically unfavourable, and thus particle hopping suppressed, the particles can switch places or just lower their kinetic energy by tunnelling with an intermediate step through a double occupancy. This is why the ground state is not a pure singlet, but has an admixture of double occupancies.

Following the perturbation approach one can derive this directly by assuming the tunnelling terms in equation 2.12 (\hat{H}_{kin}) are a perturbation and that the interaction Hamiltonian $\hat{H}_{\text{int}} = U \sum_i \hat{n}_{i,\uparrow} \hat{n}_{i,\downarrow}$ is the unperturbed one [34]. The perturbative energy shift of the singlet $|s\rangle$ is then calculated as

$$\Delta E_{|s\rangle} = \langle s | \hat{H}_{\text{kin}} | s \rangle \approx - \sum_{|d\rangle=|\uparrow\downarrow,0\rangle,|0,\uparrow\downarrow\rangle} \frac{\langle s | \hat{H}_{\text{kin}} | d \rangle \langle d | \hat{H}_{\text{kin}} | s \rangle}{\langle d | \hat{H}_{\text{int}} | d \rangle}. \quad (2.26)$$

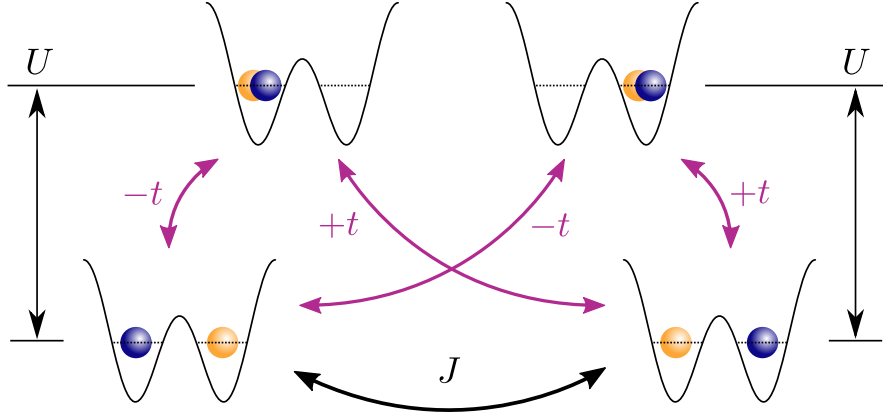


Figure 2.4: The superexchange. For large repulsive interaction strength $U \gg t$ direct tunnelling between the bottom two states with singles only is suppressed due to the high energetic cost of a double occupancy. By a virtual intermediate step to form an energetically unfavourable double, one can exchange the particles and lower their kinetic energy by the superexchange energy J . This process does not have to result in the exchange of particles, while still leading to a temporary delocalisation with a reduction in kinetic energy. The same argument is valid as well for strong attractive interactions $U \ll t$ with the virtual coupling between both states with doubles, here in the upper part of the figure. Figure inspired by [41].

We start the calculation from the simple single term:

$$\langle s | \hat{H}_{\text{kin}} | \uparrow\downarrow, 0 \rangle = \frac{1}{\sqrt{2}} (\langle \uparrow, \downarrow | - \langle \downarrow, \uparrow |) (-t | \uparrow, \downarrow \rangle + t | \downarrow, \uparrow \rangle) = -\sqrt{2}t. \quad (2.27)$$

It is very important to note that for the triplet $|t\rangle$, because of its symmetry, this term would be zero. Therefore, the triplet does not have an energy shift in this perturbation approach. For both virtual states $\langle d | \hat{H}_{\text{int}} | d \rangle = U$, so

$$\Delta E \approx - \sum_{|d\rangle=|\uparrow\downarrow,0\rangle,|0,\uparrow\downarrow\rangle} \frac{(-\sqrt{2}t)^2}{U} = -2 \times \frac{2t^2}{U} = -\frac{4t^2}{U} = -J. \quad (2.28)$$

With this perturbative calculation we could reproduce the energy difference value of equation 2.25, which indicates that the model of virtual hopping is valid for further discussions.

The superexchange allows for particle exchange even with strong repulsive interactions present, which one would naively assume to be blocked and is present in all Hubbard models with repulsive interactions. For attractive interactions a similar second order process allows a tightly bound double to move, again lowering the energy of the state through delocalisation. As we will discuss in section 2.4, this leads to antiferromagnetic spin ordering ($U > 0$) and the *charge density wave* (CDW) density ordering ($U < 0$).

The tilted double-well

In the previous section, we discussed the two-site Hubbard model with two fermions of opposite spin, where both sites have the same potential energy. We now will have a look at what happens if

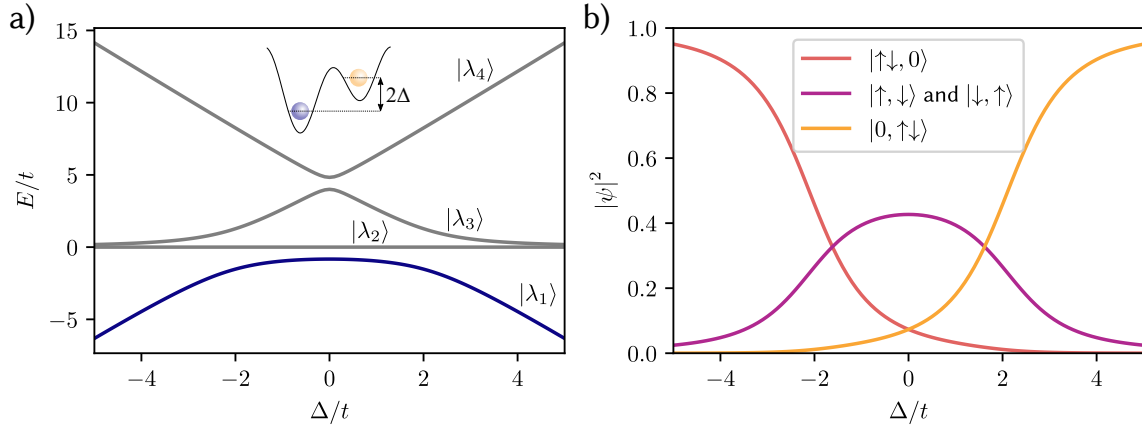


Figure 2.5: Eigenenergies and ground state composition of the tilted double-well. a) Eigenenergies of the tilted double-well obtained by solving the Hamiltonian of equation 2.29 with repulsive interactions $U = +4t$. For large site imbalance $|\Delta| > U$ the on-site interaction is not sufficient any more to repel a double occupancy of the lower site. b) This can be seen in the state decomposition of the ground state $|\lambda_1\rangle$, which has its most significant singles population when $|\Delta| < U/2$.

one lifts this degeneracy by introducing a site-dependent potential energy where 2Δ is the total energy offset between the two sites, see inset of figure 2.5 a). In the following we will focus on two points. First we will discuss how the ground state composition changes with respect to a varying Δ . We then investigate how spin correlations form through a modified version of the superexchange process.

The Hamiltonian will again be our starting point for calculating the eigenstates of a spin-balanced system at half-filling and is written in the previously used basis $|\uparrow\downarrow, 0\rangle, |\uparrow, \downarrow\rangle, |\downarrow, \uparrow\rangle, |0, \uparrow\downarrow\rangle$:

$$\hat{H} = \begin{pmatrix} U + 2\Delta & -t & t & 0 \\ -t & 0 & 0 & -t \\ t & 0 & 0 & t \\ 0 & -t & t & U - 2\Delta \end{pmatrix}. \quad (2.29)$$

By the choice of the symmetric offset around a mean potential energy, the energetic shift only manifests in the double occupancies. In figure 2.5 a) the eigenenergies for $U/t = 4$ are shown. At $\Delta = 0$ we can identify the states with the solution to the balanced double-well from the previous section, with the lowest two being the ones with only small admixture of doubles, close to the singlet $|s\rangle$ and triplet $|t\rangle$ state. Once the detuning becomes the dominant energy scale, when $|\Delta| > |U|$, the mostly doubly occupied states clearly separate, having an eigenenergy contribution proportional to $\pm 2\Delta$, in contrast to states with mostly singles that are balanced on both sides. The decomposition of the ground state, i.e. the state with the lowest energy highlighted in blue, into the basis vectors is shown in figure 2.5 b) as a function of site imbalance Δ . Here we plotted the absolute value squared of the ground state amplitudes in the initial basis in which we have defined the Hamiltonian of equation 2.29. For attractive interactions this distribution is similar, but compressed along the Δ -axis, since the doubles are energetically favourable, and remain dominant until both sites have nearly the same potential $\Delta \approx 0$. These findings will be later used in chapter 6.

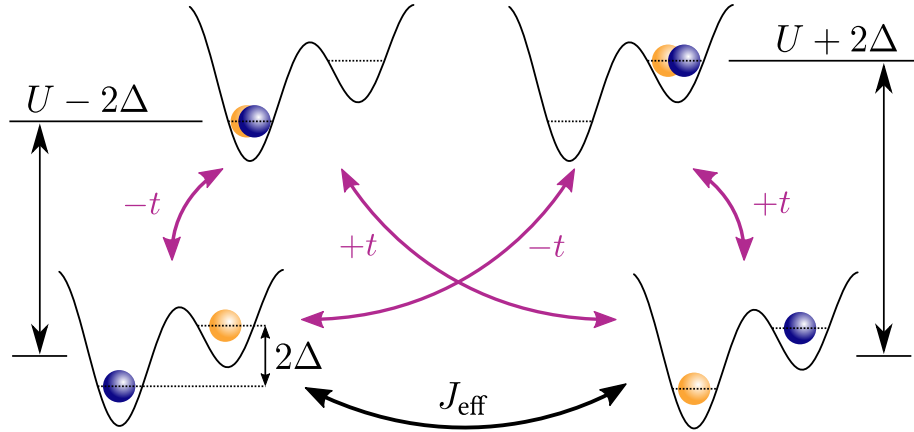


Figure 2.6: Superexchange in a tilted double-well. Even with a site dependent energy offset, the virtual interaction can occur via two intermediate states which are energetically non-degenerate. Those still allow for tunnelling, but have to be included in the calculation of the effective superexchange coupling J_{eff} . The figure is inspired by [42].

After the potential imbalance Δ has been introduced into the system the single particle tunnelling has to change to an effective tunnelling t_{eff} that includes this site dependent energy offset. This is similar as for a two-level system with off-resonant coupling, which we will discuss in the next chapter. We can do this by solving the single particle Hamiltonian

$$\hat{H} = \begin{pmatrix} \Delta & -t \\ -t & -\Delta \end{pmatrix}, \quad (2.30)$$

where we used the basis of a particle being on the left $|L\rangle$ or right $|R\rangle$ site. The resulting difference in the eigenenergies is the new effective tunnelling

$$t_{\text{eff}} = \sqrt{t^2 + \Delta^2}. \quad (2.31)$$

With the tunnelling modified, the question arises how the superexchange of two particles of opposing spin has to be adjusted. For this we use results already obtained in section 2.3, where we used a perturbation approach to calculate the additional energy shift. The intermediate levels for the second order process are, however, not degenerate as in figure 2.4 but we have to include the energy shift of $\pm 2\Delta$, as shown in figure 2.6. Similar to equation 2.28 the effective superexchange coupling can be obtained as a sum that includes contributions of both intermediate levels [42]:

$$J_{\text{eff}} = \frac{2t^2}{U - 2\Delta} + \frac{2t^2}{U + 2\Delta} = \frac{4t^2U}{U^2 - 4\Delta^2}. \quad (2.32)$$

One has to keep in mind that this comes from a calculation where tunnelling is assumed to be a perturbation, which is only valid for $J_{\text{eff}} \ll U - 2\Delta$. Even though tunnelling might be greatly suppressed due to the energy difference, the spins can build correlations mediated through superexchange.

2.4 The two-dimensional Hubbard model

The Hubbard Hamiltonian, introduced in equation 2.9, is not restricted to a certain spatial dimension, for example, it can be exactly solved in the case of a one-dimensional lattice [43]. For this thesis and our experimental setup, however, we were initially most interested in the two-dimensional Hubbard model, where the sites are positioned on a square two-dimensional lattice.

The two-dimensional Hubbard model has been studied extensively, for example in the search for an explanation of the high-temperature superconductivity in cuprates [8]. In this section I will discuss some of the expected phase diagrams and their properties. We assume a balanced number of spin up and down particles, the so called *spin-balanced* case. It is most relevant for solid state physics where a small spin-imbalance requires huge magnetic fields, which in general are not realised in real material samples. Exceptions to this, especially in the context of symmetries in the Hubbard model will be discussed in chapter 5.

We will restrict the model to only allow nearest-neighbour tunnelling and on-site interactions. This model cannot be solved analytically, only in some special cases like in the single-site limit discussed previously. Numerical simulations using approximations also struggle to get reliable results for all parameter ranges or are limited to very small system sizes. However, having introduced the Hubbard model and two solutions to it, we can use the knowledge gained to discuss some of the expected properties of the two-dimensional Hubbard model.

The Hubbard model in momentum space

We first want to extend the spatially localised description further to a very large size by changing to the momentum basis of an extended lattice. The Hubbard Hamiltonian of equation 2.9 is written in a localised basis of the lattice sites j for the creation and annihilation operators $\hat{c}_{j,\sigma}^\dagger, \hat{c}_{j,\sigma}$. We now specifically work with a two-dimensional lattice so the site index can be represented as a vector $\mathbf{j} = (j_x, j_y)$. We define the same operators in the discrete momentum space \mathbf{k} of a finite lattice with N sites [33]:

$$\hat{c}_{\mathbf{k},\sigma} = \frac{1}{\sqrt{N}} \sum_{\mathbf{j}} e^{-i\mathbf{k}\cdot\mathbf{j}a} \hat{c}_{\mathbf{j},\sigma} \quad (2.33)$$

$$\hat{c}_{\mathbf{k},\sigma}^\dagger = \frac{1}{\sqrt{N}} \sum_{\mathbf{j}} e^{i\mathbf{k}\cdot\mathbf{j}a} \hat{c}_{\mathbf{j},\sigma}^\dagger, \quad (2.34)$$

where the momentum vector is given by $\mathbf{k} = (k_x, k_y)$, and the principal lattice axes have the same spacing $a_x = a_y = a$ and are orthogonal. The kinetic part of the Hamiltonian can now be rewritten in this new operator basis, as

$$\hat{H}_{\text{kin}} = -t \sum_{\langle i,j \rangle, \sigma} \left(\hat{c}_{i,\sigma}^\dagger \hat{c}_{j,\sigma} + \hat{c}_{j,\sigma}^\dagger \hat{c}_{i,\sigma} \right) = \sum_{\mathbf{k}, \sigma} \epsilon_{\mathbf{k}} \hat{c}_{\mathbf{k},\sigma}^\dagger \hat{c}_{\mathbf{k},\sigma}, \quad (2.35)$$

with the dispersion relation

$$\epsilon_{\mathbf{k}} = -2t \left(\cos(k_x a) + \cos(k_y a) \right). \quad (2.36)$$

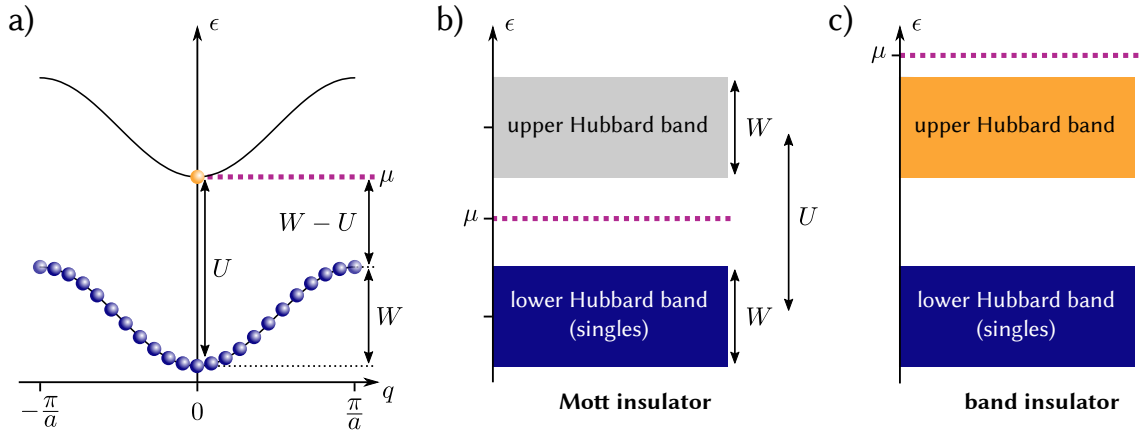


Figure 2.7: The Hubbard band picture. a) Shows a two spin component lattice where each site is filled with one spin component (blue). Since all momentum states are now occupied and the band is full it is an insulating state. An additional particle of opposite spin (orange) will have an increased energy by the on-site interaction U . However, this shift is present for all sites, so the particle can move freely as if it is in an empty band. The picture of two bands can be extended to include all particles on singly occupied sites in the lower so called *Hubbard band*, whereas a doubly occupied site has one particle in the lower and one in the upper band, shifted by U . b) If the chemical potential μ now lies in between both bands and the temperature is lower than their separation, only the lower Hubbard band is filled, and we have an insulating state due to a completely filled band. c) If the upper band is filled as well, that means we have a double occupancy on each site, we enter the band insulating regime. This picture of separated bands is only valid in the large interaction regime $U \gg W$.

In a non-interacting system where $U = 0$ or with a spin polarised population this dispersion relation is the band structure of the cubic lattice. In a lattice it is reasonable to use the quasi-momentum $\mathbf{q} = \mathbf{k}$ in the first Brillouin-zone $q_{x,y} \in [-\pi/a, \pi/a]$. We identify the bandwidth W in terms of the tunnelling energy t and the number of dimensions d :

$$W = \max_{\mathbf{k}}(\epsilon_{\mathbf{k}}) - \min_{\mathbf{k}}(\epsilon_{\mathbf{k}}) = 2t \times d = 4t \quad \text{for: } d = 2 \quad (2.37)$$

Figure 2.7 a) shows the state occupation when nearly all lattice sites are occupied with particles of one spin only. Each momentum state is occupied and due to Pauli-blocking no further particle of this spin can be present. A redistribution of particles or density movement is not possible, which is why a completely filled band is insulating. If we now add one particle of the opposite spin, it will see an empty band, shifted with the on-site interaction energy U . This is true for a lattice where all lattice sites are occupied by particles of one spin or when the on-site interaction $U = 0$.

In general interactions distort the exact band structure such that we cannot use this solution for non-zero interactions. It is, however, useful to introduce the pedagogical concept of the *Hubbard bands*, see figure 2.7 b) and c). The lower Hubbard band consists of all singly occupied sites, now allowing both spins, whereas all doubly occupied sites additionally contribute one particle to the upper band. If a band is not completely filled as in figure 2.7 a), particles can tunnel and so the system is in a metallic state. The definition of a metal or a *charge* in the Hubbard model comes from the initial motivation for this model, where the fermions on the lattice are representing the charge carrying electrons. Assuming strong repulsive interactions $U \gg W = 4t$ both bands separate with

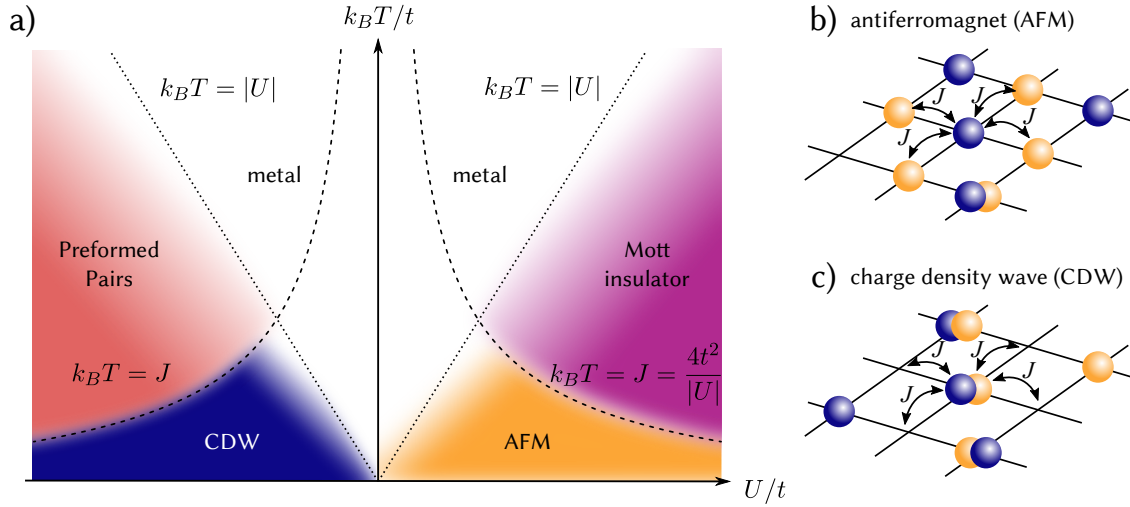


Figure 2.8: Phase diagram of the half-filled two-dimensional Hubbard model. a) When the temperature $k_B T$ is low enough, ordering appears from the hot unordered metallic phase. On the repulsive side $k_B T < |U|$ leads to density ordering by the formation of a Mott insulator. Through the superexchange J an antiferromagnetically ordered state is energetically favourable, see b). On the attractive side, a magnetic or spin ordering occurs first, by the formation of doubly occupied sites and holes, both with no effective magnetisation, in the *Preformed Pairs* phase. For even lower temperature density ordering appears as well in the formation of the *charge density wave* shown in c).

energetic distance of $\sim |U| - W$. The filling of these bands is again determined by the chemical potential μ . For very large $\mu \gg U, W$ the lattice is completely filled with all sites doubly occupied. Therefore, both bands are full and the system is insulating. This state is called a *band insulator*. At strong interactions $U \gg 4t$ and half-filling, where the site occupation is one, the chemical potential lies in between both bands. For low temperatures $k_B T < U$ particles mostly fill up the lower band, forming again an insulating state, the so called *Mott-insulator*. In contrast to the Band insulator, which is present for all interactions, even attractive ones $U < 0$, this feature emerges only from the strong repulsive interaction in the system. The behaviour of Mott insulators was discussed in condensed mater systems, especially in the transition metal oxides [7] to which the Hubbard model provides a good explanation. This interplay of interactions and kinetic energy defines the phase diagram of the two-dimensional Hubbard model.

Phase diagram at half-filling

We will continue our discussion at half-filling ($\mu = 0$) where each site has an average particle occupation of one $n = \langle \hat{n} \rangle = \langle \hat{n}_\downarrow + \hat{n}_\uparrow \rangle = 1$. The phase diagram there is shown in figure 2.8. Since the filling is fixed, any reduction in entropy can only occur in density or magnetic ordering. For strong repulsive interactions $U/t > 4$ the atoms in the Mott-insulator distribute such that most sites are singly occupied. This state is reached once the thermal energy is lower than the energy cost of a doubly occupied site $k_B T < U$, which can be treated like an excitation. This is a result we know already from the balanced double-well from section 2.3, where for large U the lowest energy states $|3\rangle = |t\rangle, |4\rangle \approx |s\rangle$ in figure 2.3 consist mostly of singles. When the temperature is even

lower than the superexchange energy $k_B T < J = 4t^2/U$ we additionally expect that the spins begin to arrange to an antiferromagnet (AFM). Both these conditions are met in figure 2.8 where the orange shaded region marks the expected AFM, with the highest critical temperature around $U/t = 8$. A somehow similar behaviour is expected for attractive interactions $U < 0$, which we can understand as well by starting with the double-well picture. For $U/t < 4$ a doubly occupied site lowers the energy by U and singly occupied sites can be seen as excitations from the ground state. Therefore, in the double-well the lowest energy states $|2\rangle = |d-\rangle$, $|4\rangle \approx |d+\rangle$ in figure 2.3 consist of a doubly occupied site with a hole. Similar for the extension to a two-dimensional lattice, at temperatures lower than the interaction strength $k_B T < |U|$, the spin-up and spin-down particles combine to form doubles and holes. This can be described as a *Preformed Pairs phase* [44]. Once even lower temperatures $k_B T < |J| = |4t^2/U|$ are reached, the density starts to order, such that the doubly occupied sites can lower their energy through the superexchange. This is optimal when they arrange in a checkerboard pattern, where doubles are neighbouring only empty sites. This *charge density wave* (CDW) is shown as well in figure 2.8. It is interesting to observe a symmetry, while on the attractive side we go from a density ordered phase, the Mott-insulator, to a spin ordering with the AFM, the reverse is happening on the repulsive side. The preformed pairs phase has spin ordering since the spins combine to form zero magnetisation on site, while with lower temperature we enter a density ordered state (CDW). We will discuss this more in chapter 5.

Doping in the Hubbard model

Up until now we looked at the phase diagram at half-filling, where $\mu = 0$. However, a lot of the interest in the Hubbard model stems from its possibility to explain the superconductivity of the cuprates, for example YBCO displayed in figure 2.9 a). The pure form of this material has a half-filled conduction plane, but is not superconducting even at low temperatures [27]. To reach superconducting conditions, the filling of the conducting plane has to be adjusted by adding or removing electron donors into the chemical sample. This so called *doping* of the material leads to an increase/decrease in electrons per site (charge carrier doping/hole doping) away from half-filling. The typical phase diagram of such a high-temperature superconductor is shown in figure 2.9 b).

A similar phase diagram is predicted for the two-dimensional Hubbard model with repulsive interactions. This is, however, still debated, especially whether the Hubbard model at low temperature could give rise to a d-wave superconducting phase or not [25, 47]. One reason why this is not settled yet is that, away from half-filling, numerical simulations struggle to produce accurate results. For example QMC calculations hit the famous *minus sign problem* [9], leading to a failure of the computation with exponential growth of the Hilbert-space. Nevertheless there are some great results from Determinant Quantum Monte-Carlo (DQMC) simulations at finite temperature [38–40], which will be used in our discussions. Especially in the frame of the results presented in this thesis I would refer to the work of my colleague Dr. Chun Fai Chan [24].

The way to introduce doping into the system in the grand canonical ensemble is to use a non-zero chemical potential ($\mu \neq 0$). As discussed in section 2.2, the resulting change in density is described with the equation of state $n(\mu, T)$, where U is fixed, since it is not an equilibrium parameter of the reservoir in the grand canonical description. An example is shown in figure 2.10, where we show the equation of state for repulsive interactions at $U/t = 8$, calculated with DQMC simulations at $T/t = 0.6$. Additionally, the single site occupation probability (singles) and the probability for doubly occupied sites (doubles) is plotted. One can clearly identify the Mott-plateau, where the

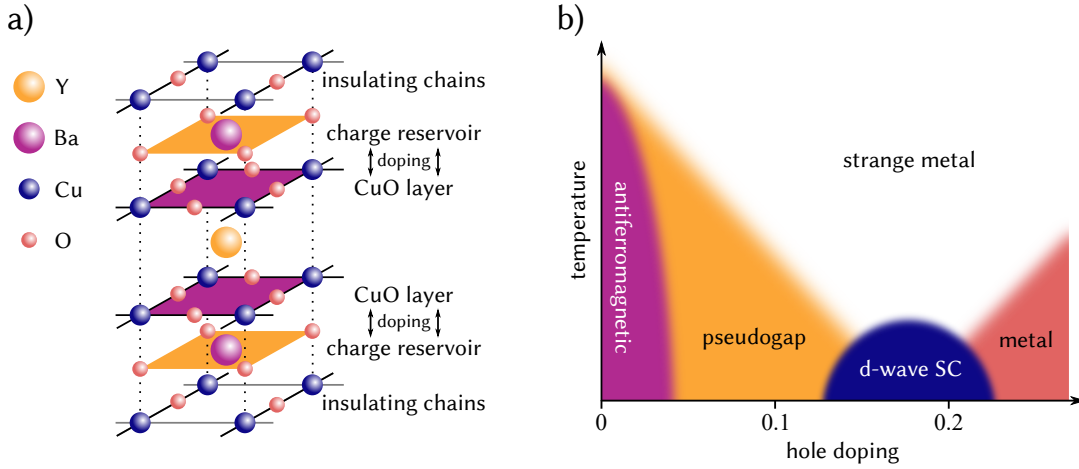


Figure 2.9: High-temperature superconductors and their phase diagram. In a) the unit cell of the undoped yttrium-barium-copper-oxide (YBCO), a high-temperature superconductor is shown. Electrons are only free to move in the copper-oxide (CuO) layers, closely bound to the copper atoms. They are sandwiched in between isolating layers of copper-oxide chains. One can achieve doping of the CuO layers by changing the chemical composition of the BaO layers which act like a charge reservoir, i.e. by adding or removing oxygen [27]. The Hubbard model was proposed to be able to describe the behaviour of charge carriers in these planes [8]. In b) the phase diagram of the cuprates like YBCO is shown. Through doping it transforms from an insulating antiferromagnet (AFM) to a d-wave superconductor at low temperatures. Between those phases is the pseudogap phase, where one assumes that pairing similar to the superconducting one occurs, but no long range coherence, i.e. *phase stiffness* is obtained [45]. For even higher doping a normal Fermi-liquid, i.e. metallic phase appears. The term *strange metal* comes from the fact that in this phase there are no quasi-particle excitations, leading to a temperature dependent resistivity outside of the normal metallic behaviour [46].

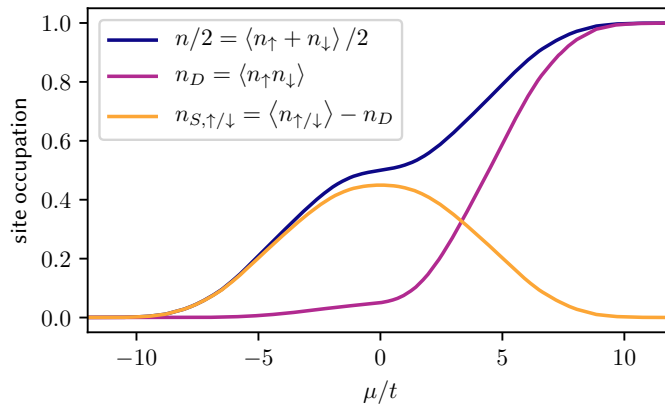


Figure 2.10: Equation of state obtained through DQMC calculations. Shown are half the averaged total site occupation $n/2$ and the averaged probability to measure a double n_D or a single $n_{S,\uparrow/\downarrow}$ on a site, depending on the chemical potential μ . Here we assumed a spin-balanced cloud, so the singles probability is independent of the spin state. Around half-filling at $\mu = 0$ a Mott plateau can be observed in the total density. The simulation used repulsive interactions $U/t = 8$ and a low temperature of $T/t = 0.6$.

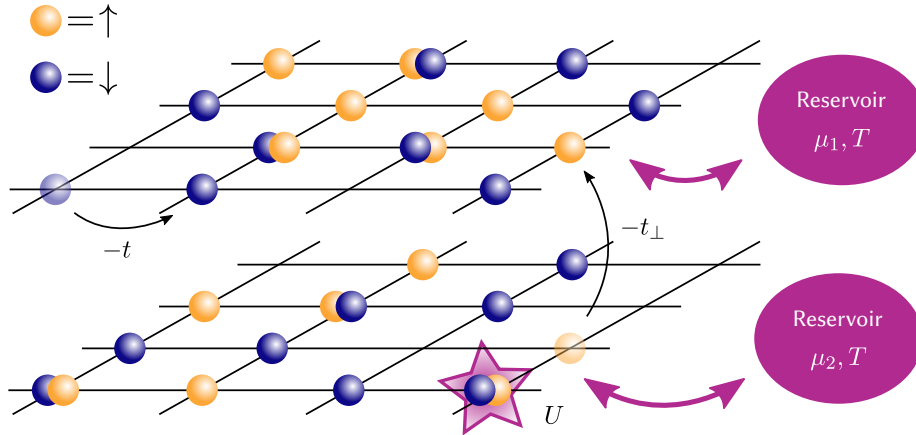


Figure 2.11: The bilayer Hubbard model. The two-dimensional model has been extended to another two-dimensional lattice layer, coupled by the inter-layer tunnelling t_{\perp} . Intra-layer tunnelling is still described with the tunnelling amplitude t , same as the on-site interactions U . We can additionally allow a different chemical potential for each layer, i.e. $\mu_1 \neq \mu_2$ which would lead to a unequal average filling of the layers.

density stays constant despite changing the chemical potential. This equation of state can be very powerful, since it allows calculating nearly all thermodynamic variables of the equilibrium system [48, 49]. From the equation of state shown in figure 2.10 one could for example extract the isothermal compressibility [50]

$$\kappa = \left. \frac{\partial n}{\partial \mu} \right|_T. \quad (2.38)$$

The Mott-plateau then shows as a reduced compressibility κ close to half-filling.

2.5 The Hubbard model extended to a bilayer

As already mentioned in the previous chapter, there is currently an ongoing debate if the two-dimensional Hubbard model truly sustains a superconducting phase [25], which would be connected to the high-temperature superconductivity of, for example, the cuprates [47], or whether the bare two-dimensional Hubbard model needs to be extended. For such an extension, some suggest for example next-to-nearest-neighbour tunnelling [26], multi-orbital lattices [51] or direct nearest-neighbour interaction terms [52].

Another possibility is to extend the two-dimensional model to two layers, with tunnelling in-between those [53, 54]. This was in part motivated by the fact that the conducting copper-oxide layers in superconductors shown in figure 2.9 a) are also coupled transversely [27], so the extension from two dimensions to the stacked model was natural. Additionally, in some solid state materials where charge movement was allowed in either a single layer of the material, or two closely stacked layers, the bilayer enhanced the superfluid fraction and the transition temperature significantly compared to the samples without bilayer structure [55]. In the search for superconducting phases, this model was again extended in some studies, for example inter-layer interaction was introduced [56], or diagonal intra-layer tunnelling which led to strongly enhanced superconductivity [57].

Here, we are discussing the bilayer model with only intra-layer, nearest-neighbour hopping t , intra-layer tunnelling t_\perp and on-site interactions U , shown in figure 2.11. The Hamiltonian is defined as

$$\begin{aligned} \hat{H} = & -t \sum_{\langle i,j \rangle, m, \sigma} \left(\hat{c}_{im, \sigma}^\dagger \hat{c}_{jm, \sigma} + h.c. \right) - t_\perp \sum_{i, \sigma} \left(\hat{c}_{i1, \sigma}^\dagger \hat{c}_{i2, \sigma} + h.c. \right) \\ & + U \sum_{i, m} \left(\hat{n}_{im, \uparrow} - 1/2 \right) \left(\hat{n}_{im, \downarrow} - 1/2 \right) - \sum_{i, m, \sigma} \mu_{m, \sigma} \left(\hat{n}_{im, \sigma} - 1/2 \right), \end{aligned} \quad (2.39)$$

where the layer is designated by the index $m = 1, 2$. The chemical potential $\mu_{m, \sigma}$ can be different for both planes, allowing for an independent filling in each plane. Later in this thesis we will work with a spin independent chemical potential that is identical for both planes and then use $\mu_{m, \sigma} = \mu$.

To get a better understanding of the physics of the bilayer model and where it differs from the ordinary two-dimensional Hubbard model we investigate how the new inter-layer tunnelling term modifies the band structure. To do so we follow the same ansatz as in section 2.4, where we define the annihilation and creation operators in *intra-layer* momentum space \mathbf{k} . The previous transformation led us to the rewriting of the intra-layer kinetic term \hat{H}_t of the Hamiltonian:

$$\hat{H}_t = \sum_{\mathbf{k}, m, \sigma} \epsilon_{\mathbf{k}} \hat{c}_{\mathbf{k}m, \sigma}^\dagger \hat{c}_{\mathbf{k}m, \sigma} = -2t \sum_{\mathbf{k}, m, \sigma} \left[\cos(k_x a) + \cos(k_y a) \right] \hat{c}_{\mathbf{k}m, \sigma}^\dagger \hat{c}_{\mathbf{k}m, \sigma}. \quad (2.40)$$

We can also rewrite the inter-layer tunnelling term:

$$\hat{H}_{t_\perp} = -t_\perp \sum_{i, \sigma} \left(\hat{c}_{i1, \sigma}^\dagger \hat{c}_{i2, \sigma} + h.c. \right) = -t_\perp \sum_{\mathbf{k}, \sigma} \left(\hat{c}_{\mathbf{k}1, \sigma}^\dagger \hat{c}_{\mathbf{k}2, \sigma} + h.c. \right) \quad (2.41)$$

Assuming again a non-interacting system $U = 0$ and combining the equations 2.40 and 2.41 we can write the Hamiltonian in a matrix [58]

$$\hat{H} = \sum_{\mathbf{k}, \sigma} \begin{pmatrix} \hat{c}_{\mathbf{k}1, \sigma}^\dagger \\ \hat{c}_{\mathbf{k}2, \sigma}^\dagger \end{pmatrix}^T \begin{pmatrix} -2t [\cos(k_x a) + \cos(k_y a)] & -t_\perp \\ -t_\perp & -2t [\cos(k_x a) + \cos(k_y a)] \end{pmatrix} \begin{pmatrix} \hat{c}_{\mathbf{k}1, \sigma} \\ \hat{c}_{\mathbf{k}2, \sigma} \end{pmatrix},$$

we get the band structure by solving for its eigenvalues:

$$\epsilon_{\mathbf{k}, 1/2} = -2t [\cos(k_x a) + \cos(k_y a)] \pm t_\perp. \quad (2.42)$$

In contrast to the result in section 2.4 for the two-dimensional Hubbard model, even for the non-interacting $U = 0$ model, separated energy bands are forming through the term $\pm t_\perp$. The lower band ($-t_\perp$) is called the *bonding* and the higher one ($+t_\perp$) the *anti-bonding* band. They both have the same band width $W = 8t$. For $t_\perp > 4t$ these bands separate in energy, shown in figure 2.12 a), similar to the separation of the Hubbard bands for the Mott insulator in two-dimensions. At half-filling $\mu = 0$ and low temperatures, the complete bonding band would be filled. This leads to an insulating behaviour, which is called a *band insulator*, not to be confused with the completely filled lattice ($n = 2$) which is a different kind of band insulator. In the limit of $t_\perp \gg t$ the bilayer can be approximated as a two-dimensional lattice of double-wells (see section 2.3) perpendicular to the principal axes of the lattice plane. In this limit we can identify the band insulator as a lattice

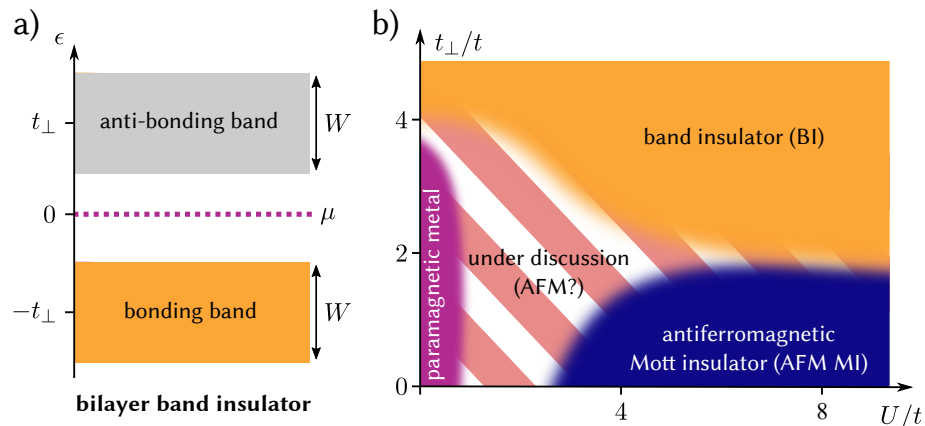


Figure 2.12: The phase diagram of the half-filled bilayer Hubbard model. a) For the non-interacting case the Band insulator can be understood similar to the Hubbard band description of figure 2.7. For $t_{\perp} > 4t$ the bonding and anti-bonding bands separate in energy, so for temperatures low enough only the bond band will be populated. There, charge transport is suppressed since it would require the breaking of one of the bonds between the layers. In b) the phase diagram as the result of several simulations is shown [53, 59–62]. The behaviour in the low to intermediate interactions $U/t < 4$ regions are still under debate, here marked with striped colours. For interactions $U/t > 4$ one assumes a transition from a Mott insulator, which is antiferromagnetically ordered in the layer direction, to a band insulator with AFM dimer formation between the layers. For the limit of very large interactions $U \rightarrow \infty$ this transition should happen at $t_{\perp}/t \approx 1.58$ [63].

filled with antiferromagnetically bound dimers. Breaking these dimers is energetically unfavourable, which leads to its insulating character.

There have been several approaches to simulate the interacting bilayer at half-filling [53, 59–62], and an approximate phase diagram for repulsive interactions $U > 0$ combining these results is shown in figure 2.12 b). It is understood best in its limits. If we have a weak interaction strength $U \approx 0$ and a low inter-plane tunnelling amplitude $t_{\perp} \approx 0$ the system is in a simple metallic state. When interaction is increased we transition to a Mott insulator, which is antiferromagnetically ordered in the layer for low temperatures. The transition from this intra-layer ordering to the band insulator of inter-layer dimers is occurring at $t_{\perp} = 4t$ for the non-interacting system. In the limit of very strong interactions $U \rightarrow +\infty$ the system can be described by a Heisenberg model [63–65]. There, each site is occupied by one spin that cannot move and only interact with its nearest neighbours via J, J_{\perp} , which we can identify with the superexchange $J = 4t^2/U$ in the Hubbard model. In [63] they observed in their numerical simulation a critical transition point from inter-layer to intra-layer coupling at $J_{\perp}/J \approx 2.51$ which is translated to a critical tunnelling $t_{\perp}/t \approx 1.58$.

The competition between the two magnetic coupling mechanisms in the bilayer adds richness to the intermediate regime of the phase diagram, which we will further investigate in chapter 7. Similar to the two-dimensional Hubbard model, it is assumed that additional doping could open the road for understanding the essential mechanisms behind high-temperature superconductivity.

Quantum simulation with ultracold atoms

Even though great effort has been put forward to tackle the two-dimensional Hubbard model with approximations and numerical techniques, a lot of questions are still unanswered. Especially intriguing is the open question whether the Hubbard model sustains a superfluid phase and how a pairing mechanism underlying this low temperature superfluidity could work. At the same time proposals to extend the basic Hubbard model further, for example to a bilayer system, are pushed forward. The numerical simulation of both of these models with statistical sampling in the quantum Monte-Carlo method (QMC) suffers the so called *sign problem* [9]. Due to the fermionic exchange statistics, calculations grow exponentially complex with respect to the required computation time with the simulated site number N . It was even shown that the sign problem is *NP hard* [66]. Additionally the Hilbert space of possible states also increases exponentially, so just the storage of a state in a large Hilbert space can easily require more storage than currently available on any supercomputer. Therefore, the exact computation of large quantum systems is impossible to perform with classical hardware.

Richard Feynman realised this arising issue and proposed to use hardware which itself was capable of processing quantum states directly [67]. This could be done for example with a universally programmable quantum computer. It would allow to store, process and measure quantum states and their evolution directly. There exist several machines today which meet these criteria [68, 69], however, they remain small in their qubit number, and limited in the number of operations that can be performed without faults or loss of coherence.

Another approach is to build a device optimised to solve only a specified subset of problems, by creating a quantum system which can be described by the Hamiltonian one wants to investigate. Through adjusting external parameters defining this Hamiltonian and changing the initial state before some time evolution, one can directly simulate the result of a computation no current computer would be powerful enough to obtain. This would then be an analogue quantum simulation in contrast to one done by an universally programmable quantum computer. Ideally the device used for this simulation, the *quantum simulator*, should allow for a lot of control and results should be easy to measure. Quantum simulators have been realised in a lot of different systems: neutral atoms, trapped ions, cavity arrays, quantum dots, superconducting circuits, photons or nuclear spins [11]. All of them have advantages and disadvantages to consider: scaling, flexibility, control and readout or just the possibility to simulate the desired Hamiltonian. Of particular interest in this thesis is the quantum simulation with neutral atoms, which was successfully used to simulate and investigate

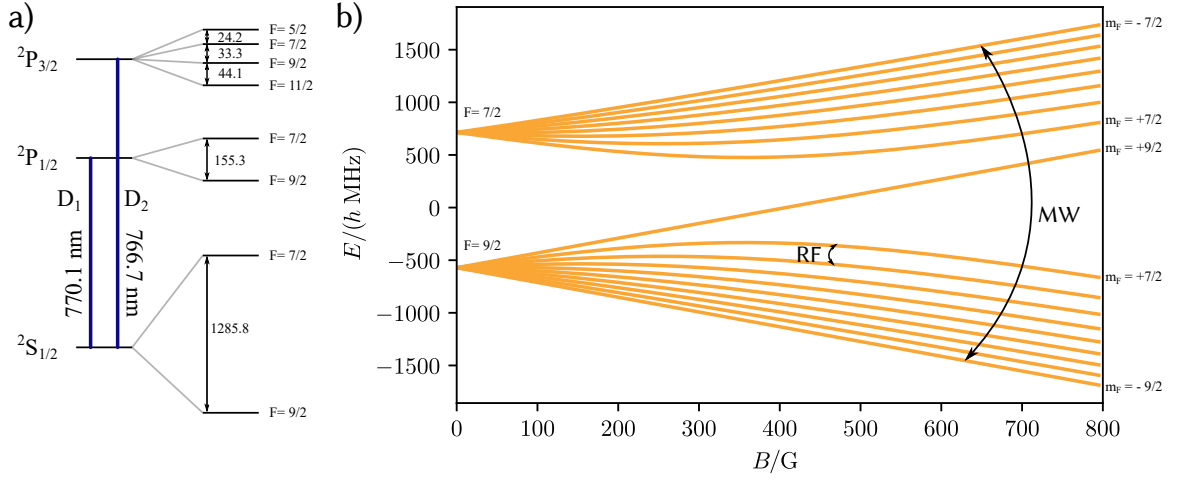


Figure 3.1: The hyperfine states of ^{40}K a) Level scheme with the main optic transitions of the D_1 and the D_2 line and the hyperfine energy splitting in units of $\text{MHz} \times h$. b) Lifting of the energetic degeneracy of the lowest two hyperfine states through an external magnetic field B . We use the states $|F = 9/2, m_F = -9/2\rangle$ and $|F = 9/2, m_F = -7/2\rangle$ as spin-up and spin-down, since they cannot energetically relax in spin-changing collisions. In most experiments we operate at about 200 G where transitions are facilitated by RF (frequency ~ 50 MHz) and microwave (frequency ~ 1.82 GHz) transfers. Figures are inspired from [74].

physical effects, for example non-equilibrium universal dynamics in quantum chromodynamics [70], BEC-BCS crossover physics close to universality [71], the quantum phase transition from superfluid to insulator [72] or the Bose-Hubbard model [73].

Following the first part of this chapter, we will focus on the quantum simulation of the Hubbard model with ultracold atoms. For this lattices filled with the fermionic particles of alkali metals like Lithium ^6Li [12–14] and Potassium ^{40}K [15–17] have been successfully used. We will discuss in the following how to create and shape a system of ultracold atoms such that it can simulate the Hubbard models previously presented.

3.1 Internal state control

In our experiment we use neutral Potassium ^{40}K atoms to represent the fermionic particles of the Hubbard model. A good summary of the physical properties of this element is given in [74]. Its ground state is the $2S_{1/2}$ state with a hyperfine splitting into $F = 7/2$ and $F = 9/2$, see figure 3.1 a). In the presence of an external magnetic field the degeneracy of the hyperfine states with different m_F quantum number is lifted. The coupling of the magnetic moments of the hyperfine states to the magnetic field B can be calculated using the Breit-Rabi formula [74], for which the results are shown in figure 3.1 b). One can identify the linear Zeeman splitting at low field $B \lesssim 100$ G, transitioning to the Paschen-Back regime for high magnetic field strengths $B \gtrsim 500$ G, where the hyperfine quantum numbers are not a suitable basis any more. Even though in this thesis we mostly work in the intermediate regime around 200 G, we will use the nomenclature of the hyperfine states.

For the quantum simulation of spin-1/2 particles we can now choose to use the lowest-lying states $|F = 9/2, m_F = -9/2\rangle := |-9/2\rangle$ and $|F = 9/2, m_F = -7/2\rangle := |-7/2\rangle$. It does not matter that

both of them have a similar magnetic moment, since the spin in the Hubbard model does not assume a real magnetic moment in its description and only requires fermionic particles with two internal states. Therefore, the choice is arbitrary, but for now we take the energetically lower state as spin-down $|\downarrow\rangle := |-9/2\rangle$ and spin-up as $|\uparrow\rangle := |-7/2\rangle$. The different magnetic moments in strong magnetic fields lead to a state dependent behaviour in magnetic field gradients. Most states in $F = 9/2$ can lower their energy by going to strong fields (*high-field-seeker*), while the opposite is true for the states of $F = 7/2$ (*low-field-seeker*). We will make use of that in section 4.1.2.

To use them as the basis for our quantum simulation we need to have methods to prepare, manipulate and read out the internal states of the atoms. We do so by coupling external electromagnetic fields to the internal states of the atoms via their electric or magnetic dipole transition elements [75].

The interaction Hamiltonian of an electric field $\mathcal{E}(\mathbf{r}, t)$ with a dipole moment $\mathbf{d} = e\mathbf{r}$ with the electric charge e is defined by

$$\hat{H}_{\text{int}} = -\hat{\mathbf{d}} \cdot \mathcal{E}(\mathbf{r}, t). \quad (3.1)$$

The whole system is then described by $\hat{H} = \hat{H}_0 + \hat{H}_{\text{int}}$ with the uncoupled Hamiltonian \hat{H}_0 . Let the atom be in a plane-wave electric field $\mathcal{E}(\mathbf{r}, t) = \hat{\mathbf{e}}E_0 \cos(\mathbf{r} \cdot \mathbf{k} - \omega t)$ with wave vector \mathbf{k} and the unity vector of the field direction $\hat{\mathbf{e}}$. If we employ the dipole approximation where we assume the size of the atom is way smaller than the wavelength of the field and use a two level system with states $|g\rangle, |e\rangle$ the coupling term can be written as

$$\hat{H}_{\text{eg}} = \hbar\Omega \cos(\omega t). \quad (3.2)$$

Here we used the Rabi-frequency Ω , which is defined as

$$\Omega = -\frac{eE_0}{\hbar} \langle e | \hat{\mathbf{r}} \cdot \hat{\mathbf{e}} | g \rangle. \quad (3.3)$$

We can transform our initial basis to a rotating frame with angular frequency ω_0 describing the energy difference of both uncoupled states $\omega_0 = (E_e - E_g)/\hbar$, with $E_g = \langle g | \hat{H}_0 | g \rangle$ and $E_e = \langle e | \hat{H}_0 | e \rangle$. The difference of the laser frequency to the rotating frame frequency is the detuning $\Delta = \omega - \omega_0$. With the rotating frame approximation [75] this leads to the coupled Hamiltonian in matrix form

$$\hat{H}' = \hbar \begin{pmatrix} \Delta & \frac{\Omega}{2} \\ \frac{\Omega^*}{2} & 0 \end{pmatrix}. \quad (3.4)$$

The eigenvectors of this matrix are the *dressed states* $|+\rangle, |-\rangle$. At $\Delta = 0$ they are given by

$$|\pm\rangle = \frac{1}{\sqrt{2}} (|g\rangle \pm |e\rangle) \quad (3.5)$$

This representation will be useful for the description of various coupled two-level systems throughout this thesis. Its eigenenergies are plotted in figure 3.2 a) as a function of Δ for fixed coupling strengths $\Omega = 0$ and $4\hbar$. The coupling opens up an avoided crossing, separating the states by an energy difference of $\Omega_{\text{effective}} = \sqrt{\Omega^2 + \Delta^2}$.

If we start with an atom in the uncoupled ground state $|g\rangle$ and very quickly turn on the coupling

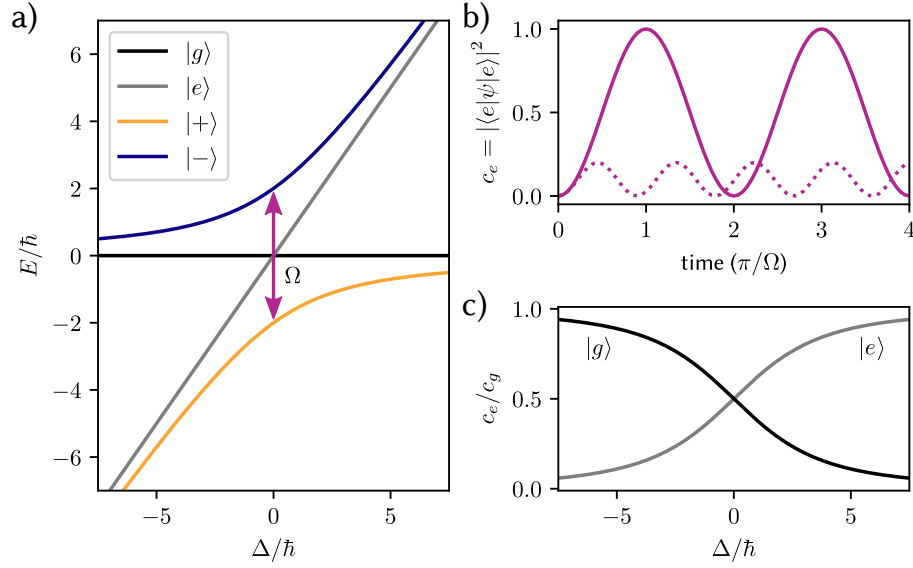


Figure 3.2: Coupled states and state transfer methods. a) The bare ground and excited state is shown in black and grey respectively. The dressed states appear with a non-zero coupling $\Omega > 0$, and connect to the bare states in the limit of large detuning Δ . b) If one starts with a populated ground state $c_g = |\langle g|\psi\rangle|^2 = 1$ and suddenly turns on resonant coupling, one can observe Rabi-oscillations shown as a solid line. After a time of $t = \pi/\Omega$, the so called π -pulse, the whole population is in the excited state. Increasing the detuning leads to faster oscillations with a smaller amplitude as shown with the dashed line for $\Delta = 2\Omega$. The decomposition of the dressed state $|+\rangle$ into the bare states $|g\rangle, |e\rangle$ is plotted in c). If one changes Δ slowly one can adiabatically follow this state and transfer population between those states with extreme efficiency.

Ω to a finite value, we will project the initial state into the dressed states, for example $|g\rangle = (|+\rangle + |-\rangle)/\sqrt{2}$ at $\Delta = 0$. Through the energy difference $\Omega_{\text{effective}}$ between the dressed states and their respective phase evolution, the populations of ground and excited state will oscillate. The amplitude of these *Rabi-oscillations* is dependent on the detuning and maximal when on resonance $\Delta = 0$. By enabling the coupling for a fixed time only, one can transfer state populations or create an arbitrary superposition. This is shown in figure 3.2 b) for the time evolution of the excited state population c_e of a state initially in the ground state.

Another way of transferring state populations is done via a *Landau-Zener* (LZ) sweep, shown in figure 3.2 c). We start with population only in the ground state $|g\rangle$. At very large detuning $\Delta \gg \Omega$ the bare states are close to the dressed states ($|g\rangle \approx |+\rangle$), so while turning on the coupling, we still have mostly population in the lower of the two dressed states. By slowly ramping to a large negative detuning, the state of the atoms adiabatically follows the dressed state. When turning off the coupling, we end up in the excited state, since $|e\rangle \approx |+\rangle$ for $\Delta \ll -\Omega$. The probability of transferring the population adiabatically $P_{\text{transferred}}$ is given by the *Landau-Zener formula* [76] as

$$P_{\text{transferred}} = 1 - \exp\left(-\frac{\pi\Omega^2}{2\frac{d\Delta}{dt}}\right). \quad (3.6)$$

Therefore, if $\frac{d\Delta}{dt} = \dot{\Delta} \ll \Omega^2$, we get a nearly complete transfer of the state population. However, this

formula can also be used for a partial transfers, by deliberately adjusting the rate to be non-adiabatic. This will be used, for example, in chapter 5. For interacting atoms in a lattice, Landau-Zener sweeps can lead to incomplete transfers and transfers into higher motional energy bands, if the wrong direction of the detuning sweep is chosen. This is described in detail in a previous thesis [21] and was considered in all experiments.

Up until now we described the coupling via the electric dipole moment, the calculation for a magnetic dipole or higher electric and magnetic moments would remain similar, and mostly change the selection rules of the possible transfers and their coupling strength. The coupling in the Hamiltonian 3.4 can be of arbitrary type. This can be seen in equation 2.30, where in the context of the single particle in a double-well, the tunnelling element t takes the role of the coupling and the detuning is described by the energy difference of both well sites. Therefore, we can even do Landau-Zener sweeps in the double-well, by adiabatically changing the energy offset, or even Rabi-oscillations, as we will see in chapter 6.

For this section we assumed an ideal two level system, however, when discussing optical transitions, spontaneous decay has to be considered. There, any population in an excited state can spontaneously decay quickly to a lower lying state while emitting a photon in a random direction. This allows for the absorption of several photons in a short period of time, which can be used to our advantage. Laser light resonant with the D₂ transition ($^2S_{1/2} \rightarrow ^2P_{3/2}$) is used for laser cooling (see section 4.1.1) or, if the laser linewidth is smaller than the state separation, to image state selectively the atomic distribution (see section 4.3.1).

With these tools we gain control of the internal states of the ^{40}K atoms in our experiment and we move on to controlling the position of the atoms by the use of laser light.

3.2 From lattice potentials to localised wave functions

Optical potentials In the previous section we already discussed how an electromagnetic field can couple to the dipole moment of the superposition of two internal states of an atom. Here we want to present a way to use high-intensity light fields to create local potentials for the atoms, in order to trap them or to arrange them into a lattice configuration.

For strong external electric fields $\mathcal{E}(\mathbf{r}, t)$ the force on the negative charge of the electron and its positive counterpart in the nucleus can lead to a polarisation, effectively inducing a dipole moment $\mathbf{d}(t)$ in the otherwise neutral atom itself. Here we will present results of the derivation outlined in [77] and [76].

We assume a complex driving field $\mathcal{E}(\mathbf{r}, t) = \hat{e}\tilde{E}(\mathbf{r})\exp(-i\omega t) + c.c.$, with complex field amplitudes \tilde{E} and its complex conjugates. The *induced* dipole is parallel to the unit field vector \hat{e} and its amplitude proportional to the electric field, such that

$$\mathbf{d}(\mathbf{r}, t) = \alpha\mathcal{E}(\mathbf{r}, t), \quad (3.7)$$

with the complex polarisability α , which is in general dependent on the driving frequency ω . We implicitly used the dipole approximation again, where the field can still vary spatially, however, we assume that the electric field is constant over the whole atom. From this we can calculate the time averaged potential this dipole interaction creates using a similar formula as in equation 3.1, taking

into account that the dipole is induced and not permanent by adding a prefactor of $1/2$:

$$V_{\text{dipole}}(r) = -\frac{1}{2} \langle \mathbf{d}(\mathbf{r}, t) \cdot \mathcal{E}(\mathbf{r}, t) \rangle_t = -\text{Re}(\alpha) |\tilde{E}(\mathbf{r})|^2. \quad (3.8)$$

The product of the two oscillating terms in the second step leads to a DC and a high frequency component $\propto 2\omega$, which gets removed by the time average. Here it is important to note that by definition the complex \tilde{E} and the real field amplitude E_0 are connected as $|E_0| = 2|\tilde{E}|$ [76].

The light intensity in vacuum is given as

$$I = 2|\tilde{E}|^2 c \epsilon_0 = \frac{|E_0|^2}{2} c \epsilon_0, \quad (3.9)$$

with c as the speed of light and the vacuum permittivity ϵ_0 . This leads to a linear dependence of the dipole potential

$$V_{\text{dipole}}(r) = -\frac{\text{Re}(\alpha)}{2c\epsilon_0} I(r). \quad (3.10)$$

on the intensity and an absorption rate Γ_{abs} connected to the imaginary part of α :

$$\Gamma_{\text{abs}}(r) = \frac{\text{Im}(\alpha)}{\hbar c \epsilon_0} I(r). \quad (3.11)$$

We get the complex polarisability as [77]

$$\alpha = \frac{e^2}{m_e} \frac{1}{\omega_0 - \omega - i\omega\Gamma_\omega}, \quad (3.12)$$

with the resonance frequency ω_0 and the damping rate Γ_ω . This rate describes the spontaneous decay of the excited state $|e\rangle$ to the ground state $|g\rangle$:

$$\Gamma_\omega = \frac{\omega_0^3}{3\pi\epsilon_0\hbar c^3} \sum_{i=x,y,z} |\langle e|\mathbf{d}|g\rangle|^2. \quad (3.13)$$

Here, $\langle e|\mathbf{d}|g\rangle$ is the transition dipole matrix element. The definition of Γ_ω is only valid for low excitation rates Γ_{abs} i.e. a small population of $|e\rangle$. This coincides with our goal of creating spatial confinement potentials, without changing the internal states of the atoms.

One way to achieve this is to increase the detuning $\Delta = \omega - \omega_0$ to reduce absorption. However, this also leads to a smaller potential created, which we would have to counteract with higher light intensity I . In this limit and by using the rotating wave approximation to neglect high frequency terms $\omega_0 + \omega$ we can simplify equations 3.10 and 3.11 to [77]

$$V_{\text{dipole}}(r) = \frac{3\pi c^2}{2\omega_0^3} \frac{\Gamma_\omega}{\Delta} I(r), \quad (3.14)$$

$$\Gamma_{\text{abs}}(r) = \frac{3\pi c^2}{2\hbar\omega_0^3} \left(\frac{\Gamma_\omega}{\Delta} \right)^2 I(r). \quad (3.15)$$

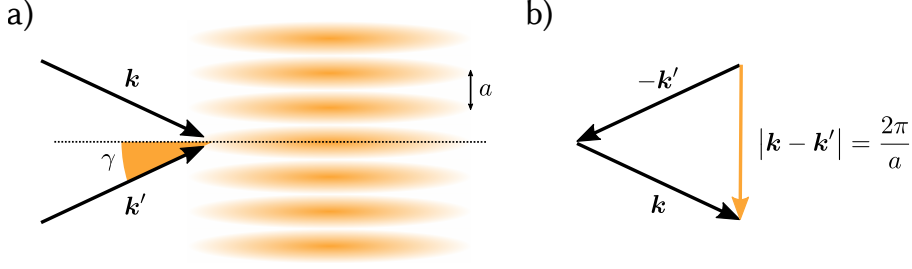


Figure 3.3: The accordion lattice. a) By interfering two plane waves with wave vectors \mathbf{k}, \mathbf{k}' meeting at an angle of 2γ one obtains a lattice pattern normal to the combined vectors. b) This can be understood as creating a *lattice* wave vector $\mathbf{k} - \mathbf{k}'$ that determines the lattice spacing a . The interference angle, therefore, determines the lattice spacing, up to an angle of $2\gamma = \pi$ where $a = 2|\mathbf{k}|/2\pi$.

We note here that the sign of the detuning determines the sign of the potential created. For an attractive potential $U_{\text{dipole}} < 0$ the detuning Δ has to be negative, so the frequency of the laser ω has to be lower than the resonance frequency ω_0 , which is called *red-detuned*. On the other hand, *blue-detuned* light with $\omega > \omega_0$ creates a repulsive potential $U_{\text{dipole}} > 0$. While the dipole potential scales with $V_{\text{dipole}} \propto I/\Delta$, the absorption rate scales as $\Gamma_{\text{abs}} \propto I/\Delta^2$. By choosing a laser with large detuning from the main resonances (D_1 and D_2 transitions) and a local high intensity we can, therefore, create *conservative* trapping potentials for neutral atoms with light.

Lattice potentials Starting with an ideal plane electromagnetic wave $\mathcal{E}(\mathbf{r}, t) = \hat{e}E_0 \cos(\mathbf{r} \cdot \mathbf{k} - \omega t)$ propagating in the x direction ($\mathbf{k} = k\hat{e}_x = 2\pi/\lambda \hat{e}_x$), one would get a homogeneous optical dipole potential shift for atoms in its path, since the intensity I is constant in space. However, if we superimpose this with another wave with opposing wave vector $\mathbf{k}' = -\mathbf{k}$ we get a locally varying electric (time-averaged) field intensity, with

$$I(r) = 2|E_0|^2 c \epsilon_0 \cos^2(kx). \quad (3.16)$$

Using equation 3.10 we obtain a spatially oscillating potential

$$V_{\text{latt}}(x) = V_0 \cos^2\left(\frac{\pi x}{a}\right) \quad (3.17)$$

with a periodicity of $a = \lambda/2 = \pi/k$ and an amplitude of V_0 . In one dimension, this would already create a potential lattice for neutral atoms. Its periodicity is fixed by the wavelength of the light.

The *accordion lattice* configuration allows for some modification of the lattice site spacing a . For two plane waves with the same wavelength λ , but wave vectors interfering at an angle 2γ this periodicity changes significantly:

$$a = \frac{2\pi}{|\mathbf{k} - \mathbf{k}'|} = \frac{\pi}{\sin(\gamma)|\mathbf{k}|} = \frac{\lambda}{2 \sin(\gamma)}, \quad (3.18)$$

with the direction of the periodic potential parallel to $\mathbf{k} - \mathbf{k}'$, see figure 3.3. One can see that for the limit of $\gamma = \pi/2$ this leads back to the result of anti-parallel beams in equation 3.17. To create a three-dimensional lattice with separated sites, as required for the simulation of the Hubbard model,

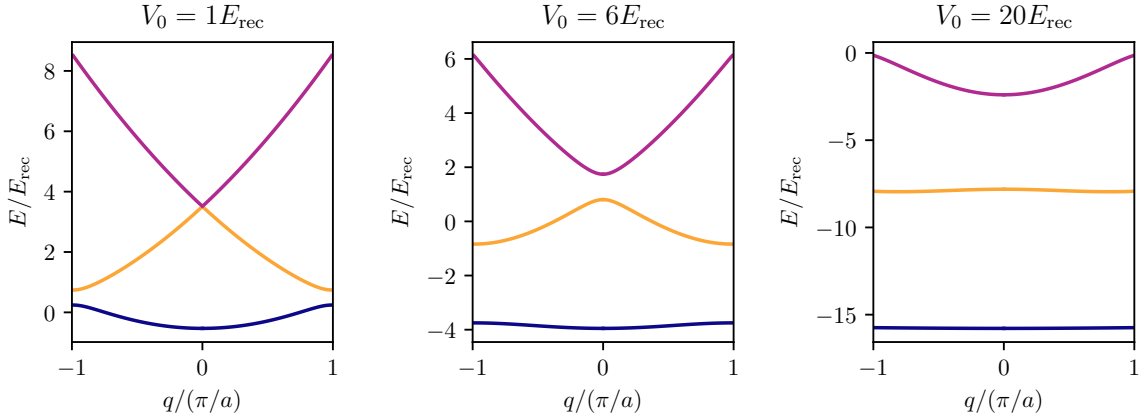


Figure 3.4: Band structure of a one-dimensional lattice. For three different lattice depths V_0 the eigenenergies of the Bloch waves for the first Brillouin zone and up to the second band are presented (0th: blue, 1st: orange, 2nd: pink). The lattice potential is set to be attractive, simulating a red-detuned lattice laser frequency.

we have to overlay several of these lattices. To avoid unwanted interference, one has to choose the polarisation of plane-wave pairs to be orthogonal or use lasers with very different frequencies.

Band structure and Bloch waves To describe a single particle in a periodic potential as the one we introduced in equation 3.17, we start with the non-interacting, single-particle Hamiltonian

$$\hat{H}_0 \phi_{n,q}(x) = \left[-\frac{\hbar^2}{2m} \nabla^2 + V_{\text{latt}}(x) \right] \phi_{n,q}(x) = E_{n,q} \phi_{n,q}(x), \quad (3.19)$$

with m , the mass of the particle. We start here with the one-dimensional description, however, results can be extended to higher dimensions if we assume to have perpendicular principal lattice axes, which make the three-dimensional Hamiltonian separable. The eigenstates to this Hamiltonian with a *periodic potential* can be found by using the Bloch wave function ansatz $\phi_{n,q}$ [34, 78]:

$$\phi_{n,q}(x) = \frac{1}{\sqrt{L}} u_{n,q}(x) e^{iqx}, \quad (3.20)$$

where n describes the band index and q the quasi-momentum in a crystal. For normalisation we assumed a lattice with a finite number of sites N and periodic boundary conditions, leading to a normalisation through the system size $L = aN$. The Bloch wave function consists of a plane wave component with quasi wave vector q and a spatially periodic function $u_{n,q}$. This periodic structure is perfectly suited for a Fourier series expansion of $u_{n,q}$ and V_{latt} into plane waves with periodicity

of a , leading to

$$u_{n,q}(x) = \sum_l \bar{u}_{n,q,l} e^{i\frac{2\pi l}{a}x} \quad (3.21)$$

$$V_{\text{latt}}(x) = \sum_l \bar{V}_{\text{latt},l} e^{i\frac{2\pi l}{a}x}. \quad (3.22)$$

For the lattice potential introduced in equation 3.17 this transformation is simple:

$$V_{\text{latt}}(x) = V_0 \cos^2\left(\frac{\pi x}{a}\right) = \frac{V_0}{2} + \frac{V_0}{4} e^{-i\frac{2\pi}{a}x} + \frac{V_0}{4} e^{i\frac{2\pi}{a}x}. \quad (3.23)$$

Using these transformations we can rewrite the Bloch waves of equation 3.20

$$\phi_{n,q}(x) = \frac{1}{\sqrt{L}} \sum_l \bar{u}_{n,q,l} e^{i\left(\frac{2\pi l}{a} + q\right)x} \quad (3.24)$$

and with it the Hamiltonian of equation 3.19

$$\sum_{l=-c}^c H_{l,j} \bar{u}_{n,q,l} = E_{n,q} \bar{u}_{n,q,l} \quad (3.25)$$

where

$$H_{l,j} = \begin{cases} \frac{\hbar^2}{2m} \left(\frac{2\pi l}{a} + q\right)^2 + \frac{V_0}{2} & \text{for } |l - j| = 0 \\ \frac{V_0}{4} & \text{for } |l - j| = 1 \\ 0 & \text{for } |l - j| > 1 \end{cases}. \quad (3.26)$$

Here, c is introduced as the order up to which the functions are expanded, leading to a finite matrix size. Diagonalising this matrix gives us the eigenenergies of the Bloch waves $E_{n,q}$ and their decomposition into the Fourier components $\bar{u}_{n,q,l}$. Numerical calculations produce the energetic band structure for any given lattice depth V_0 , which is usually described in the unit of the recoil energy $E_{\text{rec}} = \hbar^2/(8ma^2)$. In figure 3.4 the band structure is shown for $V_0 = 1, 6$ and $20 E_{\text{rec}}$. The separation of the two lowest bands, called the band gap, increases with increased lattice depth. To simulate the Hubbard Model, we required that only the lowest band is filled, so it is critical that the band gap is larger than the thermal excitation energy $k_B T$.

Wannier basis and tunnelling Bloch waves give a description of fermionic atoms in a lattice potential in the basis of delocalised wave functions. However, we can construct a different orthonormal basis out of the Bloch functions, the so called *Wannier functions* [79]:

$$w_n(x - x_i) = \frac{1}{\sqrt{N}} \sum_q e^{-iqx_i} \phi_{n,q}(x). \quad (3.27)$$

They are maximally-localised around the site i and orthogonal to each other.

In the framework of second quantisation and using only the zeroth band ($n = 0$) we can define a

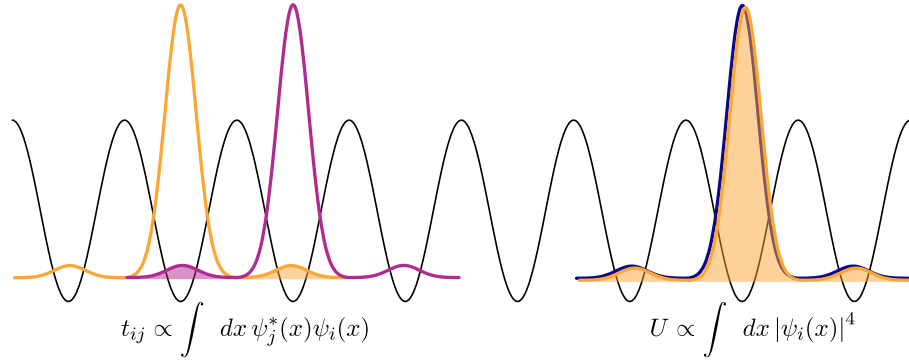


Figure 3.5: Deriving the Hubbard parameters with Wannier functions. Since the Wannier functions are the maximally-localised orthogonal basis for a lattice system, we can use them for the description of the Hubbard tunnelling of a particle from site i to j by computing the overlap of the Wannier functions on these sites. As will be shown in the later section 3.4, the on-site interaction can be calculated with the probability to find a spin-up and a spin-down particle on the same position x , which can be calculated again with the integration of the Wannier function to the power of four.

fermionic field operator

$$\hat{\psi}_{i,\sigma}^\dagger = w_0(x - x_i) c_{i,\sigma}^\dagger, \quad (3.28)$$

with which we can construct localised wave functions in the lattice frame

$$\psi_{i,\sigma}(x) = \langle \hat{x} | \hat{\psi}_{i,\sigma}^\dagger | \text{vac} \rangle = w_0(x - x_i). \quad (3.29)$$

This is ideal for the description of localised fermions as we introduced for the Hubbard model. In that model the particles are fixed on the individual sites. They now can be approximated with Wannier functions on the corresponding lattice sites, see figure 3.5.

Additionally, we can identify the tunnelling matrix element from site i to site j as the normalised overlap of the two wave functions described by Wannier functions

$$\begin{aligned} t_{i,j} &= \langle \psi_{j,\sigma} | \hat{H} | \psi_{i,\sigma} \rangle = \int dx \psi_{j,\sigma}^*(x) \hat{H} \psi_{i,\sigma}(x) \\ &= \frac{1}{N} \sum_{q,q'} E_{0,q} e^{-i(qx_j - q'x_i)} \underbrace{\int dx \phi_{0,q'}^*(x) \phi_{0,q}(x)}_{=\delta_{q',q}} \\ &= \frac{1}{N} \sum_q E_{0,q} e^{-iq(x_j - x_i)}. \end{aligned} \quad (3.30)$$

This equation is valid for all sites and distances of the tunnelling.

For nearest-neighbour tunnelling only, i.e. when dismissing all other terms that allow direct

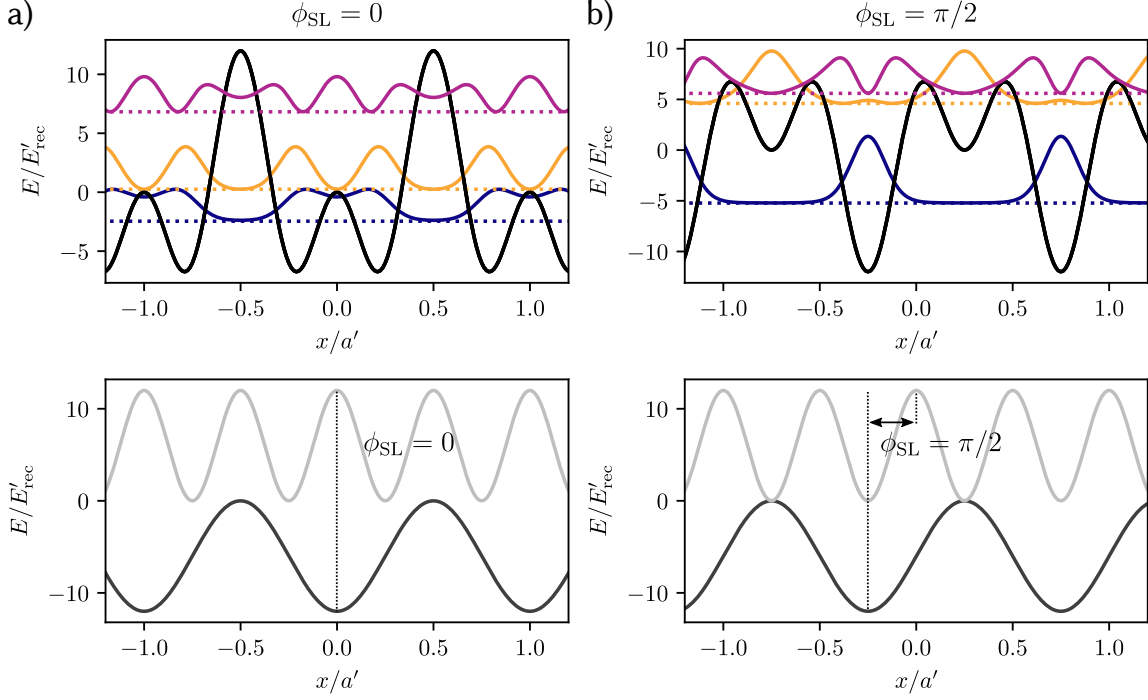


Figure 3.6: The superlattice and its eigensolutions. In the bottom plot of a) and b) the individual potentials for the short (light grey) and long lattice (dark grey) are plotted with their respective phase difference ϕ_{SL} . Similar to the experiment we assume a red-detuned (attractive) long lattice $V_{0,\text{long}} = 12 E'_{\text{rec}}$ and a blue-detuned short lattice $V_{0,\text{short}} = 3 E_{\text{rec}}$ with half the lattice spacing $a = a'/2$. E_{rec} and E'_{rec} are calculated for the individual lattice parameters, where we note that $E_{\text{rec}} = 4 E'_{\text{rec}}$. The resulting potentials are plotted in black on the upper graphs, for a superlattice phase of $\phi_{\text{SL}} = 0$ for a) and $\phi_{\text{SL}} = \pi/2$ for b). Additionally, the local probability distribution $|\psi(x)|^2$ of the $q = 0$ bloch waves are plotted in arbitrary units up to the second band (0th band: blue, 1st band: orange, 2nd band: pink), offset by their respective energy plotted with dotted lines. One can see that depending on the phase, we can create arrays of double-wells, or a lattice where each second site is significantly lower in energy with tightly bound wave functions.

tunnelling to sites further away, it reduces to

$$t_{i,i+1} = \frac{1}{N} \sum_q E_{0,q} e^{-iqa}. \quad (3.31)$$

In equation 2.36 we already discussed how the band structure should be a cosine with periodicity of $2\pi/a$ for nearest neighbour tunnelling. As we can see from equation 3.30, higher order tunnelling, for example next-to-nearest-neighbour tunnelling t_{NNN} , would lead to higher frequency contributions. Through this result we know that we can Fourier expand the exact structure of the lowest band in order to extract all higher order tunnelling elements. This allows us to calculate the minimal potential one has to use in order to restrict the system to only nearest-neighbour tunnelling.

Bi-chromatic lattices and the superlattice Up until now, we discussed mono-chromatic lattices, that means lattice potentials created with two plane waves of the same wavelength λ . It is, however,

possible to superimpose several lattices with different wavelengths λ and λ' .

As long as their frequencies are sufficiently far detuned, the interference of their lattice light fields will oscillate faster than the atom could respond, so the effective potentials of both lattices just add up. This *superlattice* will usually not have the same periodicity as the individual lattices, unless the wavelengths are a multiple of each other $\lambda' = n\lambda$ with $n \in \mathbb{N}$ and they are identical in their creation, i.e. angle of interference. If these conditions are matched, the relation for their lattice spacing results in $a' = na$. Combined, they create a periodic potential with a spatial period of a' , the longest individual lattice period, and therefore the Bloch ansatz of equation 3.24 is still valid. This will allow us to solve for the eigenstates and eigenenergies, i.e. the band structure and related terms like the tunnelling amplitudes, as was done in [80].

In this thesis we will make use of such lattices on several occasions, where $\lambda' = 2\lambda$, therefore $a' = 2a$. The combined lattice potential can be written as

$$V_{\text{SL}}(x) = V_0 \cos^2\left(\frac{\pi x}{a} + \phi_{\text{SL}}\right) + V'_0 \cos^2\left(\frac{\pi x}{2a}\right) \quad (3.32)$$

and depends on the *relative* phase of the superlattice ϕ_{SL} . It is, however, not easily possible to get a laser with high power at any arbitrary wavelength, so choosing the right wavelength for these lattices can be a challenge. One way is to use existing high power lasers, like the diode pumped Nd:YAG lasers emitting infrared light at $\lambda' = 1064 \text{ nm}$ [81, 82], and to double the frequency of this light in a non-linear crystal [83]. This reduces the wavelength to half the initial one $\lambda = \lambda'/2 = 532 \text{ nm}$, converting it to visible green light. Both these wavelengths are far detuned from the potassium D_1 ($\lambda_{D1} = 770.1 \text{ nm}$) and D_2 ($\lambda_{D2} = 766.7 \text{ nm}$) lines [74] which make them ideal for conservative trapping potentials. The $\lambda' = 1064 \text{ nm}$ is red detuned from these resonances, leading to a potential inversely proportional to the intensity. The opposite is true for the blue detuned $\lambda = 532 \text{ nm}$ light. In figure 3.6 both laser intensities and the resulting superlattice potential are shown for two superlattice phases $\phi_{\text{SL}} = 0$ (left) and $\phi_{\text{SL}} = \pi/2$ (right). The Bloch waves for $q = 0$ are also plotted, with an offset according to their energy. One can see how the choice of the superlattice phase greatly changes the states of the lowest bands, allowing for states with strongly reduced detection probability on alternating sites ($\phi_{\text{SL}} = \pi/2$).

3.3 The local-density approximation

This idealised description of light fields as simplified plane waves is not valid in the lab any more, where we work with Gaussian beams transported to the experiment via optical fibres. If we focus a red detuned laser beam down to very small waists ($\approx 100 \mu\text{m}$), the high intensity in the focus results in a local potential minimum that can be used to trap cold atoms. It is useful to remember that the dipole potential is directly proportional to the intensity, as shown in equation 3.14. The intensity distribution of a focused Gaussian beam in z -direction is given as [84]

$$I(r, z) = \frac{2P}{\pi W^2(z)} e^{-\frac{2r^2}{W^2(z)}}, \quad (3.33)$$

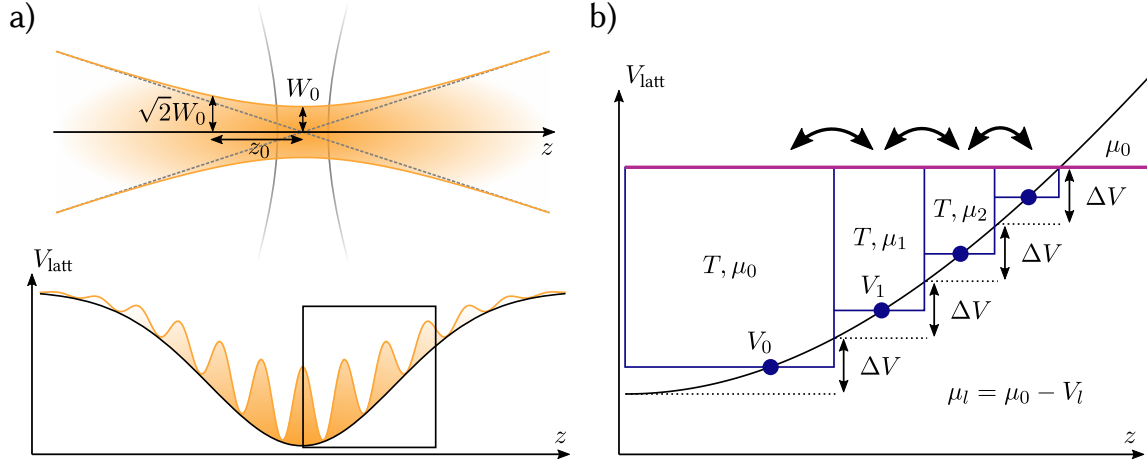


Figure 3.7: Inhomogeneous lattice potentials and the local-density approximation. a) Most lattice laser beams are Gaussian and focused down to small waists W_0 to increase the possible lattice depths. Especially when going to two- or three-dimensional lattices, we have to consider an overall trapping potential on top of the periodic lattice structure, as shown below. b) To be able to simulate Hubbard physics with an inhomogeneous system like this we have to make use of the local-density approximation [48], where we divide the trap into separated sub-systems. When these system are in chemical and thermal equilibrium one can have a unified description of the chemical potential, by including the trap potential differences.

with $r = \sqrt{x^2 + y^2}$ and the beam width

$$W(z) = W_0 \sqrt{1 + \left(\frac{z}{z_0}\right)^2}. \quad (3.34)$$

Here P is the overall optical power of the beam, W_0 the radial waist in the focus and z_0 the Rayleigh length along the propagation axis.

Since the beams which form the optical lattices have the same Gaussian intensity distribution, we have to find a way to describe a lattice system with an underlying non-homogeneous potential $V_{\text{pot}}(\mathbf{r})$, as pictured in figure 3.7 a). Under the *local-density approximation* (LDA) we assume that regions within a fixed potential range ΔV can be considered homogeneous systems in thermal and chemical equilibrium with their surrounding environment, which acts like a reservoir [48]. For this we form bins with an equal potential width of ΔV centred around $V_l = \Delta V(l + 1/2)$ for the index l . These (quasi-) isopotential regions now form the subsystems for the LDA. In the grand-canonical ensemble, we assume not only thermal but also chemical equilibrium, which means that particles redistribute between these systems, until the sum of the local chemical potential μ_l and the local confinement potential V_l is constant over all sub-systems:

$$\mu_0 = \mu_l + V_l \quad \forall l \in \mathbb{N}, \quad (3.35)$$

with the potential in the centre set to zero $V_0 = 0$. This concept is sketched in figure 3.7 and allows us to describe even non-homogeneous systems with one chemical potential μ_0 , as long as we can correctly characterise the underlying potential $V_{\text{pot}}(\mathbf{r})$. Our procedure for this will be outlined in

section 4.3.5.

3.4 Tunable interactions through Feshbach resonances

The scattering length The interaction between free particles can be described in the framework of their collision dynamics. Here I will follow the review by Jean Dalibard [85] for the derivation of the interaction parameters. For this two-body problem, we can investigate the relative motion of one particle and assume the other one as resting. For particles with the same mass m this gives us a description in terms of the reduced mass $m_r = m/2$. The relative motion of the particle is described by its wave function $\psi_{\mathbf{k}}(\mathbf{r})$ and the Hamiltonian

$$\hat{H}\psi_{\mathbf{k}}(\mathbf{r}) = \left(\frac{\hat{p}^2}{m_r} + V_{\text{int}}(\hat{\mathbf{r}}) \right) \psi_{\mathbf{k}}(\mathbf{r}) = E_k \psi_{\mathbf{k}}(\mathbf{r}), \quad (3.36)$$

where $V_{\text{int}}(\hat{\mathbf{r}})$ is the interaction potential and $E_k = \hbar^2 k^2 / (2m_r)$ the eigenenergy of the free particle. We, therefore, have to assure that there exists an effective length of the interaction b and that $V_{\text{int}}(\hat{\mathbf{r}}) \rightarrow 0$ for very large $r \gg b$. The solution to an incoming plane wave $\psi'_{\mathbf{k}}(\mathbf{r}) \propto e^{i\mathbf{k}\cdot\mathbf{r}}$ scattering on the atom and then being observed again at great distance $r \gg b$ will be

$$\psi_{\mathbf{k}}(\mathbf{r}) \propto e^{i\mathbf{k}\cdot\mathbf{r}} + f\left(k, \frac{\mathbf{k}}{k}, \frac{\mathbf{r}}{r}\right) \frac{e^{ikr}}{r}, \quad (3.37)$$

which is a superposition of the unscattered wave and the radially scattered one.

The scattering amplitude $f(k, \mathbf{k}/k, \mathbf{r}/r)$ is dependent on the momentum of the incident wave $\hbar\mathbf{k}$, the incoming angle \mathbf{k}/k and the outgoing direction \mathbf{r}/r . If the interaction potential is radially symmetric $V_{\text{int}}(r)$, we can rewrite equation 3.36 in terms of angular momentum operators \hat{L}^2 and \hat{L}_z . This allows us to write the angular dependence of the wave function $\psi_{\mathbf{k}}(r)$ as a sum of the spherical harmonic functions $Y_l^m(\theta, \phi)$ with the angular momentum $l = 0, 1, 2, \dots$ and its value along a quantisation axis $m_l = -l, -l+1, \dots, l$. This description can be understood as a transfer of angular momentum in the collision, which leads to a non-radially symmetric outgoing wave function. Scattering processes with $l = 0, 1, 2, 3$ are assigned the letters s, p, d, f. For example if only $l = 0$ terms are contributing to the outgoing wave function, it does not have any angular dependence and has thus undergone pure *s-wave* scattering.

For the solution of the remaining radial wave function we have to include the effects of the relative angular momentum by modifying the interaction potential with the so called *centrifugal barrier* [85]

$$\tilde{V}_{\text{int},l} = V_{\text{int}} + \frac{l(l+1)\hbar^2}{2m_r r^2}. \quad (3.38)$$

For particles with low kinetic energy $k \ll 1/b$, this barrier cannot be overcome, allowing only s-wave scattering ($l = 0$) [86]. All higher order partial waves are reflected by this barrier before they would be close enough to react to the potential, therefore not contributing to any potential scattering.

It is important to note that this prohibits interaction at the low energy scale for fermions of the same state, since the s-wave function does not have the required particle exchange antisymmetry

for fermions. Therefore, scattering takes place only for fermions with different internal spin states.

For s-wave scattering the isotropic scattering amplitude is given as

$$f(k) = \frac{e^{2i\eta_0(k)} - 1}{2ik} = \frac{1}{k \cot[\eta_0(k)] - ik}, \quad (3.39)$$

where $\eta_0(k)$ is the phase shift of the outgoing wave acquired through the interacting potential and s-wave scattering ($l = 0$). This phase shift will be of importance, since the exact interaction potential does not need to be known for further calculations and allows for greater flexibility in the description of scattering processes and potentials. For a van-der-Waals type potential and low momentum $k \ll 1/b$ this can be approximated as [87]

$$f_{\text{vdW}}(k) = \frac{1}{-1/a + r_0 k^2/2 - ik} \rightarrow -a \quad \text{for } k \rightarrow 0, \quad (3.40)$$

with the so called s-wave *scattering length* a and an effective interaction range $r_0 \approx b$. Depending on the interaction potential the scattering length can have any value. Repulsive interactions lead to positive values $a > 0$ whereas attractive ones lead to negative scattering lengths $a < 0$. The strength of the interaction potential scales with the amplitude of the scattering length $|a|$.

As we noted previously, equation 3.39 is only dependent on the phase $\eta_0(k)$ acquired through the scattering potential, not the exact potential itself. We can use the so called *contact potential*, which assumes only a point-like interaction (pseudo-) potential $V_{\text{int}} = g\delta(\mathbf{r})$ and allows for the simplification of some calculations. For proper regularisation it has to be written as

$$V_{\text{int}}\psi(\mathbf{r}) = g\delta(\mathbf{r})\frac{\partial}{\partial r}[r\psi(\mathbf{r})]. \quad (3.41)$$

This potential leads to a scattering amplitude of [85]

$$f_{\delta}(k) = -\frac{a}{1 - ika} \rightarrow -a \quad \text{for } k \rightarrow 0, \quad (3.42)$$

with scattering length $a = gm_r/(4\pi\hbar^2)$. For low kinetic energies we can use this pseudo-potential as an approximation, which reduces the complexity of scattering calculations tremendously.

Feshbach resonances For two atoms of the same atomic species the interaction potential is fixed and its resulting s-wave scattering length a can be measured. For a good quantum simulator we would like to have more flexibility in adjusting the collision properties. This tunability can be provided by the use of magnetic *Feshbach resonances* as presented in the review [87] this section is based on.

In the previous section we introduced the radial interaction potential V_{int} , which is zero for large distances, i.e. free atoms. The two colliding atoms, however, can be in many different combinations of hyperfine states, with different relative energy depending on their Zeeman shift, shown in figure 3.1. In this multitude of scattering potentials with different internal states we define the one the scattering atoms occupy as the *open channel*, and all state combinations with higher energy the *closed channels* [88].

In figure 3.8 a) we show two such channels with a van-der-Waals like potential. The molecular

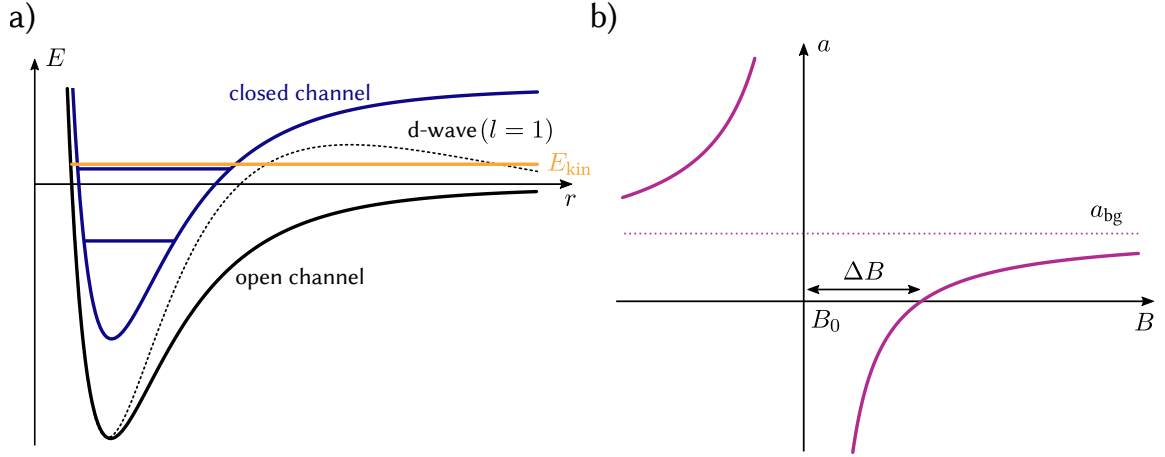


Figure 3.8: Feshbach resonances. a) If an unbound particle approaches another one with a fixed relative kinetic energy E_{kin} through the open channel and matches the energy of an internal bound state of a closed channel, a resonance behaviour changes the phase gained by the scattering event. For the low energy scattering relevant in this thesis we assume E_{kin} close to zero, so nearly constant for all small scattering momenta. Scattering with higher relative angular momentum like d-wave scattering ($l = 1$) is strongly suppressed by a centrifugal potential barrier, here marked with a dotted line. b) This phase change leads in the low energy regime to an effective change of the scattering length a . The resonance behaviour can be controlled by magnetic field B if the magnetic moment of the closed channel is different to the open channel. The difference from the resonance to the zero crossing of a is the *resonance width* $\Delta B = B(a = 0) - B_0$.

potential of the energetically higher closed channel can have one or several bound/molecular eigenstates E_{cc} . If an atom entering the effective interaction range r_0 has the correct kinetic energy $E_{\text{kin}} = E_{\text{oc}}$, it might match one of the bound state energies $E_{\text{oc}} \approx E_{\text{cc}}$. In this case a resonance behaviour can occur during the collision, leading to a coupling to the closed channel bound state. Depending on the energy difference between open and closed channel this can lead to a significant change in the phase $\tilde{\eta}_0(k)$ of the outgoing scattered wave. As we know from equation 3.39, this directly translates to a change in the scattering amplitude, modifying the collisional properties.

We are usually working in the low kinetic energy limit, where $E_{\text{kin}} \approx 0$ and which therefore can be assumed to be fixed. If the closed channel and the open channel have a different magnetic moment one can tune their relative energy difference via an external magnetic field. This allows tuning in and out of resonances where the difference is zero and with it modifying the scattering phase in the low energy limit, which can be described in terms of a change in the s-wave scattering length a [88]

$$a(B) = a_{\text{bg}} \left(1 - \frac{\Delta}{B - B_0} \right), \quad (3.43)$$

where a_{bg} is the background scattering length without resonant channel coupling, B_0 the resonance position and the resonance width Δ , which is the distance of the zero crossing $a = 0$ to the resonance B_0 , see figure 3.8 b). Scattering lengths are usually defined in units of the Bohr-radius $a_0 = 4\pi\epsilon_0\hbar/m_e e^2$.

Close to a Feshbach resonance the formation of molecules by three-body collisions, where two

atoms form a bound molecule and one atom takes away the excess energy can be enhanced, leading to increased losses of trappable atoms. Losses for scattering events where internal states are changed and excess internal energy transferred to kinetic energy are also increased. An additional loss channel related to the collision channel description is the optical coupling to higher bound states during the collision event, the so called *light-assisted collisions* [89].

Despite these enhanced loss mechanisms, the Feshbach resonances provide an easy to tune and very flexible way of manipulating the interaction of ultracold atoms, changing their strength and even switching from repulsive to attractive interactions.

Determining the on-site interaction in a lattice For the simulation of the Hubbard model the on-site interaction energy U describes the interaction. Starting with two atoms at the same site i we can calculate it with the interaction potential V_{int} and the local probability density of both particles. The overall interaction energy is given by

$$U = \int d^3\mathbf{r} d^3\mathbf{r}' |\psi_{i,\uparrow}(\mathbf{r})|^2 V_{\text{int}}(\mathbf{r} - \mathbf{r}') |\psi_{i,\downarrow}(\mathbf{r}')|^2. \quad (3.44)$$

We know from the previous section that we can use the contact interaction potential $V_{\text{int}} = 4\pi\hbar^2 a/m_r \delta(\mathbf{r} - \mathbf{r}')$ and use the Wannier basis to describe the local wave function $\psi_{i,\sigma}(\mathbf{r}) = w_0(\mathbf{r} - \mathbf{r}_i)$. This leads to

$$\begin{aligned} U &= \frac{4\pi\hbar^2 a}{m_r} \int d^3\mathbf{r} d^3\mathbf{r}' |w_0(\mathbf{r} - \mathbf{r}_i)|^2 \delta(\mathbf{r} - \mathbf{r}') |w_0(\mathbf{r}' - \mathbf{r}_i)|^2 = \\ &= \frac{4\pi\hbar^2 a}{m_r} \int d^3\mathbf{r} |w_0(\mathbf{r} - \mathbf{r}_i)|^4, \end{aligned} \quad (3.45)$$

where the on-site interaction is directly proportional to the scattering length a .

It is important to note that Wannier functions are calculated from the non-interacting Bloch waves, so using them to describe an interacting system is already an approximation. The numerical calculations used in this thesis were done including higher band contributions to simulate these distortion effects and other correction factors [21].

We have shown in this chapter how to characterise and describe a two-component Fermi gas in an optical lattice in terms of the Hubbard parameters and pointed out the restrictions that we have to apply in order to obtain a quantum simulator for the Hubbard model.

Experimental setup

In the last chapter I have motivated the use of ultracold fermions in optical lattices for the quantum simulation of the two-dimensional Hubbard model and possible extensions. The contents of this chapter are dedicated to describing the setup we use to create an ultracold atomic cloud, the process of loading these atoms into our lattice configuration and the subsequent detection methods.

4.1 Cooling to quantum degeneracy

This section describes the cooling of the initially heated atomic vapour from more than room temperature down to a quantum degenerate gas of only several nK to use as the starting point of our experiments. The experiment this thesis was done on was already set up in 2008, and therefore this section is mostly a summary of previous PhD theses where the cooling to degeneracy was reached [18–20]. An exception here is the evaporative cooling on the attractive side of the 202 G Feshbach resonance, discussed in section 4.1.3, which was implemented and optimised during this thesis.

4.1.1 Laser cooling

In the first part of our vacuum apparatus, a sample of enriched potassium is moderately heated to create a relatively high background pressure of 1×10^{-9} mbar. The atoms are slightly above room temperature at about 300 K and first need to be cooled down. This is done with *laser cooling* [75], using lasers with wavelengths close to the D₂ Line, i.e. at around 766.7 nm, see figure 4.1 b). One laser is optimised for the $|F = 9/2\rangle \rightarrow |F' = 11/2\rangle$ transition, which we call the *cooling* transition. The absorption process for laser cooling should be cyclic, i.e. after a scattering event, the atoms should quickly be ready to absorb another photon from this source. This happens through spontaneous emission of a photon in a random direction, bringing the internal state of the atom down to the original state and resulting in a net momentum transfer, i.e. a force by the initial laser photon. However, some atoms end up in the $|F' = 9/2\rangle$ state, which can decay into the $|F = 7/2\rangle$ ground state and then cannot take part in further scattering processes. An additional *repumper* laser works on the $|F = 7/2\rangle \rightarrow |F' = 9/2\rangle$ transition to pump them back into the cooling cycle.

Both of them are red-shifted relative to the bare transition frequency, since they make use of the Doppler shift to get a directional dependence on the absorption. This means that only atoms flying towards the laser direction have the light shifted into resonance and can scatter it, thereby only

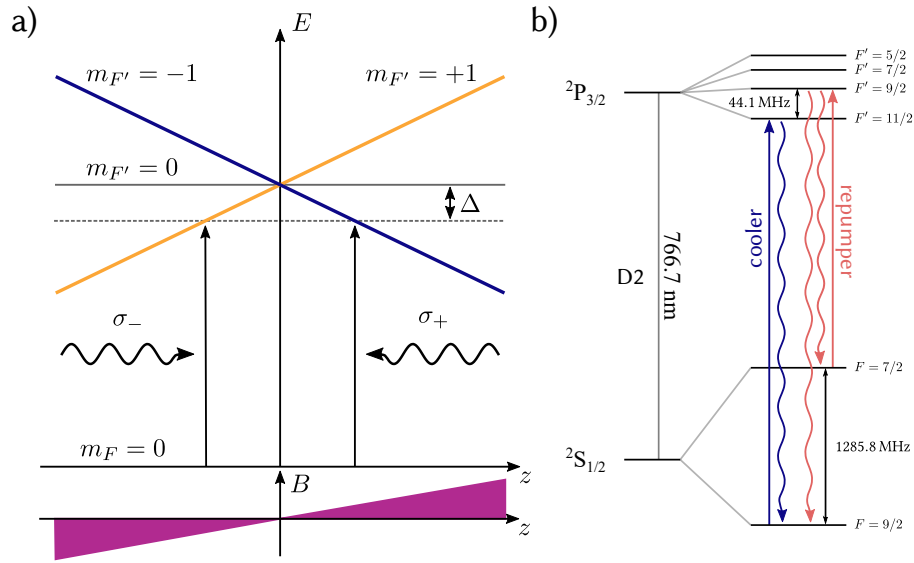


Figure 4.1: Magneto-optical trap. a) Through the energy shift in a magnetic quadrupole field, the resonance condition for incoming excitation light becomes spatially dependent. By correctly choosing the laser detuning $\Delta < 0$ the resulting effective force from continuous absorption and spontaneous emission leads to both slowing down and pushing the atoms towards the centre, i.e. cooling and trapping. For simplicity an exemplary $F = 0$ and $F' = 1$ system is shown, this can, however, be easily adapted to atoms with larger F and F' , since the general dependence for $\Delta m_F = \pm 1$ is the same. b) Optical transitions used in our experiment. The D₂-line transition from $F = 9/2 \rightarrow F' = 11/2$ is used for the *cooler* laser. By off-resonant excitation and two-photon decay the $F = 7/2$ manifold can be populated, requiring a *repumper* laser to optically pump the atom population back to the $F = 9/2$ ground state. Figure inspired by [75].

absorbing photon momenta that reduce their speed. Using six laser beams coming in from all spatial axes we can slow down atoms in the region where the beams overlap, which is called an optical molasses [75]. This, however, does not spatially trap them, so even when slowed down they will, at some point in time, escape the slowdown region.

By adding a magnetic quadrupole field centred on the crossing laser beams and by choosing the detuning correctly, we can introduce an additional spatial dependence on the force acting on the atoms: They will be on resonance only where the laser frequency detuning matches the Zeeman shift of the hyperfine states. In a quadrupole field and with linear polarisation along the quantisation axis this happens at two locations where the strength of the field is the same. In one position the beam is pushing the atoms towards the trap centre and in the other further away. By choosing the correct circular polarisation we can control this process and only allow the transition that traps atoms, which is shown in figure 4.1.

With both ingredients of cooling and spatially trapping the atoms we have created a magneto-optical trap (MOT) that can trap a cloud of approximately 5×10^8 atoms and cool them down to a temperature of about $150 \mu\text{K}$ [19]. Choosing the detuning is a trade-off of two parameters, the momentum range in which we can trap passing atoms, the so called capture range, and the decelerating force in the centre, which determines the temperature of the captured atoms. A larger detuning allows for a larger capture range, but at the same time reduces the cooling force in the

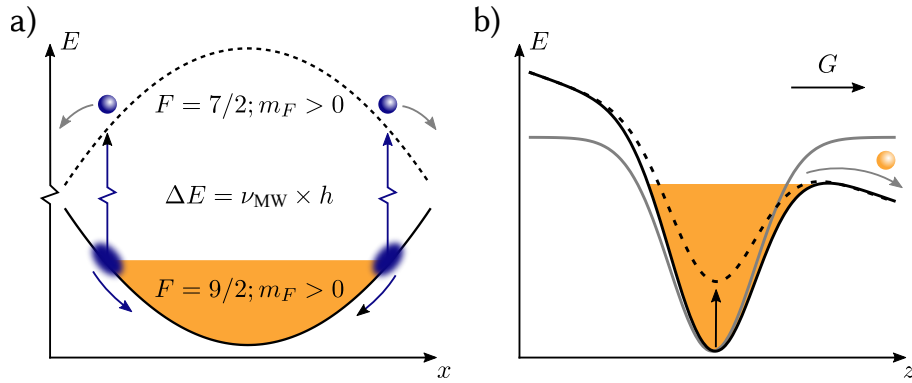


Figure 4.2: Evaporative cooling. By removing the hottest atoms from a sample, we can lower the average energy per particle, effectively cooling them. Through their large kinetic energy, the hottest atoms can reach farthest away from the centre. a) In the magnetic trap this means they also experience the largest magnetic fields, which are proportional to the trapping potential. By using microwave radiation and slowly sweeping the microwave frequency ν_{MW} they are transferred to high-field seeking states, effectively being pushed out of the trap. b) In an optical trap we gradually lower the trapping potential such that, in our case assisted by gravity, the hottest atoms can leave the trap. By this we also change the trapping potential, which can be a disadvantage since it reduces rethermalisation.

centre. Initially we use a large capture range to collect as many atoms as possible. Then we reduce the detuning further, leading to a colder, denser cloud. Here, reabsorption of the randomly scattered photons leads to the build up of light pressure, limiting the density and temperature achievable. A technique called dark MOT [90], where only a few percent of the cloud are at any given time in the cooling cycle, leads to even higher densities. To obtain this, the optical power of the repumper laser is greatly reduced to only one percent of its normal value. While the temperature only changes slightly in our case, this step increases the atom density greatly, preparing the atomic cloud for the next stage.

4.1.2 Magnetic transport and forced evaporation

In the relatively high pressure region of the MOT chamber collisions with the background gas can always heat the atoms and introduce losses. In our experiment they are, therefore, transported to an ultra-low pressure ($<1 \times 10^{-11}$ mbar) science chamber. To be able to trap them, we turn off the quadrupole field of the MOT coils and switch to a Helmholtz configuration for a constant offset field, defining a spatially uniform quantisation axis. With circularly polarised light, most of the atoms are then optically pumped into the low-field-seeking states $|F = 7/2, m_F = -7/2\rangle$ and $|F = 7/2, m_F = -5/2\rangle$ of the magnetic hyperfine splitting shown in figure 3.1, where the magnetic moment is $\mu = g_F m_F \mu_B > 0$. We then switch the coils back to the Anti-Helmholtz configuration and with a very high current, turned on rapidly, we create a magnetic trap for the atoms which are seeking the low field quadrupole centre. The coils are mounted on a mechanical sled, which then moves the trap with the atoms through a differential pressure tube into the science chamber. To minimise spin-flip induced (Majorana) losses in the centre of the trap, where the field is zero and the quantisation axis is not defined, this is done quickly in 0.7 s. The atoms are then loaded into a Ioffe-Pritchard type trap, which has the advantage of not having a zero-field location in the trapping

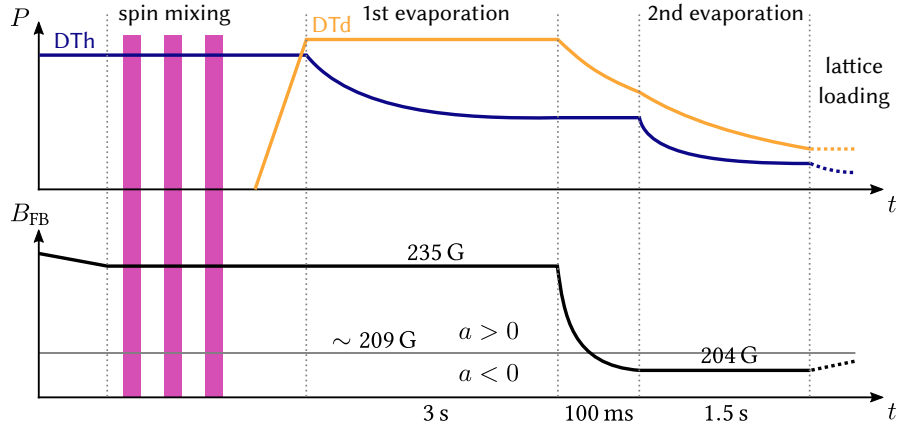


Figure 4.3: Optical evaporation sequence. After having loaded the atoms into the horizontal dipole trap (DTh), up to three successive, non-adiabatic RF sweeps are used for mixing, i.e. balancing the spins of the $m_F = -9/2$ and $m_F = -7/2$ states in the $F = 9/2$ manifold. A *dimple* laser (DTd) is then used to increase density and capture the coldest atoms in the centre region. The first evaporation is at a magnetic field of 235 G since we found that the repulsive interactions there reduce the density and help with minimising the loss rate. After that we switch to strong attractive interactions by ramping the magnetic field to 204 G while reducing the dimple laser power to minimise density changes in the trapped gas. After the second evaporation step we load into the z -lattices.

region, thus avoiding Majorana losses. Its design is described in detail in [18]. We then employ a technique called forced evaporative cooling [91], where we exploit the fact that atoms with high kinetic energy can travel further away from the trap centre, where the magnetic field is stronger, shown in figure 4.2 a). We can address these atoms with microwave (MW) and radio frequency (RF) fields, transferring them to the high-field-seeking states of the $|F = 9/2\rangle$ manifold, where g_F has a different sign. Since the trapping potential is, therefore, inverted they get expelled from the trap immediately. This effectively removes atoms locally in the trap and if chosen correctly selects only the hot atoms with high kinetic energy, reducing the mean temperature in the cloud. At the end of this step about 1×10^7 atoms at a temperature of $2.6(2) \mu\text{K}$ remain in the trap.

4.1.3 Dipole trap and initial spin preparation

In order to cool further, we switch to an all optical trap with a far detuned laser as described in section 3.2. For this, a Gaussian beam (see section 3.3 and figure 3.7) in the horizontal xy -plane is tightly focused to the centre of the magnetic trap creating an optical potential the atoms are transferred to. The beam is shaped to have a large aspect ratio of its widths of about 1:10 in its focus, with a very small waist in the vertical z -direction of about $W_{0,z} \approx 12 \mu\text{m}$. Along the propagation axis, the trapping potential is rather shallow leading to a very elongated and flat cigar-shape of the trapping potential.

The optical trap is state independent to a very good approximation. To avoid losses through spin-changing collisions, all atoms are transferred to the lowest hyperfine states $|F = 9/2, m_F = -9/2\rangle$ and $|F = 9/2, m_F = -7/2\rangle$ through a Landau-Zener (LZ) sweep, see section 3.1. Since the forced MW evaporation is spin-dependent, both states are not occupied evenly, with most atoms remaining in the $|F = 9/2, m_F = -9/2\rangle$ state [18]. In the previous chapter we already discussed how a non-

adiabatic Landau-Zener sweep can lead to an incomplete state transfer, as described in equation 3.6. By choosing the correct sweep rate $\dot{\Delta}$ relative to the RF induced coupling Ω , we can get a transfer probability of $P_{\text{transferred}} = 0.5$ leading to an equal mixing of both spin populations. This technique is made more robust by applying up to three subsequent, non-adiabatic RF frequency sweeps to obtain a spin-balanced atom cloud.

A second beam, intercepting the xy -plane at an angle of $\approx 45^\circ$ and running perpendicular to the horizontal dipole trap, is used to locally increase the phase-space density. This *dimple*-beam helps in the thermalisation of the atomic cloud by increasing the elastic collision rate [92]. Reducing the depth of the horizontal and the dimple dipole trap (named DTh and DTd respectively) leads to further evaporative cooling, this time not through forced removal, but with the help of the pull of gravity, see figure 4.2. By reducing the confinement in this step, we change the cloud compression and with it the density as well, leading to a reduction in elastic scattering events.

While elastic collisions are needed for the necessary momentum redistribution for thermalisation, a high density can as well lead to the increased probability of three-body collisions and losses, so during cooling a good compromise has to be found. One parameter used for this is the *phase-space density*, which is the normalised probability density in momentum and position space. The cooling process has to be optimised such that the temperature reduction by atom loss increases the phase-space density sufficiently to compensate for the reduction in confinement strength, while avoiding unnecessary losses [75].

Optical evaporation for systems with attractive interaction During the dipole evaporation and the following steps large Helmholtz coils create a homogeneous magnetic field along the z -direction, tuning the scattering length, and therefore the interaction strength of the atoms by exploiting the Feshbach resonances introduced in section 3.4. These are the so called *Feshbach*-coils used to create a magnetic field B close to the $m_F = -9/2, -7/2$ resonance at 202.1 G [74]. The choice of field during the evaporation usually depends on the lattice configuration we use and the Hubbard parameters we would like to simulate.

The evaporation sequence for repulsive interactions around 190 G is described in other theses [21, 22]. Here we will focus on the newly optimised sequence for the evaporation with attractive interactions, shown in figure 4.3, that allow for experiments at fields of $B = 204$ to 208 G. The temperature and atom number detection is done with absorption images after a time-of-flight (TOF) measurement, described in [19]. After the magnetic trap and the state transfer to the two lowest hyperfine states the magnetic field is around $B \approx 235$ G, where the scattering length is close to its repulsive background value $a = 137 a_0$, with a_0 as the Bohr-radius. The initial optical evaporation is happening at that field as well, where we cool by decreasing only the DTh power and concentrate the cold atoms in the dimple potential. Switching to attractive interactions immediately for the first step would have resulted in a significant increase in density, therefore an enhancement of three-body losses and other inelastic collisions, resulting in very inefficient cooling.

After this, the kinetic energy is low enough for the atoms to suppress p-wave and higher angular momentum scattering, suppressing three body losses significantly. We then tune the magnetic field to $B \approx 203.9$ G and a scattering length of $a = -512 a_0$ for further evaporation with attractive interactions. To balance the density and the number of collisions, the dimple dipole trap strength is reduced at the same time. Now the increase in scattering strength helps with the thermalisation of the atomic cloud, which is increasingly difficult due to Pauli blocking in the quantum degenerate

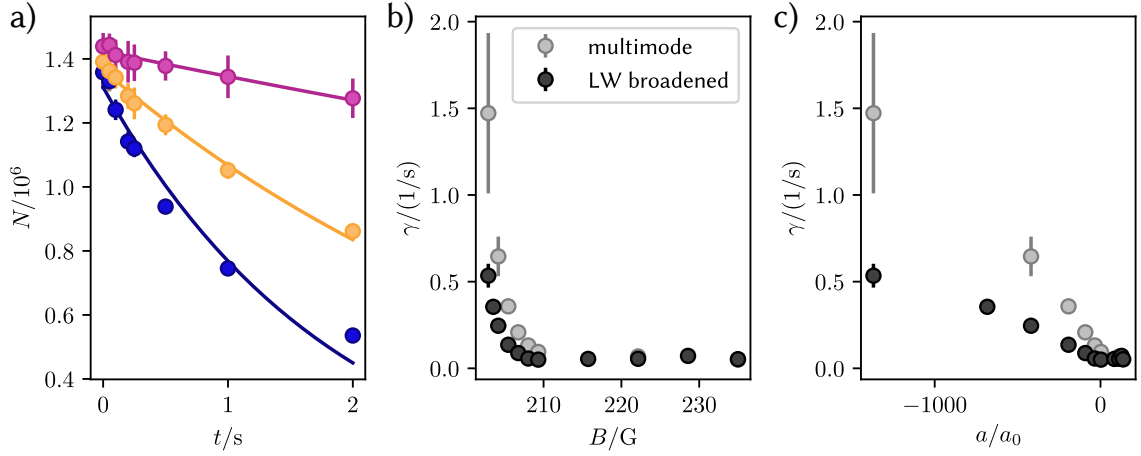


Figure 4.4: Field dependent atom loss through light-assisted collisions. a) The atom number N after a time t where the trapping potential with a strong DTh is held constant, averaged over ten measurements. Blue data was taken with the linewidth broadened laser described in the text at 202.9 G ($a = -1370 a_0$), orange at 204.2 G ($a = -419 a_0$) and pink at 208.0 G ($a = -34.2 a_0$). Their fitted decay rate γ is compared to the previous multimode laser in b) and c), where we can see a loss rate reduction by a factor of three.

regime, where $T < T_F$ with the Fermi temperature $T_F = E_F/k_B$ [93]. The ramp values are experimentally optimised to minimise the heating from a change in density, which could lead, for example, to breathing modes in the cloud. In the final evaporation step both trap beam powers are reduced simultaneously, resulting in around 2.0×10^5 atoms per spin state at a temperature of $T/T_F \approx 0.12$ with small daily fluctuations. The atomic cloud has an approximately round shape in the horizontal plane, and is strongly compressed along the vertical z -direction.

Light-assisted collisions close to the Feshbach resonance As mentioned before, it is absolutely critical to avoid heating and losses that do not contribute to reducing the phase-space density. During the optimisation we discovered that the 1070 nm fibre laser, previously used for creating the dipole trap beams, induced atom losses when working close to the Feshbach resonance at 202.1 G. A similar behaviour was reported for a laser with the same specifications i.e. wavelength and notably the broad bandwidth of >0.5 nm, see footnote 3 on page four in [94]. They attributed these losses to light-assisted collisions [87], which have narrow resonance features for red-detuned laser light far from the main optical transition. By switching to a single-mode laser seed from a Mephisto MOPA 20 W with only 1 kHz nominal linewidth, amplified with a NKT Photonics fibre amplifier *Koheras Boostik* 10 W, we could suppress these losses significantly by a factor of 3, see figure 4.4. This was, however, not a permanent solution as partial back reflection from the uncoated inside of the glass chamber led to a significant lattice-like standing wave potential for the DTh. During evaporation it would create separated pockets that are not completely thermalised with each other, reducing the overall cooling efficiency again. To solve this we increased the linewidth from 1 kHz to about 25 GHz by using an electro-optical phase modulator (EOM) and a noise generator signal amplified by 7 orders of magnitude. This drastically reduced the coherence length such that no standing wave potential was observed any more, while losses through light-assisted collisions were greatly reduced. The details of this unusual setup and its characterisation are described in appendix A.

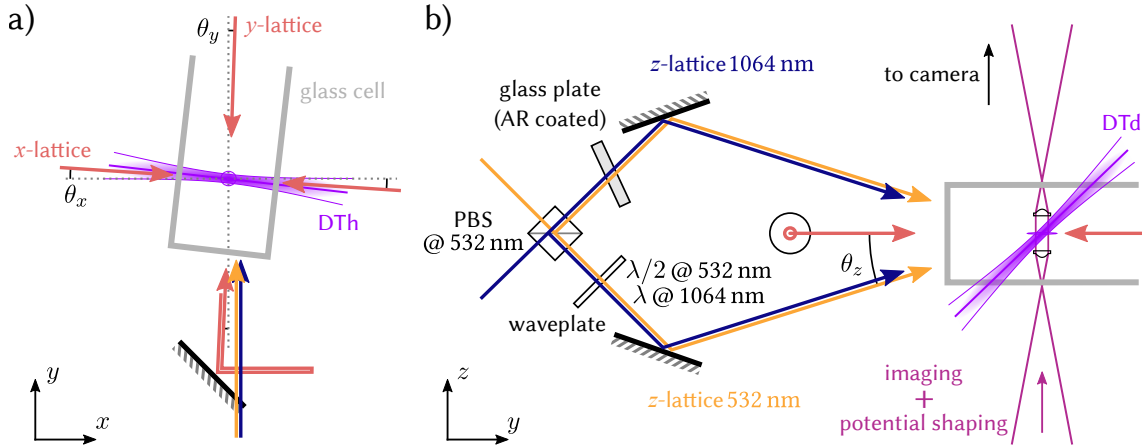


Figure 4.5: Lattice laser configurations. a) Both the y - and the x -lattice, shown in red, are not perfectly aligned with the camera/laboratory coordinate system and deviate by a small angle θ_x and θ_y . After passing the glass cell they get retro-reflected, matching their incoming beam angle. Due to spatial constraints set up by the Ioffe-trap coils, the DTh beam, here in blue, has to enter the glass cell nearly perpendicular. Since the inner side of the glass cell has no anti-reflective (AR) coating this can lead to partial back-reflection, highlighting the need for a broadband laser source with short coherence length. In b) the z -lattices are shown in the vertical zy -plane. The polarising beam splitter (PBS) is designed for operation with 532 nm light, and acts like a 75:25 non-polarising beam splitter for 1064 nm light. The waveplate in the lower beam path is used to rotate the polarisation of the green laser (in orange), while the red laser (in deep blue) polarisation remains unchanged. Since the beam paths were designed to produce a path length difference $\Delta s \simeq 0$ [21], we had to add an AR-coated glass plate with 5 mm thickness to be able to control the phase of the superlattice. Additionally the beam path for absorption imaging and potential shaping is shown in pink, including the two aspheric lenses inside the vacuum chamber.

4.2 Lattice loading and physics phase

This cloud of ultracold, quantum degenerate atoms has to be loaded into a two-dimensional lattice, while avoiding any potential increase in the temperature of the gas. It will be done in two subsequent steps, by first using a lattice in z -direction to separate the cloud into quasi two-dimensional *pancakes* and afterwards ramping up the in-plane lattices. In this section we will discuss the geometric lattice configuration, its characterisation and the loading of the atoms into the lattices, which is also described in [21, 22]. Therefore, a special focus is put onto a new method of loading using a superlattice, which was implemented and optimised during this thesis.

4.2.1 Lattice geometries

Vertical z -lattices The lattice in z -direction, in the following simply called z -lattice, is an accordion lattice as described in section 3.2 with its beams angled by $\gamma = 14.48^\circ$ relative to the xy -plane. Figure 4.5 shows its spatial orientation together with the dipole trap and the xy -lattices.

The z -lattice setup was initially designed for green $\lambda_{\text{green}} = 532 \text{ nm}$ laser light from a Coherent Verdi V10, which forms a repulsive periodic potential for the atoms since it is blue-detuned to the main optical transitions of potassium [21]. The two lattice beams are created by dividing one source beam evenly with a polarising beam-splitter (PBS) and subsequently rotating the polarisation of the

lower beam by 90° to match the upper one. With this method and the careful manufacturing of the optics mount out of a block of solid aluminium for thermal stability, the optical path length difference of the upper and lower beam $\Delta s = |s_{\text{upper}} - s_{\text{lower}}|$ is small. This reduces the magnitude of position fluctuations due to laser frequency changes, which could induce heating. With equation 3.18 we calculate the lattice periodicity as $a_z = \lambda_{\text{green}}/[2 \sin(\gamma)] = 1.064 \mu\text{m}$.

During this thesis we added an infrared $\lambda_{\text{red}} = 2\lambda_{\text{green}} = 1064 \text{ nm}$ laser beam to the second input port of the PBS. This beam splitter is only optimised for $\lambda_{\text{green}} = 532 \text{ nm}$, but acting as a non-polarising one for $\lambda_{\text{red}} = 1064 \text{ nm}$, with a splitting ratio of about $\gamma_z = 1:3$ (reflected:transmitted). Since the beam splitter cube is glued to the aluminium base plate we cannot exchange it easily and we have to work with imbalanced beam powers for the lattice. This leads to a large proportion of the laser intensity not forming a lattice potential but acting similarly to a dipole trap beam in y -direction. We switched to a low order $\lambda/2$ wave plate for the green 532 nm light, that does not affect the infrared polarisation to maximise the interference potential for both wavelengths.

Super-lattice phase Since both lattices use independent input paths, we can employ them simultaneously and create a superlattice potential in z -direction. At a fixed position \mathbf{r} at the centre of the dipole trap, the phase of the lattice potential created by light with wavelength λ is given by

$$\phi_\lambda = 2\pi \frac{\Delta s(\lambda)}{\lambda}, \quad (4.1)$$

where $\Delta s(\lambda)$ is the optical path length difference of the upper and lower beams, which is wavelength dependent in general. The superlattice phase, as defined in equation 3.32, is then

$$\phi_{\text{SL}} = \phi_{532 \text{ nm}} - 2\phi_{1064 \text{ nm}} = 2\pi \left[\frac{\Delta s(\lambda_{\text{green}})}{\lambda_{\text{green}}} - \frac{2\Delta s(\lambda_{\text{red}})}{\lambda_{\text{red}}} \right] = 2\pi \frac{\delta s}{\lambda_{\text{green}}}, \quad (4.2)$$

and therefore determined by the deviation of the optical path length differences of both wavelengths $\delta s = \Delta s(\lambda_{\text{green}}) - \Delta s(\lambda_{\text{red}})$. δs was observed to be stable over several weeks, leading to a geometrically fixed offset phase of ϕ_{SL} . Here we assumed that $\lambda_{\text{green}} = \lambda_{\text{red}}/2$. To allow for further tuning of the superlattice phase, we introduce a wavelength detuning to the green light $\Delta\lambda_{\text{green}} = \lambda_{\text{green}} - \lambda_{\text{red}}/2$. Assuming $\Delta\lambda_{\text{green}}/\lambda_{\text{green}} \ll 1$ we can use following approximation:

$$\phi_{532 \text{ nm}} = \frac{\Delta s(\lambda_{\text{green}})}{\lambda_{\text{green}}} = \frac{\Delta s(\lambda_{\text{green}})}{\lambda_{\text{red}}/2} \frac{1}{(1 + 2\Delta\lambda_{\text{green}}/\lambda_{\text{red}})} \quad (4.3)$$

$$\approx \frac{\Delta s(\lambda_{\text{green}})}{\lambda_{\text{red}}/2} \left(1 - \frac{2\Delta\lambda_{\text{green}}}{\lambda_{\text{red}}} \right). \quad (4.4)$$

Using this in equation 4.2 and with the assumption that the optical path difference $\Delta s(\lambda_{\text{green}})$ does not change in that range, we get

$$\phi_{\text{SL}} = 2\pi \left[\frac{2\Delta s(\lambda_{\text{green}})}{\lambda_{\text{red}}} \left(1 - \frac{2\Delta\lambda_{\text{green}}}{\lambda_{\text{red}}} \right) - \frac{2\Delta s(\lambda_{\text{red}})}{\lambda_{\text{red}}} \right] \quad (4.5)$$

$$= 2\pi \frac{2\delta s}{\lambda_{\text{red}}} + 2\pi \frac{4\Delta s(\lambda_{\text{green}})\Delta\lambda_{\text{green}}}{\lambda_{\text{red}}^2}. \quad (4.6)$$

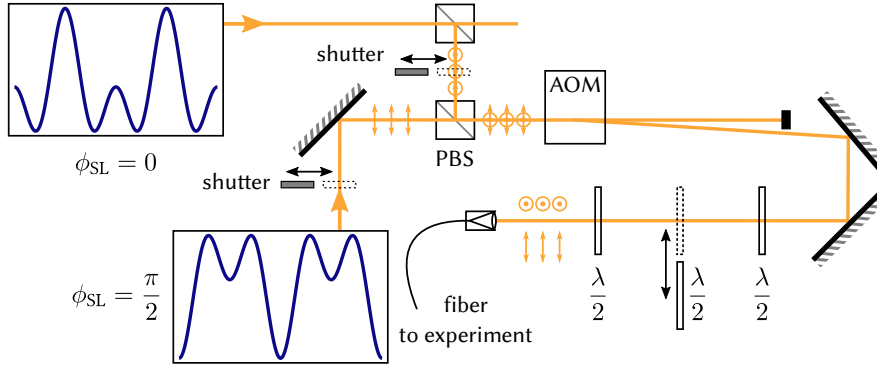


Figure 4.6: Laser switch for the superlattice phase. In the experiment we require two superlattice configurations, the symmetric $\Phi_{SL} = 0$ and the asymmetric $\Phi_{SL} = \pi/2$ one. Since tuning the 1 064 nm laser by ~ 30 GHz (~ 60 GHz for the 532 nm laser) in a few milliseconds is very hard, we use two different laser sources, which are shifted in frequency to support these conditions. To avoid a loss in power during the beam combination, we use a polarising beam splitter (PBS) before the acousto-optical modulator (AOM) and rotate the polarisation depending on which beam is used. This *half-wave shutter* is synchronised with the other beam shutters.

This means that we have a constant phase offset with the first term that depends on δs and is mostly fixed, but by detuning the wavelength of the lasers with respect to each other we can get an additional variable phase contribution. However, these path length differences Δs were initially designed to be very small [21]. To increase the path length difference we placed a piece of glass with an anti-reflection coating and a thickness of about 5 mm into the upper beam path.

With techniques shown later in this thesis we determine that by increasing the green laser frequency by $\delta\nu_{\text{green}} = c/\lambda_{\text{green}} - c/(\lambda_{\text{green}} + \Delta\lambda_{\text{green}}) \approx 60$ GHz the superlattice phase shifts by $\pi/2$. Putting this into equation 4.6 gives us an estimate of the path length difference to $\Delta s(\lambda_{\text{green}}) \approx 2.56$ mm.

In this thesis we work with two superlattice configurations, the first one in which a superlattice phase $\phi_{SL} = 0$ creates a lattice of symmetric double-wells (*symmetric/double-well configuration*) and the second one with $\phi_{SL} = \pi/2$ where the lattice with longer lattice spacing $a' = 2a$ lowers every other site, binding atoms more tightly there (*asymmetric configuration*). Both superlattice configurations are needed in the same sequence, with switching times of less than a second. Since the mode-hopping free tuning range of lasers is not always as large as 60 GHz, we use two different lasers for the $\lambda_{\text{red}} = 1\,064$ nm light. Both are Innolight Mephisto Nd:YAG lasers, one as master-oscillator power-amplifier (MOPA) for the symmetric configuration, which provides enough power for the in-plane lattices as well, and the other one for the asymmetric configuration with just a master laser module.

These laser beams have to be combined and launched into the same optical fibre with the same polarisation. This could be done with a non-polarising beam splitter (1 : 1), which would, however, result in the loss of half the power in each beam, which is very undesirable. Figure 4.6 shows the solution implemented during this thesis, where we combine both beam paths with a polarising beam splitter to one output beam. To switch between the laser sources one has to open or close beam shutters, which consists of a metallic flag that is rotated in or out of the beam, on the respective input port and additionally rotate the polarisation of the light. This rotation is done with a *half-*

wave shutter: a half-wave plate glued onto a shutter flag. The desired 90° polarisation rotation is only achieved for the correct polarisation of the input beam. Since after the gluing this cannot be optimised, we added two half wave plates in front and back of the half-wave shutter to be able to freely choose the polarisation basis. The switching between both beams and therefore the superlattice configurations can now be done in less than 10 ms.

In-plane lattices The in-plane x - and y -lattices are created by red-detuned $\lambda_{\text{red}} = 1\,064$ nm beams that are retro-reflected to be used twice as forward and backward propagating beams. Since both beams are interfering at an angle of 180° , the lattice spacing is $a_{xy} = \lambda_{\text{red}}/2 = 532$ nm. The decrease in power of the back reflected beam due to losses is described with the ratio of the powers in forward and backward propagating beam $\gamma = P_{\text{backward}}/P_{\text{forward}}$, which is different for both beams: $\gamma_x = 0.84$ and $\gamma_y = 0.77$. As shown in figure 4.5 a) both lattices do not intercept at exactly 90° and are slightly tilted relative to the x -axis ($\theta_x = -4.85(4)^\circ$) and the y -axis ($\theta_y = -0.42(6)^\circ$) respectively. This asymmetry relative to the square lattice is, however, only relevant if we have more than nearest-neighbour hopping, for example diagonal next-nearest-neighbour tunnelling. Since this is a requirement for the quantum simulation of the two-dimensional Hubbard model as well, we will work only with lattice depths that prohibit these higher-order tunnellings and therefore can ignore this detail.

Parametric heating To calibrate the laser power needed to create a desired lattice depth V_{latt} we can use the technique of *parametric heating* [96, 97]. For this we modulate the laser power that generates a deep lattice potential with the angular frequency ω_{PH} , leading to a modulation of the lattice potential itself $V_{\text{latt}} = V_{\text{latt},0} \cdot [1 + A \sin(\omega_{\text{PH}}t)]$, where A is a small modulation amplitude $A \ll 1$. This modulation leads to a perturbative coupling of the energy states that have a spatial wave function overlap. In a lattice structure this would be the band structure $E_{n,q}$ derived in section 3.2 and the corresponding Bloch waves. By varying the modulation frequency ω_{PH} we can, therefore, probe the potential we have created and compare it with band structure simulations to determine the created lattice potential V_{latt} . The eigenfunctions of a deep lattice are represented by the different bands n and have alternating parity, similar to the solutions of the harmonic oscillator. For a non-zero coupling, the overall parity has to be even, and therefore the spatially symmetric modulation of each site can only couple the ground state to each second excited band, i.e. from lowest ($n = 0$) to second ($n = 2$), fourth ($n = 4$), ... excited band.

Band mapping Detecting higher band occupations, as generated by the parametric heating, can be difficult since the spatial detection probability of a particle on a specific site in general does not change when it is motionally excited to a higher band. In general the particles have an increased tunnelling rate due to the larger bandwidth of higher bands and can, therefore, leave the trapping potential in some cases and get lost. A far more accurate detection technique is *adiabatic band mapping* [15, 95]. By adiabatically reducing the lattice potential, the particles in a higher band n_x with quasi-momentum q_x will obtain the momentum $k_x = n_x \frac{\pi}{a_x} + q_x$ as free particles. In a so called time-of-flight (TOF) measurement we let the atoms expand in time t_{TOF} of free fall without the lattice in a very shallow or no potential. The spatial distribution will closely match the momentum distribution $x = k_x t + x_0$ if $x_0 \ll k_x t$. An example of parametric heating resonances visible due to loss of the atoms in higher bands after band mapping is shown in figure 4.7.

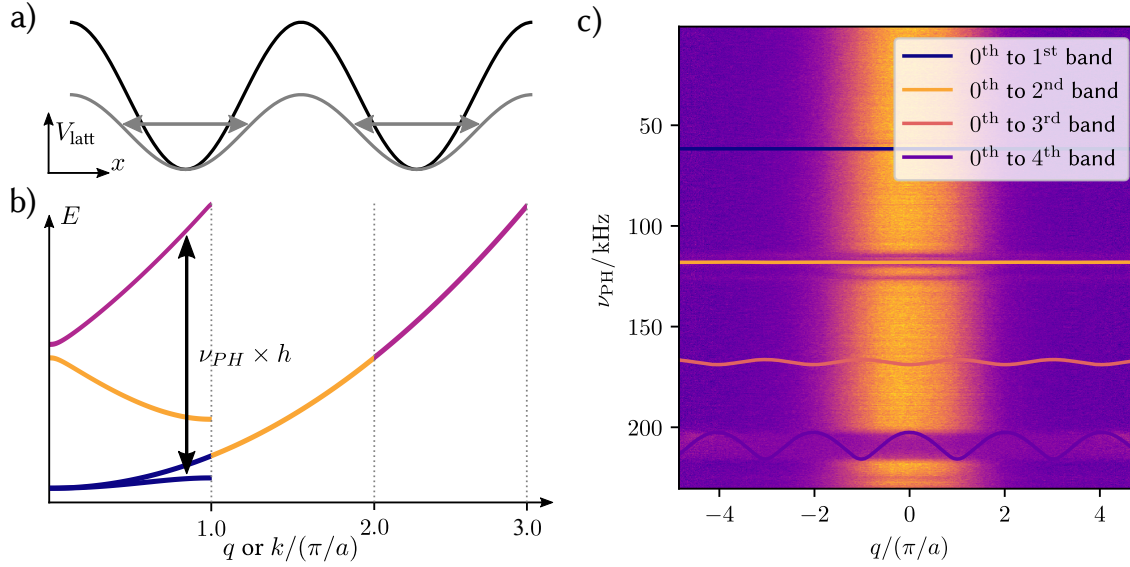


Figure 4.7: Parametric heating a) For a deep optical lattice, a periodic modulation of the lattice potential V_{latt} with frequency ν_{PH} leads, at a single site, to a symmetric contraction and expansion of the confinement potential. The wave function of an atom at this site is modulated the same way, which can result in coupling to excited states. This, however, depends on the wave function overlap, symmetry conditions and that the energy difference to the excited state has to be matched by $\Delta E = \nu_{PH} \times h$ as shown in b). Once the higher bands are populated we can observe them through *band mapping* [15, 95]. There we ramp down the lattice potential fast enough such that the populations of the bands do not mix and map to the dispersion relation of the free particles. In a time-of-flight (TOF) measurement we can then infer the momentum distribution by measuring the local density after a fixed release time. c) Shows such a measurement for the x -lattice, where the y -dependence is integrated out and clear resonances appear. Only transitions to even bands are allowed due to the symmetry constrains. The small resonances close to the 0th \rightarrow 2nd transition are due to coupling to the y -lattice band transitions at their respective resonance.

4.2.2 Loading into two dimensions

The main challenge in loading a two-dimensional lattice for quantum simulation is doing so with minimal increase in temperature and entropy. Therefore, the sequence in which the lattice lasers ramp up their power for the final configuration requires careful adjustments and optimisation. An especially critical step is the transition from three dimensions in the dipole trap to the quasi-two-dimensional clouds in the green z -lattice due to the reduction in dimensionality.

For very strong lattice depths one can approximate the lattice potential with separated harmonic potentials with harmonic oscillator frequency ω . For increasing lattice depth, ω becomes so large that the energy required for an excitation to a higher oscillator state $\hbar\omega$ in that direction cannot be provided by thermal excitations any more ($\hbar\omega \gg k_B T$) and the system can be described as two-dimensional in most physical aspects. The slow increase of the blue-detuned, repulsive lattice intensity up to the final value of $120 E_{\text{rec}}$ leads to a reduction of the central trapping potential, allowing hotter atoms to spill over into the side-arms of the horizontal dipole trap beam where they get lost. Since the thermalisation rate is reduced in two-dimensions, this further evaporation is most efficient with a very slow ramp-up time of 3 s. The final evaporation point can be set by the power of

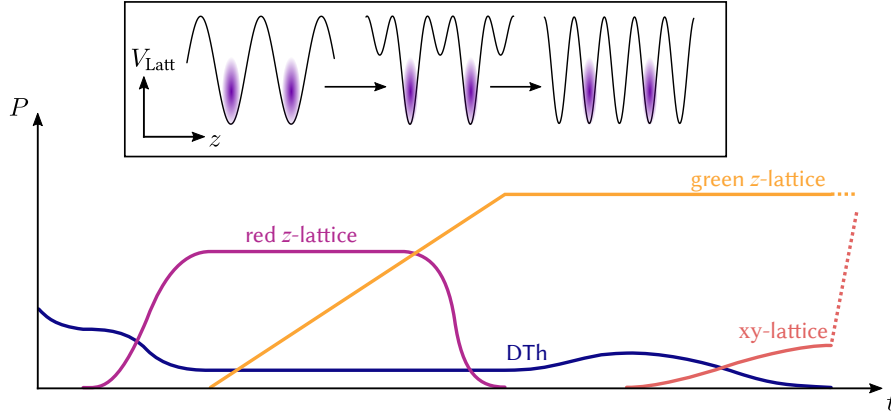


Figure 4.8: z -superlattice loading sequence To only populate each second z -plane we introduced a new loading scheme, where after the dipole trap evaporation we load the atoms into the infrared z -lattice (shown in pink), which now holds them against gravity. Then we slowly increase the green z -lattice (shown in orange) forming a superlattice with $\Phi_{\text{SL}} = \pi/2$. The repulsive potential of the blue-detuned 532 nm lattice provides additional evaporation, especially once the red-detuned 1064 nm potential is turned off. Before loading the atoms into the xy -lattices, we use the dipole trap beams DTh and DTd to match the two-dimensional density distribution to the expected lattice configuration. Finally, after having created the system we want to investigate, the xy -lattices are ramped up quickly to freeze the density distribution for detection.

the attractive dipole trap beams, allowing to trade a reduced atom number for a lower temperature.

The shape of the two-dimensional clouds can be manipulated as well by the attractive dipole trap beams just before ramping up the in-plane xy -lattices. This reshaping aims to match the density in two dimensions to the one expected in the final lattice configuration, as the then necessary density redistribution is assumed to be the major contribution to heating during lattice loading [98]. Finally, the xy -lattices are ramped up to a value of $6 E_{\text{rec}}$ in a time of usually 500 ms, which we could show results in a fermionic lattice gas in thermal equilibrium [29].

Super-lattice assisted loading

After the dipole trap evaporation there is only a fixed number of atoms in the three-dimensional cloud that can be loaded into the horizontal xy -planes. With an initial vertical atom cloud size of around $10 \mu\text{m}$ and lattice spacing of $a_z \approx 1 \mu\text{m}$ approximately 12 horizontal planes are loaded, however, not evenly populated. Since these atoms act as a coolant during the green lattice evaporation step, the initial atom number per plane can also influence the temperature obtainable in two-dimensions.

By loading the atoms via a superlattice in the asymmetric configuration ($\phi_{\text{SL}} = \pi/2$), we can increase the atom number in every other plane, leaving the intermediate planes empty. The sequence we implemented during this thesis is shown in figure 4.8 and consists of a first hand-over from the three-dimensional dipole trap to a purely infrared z -lattice. Subsequently, the green lattice is ramped up, creating the asymmetric superlattice. The ramping down of the infrared power was optimised to the final temperature of the atoms and the complete depopulation of the intermediate planes. The increase of the effective lattice spacing of the occupied planes to $2a_z \approx 2 \mu\text{m}$ also has other significant advantages, which we will discuss in section 4.3.3.

4.3 Detection and data analysis

After the atoms have equilibrated in the two-dimensional lattice, the xy -lattices are ramped up to $60 E_{\text{rec}}$ and all atomic movement is essentially frozen. We are then able to detect the spatial density distribution, spin-state occupation and the fraction of doubly occupied sites, the doubles fraction. In this section we will describe the methods used already in previous theses [21, 22, 24] and introduce improvements implemented during this work.

4.3.1 In-situ imaging

For the detection of the spatial atomic distribution we use an *absorption imaging* technique [99–101]. For near-resonant light ($\Delta \approx 0$) passing a non-transparent medium like our atomic clouds the light intensity I decays exponentially along the propagation direction z . For a given particle density n and the corresponding scattering cross section σ the intensity is given through the equation

$$\frac{dI(z)}{dz} = -\sigma n(z)I(z). \quad (4.7)$$

Integration along the z -axis leads to

$$\sigma \int_{-\infty}^{\infty} n(z) dz = -\ln \left(\frac{I_{\text{out}}}{I_{\text{in}}} \right) = OD, \quad (4.8)$$

where OD is the *optical density*. For simplicity, the formula above assumes a homogeneous intensity and density distribution in a certain area perpendicular to the propagation direction. In the experiment this could be the detection area of a camera pixel.

The scattering cross section σ can be derived with the two-level atom, as described in section 3.1, with spontaneous decay of the excited state. The excitation probability and therefore σ as well depend on the laser frequency detuning $\Delta = \omega_L - \omega_0$ to the optical transition frequency ω_0 . An atom in the excited state, however, cannot absorb another photon until a spontaneous decay with a photon emission in a random direction has occurred. This is described by the saturation parameter $s = I/I_{\text{sat}}$, with the saturation intensity I_{sat} . With it, we can define the scattering cross section

$$\sigma = \frac{\sigma_0}{1 + \left(\frac{2\Delta}{\Gamma}\right)^2 + s}, \quad (4.9)$$

where Γ is the linewidth of the optical transition and $\sigma_0 = 3c^2/(2\pi\omega_0^2)$ is the bare cross section. To include imperfections like frequency fluctuations and polarisation misalignment one adds a scaling factor α for an effective saturation intensity $I_{\text{sat}}^{\text{eff}} = \alpha I_{\text{sat}}$ and an effective base cross section $\sigma_0^{\text{eff}} = \sigma_0/\alpha$. Including this into equation 4.8 and considering the case of a non-homogeneous density and intensity distribution in xy -plane, we get the description for the integrated column density

$$n_{2D}(x, y) = \frac{1}{\sigma^{\text{eff}}} \left[-\ln \left(\frac{I_{\text{out}}(x, y)}{I_{\text{in}}(x, y)} \right) + \frac{I_{\text{in}}(x, y) - I_{\text{out}}(x, y)}{I_{\text{sat}}^{\text{eff}}} \right]. \quad (4.10)$$

By detecting the intensity of light after it has passed the atomic cloud on a CCD camera we get a

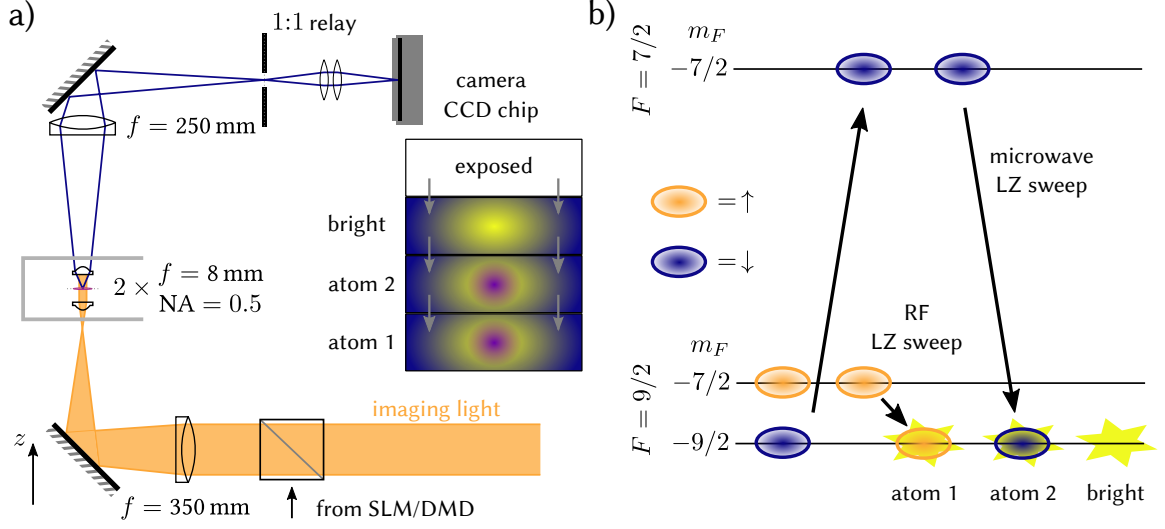


Figure 4.9: In-situ absorption imaging. a) The optical path of the imaging light (in orange) to the atoms and then further to the CCD camera is shown. The atoms are not perfectly centred in between both aspheric lenses ($NA = 0.5$), but slightly shifted to the top. The atomic cloud is then imaged to an intermediate image plane that gets projected onto the camera chip through a 1:1 optical relay. The camera is positioned such that, in combination with a cover in the first image plane, only half of the active CCD chip is illuminated. By rapidly shifting the picture taken into the unexposed regions of the chip, including a covered readout area, we take three high resolution images in quick succession. The imaging sequence is shown in b). We first use a Landau-Zener sweep to shelve the $m_F = 9/2$ atoms in the $F = 7/2$ manifold. After the first absorption picture is taken, all atoms have absorbed enough momentum to leave the trap and we can transfer the shelved atoms back, image them and after a short time take the bright picture without atoms.

count-per-pixel value $C(i, j) \propto \int_{A(i, j)} I(x, y) dx dy$ with the pixel area at position i, j as $A(i, j)$. This area is determined by the physical pixel size on the camera chip and the magnification of our imaging system M and was measured to be $A(i, j) = (0.564 \mu\text{m})^2 = (1.06 a_{xy})^2$. We now can rewrite equation 4.10 as [102]

$$n_{2D}(i, j) = \frac{1}{\sigma^{\text{eff}}} \left[-\ln \left(\frac{C_{\text{out}}(i, j)}{C_{\text{in}}(i, j)} \right) + \frac{C_{\text{in}}(i, j) - C_{\text{out}}(i, j)}{C_{\text{sat}}^{\text{eff}}} \right], \quad (4.11)$$

where we included all camera specific proportionality factors like quantum efficiency, pixel size and gain to the value of $C_{\text{sat}}^{\text{eff}}$. The calibration procedure for $C_{\text{sat}}^{\text{eff}}$, σ^{eff} and magnification M in our experiment is described in detail in [21, 22].

The optical imaging system we use is sketched in figure 4.9. One of its main features are the high $NA = 0.5$ aspheric lenses in the vacuum chamber close to the atoms. They allow for high resolution imaging of our atomic cloud, with a point-spread function (PSF) radius of $\text{PSF}_{\text{HWHM}} \approx 1.25 \mu\text{m} \approx 2.5 a_{xy}$ [22, 23]. That means the signal of an atom in the lattice is smeared out over a circle with diameter of five lattice sites.

The images are taken with an Andor Ixon 888 camera by Oxford Instruments. We use the kinetics mode, which shifts exposed images into unused regions of the CCD chip, which can then be read out with low noise later. We usually take two images with local absorption of atoms for $C_{\text{out}}(i, j)$

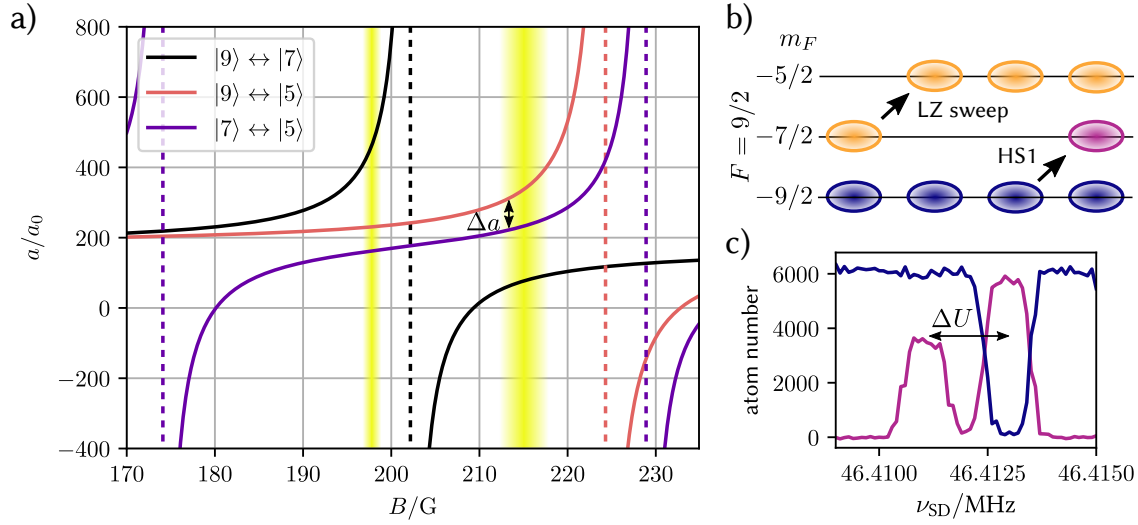


Figure 4.10: Feshbach resonances in ^{40}K and doubles detection a) A selection of relevant s-wave Feshbach resonances is shown [22, 103–105] with the background scattering length $a_{\text{BG}} = 174(7) a_0$ [106]. Most relevant in this thesis is the $|9\rangle \leftrightarrow |7\rangle$ resonance at (202.13 ± 0.10) G, with which we tune the interaction of the atoms during optical evaporation, lattice loading and the simulation of Hubbard physics. In yellow the position of p-wave resonances between $|7\rangle \leftrightarrow |7\rangle$ ((198.3 ± 0.1) G and (198.8 ± 0.1) G) [103, 106] and $|9\rangle \leftrightarrow |5\rangle$ ((215 ± 5) G) [89] are marked, that can lead to losses. We use the difference in scattering lengths $\Delta a = a_{97} - a_{75}$ to separate the atoms on double occupancies, i.e. doubles. In b) the sequence is detailed where we prepare the atoms in a $|9\rangle$ and $|5\rangle$ mixture and then use a narrow frequency HS1 transfer pulse to resolve the energy shift $\Delta U \propto \Delta a$. Calibration data is presented in c), where we used a 1.0 kHz wide pulse to resolve the energy shift $\Delta U \approx 1.8$ kHz. In pink the transferred atoms in the first picture are shown, while the shelved and then imaged atoms are shown in dark blue. Note here that atoms on doubly occupied sites are lost when they are shelved to the $F = 7/2$ manifold, and therefore are only detected when transferred with the HS1 pulse. The left peak at $\nu_{\text{SD}} \approx 46.4115$ MHz can be identified as the doubles peak and once calibrated the HS1 pulse can be used in the detection routine.

and one reference picture without atoms for $C_{\text{in}}(i, j)$, 8 ms later. Taking two images allows us for example to image both spin components, i.e. the two lowest hyperfine ground states of one realisation subsequently. The energy splitting of the states at the imaging field of about 208 G is large enough (≈ 45 MHz) to do state selective imaging, since the natural linewidth of potassium is nearly an order of magnitude smaller than the state separation: $\Gamma/2\pi = 6.035(11)$ MHz [74].

Nevertheless, there might be some off-resonant light absorption, leading to wrong signals. By using a sequence of Landau-Zener sweeps as shown in figure 4.9, we transfer atoms to the $F = 7/2$ manifold during imaging of the first state, which is extremely far (~ 1.82 GHz) detuned for the imaging light. The efficiency of one microwave transfer is 99.2(5)%. With this *microwave shelving* of one spin state, we can ensure minimal cross imaging of both populations.

4.3.2 Double occupancy detection

An atom on a doubly occupied site (double) in the shelved state introduced in the previous section can undergo spin-changing collisions, leading to the release of kinetic energy and finally the loss

of both atoms. Comparing atom numbers with and without this shelving process can give us an estimate on the fraction of doubly occupied sites, i.e. the *doubles-fraction*. We need, however, a more deterministic and reproducible approach for this measurement. Since the on-site interaction U is dependent on both atoms, changing the state of one of them leads to a change in the interaction energy $\Delta U = U' - U$. This energy difference has to be included in the RF frequency for resonant state transfers, like the Landau-Zener sweep, and therefore allows for spectroscopically separating atoms on singly-occupied sites (singles) and doubly-occupied sites (doubles). The interaction difference is determined by the scattering length difference $\Delta a(B) \propto \Delta U$, given by the Feshbach resonances introduced in section 3.4. In figure 4.10 a) we show the relevant Feshbach resonances for the lowest hyperfine states. For simplicity we will refer to the states in the lowest hyperfine manifold in the following $|x\rangle := |F = 9/2, m_F = -x/2\rangle$ such that for example $|9\rangle := |F = 9/2, m_F = -9/2\rangle$ and that U_{97} is the on-site interaction between the states $|9\rangle$ and $|7\rangle$.

This spectroscopic separation of singles and doubles was previously done in our experiment at $B \approx 180.2$ G in a $|9\rangle, |5\rangle$ mixture with an RF transfer $|9\rangle \rightarrow |7\rangle$, see figure 4.10 b). The interaction energy difference at that field was $\Delta U/h = (U_{95} - U_{75})/h \approx 6.6$ kHz [21, 22].

HS1 pulse To resolve this small frequency difference we use a specially formed pulse known from NMR tomography, the *hyperbolic secant* (HS1) pulse [107], performing an adiabatic Landau-Zener type sweep with a state transfer in only a very narrow frequency range. It has not only a shaped amplitude envelope $A(t)$, but also a time dependent frequency $\nu(t)$, ramping across a centre value ν_{HS1} over a frequency range of Δ_{HS1} . The RF waveform of the HS1 is generated as

$$V_{\text{HS1}}(t) = A(t) \cos [2\pi\nu(t) t], \quad (4.12)$$

where

$$A(t) = A_0 \operatorname{sech} \left[C_{\text{trunc}} \left(\frac{2t}{T} - 1 \right) \right] \quad (4.13)$$

and

$$\nu(t) = \nu_{\text{HS1}} + \frac{\Delta_{\text{HS1}}}{2} \tanh \left[C_{\text{trunc}} \left(\frac{2t}{T} - 1 \right) \right]. \quad (4.14)$$

Here, C_{trunc} denotes a truncation parameter that needs to be optimised for the pulse duration T one has chosen. Similar to the Landau-Zener sweep previously discussed it has close to 100% transfer efficiency if the centre frequency of the pulse ν_{HS1} is close to the resonance frequency ν_0 , i.e. $\Delta = \nu_{\text{HS1}} - \nu_0 < \Delta_{\text{HS1}}$ and quickly drops to zero for $\Delta > \Delta_{\text{HS1}}$ leading to a *flat-top* transfer. This allows for the spectroscopy of narrowly separated states while being robust to small frequency changes due to magnetic field drifts [21, 22]. The pulse duration T , however, limits the transfer width of the pulse, such that the spectroscopy of closely spaced frequencies requires longer pulses and therefore requires also less overall resonance frequency drifts.

Singles-doubles separation at 212.5 G For the experiments presented in this thesis we chose to perform this singles-doubles separation at $B \approx 212.5$ G, which leads to a frequency separation of only $\Delta U/h = (U_{95} - U_{75})/h \approx 1.8$ kHz, less than one third of the original separation. This

required an HS1 pulse with a longer pulse length $T = 7$ ms, with the truncation value optimised via numerical simulations of $C_{\text{trunc}} = 4.5$. A big issue for the spectroscopy of states with such small frequency separation is the time periodic variation of the magnetic field due to the main power oscillation frequency of 50 Hz and its higher harmonics, mostly at 150 Hz. The pulse therefore was synchronised to the power line oscillations and performed in a time window with minimal change of magnetic background field. Figure 4.10 c) shows the optimised spectroscopy signal for $\Delta_{\text{HS1}} = 1\,000$ Hz, with the transferred atoms and the microwave shelved remaining atoms numbers. Two transfer resonances are clearly visible, corresponding to the doubles and singles, both with a flat-top transfer shape. In the following the pulse frequency width was increased to $\Delta_{\text{HS1}} = 1\,500$ Hz for a more stable and robust transfer.

4.3.3 Radio frequency tomography of a single plane

All previously introduced detection methods manipulate all atoms in the cloud, i.e. act globally. However, since during the z -lattice loading we not only create one, but up to 12 two-dimensional clouds in vertical direction, we would also image all of these realisations of the Hubbard model stacked on top of each other, therefore losing information. To selectively image atoms from only a single plane we do tomography in a strong magnetic field gradient along the z -direction, which results in a different energy splitting for each plane that can in turn be addressed by narrow RF pulses. Both [22] and [21] describe how the magnetic fields were generated, calibrated, optimised and how the tomography was initially implemented with resonant, fixed frequency π -pulses. In this section I will summarise the important features of this technique and then detail the new implementation of HS1 pulses for this tomography and the optimisation required for their use.

Magnetic field generation and control One of the key requirements for tomography is the precise control of constant magnetic fields and field gradients. For this, several coils are installed close to the atom position with different purposes. In this description we explicitly leave out the coils used for the magnetic trap, since we only use them for the cooling to degeneracy and not in the detection sequence. Details on all coils used except the in-plane gradient coils can be found in [18]. Previously introduced were the main Feshbach coils, a pair of coils in Helmholtz configuration that create the large homogeneous background fields defining the quantisation axis in z -direction. They have a large inductance of about 2.3 mH reducing noise but also allowing only relatively slow ramps, which is why they are named *slow Feshbach coils*. Controlled by a low noise PID regulation and a fast feedback circuit to suppress 50 Hz noise on the current [22] they have a high field stability of < 1 mG at $B \approx 200$ G.

For fast changes of the magnetic field a pair of small rectangular coils is used with a slew rate of up to 0.3 G/ μ s [21]. These are for obvious reasons called the *fast Feshbach coils*, which can be operated either in Helmholtz configuration to add or subtract constant fields or in anti-Helmholtz configuration to generate magnetic field gradients in the z -direction. Two coil pairs in the horizontal plane, the *offset coils* of the Ioffe trap in x -direction and a pair of *elliptical coils* in y -direction shift the centre of the fast Feshbach coil's quadrupole field onto the z -axis, therefore allowing precise alignment of the gradient direction. To cancel or generate horizontal gradients in the absence of the quadrupole field, two separate *gradient offset coils* were added which generate in-plane gradients along the x - y -diagonals [21, 22, 108].

Single plane RF transfer With the tomography we would like to have access to both the singles and doubles of one single plane. Considering the interaction energy shift of a doubly occupied site relative to a singly occupied one, introduced in the previous section, a magnetic field and a state combination is needed, where this relative energy shift is negligible $\Delta U \approx 0$. This is the case for the state combination of $|7\rangle, |5\rangle$ and $|7\rangle, |3\rangle$ at a field of ~ 213.8 G, where $U_{75} = U_{73}$ [22]. At that field the RF frequency for a transfer of $|5\rangle$ to $|3\rangle$ is $\nu_{53} = E_{53}/h \approx 52.197$ MHz.

With the fast Feshbach coils we generate a magnetic field gradient of $\partial|B|/\partial z = 33.3(5)$ G/cm [22] which translates to a difference in transition frequency of ~ 640 Hz $\approx 10^{-6} \nu_{53}$ for the ~ 1 μ m distanced planes of the green z -lattice. This small frequency separation requires in turn a relative magnetic field stability of 1 ppm as well. The oscillation of the background field due to the main power line 50 Hz noise is, however, much larger than that. This is partly compensated by the bypass circuit of the slow Feshbach coils, but not sufficiently. One way to avoid these oscillations with periodicity of 20 ms was to use a very short $T \leq 3.5$ ms RF-pulse with constant frequency that induced resonant Rabi-oscillations on one plane only. With some calibration and pulse shaping one could use them for π -pulses that lead to a near complete transfer of a single plane with less than 5 % transfer of neighbouring planes. For reproducibility this was again synchronised with the power line oscillations. More details on this *slicing* technique can be found in [21, 22].

Still, here were some issues, e.g. high sensitivity of the transfer to small field drifts, requiring constant tracking of the transfer peaks and post selection of less than 1/6-th of the data taken. A better solution would have been an HS1 pulse as introduced in section 4.3.2. To still minimise the effects of the background noise with 20 ms periodicity, a reasonably short pulse time $T = 7$ ms is required that still allows a Fourier limited transfer window of $\Delta_{\text{HS1}} = 1$ 000 Hz.

HS1 slicing Since this is still larger than the separation of the planes of the green z -lattice, we implemented the superlattice assisted z -loading introduced in section 4.2.2 in the course of this thesis, which only populates each second plane, leaving the other ones empty. This doubles the atomic cloud separation in frequency space to ~ 1 280 Hz.

Even though the tomography was now possible in theory with HS1 pulse transfer sweeps, magnetic field drifts and the background field noise made it hard to cleanly separate the signals of the individual planes. For well reproducible fields one can characterise these drifts and even the periodic fluctuations if one has the means to synchronise to the 50 Hz power line as we do. To get a high temporal resolution we used short π -pulses with $T = 3$ ms (main transfer during $\Delta t_{\text{FWHM}} \approx 1$ ms) in a homogeneous field without any gradient, so we would get an equal RF transfer behaviour over the global atom cloud. By adding a variable shift to the synchronisation trigger t_{syncline} we can detect the 50 Hz and 150 Hz noise and a background drift $\gamma = \partial|B|/\partial t$ as shown in figure 4.11. A fit to the resonance frequencies $\nu(t)$ in the form of

$$\begin{aligned} \nu(t) = \nu_0 + \nu_{\text{drift}}(t) = & \nu_0 + A_{50\text{Hz}} \cos(50\text{ Hz} \times 2\pi t + \Phi_{50\text{Hz}}) \\ & + A_{150\text{Hz}} \cos(150\text{ Hz} \times 2\pi t + \Phi_{150\text{Hz}}) + \gamma t \end{aligned} \quad (4.15)$$

reveals that we have an amplitude of the 50 Hz (150 Hz) oscillations of $A_{50\text{Hz}} = 242(20)$ Hz ($A_{150\text{Hz}} = 110(18)$ Hz) with a magnetic field drift of $\gamma = -2.9(12)$ Hz ms $^{-1}$. By using this fitted frequency drift $\nu_{\text{drift}}(t)$ as feed-forward correction in equation 4.14 to replace the constant ν_{HS1} with one that includes the time dependent drift terms $\tilde{\nu}_{\text{HS1}} = \nu_{\text{HS1}} + \nu_{\text{drift}}(t)$ we can compensate the measured field drifts and therefore reach a far more optimal condition for narrow state transfer.

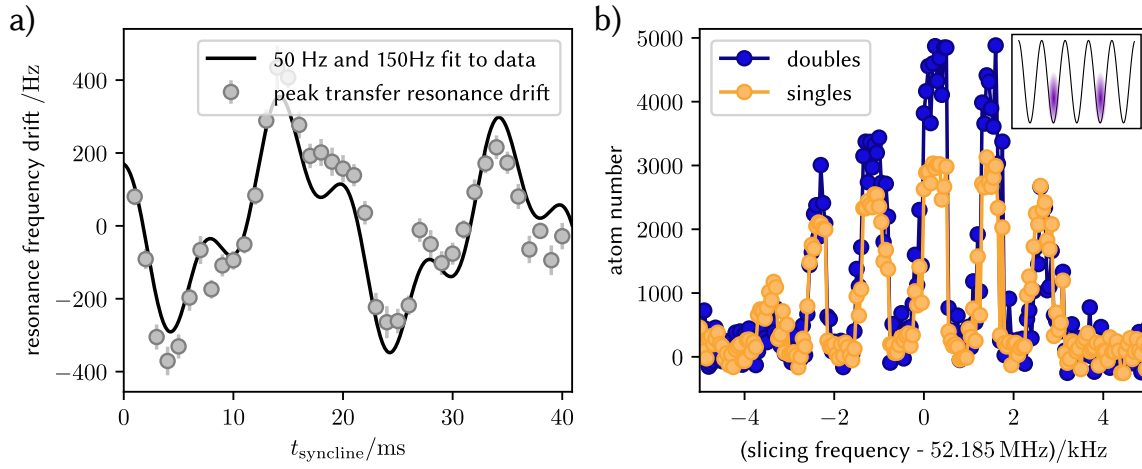


Figure 4.11: Single plane detection. a) Without very careful shielding there will always be a background oscillation in the magnetic field with the power line frequency of 50 Hz and its third harmonic at 150 Hz. We characterise this magnetic field oscillation by synchronising the detection sequence to the power line oscillation and after a variable time t_{syncline} measure the $|3\rangle \rightarrow |5\rangle$ resonance frequency with a very short RF pulse ($\Delta t_{\text{FWHM}} \approx 1$ ms). By fitting a periodic oscillation with both frequencies to the data shown in grey, we can describe the expected frequency drift $\nu_{\text{drift}}(t)$ during a longer transfer pulse. In b) the atom transfer of such a long transfer pulse is shown with a length of $T = 14$ ms and a transfer frequency width of $\Delta_{\text{HS1}} = 500$ Hz. We can resolve the number of singles and doubles over the whole atom cloud with in total around five planes filled. Since only each second z -plane is populated we see the distance of the atomic layers of ~ 1280 Hz. This technique also allows the separate detection of the planes with all of them filled.

This measurement was, however, done on the global atom cloud and did not include the strong magnetic field gradient created by the fast Feshbach coils. As it turns out these induce a very strong magnetic field drift, probably due to thermal effects, as the fast Feshbach coils are not water cooled. Nevertheless, we can optimise this by varying the γ in the feed forward function we add to the frequency sweep of the HS1 pulse, which we optimised to be $\gamma = 185 \text{ Hz ms}^{-1}$. These pulses are generated and uploaded automatically for each experimental realisation using a Keysight 33622A arbitrary waveform generator (AWG), which is detailed in [109].

With this feed forward compensation of magnetic field changes we are no longer bound to short pulses, but we successfully used pulses with times up to $T = 20$ ms. The longer available time span and the drift cancellation allow us to use even smaller transfer windows $\Delta_{\text{HS1}} = 500$ Hz as shown in figure 4.11. We, therefore, are not only reliant on the superlattice loading of every second plane, but if wanted to we could even resolve a fully populated green z -lattice.

4.3.4 Singles-doubles and spin-spin detection sequences

Combining the presented detection methods allows us to detect the in-situ density distributions of singles and doubles of one spin of an atomic cloud in a two-dimensional lattice plane, i.e. one representation of the two-dimensional Hubbard model. This is especially useful when examining density distributions of spin-balanced ensembles, since then $\langle n_{\uparrow} \rangle = \langle n_{\downarrow} \rangle$ so we can extrapolate the average local density distributions of all possible occupation states. One has to be careful in preparing the sequence such that all of these components can work together, for example by

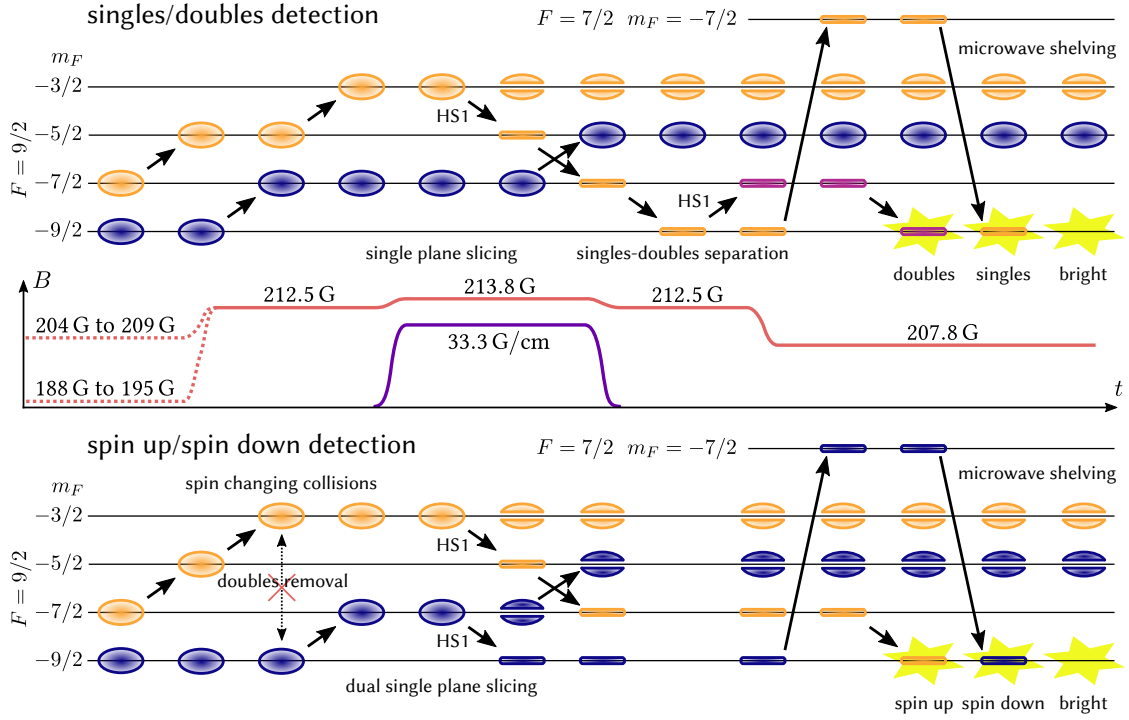


Figure 4.12: Sequences for spin-spin or singles-doubles detection. Shown are both detection sequences used in this thesis. They are adjusted such that one can switch between them by just changing the order of some RF sweeps and by turning on and off RF pulses, without the need for any change in magnetic fields or timings. We can use these sequences for both measuring repulsive (188 to 195 G) and attractive interactions (204 to 209 G). To avoid ramping over the $|9\rangle \leftrightarrow |7\rangle$ Feshbach resonance at ~ 202.2 G we first transfer to a $|9\rangle, |5\rangle$ mixture and then ramp to the detection field at 212.5 G. For the spin up/spin down detection we also remove all doubly occupied sites by going to a $|9\rangle, |3\rangle$ mixture, which allows spin changing collisions to $|7\rangle$ and $|5\rangle$, with all excess energy transferred to kinetic momentum, removing these atoms from the trap.

choosing the right magnetic field for slicing, where no on-site shift is present ($\Delta U = 0$).

Especially the doubly occupied sites have to be considered, since being tightly bound in the deep lattice increases their on-site interaction strength, such that losses due to two-body scatterings can occur. These two-body losses are greatly enhanced close to s-wave Feshbach resonances, but also in the close vicinity of p-wave resonances as indicated in figure 4.10, where their suppression due to the low kinetic energy is not sufficient any more. Additional losses can occur because of spin changing collisions, for example when the atom pair is in the states $|9\rangle, |3\rangle$ which can decay into $|7\rangle, |5\rangle$ by exchanging $1\hbar$ in angular momentum, absorbing the difference in energy as kinetic momentum and leaving the trap. We can utilise this to intentionally remove all double occupancies, and then use a different detection sequence to image the singles distribution of both spin components. For this we need the slicing to work for both spin components at the same time. We do this by combining two HS1 functions with different centre frequencies corresponding to ν_{53} and ν_{97} and uploading the combined waveform to the AWG. Being able to detect both spin components of one plane is essential for investigating spin imbalanced systems or detecting magnetic correlations.

The two sequences discussed are sketched in figure 4.12. Since they both use the same magnetic

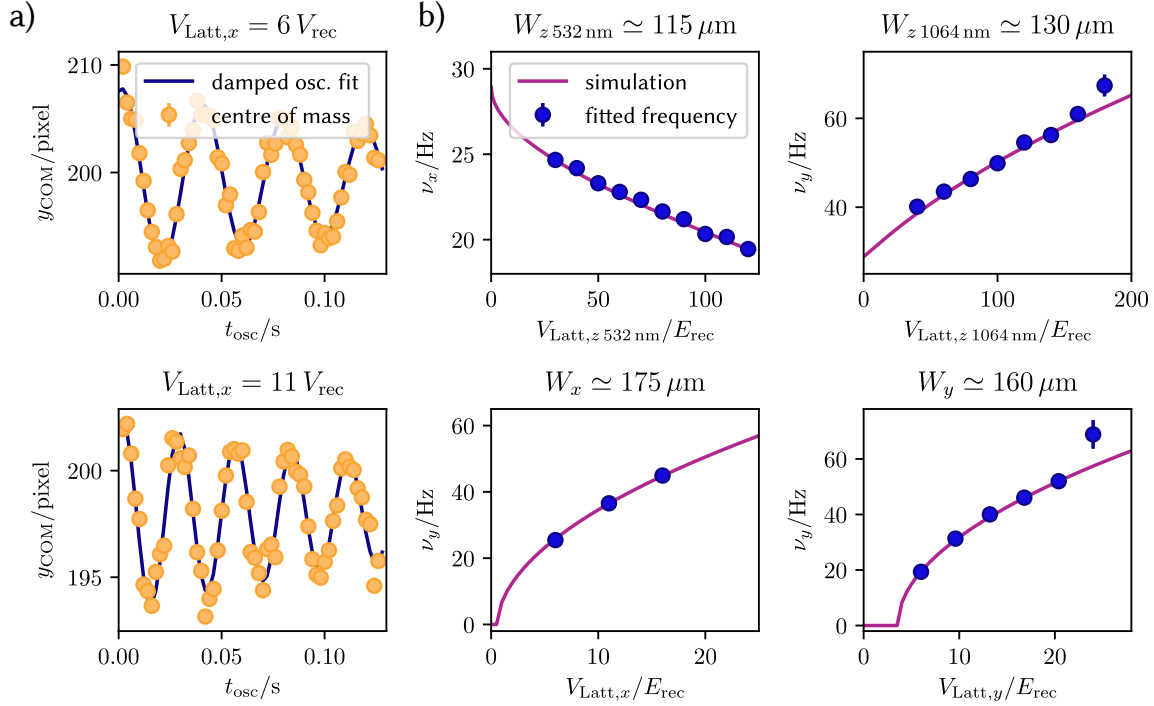


Figure 4.13: Trap frequency and beam waist calibration. a) Trap frequency measurements in y -direction for two different x -lattice depths. By increasing the lattice depth, the frequency of the centre of mass (COM) oscillation increases (from 25.45(12) to 36.55(16) Hz). Using a fit to the damped oscillation (in dark blue) we can extract the frequency $\nu_{x,y}$ that we can then compare in b) to expected trap frequencies simulated (in pink) with the equations 4.17 to 4.20. By measuring the change in trap frequency perpendicular to the beam direction and relative to its power we can manually adjust the waist parameters of the simulations. The beam waists used for the simulation in the figure are displayed as well and have an estimated uncertainty of $2.5 \mu\text{m}$.

fields for detection, we can switch quickly between the two modes by changing the order and by turning off/on a few RF pulses.

4.3.5 Potential mapping with the local density approximation

With the introduced detection method we can, for a fixed set of parameters t and U , obtain a local density distribution of the doubles $n_D(\mathbf{r}) = \langle n_{\uparrow} n_{\downarrow} \rangle$ and the singles $n_{S,\uparrow/\downarrow}(\mathbf{r}) = \langle n_{\uparrow/\downarrow} \rangle - \langle n_{\uparrow} n_{\downarrow} \rangle$. To compare this with theoretical predictions we need to find the local chemical potential $\mu(\mathbf{r})$ and for a thermally equilibrated system a global temperature T . For a known local potential $V_{\text{pot}}(\mathbf{r})$ we can use the local-density approximation (LDA) discussed in section 3.3 to get the relative chemical potential of our system, with only one free parameter μ_0 defined by the atom number and the temperature. In this section we will summarise [21, 22, 24] how to obtain this local potential $V_{\text{pot}}(\mathbf{r})$ and use it to compare the data to theory.

Full potential calculation There are two terms to consider when calculating the local potential $V_{\text{pot},i}$ of a lattice beam $i = x, y, zr, zg$ (zr for the infrared z -lattice and zg for the green one). First, the lattice potential created by a spatially varying intensity distribution and second, the zero-point

energy of the local lattice sites, similar to the energy offset of the lowest harmonic oscillator state $\omega_i \hbar/2$. For this we need to obtain the parameters defining the spatial distribution, i.e. the wave vector \mathbf{k}_i given by the lattice angle θ_i and the lattice waist at the focus position $W_{0,i}$, see figure 3.7. We also need to know whether the potential is attractive or repulsive for the atoms. The waist is assumed to be constant, since the Rayleigh length z_0 is orders of magnitude larger than our system size. For the lattice potential two beams are overlapped and any power imbalance can be described with the power ratio of the beams γ_i . For retro-reflected beams this is less than the ideal value of one due to losses in the optical path mainly caused by the vacuum glass cell. The parametric heating technique as shown in figure 4.7 can give us the pure lattice potential $V_{\text{latt},i}$ and with the knowledge of γ_i the complete potential can be calculated.

For the second term we can approximate the sinusoidal lattice with a harmonic potential at the centre of each well. This leads to $\omega_{\text{well},i} \approx (4E_{\text{rec},i} V_{\text{latt},i}/\hbar^2)^{1/2}$ and therefore a zero point energy of $\omega_{\text{well},i} \hbar/2 \approx (V_{\text{latt},i} E_{\text{rec},i})^{1/2}$. The full potential for all four lattice beams is given by

$$V(x, y) = V_{\text{pot},x}(x, y) + V_{\text{pot},y}(x, y) + V_{\text{pot},zr}(x, y) + V_{\text{pot},zg}(x, y), \quad (4.16)$$

with the individual contributions of each of the four lattices:

$$V_{\text{pot},x}(x, y) \simeq -V_{\text{latt},x} \frac{(1 + \sqrt{\gamma_x})^2}{4\sqrt{\gamma_x}} e^{-2\left(\frac{x \sin \theta_x + y \cos \theta_x}{W_x}\right)^2} + \sqrt{V_{\text{latt},x} E_{\text{rec},x}} e^{-\left(\frac{x \sin \theta_x + y \cos \theta_x}{W_x}\right)^2}, \quad (4.17)$$

$$V_{\text{pot},y}(x, y) \simeq -V_{\text{latt},y} \frac{(1 + \sqrt{\gamma_y})^2}{4\sqrt{\gamma_y}} e^{-2\left(\frac{x \cos \theta_y - y \sin \theta_y}{W_y}\right)^2} + \sqrt{V_{\text{latt},y} E_{\text{rec},y}} e^{-\left(\frac{x \cos \theta_y - y \sin \theta_y}{W_y}\right)^2}, \quad (4.18)$$

$$V_{\text{pot},zr}(x, y) \simeq -V_{\text{latt},zr} \frac{(1 + \sqrt{\gamma_{zr}})^2}{4\sqrt{\gamma_{zr}}} e^{-2\left[\left(\frac{x}{W_{zr}}\right)^2 + \left(\frac{y \sin \theta_z}{W_{zr}}\right)^2\right]} + \sqrt{V_{\text{latt},zr} E_{\text{rec},zr}} e^{-\left[\left(\frac{x}{W_{zr}}\right)^2 + \left(\frac{y \sin \theta_z}{W_{zr}}\right)^2\right]}, \quad (4.19)$$

$$V_{\text{pot},zg}(x, y) \simeq +V_{\text{latt},zg} \frac{(1 - \sqrt{\gamma_{zg}})^2}{4\sqrt{\gamma_{zg}}} e^{-2\left[\left(\frac{x}{W_{zg}}\right)^2 + \left(\frac{y \sin \theta_z}{W_{zg}}\right)^2\right]} + \sqrt{V_{\text{latt},zg} E_{\text{rec},zg}} e^{-\left[\left(\frac{x}{W_{zg}}\right)^2 + \left(\frac{y \sin \theta_z}{W_{zg}}\right)^2\right]}. \quad (4.20)$$

Here we used that the green and infrared z -lattice share the same lattice angle θ_z . Note that the prefactor for the lattice term reflects whether the lattice is repulsive or attractive. Also, since the z -lattices are not parallel to the xy -plane but crossing it, they have to be described with an elliptical beam profile whereas in-plane lattice beams have an approximately constant intensity distribution along their propagation axis.

Trap frequency measurement In the centre of the trap one can approximate its potential with a two dimensional harmonic oscillator potential, described by the harmonic oscillator frequencies of

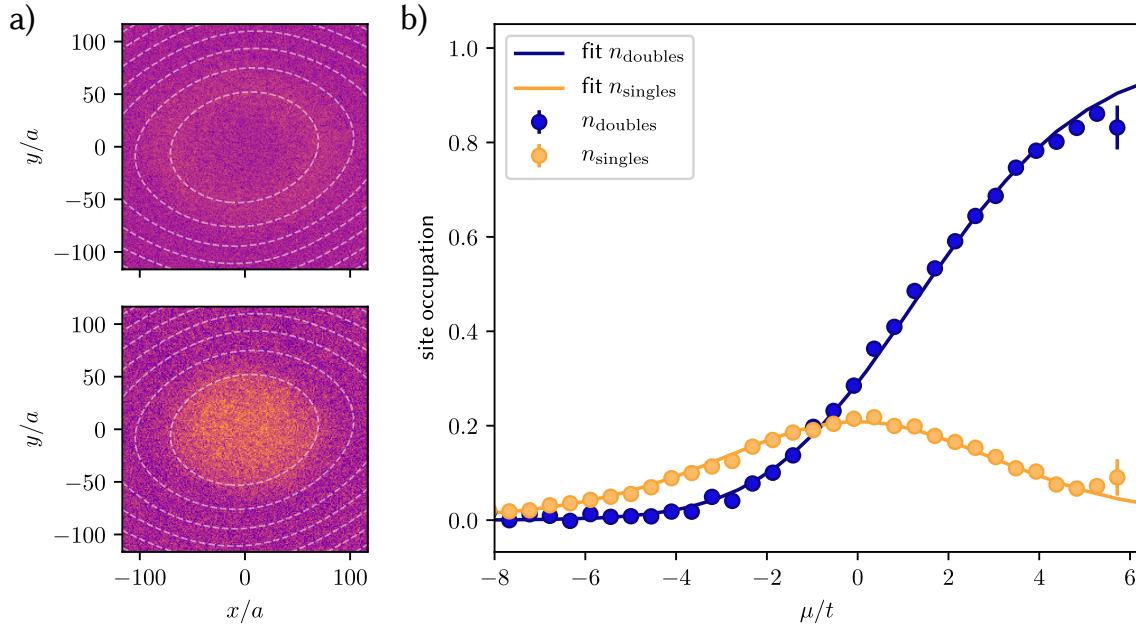


Figure 4.14: Potential mapping and the equation of state fit. a) Local density distribution for singles (upper picture) and doubles (lower picture) of a single plane averaged over ten measurements. The centre region features a large doubles density, which shows as a reduced density in the singles picture. The narrow and low density ring of singles is expected for the calculated attractive interactions of $U/t = -1.74$ with $t(6 E_{\text{rec}}) = 224$ Hz. The white dashed lines indicate equipotential lines from the trap potential calculation calibrated with the measurement shown in figure 4.13. We can use this calculated potential to map the densities to isopotential regions. The averaged densities in these regions can be fitted with numerical calculations, for example DQMC, as shown in b). The four free parameters for the fit to the data shown as solid line are the temperature $T/t = 1.89(6)$, the central chemical potential $\mu_0/t = 5.72(6)$ and the global density scaling parameters $\sigma_{\text{doubles}} = 1/0.48(2)$ and $\sigma_{\text{singles}} = 1/0.82(2)$. The data in a) and b) have already been scaled accordingly to give the reader a sense of the real ratio between both occupation probabilities.

both axes $\omega_{x/y} = \nu_{x/y} \times 2\pi$. In a dipole trap we can measure these trap frequencies by loading only a very small number of atoms $\sim 2 \times 10^3$, applying a small momentum kick and then extracting their spatial oscillation frequencies $\nu_{x/y}$. In a lattice this macroscopic motion is suppressed, but by blocking one of the retro-reflected beams and increasing this laser's intensity by a factor of four, motion along this direction is again possible, while the overall trap potential still approximates the real lattice configuration. We displace the cloud slightly from the centre with the magnetic field gradient coils [24] and then measure the centre-of-mass sloshing motion, as shown in figure 4.13. Through the fit of the equation of motion of a damped oscillator we get the trap frequency $\nu_{x/y}$. Repeating this measurement for different lattice powers and comparing the resulting trap frequencies to the harmonic centre of the full trap potential simulation of the equations 4.17 to 4.20, we can extract the waists of all lattices and are now able to simulate the full local potential. This method also allows the description of small beam misalignments by fitting a larger effective waist [21].

Potential mapping for the equation of state With the knowledge of the local potential $V(x, y)$ we can use the LDA and assign equipotential regions. In a lattice filled with atoms, the chemical potential of all these regions is now defined by a single parameter, the central chemical potential $\mu_0 = \mu(\mathbf{r}) + V(\mathbf{r})$, see section 3.3. By fitting the measured densities averaged over equipotential regions with data simulated using DQMC calculations, we can extract μ_0 and T , as shown in figure 4.14. Since U can be calculated, the only additional free parameters needed are global density scaling factors, accounting for example for losses in the detection sequence or imperfect tomography of the z -plane. We note that the chemical potential is mostly determined by the maximum of the singles at half filling, where $\mu = 0$. At that point, several simulation methods work best which leads to a very robust scaling determination. In contrast to that, temperature effects are most prominent in the regions with lower filling. This separation of features reduces cross-dependence of the fit parameters and allowed for the measurement of the equation of state of the two-dimensional Hubbard model [50]. Through the determination of the chemical potential, several measurements with different atom numbers, i.e. central chemical potential μ_0 can be combined, resulting in experimental data with enough accuracy to deduce thermodynamic variables like entropy [49] and compressibility [110] for different repulsive interactions.

4.4 Potential engineering with a spatial light modulator

By mapping the spatial position to a chemical potential, we can use the inhomogeneity of the trap to our advantage. This comes with the cost of potentially very small isopotential regions further away from the trap centre. Being able to arbitrarily shape the lattice potential could circumvent this, by creating a homogeneous lattice potential. This could allow the observation of macroscopic, i.e. long range physical effects and the averaging of very large data regions, increasing the data quality. There are, however, a lot more uses for the ability to locally manipulate potentials, for example, for transport measurements by creating constrictions [111], periodically modulated potentials [112, 113] or tilted potentials for atom movement [114]. Other research with potential shaping focuses on homogeneous box traps [115–117], optical tweezers for few atom control [118, 119] or even the direct creation of three dimensional lattices for Rydberg atoms [120].

For our experiment we looked at proposals to use potential shaping to redistribute the entropy of a system to obtain very cold samples [121, 122]. There, one generally creates two trap regions \mathcal{A} and \mathcal{B} with different local potentials $V_{\mathcal{A}}$ and $V_{\mathcal{B}} > V_{\mathcal{A}}$. After loading an atomic cloud into that system, it exhibits a chemical potential $\mu_{\mathcal{A}} > \mu_{\mathcal{B}}$. Since the entropy per particle S/N is dependent on the chemical potential, we can choose the potentials such that region \mathcal{B} potentially has a lot higher entropy per particle $(S/N)_{\mathcal{B}} > (S/N)_{\mathcal{A}}$ and any atom moving from region \mathcal{A} to \mathcal{B} could remove entropy from region \mathcal{B} . Therefore, region \mathcal{B} acts as an entropy reservoir for region \mathcal{A} . For the two-dimensional Hubbard model the entropy distribution at a fixed temperature and repulsive interactions as a function of chemical potential is shown in figure 4.15. To obtain, for example, cold systems with a region at half-filling where $n = 1$, an entropy reservoir with very low density $n \ll 1$ would be ideal. Even though it is not yet completely understood how entropy is transported and how a redistribution would work on a microscopic level, recently such a scheme was realised, leading, among other things, to the coldest yet measured two-dimensional Hubbard system with $T/t = 0.25$ [123, 124].

This section summarises some of the previous conceptual and experimental work on this experi-

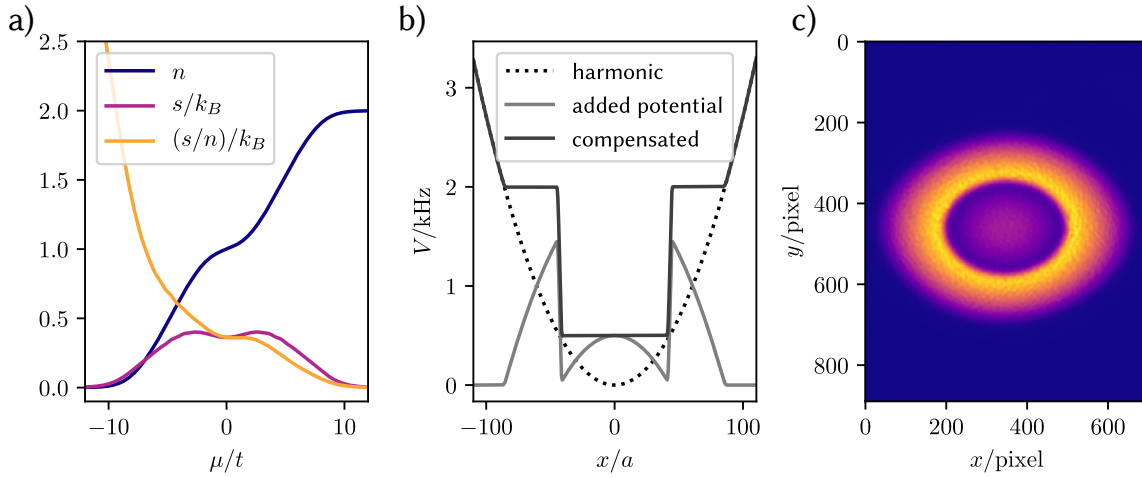


Figure 4.15: Entropy cooling and potential shaping. a) Shown in blue is the density equation of state n for a repulsive system with $U/t = 8$ at $Tk_B/t = 0.8$, and the entropy per lattice site s as a function of chemical potential μ , simulated with NLCE [37]. As one can see we have a local minimum in entropy close to half filling $\mu = 0$ due to the charge excitation gap of the Mott insulator [49]. For the consideration of entropy redistribution and loading of the system, a different quantity is relevant. We start with a fixed atom number N in the dipole trap and a fixed total entropy S , which should remain constant for adiabatic changes to the system, like loading into a lattice. Therefore, the entropy per particle $S/N = s/n$ is most relevant and shown in orange. While particles close to the band insulator $\mu \gg t$ cannot store any entropy, particles in the low density region could potentially carry a lot of entropy. For an efficient entropy cooling scheme we, therefore, would like to have a large low-density region where particles can store a lot of entropy. Such a potential is plotted in b), where an added potential in grey creates a homogeneous centre region with a flat potential, and an outer ring for the bath region. By adjusting the size of the regions or the total atom number loaded, we can control the approximate filling of each region. c) shows such a shaped potential created with a digital micro-mirror device (DMD) in our experiment.

ment to implement a spatial light modulator (SLM) for local potential manipulation [125, 126], but will focus on the optical setup which was completely reworked and optimised during this thesis.

SLM optical setup To shape potentials we use the optical dipole force of far-detuned laser light, with all the advantages discussed in the previous sections. Here we could either use blue- or red-detuned laser light resulting in the addition or subtraction of a local potential. For creating a stepped potential as shown in figure 4.15 b) less light is required for adding a repulsive potential compared to an attractive one, since the harmonic trapping potential offers already the general shape we desire. We therefore choose to use blue-detuned laser light. This especially requires less light in the centre of the trap, where the low entropy region might be even more sensitive to intensity fluctuations, which could induce heating. For optical access to the atoms a beam splitter was placed in the imaging path below the science chamber, shown in figure 4.9.

The initial setup with a Liquid Crystal on Silicon (LCoS) SLM, which modulates the light phase pixel-wise, was exchanged to a digital micro-mirror device (DMD), the DMD DLP 6500 from Texas Instruments. It consists of an array of small square mirrors which can be tilted along one diagonal axis. There are two possible states the mirrors can be in, with angles of $\pm 12^\circ$, hence the digital nature of this SLM. If all or many mirrors are on, it additionally acts like a blazed grating, therefore

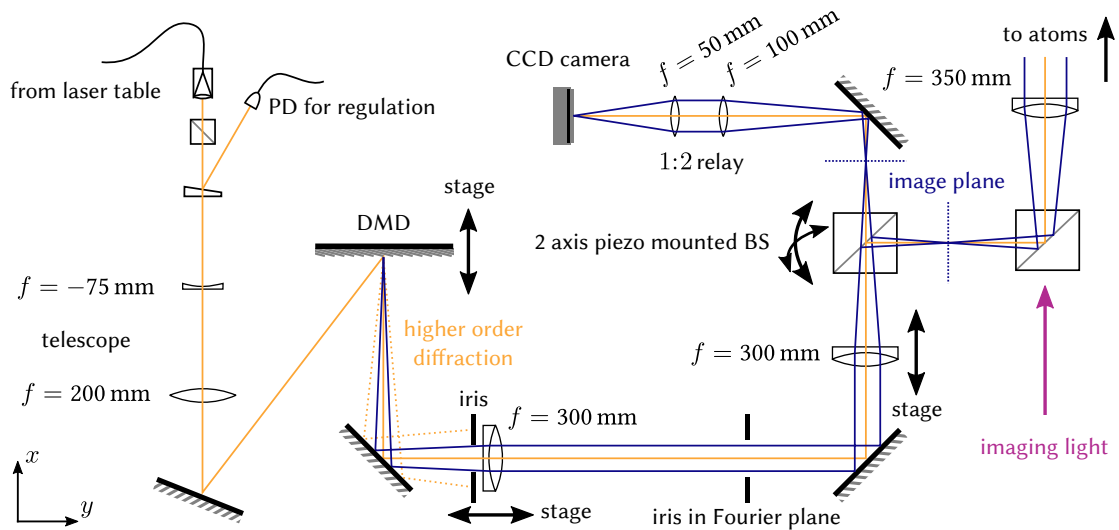


Figure 4.16: SLM optical setup. The optical setup of the digital micro-mirror device (DMD) acting as a spatial light modulator (SLM) was initially set up in [125, 126] and completely reworked during this thesis. The Gaussian beam out of the single mode fibre gets enlarged by the first telescope, before hitting the DMD. The incoming angle is adjusted to fulfil the blazing condition. The pattern the DMD creates is then projected through a $4f$ -lens system with two achromatic lenses, before being imaged at the atoms through the optical microscope shown in detail in figure 4.9. Translation stages and a piezo-actuated beam splitter mount are essential for the alignment of the system described in the text. For generating and monitoring the created potential a small CCD camera behind a 1:2 relay is used.

one has to match the incident angle such that the beams off the grating rows interfere constructively for maximal pattern intensity, which is called the *blazing condition*. We project the image of the mirror array via two lens pairs onto the atom plane. Hereby, the last two lenses are shared with the imaging light path after having been overlapped with a beam splitter. This setup is shown in figure 4.16, including the necessary improvements to the previous version of the setup [126], which we will discuss later in this section.

DMD pattern creation The image in between the lens pairs is projected onto a small CCD camera after a beam splitter cube. This allows for direct monitoring of the image projected onto the atoms without any physical changes to the optical setup.

The potentials we want to project are all continuous in space, and therefore we have to translate them to the digital nature of the SLM. This can in part be done by choosing a suitable magnification that leads to the imaging of several DMD pixels to a lattice site. In our case $\sim (3.4)^2 \approx 12$ pixels get mapped to one single lattice site. Since the projection of the pattern onto the atoms has a worse resolution than the much more optimised imaging system, small patterns on less than a site level get smeared out and we can use pixel clusters to have more intermediate intensity steps available.

The error diffusion algorithm builds and extends the idea of pixel binning and is another method of mapping a gray-scale picture onto a digital pattern [127, 128]. There, the cost of wrongly assigning a pixel value due to the digital nature of the DMD is distributed to the next pixels, allowing for a smooth image generation. Its implementation in the experiment is described in detail in [126]. Here

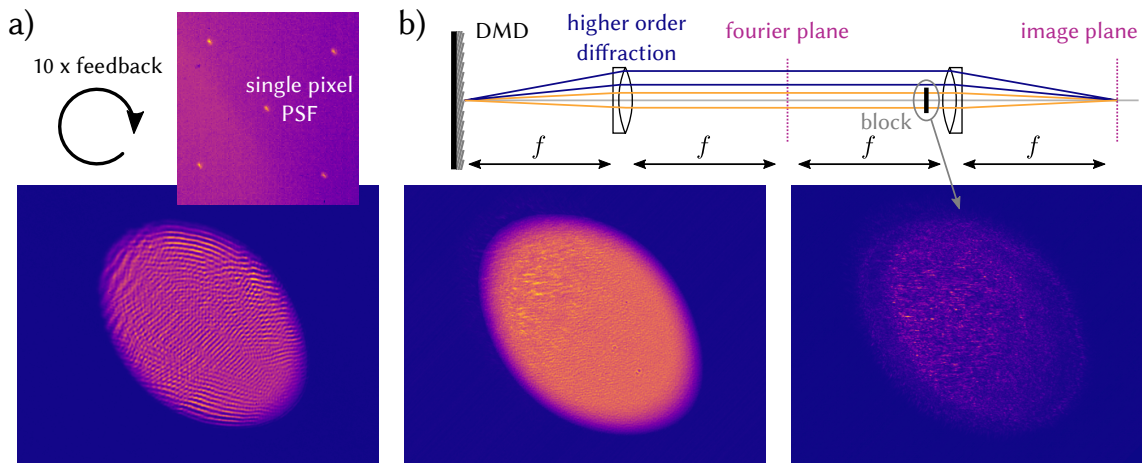


Figure 4.17: Errors in the potential pattern generation. a) If the projection of the DMD onto the feedback camera is not aligned well enough, the point-spread-function (PSF) will be malformed. For the asymmetric PSF shown in the small picture in the top, where we turned on single pixels on the DMD chip, the feedback routine fails to generate the required local correction. The stripes in the potential visible in the bottom picture are the result of ten feedback iterations with a wrong projection alignment. b) Another source of imaging and feedback errors were previously unnoticed higher diffraction orders of the DMD that were also projected onto the imaging camera providing the feedback. A flat potential created as shown in the centre bottom displays an irregular noise pattern in the top left part of the potential. By blocking the centre of the second lens the unwanted higher order diffraction becomes clearly visible as shown in the bottom right. We can get rid of this by placing an iris on the first lens, as shown in figure 4.16. An unsmoothed image of a real potential created after removing all these feedback errors is shown in figure 4.15 c).

it is important to note that the DMD only allows to change the local reflectivity, so any light pattern generated depends on the light that is put onto the DMD first. Therefore, we first take an image of the Gaussian input beam with the small monitor camera, and scale the pattern we want to create with its inverse, thereby taking into account that a DMD pixel in the centre of the beam has a larger effect on the pattern generation compared to one on the outer edge.

A feedback algorithm was put into place by my colleague Dr. Chun Fai Chan that compares the image taken by the small camera to the desired one and adds the difference to the pattern used as the input to the error diffusion algorithm. To compare the DMD pattern and the camera picture a three-point calibration of rotation and position is done regularly [126].

We learned that for this feedback routine to work, the optical system projecting the DMD pattern onto the feedback camera has to be optimised very well. It is especially sensitive to astigmatism and coma, since these effects lead to an asymmetry of the point spread function (PSF) of a single pixel. Running the three-point calibration and the feedback algorithm with imaging errors like that results in the appearance of stripes, see figure 4.17 a). By properly aligning the $4f$ -lens system, passing each lens centred and perpendicular, the PSF is symmetric and the feedback algorithm converges.

Still, we observed a persistent pattern on the feedback-optimised picture, see left image in figure 4.17 b). We found out that the DMD acts, dependent on the pixel pattern that is shown, as a grating with varying periodicity. Therefore, there exist several diffraction orders apart from the one we optimised on with the blazing condition. The picture to the right shows the pattern observed

when the centre of the second lens is blocked and the desired zeroth diffraction order cannot pass any more, as shown in the schematic above. We solve this by adding an iris to the first lens and blocking all orders but the one we want. The final result can be seen in figure 4.15 c) which is a picture of the DMD generated light pattern taken by the feedback camera.

Projection onto the atoms and alignment This pattern has to be cast onto the atoms as accurately as possible. For this we use the z -camera, which is focused on the desired atom plane. However, due to the different wavelengths used for absorption imaging (769 nm) and potential shaping (\sim 728 nm), the focus point is shifted. The shift is calculated with the optics software OSLO to -5.45 mm, by which we have to shift the camera position.

We align the system by removing both lenses of the $4f$ -system and using the DMD as a mirror. The collimated Gaussian beam should then pass the optical path up to the z -camera without much clipping. Afterwards, we insert the lens closer to the atoms and align its focus position on a stage such that the focus point size is minimised on the camera. By shifting the lens back and forth from the centre position, we can additionally check the angle it passes the imaging system with and iteratively correct it. We then position a mirror in the focus after the lens we just put in and align it such that the beam gets perfectly back-reflected to the optical fibre. The second lens is then inserted and aligned to keep the back-reflection on the fibre. Last, we project a pattern of only a few pixels on the DMD, and align its position to get the projected image plane into the focus of the camera. We optimise the angle with the electronically controlled beam splitter mount to minimise optical aberrations. Additionally, the angle influences the position where the potential shaping beam hits the glass cell, so we have to take care to avoid large dust particles, seen as large distortions of a pattern. Then the small CCD camera for feedback can be mounted and aligned. For fine adjustment of the generated image pattern, we shift the centre position of the DMD pattern on the DMD chip itself, since it occupies only about one fifth of the whole chip.

Calibration of the generated potential depth When creating a digital pattern with the DMD, we optimise the overall shape and relative intensity of each pixel. In a next step we have to now scale the overall light intensity going onto the DMD such that the resulting light pattern creates the desired absolute potential shift for the atoms. For this calibration we use the small CCD monitor camera as well. Each pixel on the camera has a possible output $C(x, y)$ in the range of 0 to 255 counts (8bit). For the generation of the spatial shape of the target potential $V_{\text{target}}(x, y)$, we scale the potential by setting its maximum value to $C_{\text{max}} = \beta \times 255$ counts. A usual parameter is $\beta = 0.5$, which allows us to use a large dynamic range for the feedback optimisation process. The initial spatial profile of the Gauss mode on the DMD is taken using a fixed laser power, controlled by PID regulation to a photo-diode voltage U_{PD} . The exposure time for the monitor camera was chosen such that the initial Gaussian profile is not saturating the camera. Then the scaled down potential is created using the feedback loops described above. What is missing for the experimental scaling calibration is the actual potential the atoms see $V_{\text{actual}}(x, y)$ for a certain regulated intensity and a prepared pattern. We get this information by scanning the regulation set point U_{set} with an inverted trap potential shaped pattern on the DMD, until the potential is actually compensated, and therefore the atom

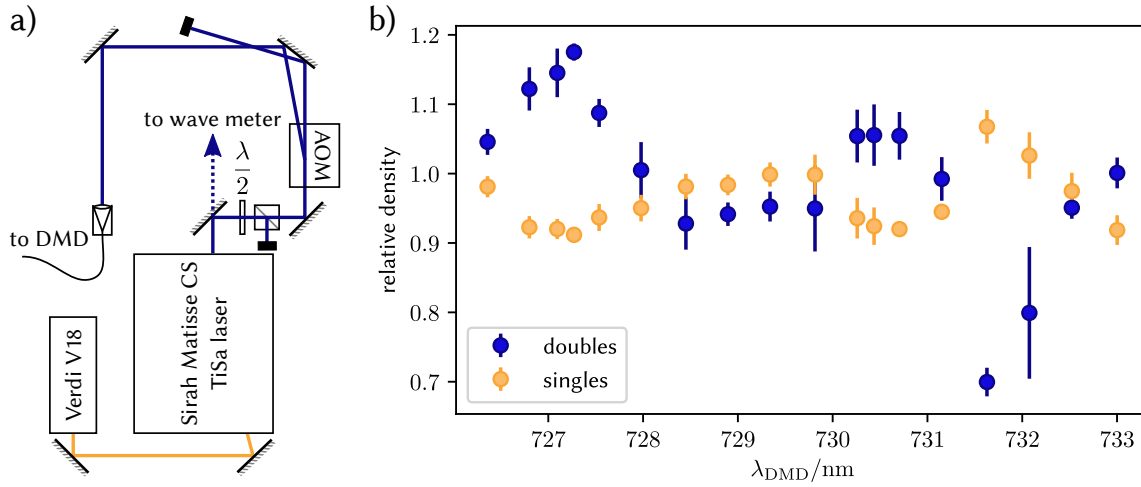


Figure 4.18: Potential shaping laser and wavelength dependent losses. a) The light for the potential shaping is generated using a titanium-sapphire (TiSa) laser, pumped by a 532 nm Coherent Verdi V18. The output intensity is regulated with an AOM before being coupled into a fibre. b) We measured the wavelength dependent losses by using the DMD to make a large homogeneous region in the trap centre. In blue (orange) the doubles (singles) density is shown in arbitrary units, averaged over five measurements per data point. Any reduction in the doubles density always seems combined with a small increase in the singles density, probably as the sample is getting much hotter due to density redistribution after the doubles get lost. We choose a wavelength of $\lambda_{\text{DMD}} \approx 727.24$ nm, where a maximum of doubles indicates a relative loss minimum.

density is flat at $U_{\text{set}} = U_{\text{comp}}$. From this we can calculate a scaling factor

$$\alpha_{\text{DMD}} = \frac{V_{\text{max}}}{U_{\text{comp}} * \beta * 255 \text{ counts}} \quad (4.21)$$

which we can use for any potential by scaling U_{comp} with the respective V_{max} .

Laser light generation and wavelength determination A titanium-sapphire (TiSa) laser, a Sirah Matisse CS pumped by a Verdi V18, is used for the generation of the potential shaping light. Its wavelength is tunable over a range of approximately 700 to 950 nm with output powers of more than one watt. The optical setup including the launch into an optical fibre is shown in figure 4.18. The initial choice of 730 nm was motivated by the sufficiently large detuning to the D_2 line (~ 39 nm) and the availability of laser diodes at that wavelength. The switch to the TiSa became necessary as the tapered amplifier diode we used was discontinued and no replacement was available.

One disadvantage of blue-detuned light is the increased possibility of photo-association processes also called light-assisted collisions, where colliding atoms close to a Feshbach resonance can use the excess photon energy to form a bound molecule with one excited atom [129]. Atoms in these bound states usually decay with a large increase in kinetic energy, resulting in a loss from the trap. While red-detuned light needs to match exact resonance frequencies, as discussed quickly in section 4.1.3, this is not true any more for blue-detuned light, since the excess energy to match the resonance condition can be transformed into kinetic motion. However, other experiments with ultracold potassium reported the existence of specific wavelengths, where these losses are suppressed [104].

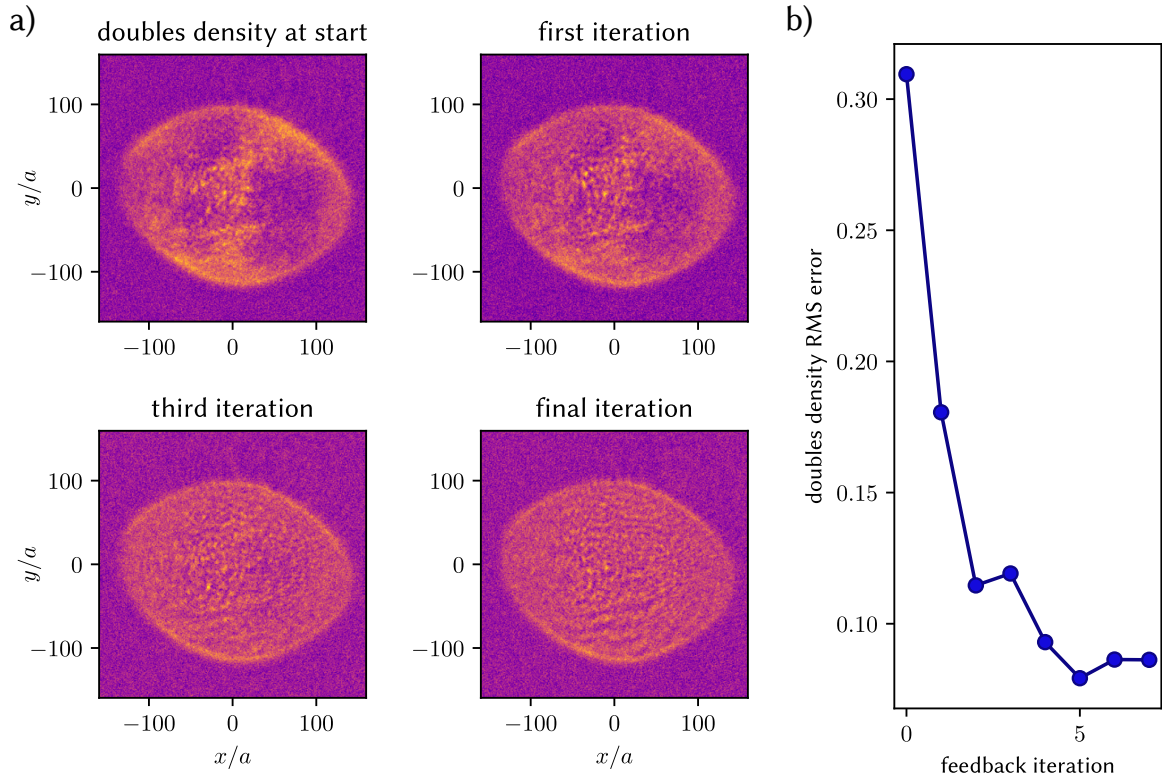


Figure 4.19: Atom feedback for potential generation. For creating a universally applicable local scaling map $R(x, y)$ as described in the text, we use the local doubles density as a feedback parameter. For attractive interactions $U < 0$ and close to half-filling they scale nearly linear relative to a change in local chemical potential. a) From the top left picture down to the bottom right one the averaged doubles density of 15 measurements is displayed. One can see that the initial potential is greatly deformed when reaching the atoms. Reasons can be diffraction and absorption in the optical path. After the last iteration the potential is already relatively smooth and more even, as the doubles density RMS error plotted in b) also shows.

Without further examining the physical process, we wanted to minimise these losses by tuning the wavelength of the laser while using an arbitrary potential on the atoms. The average detected atom number relative to the wavelength can be seen in figure 4.18 b), where clear atom number maxima, i.e. loss minima can be observed, for example, at ~ 727.24 nm. These minima depend on the scattering potential and its bound channels and, therefore, also on the magnetic field one uses. The measurement should be repeated for different magnetic fields individually.

Atom distribution to potential feedback In some cases very large potentials are required and small *relative* imperfections in the generated potential $V_{\text{actual}}(x, y)/V_{\text{target}}(x, y)$ can in some regions be very large in absolute potential difference $\Delta V = V_{\text{actual}}(x, y) - V_{\text{target}}(x, y) \gg t$ leading to spatial density inhomogeneities $\Delta n(x, y) = n(x, y) - \bar{n}$. Under the assumption that these effects

are caused by absorption for example and scale linearly, one could imagine a localised scaling map

$$R(x, y) = \frac{V_{\text{required}}(x, y)}{V_{\text{target}}(x, y)} \quad (4.22)$$

that could be used to adapt the initially generated pattern to compensate for the local imperfections.

As an optimisation quantity we use our atoms and an iterative feedback procedure that decreases (increases) the SLM pattern in places where the doubles density is below (above) average $\Delta n(x, y) < 0$ ($\Delta n(x, y) > 0$) as is shown in figure 4.19. For attractive interactions, the doubles density is relatively linear near the half filling point $\mu = 0$, see figure 4.14 and, therefore, ideal to use as a feedback quantity in the algorithm. For the optimisation in figure 4.19 we used a Gaussian filter with 4 pixel radius and 15 density measurements averaged per iteration.

From the optimised potential after the iterative feedback $V_{\text{required}}(x, y)$ we can extract the scaling map $R(x, y)$. Calibrating this once allows using this localised scaling map for any other potential $V_{\text{required}}(x, y) = R(x, y) \times V_{\text{target}}(x, y)$, as long as the scaling map is large enough, meaning it has a smaller size than the one the feedback ran on. This works surprisingly well, partially validating the theory that the local defects scale linearly with intensity.

Simulating a Mott insulator using attractive interaction

Exact solutions to the Hubbard model at low temperatures are still out of reach at the moment. Therefore, a lot of effort has been directed to find suitable ways to simplify the model even further [34, 44, 130, 131]. One path towards this goal is the use of symmetries in the Hubbard model, which additionally might provide more insight to its physics. In this chapter we will discuss the most relevant symmetries and provide an experimental validation of a very versatile one through our quantum simulator [30].

5.1 Symmetries of the Hubbard model

In the discussion of the effects of interaction and emerging order in the Hubbard model in chapter 2 one could note the similarities between repulsive ($U > 0$) and attractive ($U < 0$) interactions. The superexchange mechanism with its relevant energy $J = 4t^2/U$ for example leads to antiferromagnetic (AFM) spin ordering for repulsive interactions as well as to the checkerboard pattern of the charge-density-wave (CDW) at attractive interactions. This is illustrated best in the phase diagram at half-filling $\mu = 0$ shown in figure 2.8, which implies the existence of some sort of symmetry in the Hubbard model.

The simplicity of the Hubbard Hamiltonian should allow us to describe these symmetries. We will start with the most trivial of them and at the end of this section answer the question about a symmetry connecting the attractive to the repulsive Hubbard model.

Spin-exchange symmetry Some symmetries we will discuss are discrete symmetries, where a system description/Hamiltonian stays invariant under an exchange transformation. One example is a transformation interchanging the spin of the creation and annihilation operators, the *spin-exchange* (\mathcal{SE}) transformation :

$$\begin{aligned} \mathcal{SE} : \quad \hat{c}_{i,\uparrow} &\leftrightarrow \hat{c}_{i,\downarrow}; & \hat{c}_{i,\uparrow}^\dagger &\leftrightarrow \hat{c}_{i,\downarrow}^\dagger \\ \hat{c}_{i,\downarrow} &\leftrightarrow \hat{c}_{i,\uparrow}; & \hat{c}_{i,\downarrow}^\dagger &\leftrightarrow \hat{c}_{i,\uparrow}^\dagger, \end{aligned} \quad (5.1)$$

which directly results in

$$\hat{n}_{i,\downarrow} = c_{i,\downarrow}^\dagger c_{i,\downarrow} \leftrightarrow c_{i,\uparrow}^\dagger c_{i,\uparrow} = \hat{n}_{i,\uparrow}. \quad (5.2)$$

By transforming the individual terms of the Hubbard Hamiltonian in equation 2.9, we can observe how this transformation acts on the model:

$$-t \sum_{\langle i,j \rangle, \sigma} \left(\hat{c}_{i,\sigma}^\dagger \hat{c}_{j,\sigma} + \hat{c}_{j,\sigma}^\dagger \hat{c}_{i,\sigma} \right) \leftrightarrow -t \sum_{\langle i,j \rangle, \sigma} \left(\hat{c}_{j,\sigma}^\dagger \hat{c}_{i,\sigma} + \hat{c}_{i,\sigma}^\dagger \hat{c}_{j,\sigma} \right) \quad (5.3)$$

$$+U \sum_i \left(\hat{n}_{i,\uparrow} - 1/2 \right) \left(\hat{n}_{i,\downarrow} - 1/2 \right) \leftrightarrow +U \sum_i \left(\hat{n}_{i,\downarrow} - 1/2 \right) \left(\hat{n}_{i,\uparrow} - 1/2 \right) \quad (5.4)$$

$$- \sum_{i,\sigma} \mu_\sigma \left(\hat{n}_{i,\sigma} - 1/2 \right) \leftrightarrow - \sum_i \left[\mu_\uparrow \left(\hat{n}_{i,\downarrow} - 1/2 \right) + \mu_\downarrow \left(\hat{n}_{i,\uparrow} - 1/2 \right) \right]. \quad (5.5)$$

While the tunnelling and the interaction terms are invariant under this transformation, the chemical potential term is modified, since the transformation does not also exchange the chemical potential for the individual spin components.

For the further discussion we separate the spin dependent chemical potential into two parts: a spin independent mean chemical potential $\mu = (\mu_\uparrow + \mu_\downarrow)/2$ and the difference in chemical potential for both spins $h = (\mu_\uparrow - \mu_\downarrow)/2$, which is called an *effective Zeeman shift*. It is a useful parameter to describe a spin-imbalance, i.e. $n_\uparrow \neq n_\downarrow$ and is zero for the spin-balanced case. Using this to rewrite equation 5.5 and applying the previous transformation

$$- \sum_{i,\sigma} \mu_\sigma \left(\hat{n}_{i,\sigma} - 1/2 \right) = - \sum_i \left[\mu \left(\hat{n}_{i,\uparrow} + \hat{n}_{i,\downarrow} - 1 \right) + h \left(\hat{n}_{i,\uparrow} - \hat{n}_{i,\downarrow} \right) \right] \quad (5.6)$$

$$\leftrightarrow - \sum_i \left[\mu \left(\hat{n}_{i,\uparrow} + \hat{n}_{i,\downarrow} - 1 \right) - h \left(\hat{n}_{i,\uparrow} - \hat{n}_{i,\downarrow} \right) \right], \quad (5.7)$$

we see that the spin-exchange only acts on the spin dependent chemical potential term, where then $h \leftrightarrow -h$, and not on the spin independent one.

Therefore, the full Hamiltonian transforms as

$$\hat{H}(t, U, \mu, h) \xleftrightarrow{\mathcal{SE}} \hat{H}(t, U, \mu, -h). \quad (5.8)$$

It is important to understand that due to the mapping of the Hamiltonian, its eigenstates and their time evolution transforms as well onto new eigenstates of the Hubbard Hamiltonian, where the sign of the effective Zeeman shift h is flipped. In contrast to that, no change will be observed if both spins are populated evenly, i.e. $h = 0$.

Spin SU(2) symmetry For a spin-balanced filling $h = 0$ the spin-exchange transformation maps onto exactly the same Hamiltonian. There, the Hubbard Hamiltonian has an SU(2) rotational symmetry. To see this we define the on-site spin operator $\hat{\mathbf{S}}_i = (\hat{S}_i^x, \hat{S}_i^y, \hat{S}_i^z)$ with

$$\hat{S}_i^z = \left(\hat{n}_{i,\uparrow} - \hat{n}_{i,\downarrow} \right) / 2 \quad (5.9)$$

and the ladder operators

$$\hat{S}_i^+ = \hat{S}_i^x + i\hat{S}_i^y = \hat{c}_{i,\uparrow}^\dagger \hat{c}_{i,\downarrow} \quad (5.10)$$

$$\hat{S}_i^- = \hat{S}_i^x - i\hat{S}_i^y = \hat{c}_{i,\downarrow}^\dagger \hat{c}_{i,\uparrow}. \quad (5.11)$$

At $h = 0$, the global spin operators $\hat{S}^z = \sum_i \hat{S}_i^z$ and $\hat{\mathbf{S}} = \sum_i \hat{\mathbf{S}}_i$ commute with the Hubbard Hamiltonian

$$[\hat{H}, \hat{S}^z] = [\hat{H}, \hat{\mathbf{S}}^2] = 0, \quad (5.12)$$

which shows the existence of a rotational invariance e.g. a $SU(2)$ -symmetry of the Hubbard model. This can be understood as that for a spin-balanced system, the measurement results does not depend on the spin basis one chooses. This basis can even be actively rotated by RF pulses without affecting the physical results, which will be a precondition for some measurements in chapter 7.

Particle-hole exchange symmetry I Another discrete symmetry in the Hubbard model can be described by the exchange of the annihilation and the creation operator of both spins:

$$\mathcal{PH}1 : \hat{c}_{i,\sigma} \leftrightarrow \hat{c}_{i,\sigma}^\dagger. \quad (5.13)$$

The number operators for both spins σ , therefore, transform with

$$\hat{n}_{i,\sigma} = c_{i,\sigma}^\dagger c_{i,\sigma} \leftrightarrow c_{i,\sigma} c_{i,\sigma}^\dagger = 1 - c_{i,\sigma}^\dagger c_{i,\sigma} = 1 - \hat{n}_{i,\sigma}, \quad (5.14)$$

where we used the anti-commutation relation of equation 2.1. Under this transformation, the individual site occupation is inverted, since the maximal population of a site is one for each spin. This is usually referred to as a *particle-hole* (\mathcal{PH}) transformation. There are two particle-hole transformations in the Hubbard model, the second one being discussed later in this section.

In the spin-1/2 Hubbard model doubles $n_D = \langle \hat{n}_\uparrow \hat{n}_\downarrow \rangle$ will be exchanged with holes n_H , while the singles occupation $n_{S,\sigma} = \langle \hat{n}_\sigma - \hat{n}_D \rangle$ changes its spin σ . To show this we will use that the basis for the site occupation is complete $n_{S,\uparrow} + n_{S,\downarrow} + n_D + n_H = 1$:

$$\begin{aligned} n_D = \langle \hat{n}_\uparrow \hat{n}_\downarrow \rangle &\leftrightarrow \langle \hat{n}_\uparrow \hat{n}_\downarrow - \hat{n}_\uparrow - \hat{n}_\downarrow + 1 \rangle \\ &= \langle -\hat{n}_D - \hat{n}_{S,\uparrow} - \hat{n}_{S,\downarrow} + 1 \rangle = n_H \end{aligned} \quad (5.15)$$

$$\begin{aligned} n_{S,\uparrow} = \langle \hat{n}_\uparrow - \hat{n}_D \rangle &\leftrightarrow \langle 1 - \hat{n}_\uparrow - \hat{n}_H \rangle \\ &= \langle 1 - \hat{n}_{S,\uparrow} - \hat{n}_D - \hat{n}_H \rangle = n_{S,\downarrow} \end{aligned} \quad (5.16)$$

Applying this transformation to the kinetic term of the Hubbard Hamiltonian and again utilising the anti-commutation relation of equation 2.1, one easily sees that it remains invariant under it. The same is true for the interaction term, where we use equation 5.14 for the transformation:

$$\begin{aligned} +U \sum_i (\hat{n}_{i,\uparrow} - 1/2) (\hat{n}_{i,\downarrow} - 1/2) &\leftrightarrow +U \sum_i (1 - \hat{n}_{i,\uparrow} - 1/2) (1 - \hat{n}_{i,\downarrow} - 1/2) \\ &= +U \sum_i (\hat{n}_{i,\uparrow} - 1/2) (\hat{n}_{i,\downarrow} - 1/2). \end{aligned} \quad (5.17)$$

We use the chemical potential definitions introduced previously, with a spin independent chemical potential μ and an effective Zeeman shift h . This term then transforms as

$$\begin{aligned} -\sum_i [\mu (\hat{n}_{i,\uparrow} + \hat{n}_{i,\downarrow} - 1) + h (\hat{n}_{i,\uparrow} - \hat{n}_{i,\downarrow})] &\leftrightarrow -\sum_i [\mu (-\hat{n}_{i,\uparrow} - \hat{n}_{i,\downarrow} + 1) + h (-\hat{n}_{i,\uparrow} + \hat{n}_{i,\downarrow})] \\ &= -\sum_i [-\mu (\hat{n}_{i,\uparrow} + \hat{n}_{i,\downarrow} - 1) - h (\hat{n}_{i,\uparrow} - \hat{n}_{i,\downarrow})]. \end{aligned} \quad (5.18)$$

Therefore, it maps again onto a valid Hubbard Hamiltonian, with a change in the sign of both the effective Zeeman shift h and the spin-independent chemical potential μ :

$$\hat{H}(t, U, \mu, h) \xrightarrow{\mathcal{PH}1} \hat{H}(t, U, -\mu, -h). \quad (5.19)$$

Note that this is the motivation of the special formulation of the Hamiltonian, introduced without explanation in section 2.1, where we added a constant energy offset.

To further highlight the connection between h and the spin-imbalance in the singles densities $n_{S,\sigma}$ and between the chemical potential μ and the general filling, mostly determined by the doubles n_D and holes densities n_H , we can rewrite the chemical potential term

$$-\sum_i [\mu (\hat{n}_{i,\uparrow} + \hat{n}_{i,\downarrow} - 1) + h (\hat{n}_{i,\uparrow} - \hat{n}_{i,\downarrow})] = -\sum_i [\mu (\hat{n}_{i,D} - \hat{n}_{i,H}) + h (\hat{n}_{i,S,\uparrow} - \hat{n}_{i,S,\downarrow})], \quad (5.20)$$

from which the symmetry relations can be accessed directly. In this equation we can identify the doping $\tilde{n} = \langle \hat{n}_D - \hat{n}_H \rangle$ and the magnetisation $m = \langle \hat{n}_\uparrow - \hat{n}_\downarrow \rangle = \langle \hat{n}_{S,\uparrow} - \hat{n}_{S,\downarrow} \rangle$ as the relevant measurement values of the system, which we will use in the following.

This symmetry can directly be seen in the equation of state, especially if one plots it including the holes density n_H , as shown in figure 5.1. It is of much practical use to anchor the chemical potential in experimental data through finding the symmetry point of the singles density and setting $\mu = 0$ there. This is very robust, since it does not depend on the shape of the density distribution, which is defined mostly by temperature and true even for spin-imbalanced ($h \neq 0$) systems.

Particle-hole exchange symmetry II All of the transformations discussed above do not connect or change the interactions in the system under transformation. There is, however, a second particle-hole transformation [34, 44] with the operators of only one spin modified:

$$\begin{aligned} \mathcal{PH}2 : \quad \hat{c}_{i,\uparrow} &\leftrightarrow \hat{c}_{i,\uparrow} \\ \hat{c}_{i,\downarrow} &\leftrightarrow (-1)^{i_x+i_y} \hat{c}_{i,\downarrow}^\dagger \end{aligned} \quad (5.21)$$

where the prefactor with the two-dimensional site index $i = (i_x, i_y)$ leads to an alternating sign per lattice site. The number operators for both spins transform as

$$\begin{aligned} n_{i,\uparrow} &\leftrightarrow n_{i,\uparrow} \\ n_{i,\downarrow} &\leftrightarrow 1 - n_{i,\downarrow}. \end{aligned} \quad (5.22)$$

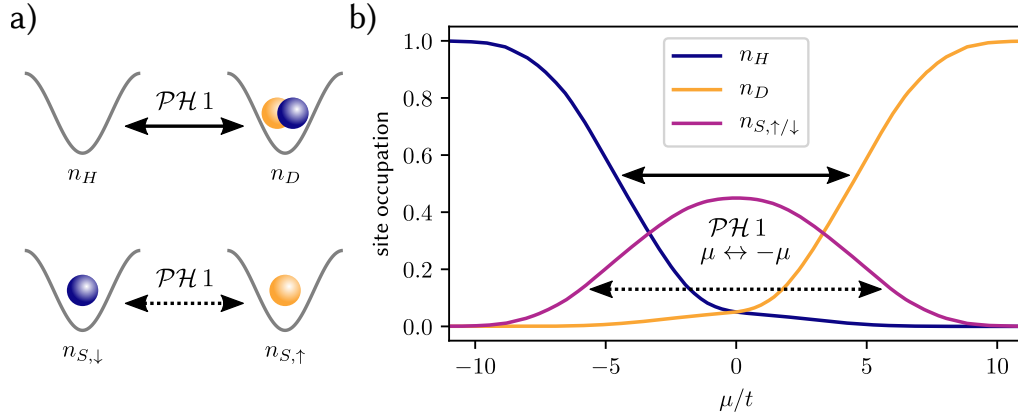


Figure 5.1: Particle-hole exchange symmetry I. a) The transformation $\mathcal{PH}1$ interchanges doubly occupied sites (doubles) with empty sites (holes) and the spin of the singly occupied sites (singles). Additionally, it transforms the parameters of the Hubbard model with $\mu \leftrightarrow -\mu$ and $h \leftrightarrow -h$. For a spin-balanced Hubbard model ($h = 0$) this can be directly observed in the density equation of state, shown in b). The holes are plotted as well in dark blue, even though in the experiment we can only indirectly infer them from the other densities. The mirror symmetry of the singles density around half-filling at $\mu = 0$ is a direct consequence of it, even for spin-imbalanced systems $h \neq 0$.

Then, the mapping of singles, doubles and hole densities through this transformation are given as

$$\begin{aligned} n_{S,\uparrow} &= \langle \hat{n}_\uparrow - \hat{n}_\uparrow \hat{n}_\downarrow \rangle \leftrightarrow \langle \hat{n}_\uparrow - \hat{n}_\uparrow + \hat{n}_\uparrow \hat{n}_\downarrow \rangle = n_D \\ n_{S,\downarrow} &= \langle \hat{n}_\downarrow - \hat{n}_\uparrow \hat{n}_\downarrow \rangle \leftrightarrow \langle 1 - \hat{n}_\downarrow - \hat{n}_\uparrow + \hat{n}_\uparrow \hat{n}_\downarrow \rangle = \langle 1 - \hat{n}_{S,\downarrow} - \hat{n}_{S,\uparrow} - \hat{n}_\uparrow \hat{n}_\downarrow \rangle = n_H. \end{aligned} \quad (5.23)$$

This means that spin-up singles get transformed into doubles, spin-down singles into holes and vice versa, see figure 5.3 a) as well.

In the interaction term this transformation leads to the expected sign change of U :

$$+U \sum_i (\hat{n}_{i,\uparrow} - 1/2) (\hat{n}_{i,\downarrow} - 1/2) \leftrightarrow -U \sum_i (\hat{n}_{i,\uparrow} - 1/2) (\hat{n}_{i,\downarrow} - 1/2). \quad (5.24)$$

Additionally, the roles of the chemical potential μ and the effective Zeeman shift h are interchanged when transforming the chemical potential of equation 5.20

$$- \sum_i [\mu (\hat{n}_D - \hat{n}_H) + h (\hat{n}_{i,S,\uparrow} - \hat{n}_{i,S,\downarrow})] \leftrightarrow - \sum_i [\mu (\hat{n}_{i,S,\uparrow} - \hat{n}_{i,S,\downarrow}) + h (\hat{n}_D - \hat{n}_H)]. \quad (5.25)$$

The full Hamiltonian transforms as

$$\hat{H}(t, U, \mu, h) \xrightarrow{\mathcal{PH}2} \hat{H}(t, -U, h, \mu), \quad (5.26)$$

and is, therefore, mapped onto another Hubbard Hamiltonian with the opposite interaction and an exchange of the values of h and μ . This means that the roles of density doping $\tilde{n} = n_D - n_H$ and magnetisation $m = n_\uparrow - n_\downarrow$ are switched, i.e. a system initially spin-balanced $h = 0$ but doped transforms into a spin-imbalanced system at half-filling $\mu = 0$. Additionally it connects the repulsive

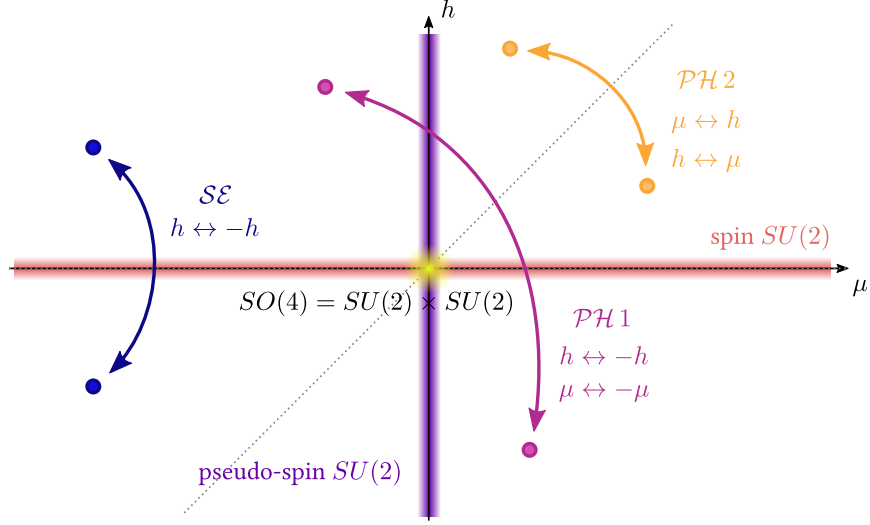


Figure 5.2: The symmetries of the Hubbard model. Shown are the symmetries discussed in this chapter and their effect in the h - μ parameter space. While \mathcal{SE} and $\mathcal{PH}2$ are mirror symmetries about the μ -axis and the dotted diagonal, $\mathcal{PH}1$ is a point symmetry with respect to the origin. There are two $SU(2)$ symmetries as well, the spin $SU(2)$ symmetry at $h = 0$ and the pseudo-spin $SU(2)$ symmetry at $\mu = 0$, connected through the $\mathcal{PH}2$ transformation. At their intersection lies the $SO(4) = SU(2) \times SU(2)$ symmetry.

and attractive side of the phase diagram, while interchanging density with spin ordering.

Pseudo-spin $SU(2)$ symmetry If the particle-hole symmetry $\mathcal{PH}2$ holds, then the spin $SU(2)$ rotational symmetry should transform under it as well. Transforming the spin operator \hat{S}_i and its ladder operators \hat{S}_i^+ , \hat{S}_i^- gives us their *pseudo-spin* equivalent $\hat{\eta}_i$: $\mathbf{S}_i \leftrightarrow \boldsymbol{\eta}_i$. It is, therefore, given as

$$\hat{\eta}_i^z = (\hat{n}_{i,D} - \hat{n}_{i,H} - 1) = (\hat{n}_{i,\uparrow} + \hat{n}_{i,\downarrow} - 1) \leftrightarrow (\hat{n}_{i,\uparrow} - \hat{n}_{i,\downarrow}) / 2 = \hat{S}_i^z \quad (5.27)$$

$$\hat{\eta}_i^+ = (-1)^{i_x+i_y} \hat{c}_{i,\uparrow}^\dagger \hat{c}_{i,\downarrow}^\dagger \leftrightarrow \hat{c}_{i,\uparrow}^\dagger \hat{c}_{i,\downarrow} = \hat{S}_i^+ \quad (5.28)$$

$$\hat{\eta}_i^- = (-1)^{i_x+i_y} \hat{c}_{i,\uparrow} \hat{c}_{i,\downarrow} \leftrightarrow \hat{c}_{i,\downarrow} \hat{c}_{i,\uparrow} = \hat{S}_i^- . \quad (5.29)$$

It can be shown that for $\mu = 0$ ($h = 0$ for the spin $SU(2)$ symmetry) this indeed creates another $SU(2)$ symmetry of the Hubbard model, the *pseudo-spin symmetry* [130]. The $\hat{\eta}$ operator was introduced as a creator for quasi-particles (η -pairs) with possible off-diagonal long-range order, which is necessary for superconductivity [132].

Figure 5.2 sketches this and the previously discussed symmetries in the h - μ parameter space. At $h = \mu = 0$ it features a point where both symmetries exist simultaneously, resulting in a $SO(4) = SU(2) \times SU(2)$ symmetry [131].

Mapping of phases in parameter space This particle-hole symmetry is very useful for numerical simulations, like QMC, which struggle to work in some parameter regions [33]. There, one calculates the properties or states of a system within a parameter region known to work correctly and reliably and then transforms the results, which transforms the parameters of the simulation as well. A

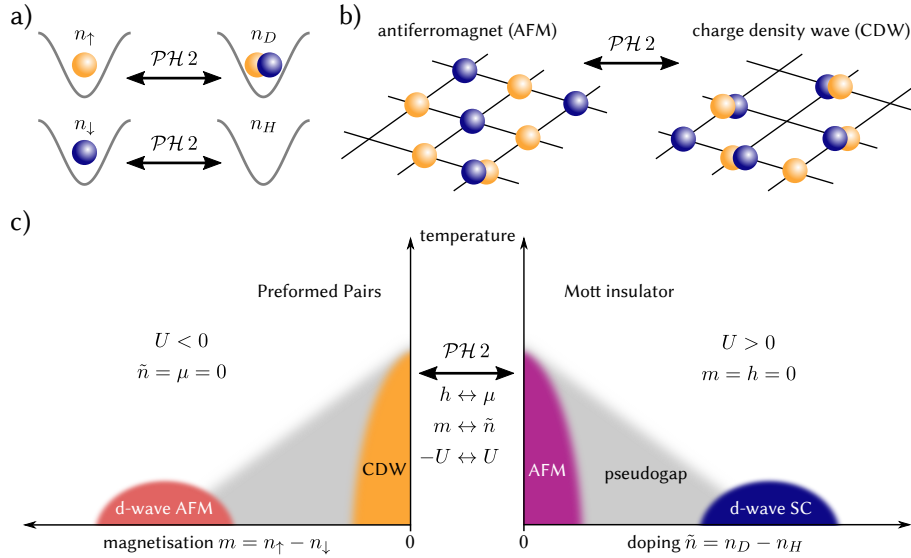


Figure 5.3: Particle-hole exchange symmetry II and its mapping of phases. a) The second particle-hole transformation $\mathcal{PH}2$ transforms spin-up singles to doubles and spin-down singles to holes. This not only transforms local site occupations and the Hubbard parameters $\mu \leftrightarrow h$ and $+U \leftrightarrow -U$, but many body states as well, for example shown in b) the antiferromagnet at repulsive interactions changes to the charge-density wave with attractive interactions. c) In general all phases and other features of the Hubbard model will have a corresponding feature under the transformation, which might be easier to detect, depending on the quantum simulator one uses [44].

method that fails to converge for doped systems could be calculated with an effective Zeeman shift, i.e. a spin-imbalance, at the inverse interaction and then one could use the transformation to acquire the desired results.

There were, however, some early suggestions to use this not only for numerical, but for experimental quantum simulations as well [44]. Quantum simulators also only have access to a limited range of temperatures and interactions or dopings and magnetisations. For example, previous experiments with spin-imbanced Fermi gasses simulating the attractive two-dimensional Hubbard model reached an effective Zeeman-shift of only $h/t = 0.21(1)$ for cold temperatures [14, 133].

The particle-hole symmetry $\mathcal{PH}2$ would enable the use of the optimal parameter space for each quantum simulator to additionally simulate the physics of the transformed Hubbard Hamiltonian. This concept can be illustrated, for example, for the antiferromagnetic (AFM) ordering at half-filling that is a low temperature feature of the repulsive Hubbard model and the high temperature superconductors as well. When measured, it should show signs of an alternating spin ordering, with most sites occupied with one spin only. If, however, a quantum simulator reaches colder temperatures for attractive interactions, one could measure the physics of the charge-density-wave (CDW) which is the phase the AFM is transformed into through the particle-hole transformation, see figure 5.3. The CDW would consist of doubles and holes, again ordered in a chequerboard fashion, but having only little local magnetic order. As shown in figure 5.3, this symmetry should also map not yet observed phases, like the d-wave superconducting phase, which would map to a d-wave antiferromagnet on the attractive side ($U < 0$).

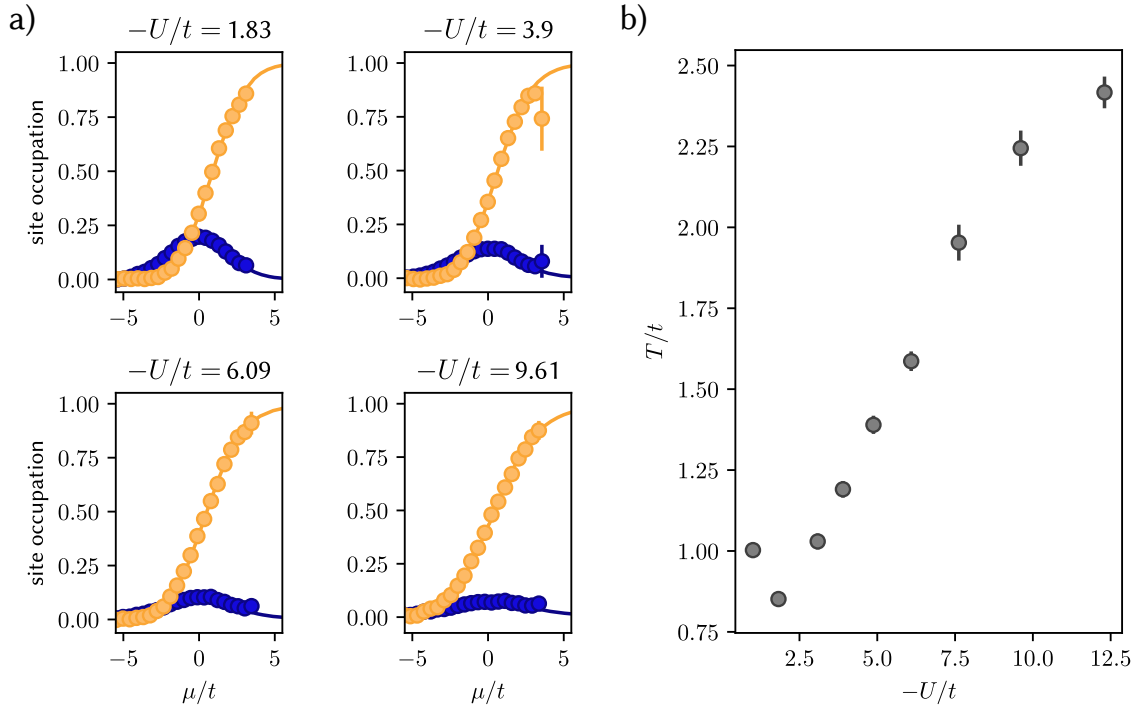


Figure 5.4: Preparing the attractive Hubbard model. a) Measured density equations of state $n(\mu, T_{\text{fixed}})$ for different attractive interaction strengths $U < 0$ are shown. The blue (orange) circles represent the measured singlets (doubles) density averaged over several measurements. The solid line shows the fit, which was used to extract the centre chemical potential μ_0 , the global density scaling parameters $\sigma_{S/D}$ and the temperature T , plotted in b). The observed higher temperature for increased interaction strength could be due to losses close to the Feshbach resonance as shown in figure 4.4. The temperature minimum is located at weak interactions of $U/t = -1.83$.

With our quantum simulator we have the possibility to access both complementary parameter spaces with low temperature samples and are therefore in the unique position to experimentally test and validate this symmetry.

5.2 The simulation of the spin-imbalanced Hubbard model

Previous results produced in our experiment worked predominantly with repulsive interactions [28, 29, 49, 50, 110]. This was due to our focus on the detection of antiferromagnetic spin ordering at cold temperatures and the heating caused by light assisted losses close to the Feshbach resonance at 202.1 G, as discovered during this thesis, see section 4.1.3. With the design and implementation of a linewidth broadened laser, described in appendix A, we were able to prepare ultracold lattice systems with attractively interacting fermions, as I will describe in this section. Furthermore, I will introduce techniques to create spin-imbalance in our system and detect them.

Preparing an attractive Hubbard simulation Following the initial evaporation with attractive interactions, the z -lattice is loaded at a field of 204.5 G. After that the magnetic field is ramped to

its final simulation value B_{sim} in the range of 204 to 209 G in 200 ms. For this, the fast Feshbach coils subtract a variable magnetic field from the large offset field given by the slow Feshbach coils. By turning off the current in the fast Feshbach coils one can quickly ramp to 212.5 G for the detection. The fixed field during the loading ensures that even for the weakly interacting atomic cloud close to 209 G the thermalisation and the final evaporative cooling in the z -lattice is working well. Additionally, it ensures that all further lattice loading starts with approximately the same atom number and temperature. The slow change in the magnetic field minimises heating due to the density change with reduced interaction strength.

Figure 5.4 shows the measured equation of state with varying magnetic fields and therefore interactions. They range from $U/t \simeq -0.9$ at 208.2 G to $U/t \simeq -12.3$ at 204.1 G for an in-plane lattice with $6 E_{\text{rec}}$ and a resulting tunnelling amplitude of $t/h = 224$ Hz. All of this data is fitted with results of DQMC simulations, with the Hubbard parameters T, μ_0 and the global density scales $\sigma_{S/D}$ as free fit parameters.

One can observe the expected strong reduction in the peak value of the singles densities at half-filling $\mu = 0$ for stronger attractive interactions. The most significant change, however, is visible in the temperature which rises from the lowest temperature $T/t = 0.85(1)$ at weak interactions $U/t \simeq -1.83$ up to $T/t = 2.42(5)$ at very strong attraction $U/t \simeq -12.3$. One reason for this could be the increased heating through scattering losses, which are still significant in the close vicinity of the Feshbach resonance, see figure 4.4. To reach colder temperatures, we can lower the dipole trap power during the z -lattice ramp-up, which then allows for a lower final evaporation potential. The resulting trade-off between atom number and temperature has to be chosen such that the chemical potential in the centre is still above half-filling, i.e. $\mu_0 > 0$, otherwise the DQMC fit might fail since it is missing the singles peak symmetry feature it relies upon.

Creating spin-imbalanced systems At the end of the forced evaporative cooling in the magnetic trap, and just after being loaded into the optical dipole trap, the population of the two lowest hyperfine states is strongly imbalanced. For further evaporation in the optical trap we usually mix these spin populations with several non-adiabatic Landau-Zener sweeps, to reach a 1:1 distribution of spin-up to spin-down particles, as explained in section 4.1.3. The population transfer in these pulses is given with the Landau-Zener formula in equation 3.6 and can be adjusted by the sweep rate $\dot{\Delta} = \Delta\nu/T$, where $\Delta\nu \approx 2$ MHz is the usual RF frequency sweep range and $T = 2$ ms the pulse duration.

For the creation of a spin-imbalanced population after the evaporation, we reduce the number of spin-mixing pulses to only a single one and vary its sweep range for a fixed pulse duration. By reducing the sweep range the transfer becomes more adiabatic and more efficient, so the initial imbalance is only slightly reduced. Nonetheless, one has to remember that the mixing pulses are used before the final evaporation, during which we reduce the atom number by nearly two orders of magnitude. When the spin-imbalance gets too large, rethermalisation and with it cooling becomes inefficient since collisions between particles of the same spin are suppressed.

To detect this spin-imbalance we switch to the detection of spin-up and spin-down singles. We use the same mapping of the local chemical potential μ previously explained and compare it to DQMC calculations with different effective Zeeman shifts h , which becomes a further free fit parameter. For measuring an imbalance in the spin components and determining h via a fit, we have to be able to accurately determine the local ratio of both spin state populations. However, this is difficult if both densities are scaled individually with $\sigma_{S\uparrow}, \sigma_{S\downarrow}$, since, as we know from the first particle

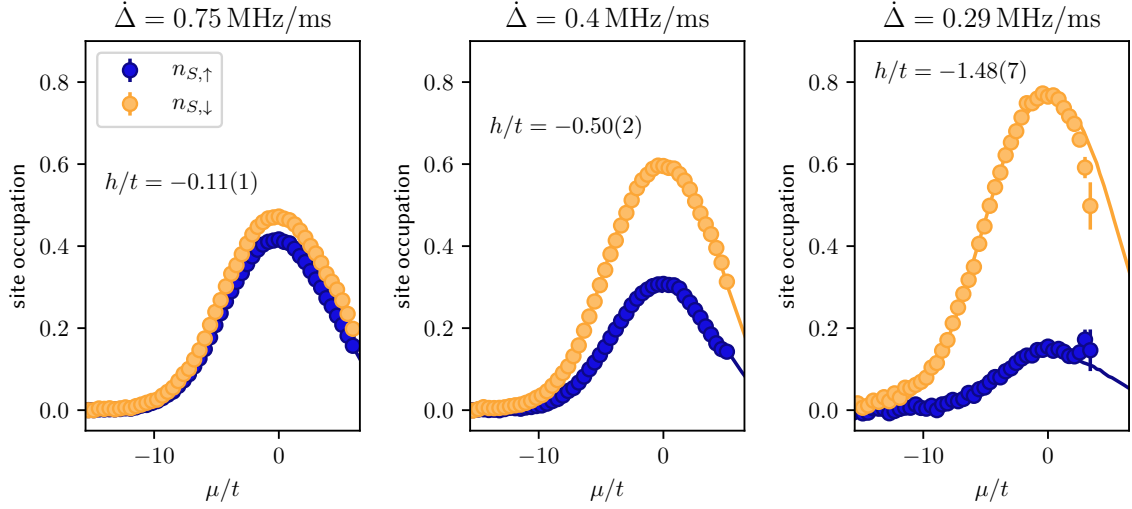


Figure 5.5: Creating a spin-imbalanced system. To introduce a spin-imbalance in the atom populations, we change the frequency ramp speed of the spin mixing Landau-Zener RF sweep $\dot{\Delta}$. Equation 3.6 shows how the ramp speed of the RF sweep determines the transfer efficiency. In the usual configuration a spin-balanced mixture is created by several pulses with $\dot{\Delta} \approx 1$ MHz/ms. The singles density, shown as circles in the plots, are fitted with DQMC simulation results at $U = +7.6$, indicated with solid lines. These fits allow for the extraction of, among other things, the effective Zeeman shift h . For a slower ramp speed like the $\dot{\Delta} = 0.29$ MHz/ms on the right plot, the variance in atom number, temperature and imbalance grows larger. Therefore, averaging all data like shown here is not ideal any more, as can be seen in the deviation of the data to the fit in the high chemical potential region.

hole symmetry $\mathcal{PH}1$ introduced in the previous section, both singles densities have approximately the same shape. An individual scaling factor for each spin component separately could not be distinguished from a real imbalance of the populations. However, since losses in detection are usually mostly present for doubles and the dual slicing efficiency for the spin singles is nearly equal (within 3%), we can use a common slicing scaling factor $\sigma = \sigma_{S\uparrow} = \sigma_{S\downarrow}$ for both singles densities.

In figure 5.5 some spin-spin measurements are shown for different sweep rates $\dot{\Delta}$, creating an imbalance of both populations. As one can see from the high singles densities, this data was taken with a repulsive experimental sequence, here at 189 G and a lattice depth of $5.8 E_{\text{rec}}$ resulting in $U/t = +7.6$. For a fixed sweep rate $\dot{\Delta}$, the extracted h values fluctuate in between measurements, partially due to their dependence on the varying efficiency of the final evaporation. Nevertheless we are able to fit each individual measurement separately and extract h , μ_0 and T , similar as for the spin-balanced data. This allows for the binning the results, i.e. averaging measurements with similar h , reducing the uncertainty on h in the combined data.

It is important to realise that while the local magnetisation $m = n_{\uparrow} - n_{\downarrow}$ can vary, the effective Zeeman shift h is global and independent of the position in the trap, when the atoms are in thermal equilibrium. This can be seen with the definition of the local chemical potential in equation 3.35, which we now write spin dependently

$$\mu_{0,\sigma} = \mu_{l,\sigma} - V_l, \quad (5.30)$$

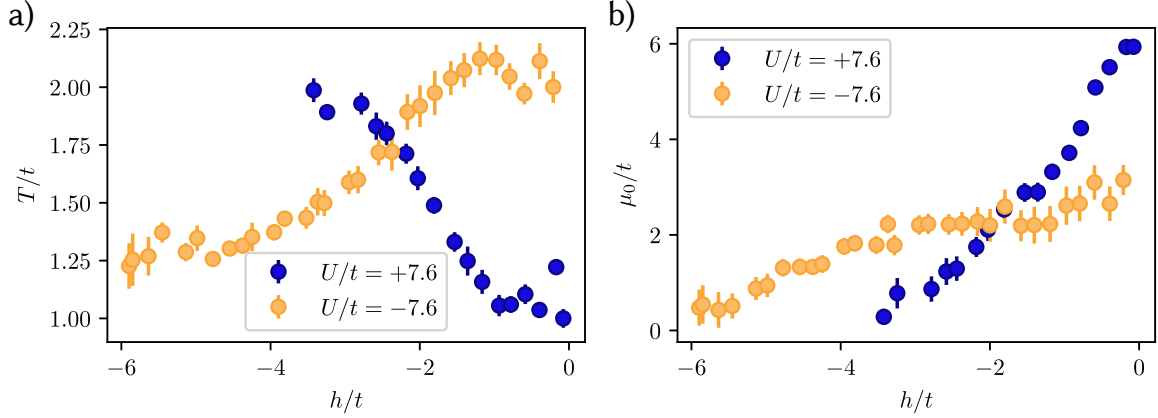


Figure 5.6: Post-selective data binning in h . Since the final spin-(im-)balance of the atom cloud strongly fluctuates, each measurement is first fitted using DQMC simulation results and sorted into bins with nearly equal h . The data of these bins is then averaged, retaining the extracted chemical potential information and the result again compared to simulation. a) For repulsive interactions (blue data points) the temperature increases with stronger spin-imbalance, as one would expect, since the cooling should become more inefficient. This is, however, not true for attractive interactions (orange data points), where we observe a decrease in temperature. This might be due to the increased number of singly occupied sites, which have a potentially higher entropy per particle than the doubly occupied ones. b) For both interactions the central chemical potential μ_0 is reduced with higher spin-imbalance. Since the DQMC fit is not reliable for data with $\mu_0 < 0$ we are limited in the obtainable effective Zeeman field h for a fixed set of evaporation parameters .

where $\sigma = \uparrow, \downarrow$ is again an index for the spin, and l represents the individual equipotential region. The trap potential V_l is spin independent, so we can write

$$h_l = \frac{\mu_{l,\uparrow} - \mu_{l,\downarrow}}{2} = \frac{\mu_{0,\uparrow} - \mu_{0,\downarrow}}{2}, \quad (5.31)$$

which is constant for all l , since $\mu_{0,\sigma}$ is constant for each spin individually.

Temperature changes with induced spin-imbalance As already hinted, by changing the spin-imbalance, we directly influence the evaporative cooling process, and therefore should see a decrease in temperature for a larger spin-imbalance. This is true for repulsive interaction, where we get a nearly linear increase in temperature for increasing $|h|$, as shown in blue in figure 5.6 a). This, however, is not true any more for measurements at attractive interactions, as can be seen in the orange data points. Initially, the temperature drops, and then stays constant for strong effective Zeeman shifts $h/t > 4$. These measurements were done at $U/t = -7.6$.

An explanation for this counter-intuitive behaviour could lie in the entropy which is stored in the close to band-insulating centres for attractive systems. As shown in figure 4.15, regions with a high doubles fraction have a very small entropy per particle S/N . Therefore, they cannot absorb much of the initially present total entropy, while the high central filling still reduces the atom number. The imbalance leads to a smaller doubles fraction, increasing the number of singles substantially which then can store a lot of entropy. The spin-imbalance also leads to a reduction of the central chemical potential μ_0 as shown in figure 5.6 b) for repulsive and attractive interactions. This limits

the spin-imbalance, i.e. effective Zeeman shift we can measure, since the DQMC fit is not able to give reliable results for $\mu_0 < 0$.

5.3 Testing and validating the particle-hole symmetry

The particle-hole symmetry $\mathcal{PH}2$ introduced in section 5.1, in the following only referenced as *the* particle-hole symmetry and transformation, promises the possibility to extend the capabilities of any quantum simulator of the Hubbard model significantly, by providing an alternative route to measure physical properties or phases of interest [44]. This is, however, only true if the quantum simulator reproduces the true Hubbard model without additional terms. Things that would destroy this symmetry are, for example, diagonal next-nearest-neighbour tunnelling [33] and higher band population or non-binary state occupation (three or more hyperfine states occupied). Testing the particle-hole symmetry in our system, therefore, can be seen as a probe on how accurate and clean our quantum simulation of the Hubbard model actually is.

With the tools described in section 5.2, we now have the possibility to access spin-imbalanced systems with both attractive and repulsive interactions, while being able to measure the density equation of state for different chemical potentials as well. We can access the density doping $\tilde{n} = n_D - n_H$ for spin-balanced systems, where $h = 0$, by detecting singles and doubles simultaneously. By switching the detection to both spin-up and spin-down singles, we obtain the local magnetisation $m = n_{S,\uparrow} - n_{S,\downarrow}$.

Transforming spin-balanced systems at half-filling The easiest point in parameter space to check the particle-hole symmetry is at half-filling with spin-balanced populations, since there $\mu = h = 0$, and therefore $\mu \leftrightarrow h$ is automatically fulfilled. The transformation still modifies the interaction $U \leftrightarrow -U$ and exchanges the site occupations, see equation 5.23. Since we cannot directly measure hole densities, we focus on the exchange of $n_{S,\uparrow} \leftrightarrow n_D$, which we are able to detect in the same run. These data points for varying interaction strength at half-filling ($\mu = 0$) in a spin-balanced system ($h = 0$) are shown in figure 5.7. The data presented is taken from the measurements with the lowest obtained temperatures at the individual interaction strengths and combines old data with repulsive interaction strengths [50] with newly measured, temperature optimised data similar to the measurements shown in figure 5.4. The exchange symmetry, mirroring the densities about $U = 0$ is clearly visible, and highlighted by DQMC calculations with a similar temperature range of $0.625 < k_B T/t < 2.2$. Even though this temperature range is rather large, the data agrees very well with the predictions and allows the connection of repulsive to attractive interactions in the Hubbard model.

Transformations away from half-filling and spin-balanced systems Next we would like to check whether, apart from the sign change of U , the chemical potential and the effective Zeeman shift change roles as well. A system which is not at half-filling, i.e. $\mu \neq 0$, has to have a spin-imbalance $h \neq 0$ after the transformation ($\mu \leftrightarrow h$). To do so we choose an interaction strength absolute value of $|U|/t = 7.6$, at which we can both prepare repulsive $U/t = +7.6$ and attractive $U/t = -7.6$ systems at low temperatures.

For the accurate measurement of doping we ideally work with a spin-balanced sample, since by measuring the singles of one spin, we can infer the other spin component as well. This in turn allows

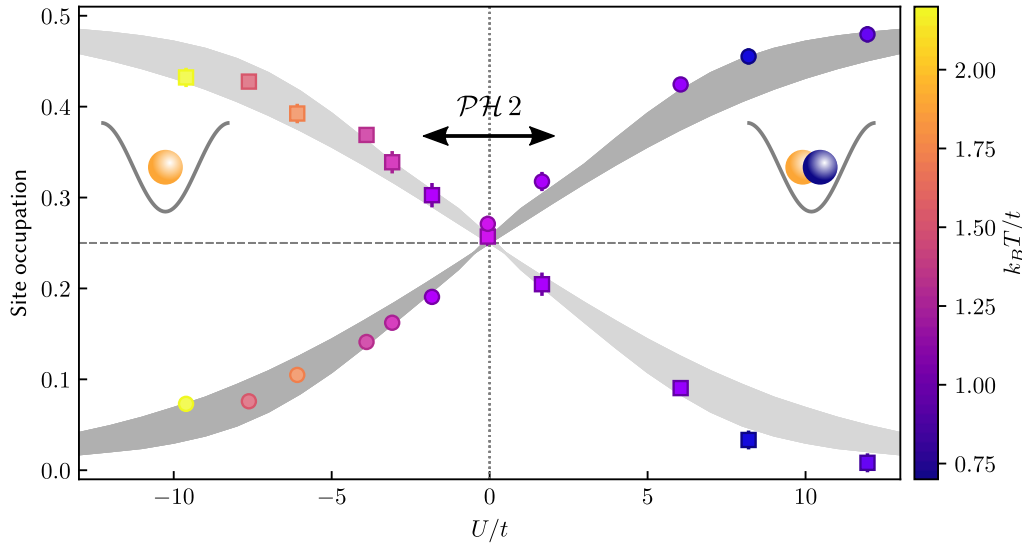


Figure 5.7: Particle-hole symmetry with varying interactions. At half-filling ($\mu = 0$) and with a spin-balanced population ($h = 0$), the transformation exchanges the population of spin-up singles (squares) and doubles (circles), while also changing the sign of the interaction U . The data points with the lowest obtained temperatures for each interactions were chosen, with the temperature colour coded, ranging from $k_B T/t = 0.75$ to 2.20 . Here the measurements confirm the symmetry predictions. In grey the theory calculations are shown for temperatures between $k_B T/t = 0.625$ to 2.20 . Especially for cold temperatures $k_B T/t < 1.5$ the data lies on the outer edge of this shaded region, indicating very good agreement with theory. This figure was presented in [30], while all data with repulsive and vanishing interaction strength $U/t \geq 0$ taken from previous experiments [50].

us to more accurately determine the doubles density, fixing its global scaling factor σ_D . Therefore we will compare a spin-balanced sample ($h = 0$) with density doping ($\mu \neq 0$) to a spin-imbalanced one ($h \neq 0$) at half-filling ($\mu = 0$).

In figure 5.8 b) measurement data of spin-imbalanced systems with repulsive interactions $U/t = +7.6$ are shown. For each measurement the Hubbard parameters h, μ, T and the global scaling factor for both singles densities σ were extracted with a fit to DQMC data, and then rebinned in h , as explained in the previous section. As can be seen from figure 5.6, the temperature T changes with varying the spin-imbalance as well. To counteract this we adjust the final evaporation depth for the more spin-imbalanced measurements and select only data with temperatures of $k_B T/t = 1.4 \pm 0.1$.

As previously explained, we use the singles density of the spin-imbalanced data at half-filling $\mu = 0$ and compare it to the spin-balanced attractive density data, which is shown in figure 5.8 a). The configuration where both the initial and the transformed state occupation are directly observable is $n_{S,\uparrow} \leftrightarrow n_D$. To use the information of the spin-down densities $n_{S,\downarrow}$ as well, we can use the spin-exchange transformation \mathcal{SE} introduced in the first section of this chapter, where $n_{S,\downarrow} \leftrightarrow n_{S,\uparrow}$ and $h \leftrightarrow -h$. This means by changing the sign of the effective Zeeman shift we can use the spin-down particles as if they were spin-up particles, and compare them with the particle-hole transformation equivalent. This is done in figure 5.8 c), where the spin-imbalanced repulsive data of both singles densities (shown in orange and dark blue) is overlapped with the measured doubles density (black

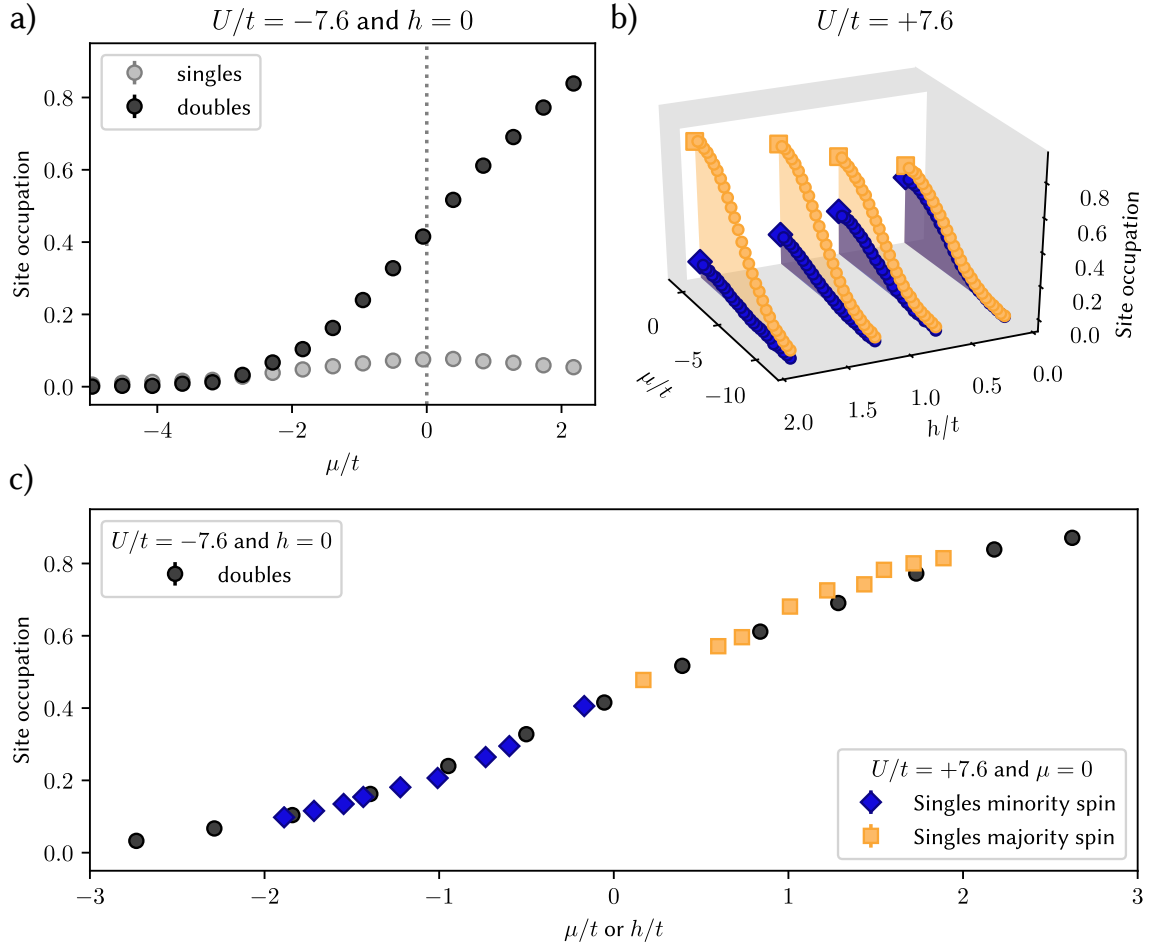


Figure 5.8: Interchanging the chemical potential with the effective Zeeman shift. a) The density equation of state $n(\mu, T_{\text{fixed}})$ for a spin-balanced system $h = 0$ and attractive interactions $U < 0$. From a fit to DQMC data a temperature of $k_B T/t = 1.53(3)$ is extracted. b) shows the singles densities of spin-imbalanced systems $h \neq 0$ with repulsive interactions $U > 0$. Half-filling $\mu = 0$ is indicated with a white plane and larger size of the data points lying on it. The data was binned in h and pre-selected on temperature within $k_B T/t = 1.4 \pm 0.1$. Both repulsive minority and majority spin components at $\mu = 0$ are then overlaid with the doubles density in c), using a shared axis for μ (attractive spin-balanced) and h (repulsive at half-filling). This data was presented in [30].

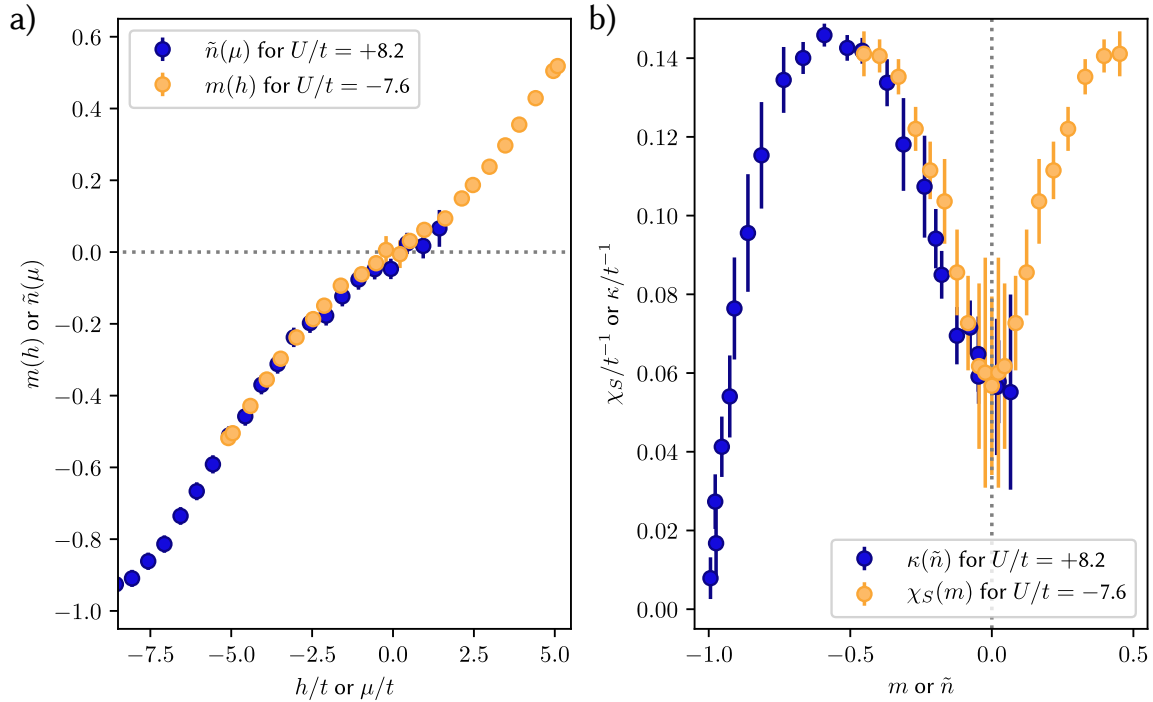


Figure 5.9: Simulating a Mott insulator using attractive interactions. a) With the same methodology used in figure 5.8 we compare the density doping $\tilde{n} = n_D - n_H$ at repulsive interactions $U/t = +8.2$ and $h = 0$ with the magnetisation $m = n_{S,\uparrow} - n_{S,\downarrow}$ at attractive interactions $U/t = -7.6$ and $\mu = 0$. Through a fit to the data with repulsive interactions a temperature of $k_B T/t = 0.76(6)$ is extracted. The individual attractive interaction measurements were fitted, binned in h and pre-selected in a temperature range of $k_B T/t = 1.5 \pm 0.1$. The slope of both curves is extracted by a linear fit to four surrounding data points which are then plotted in b) as the compressibility $\kappa(\tilde{n}) = \partial\tilde{n}/\partial\mu$ and the static spin susceptibility $\chi_S(m) = \partial m/\partial h$ with a shared x -axis of m and \tilde{n} . With the quantitative agreement of both curves, reproducing the minimal compressibility feature of the Mott insulator, we can claim to have simulated the Mott insulator with a quantum simulator with attractive interactions. This data was presented in [30].

circles) at attractive interactions $U/t = -7.6$. The axes have the same unit, however, they describe the variables connected through the symmetry $h \leftrightarrow \mu$. We see an excellent quantitative agreement of the data and can, therefore, confirm the validity of the particle-hole symmetry for our system.

Mott insulator in a quantum simulator with attractive interaction To go a step further, we want to test the symmetry mapping of the phase diagram in figure 5.3. For most of the parameter space of h and μ we are able to simulate the Hubbard model with temperatures of $k_B T/t \approx 1.5$, which is more than sufficient to study the Mott insulator. This feature of the repulsive Hubbard model has been examined extensively in several experiments [50, 134–137]. Close to half-filling $\mu = 0$ and for large interaction strengths $U \gg t$ most sites are occupied with one atom, i.e. a single, since the formation of doubles is energetically unfavourable. Adding further atoms into the system, i.e. increasing the doping \tilde{n} comes with an energy cost, which is represented as a significant increase in chemical potential, largest at half-filling itself. This energy cost, associated with the on-site interaction, is quantified with the isothermal compressibility $\kappa = \partial\tilde{n}/\partial\mu$, which has a

pronounced minimum at half-filling [50]. When the filling approaches the band insulator ($\tilde{n} = +1$), Pauli blocking leads to another incompressible phase, which is mirrored close to the empty lattice ($\tilde{n} = -1$).

For a system with attractive interactions there is no incompressible Mott phase close to half-filling, since the formation of doubles lowers the overall energy. However, the particle-hole symmetry indicates that there should be a similar, incompressible feature in the static spin susceptibility $\chi_S = \partial m / \partial h$, since $\tilde{n} \leftrightarrow m$ and $\mu \leftrightarrow h$, so $\kappa \leftrightarrow \chi_S$. To test the equivalence of both quantities through the particle-hole symmetry we measure the magnetisation $m = n_{S,\uparrow} - n_{S,\downarrow}$ as a function of the effective Zeeman shift h . In figure 5.9 a) the results of this measurement at $U/t = -7.6$ are plotted in orange. Similar to the previous measurement, the individual spin-imbalanced measurements were preselected to a temperature range of $k_B T/t = 1.45 \pm 0.10$, in order to avoid the strong decrease in temperature with bigger spin-imbalance. In the same plot we add the results of a measurement of the density doping $\tilde{n}(\mu) = n(\mu) - 1$ at $U/t = +8.2$ in dark blue. Both show a flattened slope close to $\mu = 0$ or $h = 0$.

By numerically calculating the slope of both curves we extract the spin susceptibility χ_S and the compressibility κ which are plotted in figure 5.9 b) with interchanged axis descriptions $m \leftrightarrow \tilde{n}$ and $\chi_S \leftrightarrow \kappa$. The quantitative agreement of the data shows that we indeed could reproduce a feature of the repulsive Hubbard model, the incompressible Mott phase, by simulating it with a spin-imbalanced system with attractive interactions.

This highlights the versatility of the particle hole symmetry in quantum simulation and might be a potential route to overcome detection or preparation issues specific to individual experiments. As shown in figure 5.3, a d-wave AFM phase at attractive interactions and non-zero magnetisation is predicted. Using the excellent detection capabilities for magnetic order reported by several quantum gas lattice experiments [29, 123, 136, 138–140] one could, similarly to what we showed here, detect this feature and hence, investigate the corresponding d-wave superconducting phase still currently under debate [141].

Creating and characterising a Hubbard bilayer quantum simulator

Early on, the two-dimensional Hubbard model was proposed to feature a superconducting phase, connected to high-temperature superconductivity [8]. However, recently some arguments were made against that claim [25], resulting in a continued search towards extensions of the Hubbard model that could in turn sustain a superconducting phase. One proposal is the bilayer Hubbard model [53] introduced in section 2.5. In this chapter I will present the experimental changes incorporated in our system to simulate the bilayer Hubbard model and the required calibration of its parameters like inter-plane tunnelling t_{\perp} or on-site interaction U .

6.1 Tuning the superlattice phase with a 30 GHz frequency lock

To create a bilayer the z -superlattice is used in symmetric configuration ($\phi_{\text{SL}} = 0$) to form double-wells in the vertical direction. Together with the xy -lattices they then form a spatial lattice potential that creates the desired bilayer structure.

Since it is critical to be able to control the potential difference between both connected planes, i.e. the potential imbalance Δ in the double-well in z -direction and to avoid heating by a fluctuating superlattice phase ϕ_{SL} we need to devise a mechanism to fix and dynamically manipulate the phase by locking the frequencies of both superlattice lasers. This locking mechanism needs to have a large tuning range to adjust ϕ_{SL} and with it the potential imbalance Δ , have a robust, repeatable operation with little noise and must allow fast tuning for dynamical control.

The task is complicated by the experimental construction of the accordion z -lattice with very little path length difference for both beams. This requires large frequency shifts in order to perform small superlattice phase changes. To change the superlattice phase from $\phi_{\text{SL}} = 0$ to $\pi/2$ we estimated that the frequency of the green 532 nm laser would have to shift by approximately 60 GHz. Additionally, the lasers we used for this superlattice, the Coherent Mephisto (ν_{red}) and the Coherent Verdi V10 (ν_{green}), have several limitations in their available tuning range and their ability to change frequencies fast. Initial measurements indicated that the symmetry point $\phi_{\text{SL}} = 0$, where we would like to prepare the bilayer, would be achieved at a difference frequency of approximately $|\delta\nu_{\text{green}}| = |\nu_{\text{green}} - 2\nu_{\text{red}}| \approx 25$ GHz. We, therefore, aimed at a laser lock with a maximal beat frequency of 30 GHz.

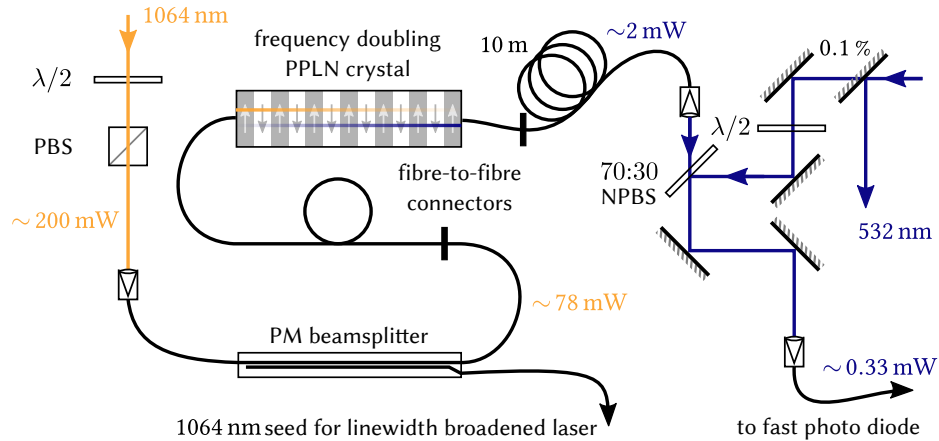


Figure 6.1: Optical setup for frequency doubling and beating. 1 064 nm light from the Mephisto is feed to a fibre-coupled frequency doubling crystal. The created 532 nm light is then sent to another optical table, where it is overlapped with a few milliwatts of light from the Verdi V10 on a non-polarising beam splitter (NPBS). The combined light is then sent to a fast photo-diode to detect the frequency difference via the optical beat note. Note that before the frequency doubling, some light is split-off to act as a seed for the linewidth broadened laser, described in appendix A.

6.1.1 Optical up-conversion and beat detection

A direct way to compare the frequencies of both lasers is by doubling the frequency of the Mephisto laser ν_{red} and then superimposing it with light from the Verdi V10 with frequency ν_{green} , which produces an optical beat note, oscillating with the frequency difference $|\delta\nu_{\text{green}}|$. To detect this beat frequency of up to 30 GHz we use the fibre coupled photo-diode DXM30AF produced by Thorlabs. Coupling both lasers into the same single mode fibre additionally guarantees perfect overlap of both spatial modes.

The optical setup for creating this beat note is shown in figure 6.1. Light from the Mephisto laser, that generates the xy -lattices as well, is coupled into a fibre which leads to a following fibre based polarisation maintaining beam splitter to provide ~ 78 mW of power. By passing a periodically poled lithium niobate (PPLN) crystal with temperature adjusted phase matching, its frequency is doubled [142]. With the crystal we use (Global Fiberoptics, Ltd.) and the stated input power, a frequency-doubled output of about 2 mW is achieved at a crystal temperature of 69.5 °C. The light is then transported to another optical table and combined with the Verdi light, taken from the transmitted residual power after the first mirror in its beam path. With the polarisation adjusted by a half-wave plate it is then overlapped with the frequency doubled light on a 70:30 non-polarising beam splitter. In front of the final fibre coupler we then achieve 1.1 mW frequency-doubled Mephisto light and 2.4 mW light from the Verdi. The coupling process, however, is not efficient and only 0.3 mW reach the photo diode after a single mode fibre which is still sufficient for all further purposes.

6.1.2 High frequency signal processing

The DXM30AF photo diode is specified for 750 to 1 650 nm and not amplified, but still has a respectable responsivity of around 0.2 A/W at 532 nm [143]. Since the relative power of both beams is

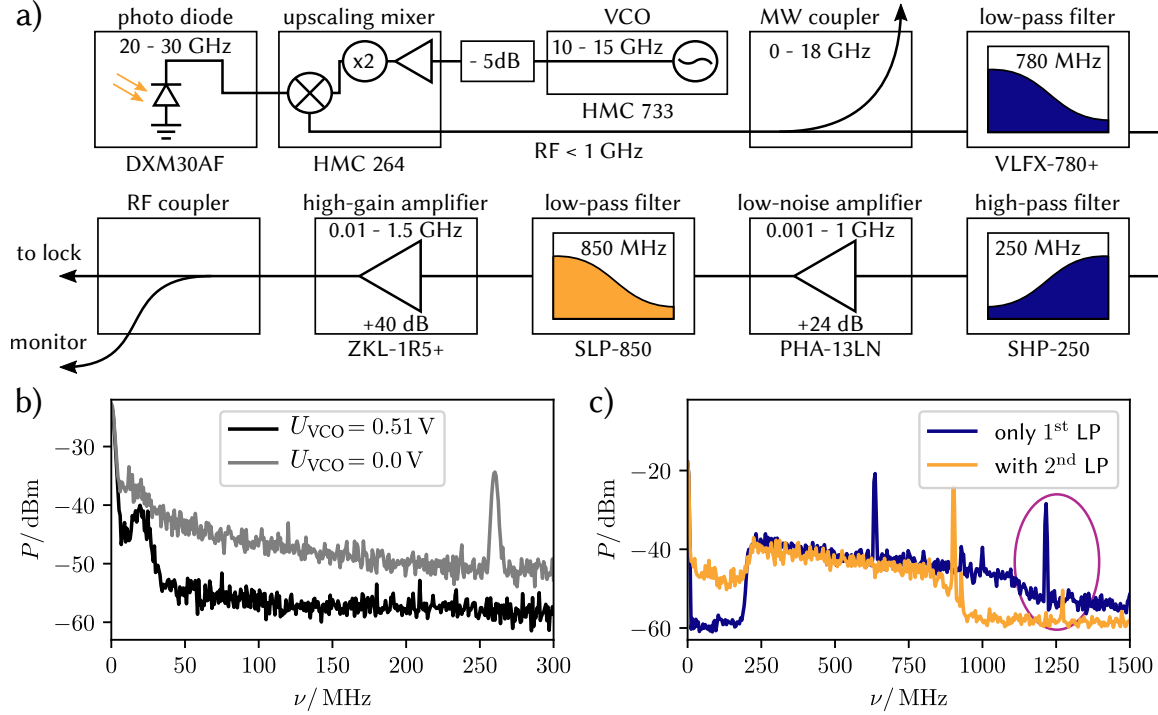


Figure 6.2: Microwave beat note down-conversion and signal processing. a) The high frequency signal of the optical beat note is quickly down-converted using a voltage controlled oscillator (VCO) and a frequency doubler. This converts the microwave frequencies of 20 to 30 GHz down to more processable RF frequencies, that get subsequently amplified. b) We observed internal resonances for certain VCO control voltages U_{VCO} , which lead to a loss of the beat note signal. In grey a signal trace away from any resonance is shown and a clear signal at about 260 MHz is observed for $U_{VCO} = 0$ V. Tuning to one of these resonances at $U_{VCO} = 0.51$ V should shift this beat note to about 900 MHz, however, no signal is detected there. In black one feature of this signal processing resonance is shown, a low frequency noise region at about 20 MHz, seemingly saturating the amplifiers. c) Adding low- and high-pass filters before the amplification removes the effects of most of these resonances. The last high-gain amplifier, however, still picks up signals from the microwave-evaporation around 1.2 GHz, as pictured in the blue trace. The orange curve shows the signal after adding a second low-pass filter before this amplification stage, leading to a sufficient suppression of the microwave evaporation frequencies while the beat-signal at ~ 900 MHz is still clearly visible. We therefore aim to lock the down-converted signal in a frequency range of 200 to 800 MHz.

not balanced and through working outside of the specified wavelength regime, we expect to get a microwave (MW) beat signal power of $P_{\text{MW, beat}} \leq -40$ dBm at a 50Ω load. To make use of this very high frequency signal it first needs to be down-converted to more moderate RF frequencies < 1 GHz. This is usually done by frequency mixers with the use of a local oscillator (LO) with tunable frequency ν_{LO} . By shifting ν_{LO} one can make sure that the down-converted frequency $\nu_{\text{RF}} = \nu_{\text{MW, beat}} - \nu_{\text{LO}}$ stays in the RF frequency range for further processing.

Mixer and MW sources spanning the whole optically detectable beat range of 0 to 30 GHz are not available within a reasonable budget, so by evaluating early superlattice phase measurements, we decided on a fixed detection range of 20 to 30 GHz for which the signal processing would be optimised. This was achieved by a combination of evaluation boards for the HMC733 and HMC264 chips produced by Analog Devices, Inc. The HMC733 is a voltage controlled oscillator (VCO) with a buffer amplifier providing a tunable frequency ν_{VCO} in the range of 10 to 21 GHz with relatively constant output power of ~ 3 dBm [144]. This signal is then sent to the active sub-harmonically pumped mixer HMC264, where it is amplified, frequency-doubled and mixed with the photo diode signal [145]. Since this mixer only operates at $\nu_{\text{LO}} = 2 \times \nu_{\text{VCO}} = 20$ to 30 GHz, the VCO only needs to operate within $\nu_{\text{VCO}} = 10$ to 15 GHz achieved with control voltages U_{VCO} between 0 to 10 V. The output of the VCO additionally needs to be attenuated by 5 dB to not oversaturate the pre-amplifier in the mixer. This is shown in figure 6.2 a) including the following filter and amplification stages.

At the mixer output and by choosing the right VCO frequency we detect the down-converted beat signal with about ~ -55 dBm at 400 MHz. With a nominal conversion loss of -9 dB and including additional losses at the various connectors this agrees with our estimated photo diode output power. To filter out the high frequency signals of the LO ν_{LO} and the VCO ν_{VCO} after the mixer, a low-pass filter with a cut-off frequency of 780 MHz is added. The filter used, VLFX-780+ from Mini-Circuits, is specified to more than 20 GHz, effectively suppressing all MW signals still present.

The remaining down-converted signal then gets amplified by around 24 dB with a low noise amplifier PHA-13LN. In tests we observed for particular VCO frequencies some sort of resonance behaviour where a large amount of low frequency noise was introduced, which led to the suppression of the desired signal, see figure 6.2 b). By adding a high-pass filter SHP-250 with a cut-off frequency of 250 MHz before the amplification we could eliminate this behaviour and use the whole VCO frequency range without loss of signal.

Since the signal strength is still just about 1 mW (-30 dBm) we amplify it further by more than 40 dB with a single ZKL-1R5+ amplifier. This high-gain module works up to 1.5 GHz and can pick up the 1.2 to 1.278 GHz microwave signal used for the forced evaporation in the magnetic trap, discussed in section 4.1.2. We remove it with an additional SLP-850 low-pass filter directly in front of the amplifier as can be seen in figure 6.2 c).

With this setup we are able to detect a beat signal of the two lasers with frequency difference $\nu_{\text{MW, beat}} = 20$ to 30 GHz and through down-conversion, filtering and amplification obtain a signal within the frequency range of 200 to 800 MHz with more than 10 dBm RF-power.

6.1.3 Regulation and characterisation of the lock performance

To stabilise the relative frequencies of these lasers we use a frequency offset lock technique [146]. In this method one mixes a part of the laser beat signal, that has a frequency dependent phase shift added, with parts of the unmodified signal. This results in a DC voltage that can act as an error signal, with its zero-crossings used as lock-points with a fixed frequency difference. Even

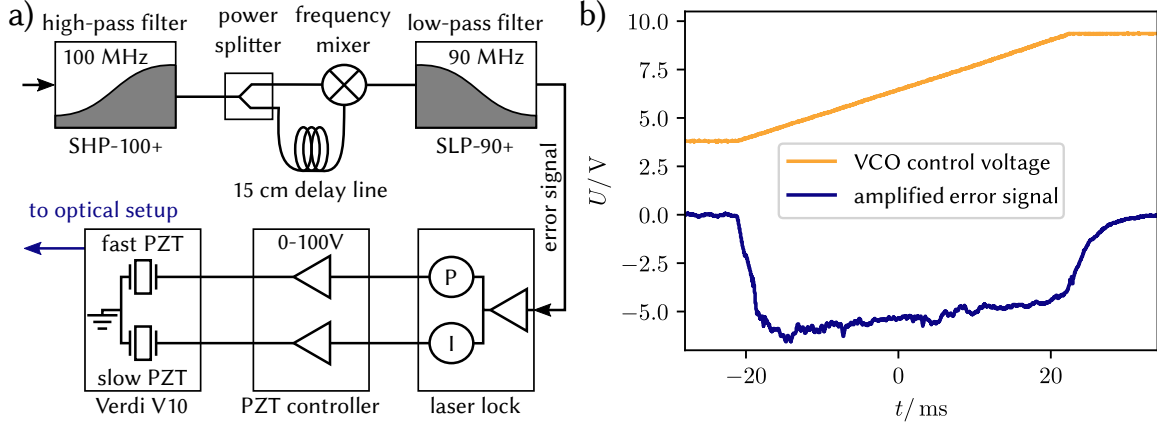


Figure 6.3: Closed feedback loop of the frequency lock. a) By splitting the down-converted beat signal and delaying one of its paths before recombining it, one creates an error signal which we use for the laser lock [146]. The proportional (P) and integral (I) regulation signal are fed back to the Verdi V10, closing the feedback loop. b) By adjusting the VCO frequency through the VCO control voltage U_{VCO} (in orange) we can ramp the frequency difference of both locked lasers $\delta\nu_{\text{green}}$. With the conversion factor $\delta\nu_{\text{green}}/U_{\text{VCO}} \approx 1 \text{ GHz/V}$ this corresponds to a frequency change of 5.5 GHz in 40 ms. The error signal in blue shows no sudden changes or drops in amplitude, which would indicate mode or frequency jumps.

after locking to one of the zero crossings of the error signal, we can tune the absolute frequency difference by tuning the MW VCO frequency which is subtracted from the original signal in the down-conversion process.

The setup we use is shown in figure 6.3 a). After an initial SHP-100+ high-pass filter to remove remaining low frequency noise introduced by the amplification and RF pick-up the signal is divided into two equal parts by a power splitter. The ZFSC-2-1-S+ is specified for a range of 5 to 500 MHz [147], however, in tests also operated above these values. One part is then sent through a delay line consisting of an RF cable, which introduces a time delay τ relative to the original signal. Under the approximation that the signal propagation speed is independent of the frequency of the signal, τ is constant. The phase delay ϕ_{delay} , by contrast, is frequency dependent

$$\phi_{\text{delay}} = 2\pi\nu_{\text{RF}}\tau. \quad (6.1)$$

By combing both signals in a frequency mixer, we get a (low frequency) DC interference term whose power is dependent on their phase difference $\Delta\phi = \phi_{\text{delay}} - \phi_0$, where ϕ_0 is the phase of the signal that is not sent through the delay line. This signal is oscillating in frequency space, therefore close to a zero crossing we are able to use it as an error signal for a locking feedback loop with an approximately linear frequency response.

By adjusting the length of the delay line one can modify the periodicity and also control the frequency range where the error signal can be used as a feedback. Long delay lines would give very tight locks with large slopes at the zero crossings of the error signal. However, since the relevant frequency scale for the superlattice phase is in the order of several hundreds of megahertz, we are more concerned with a large capture range of the lock, allowing for high ramp speeds during frequency changes and an overall better stability. We achieve this with a delay line length of

only 15 cm, giving an error signal zero crossing at $\nu_{\text{RF}} \approx 380$ MHz, with a capture range of about ± 200 MHz. To filter any remaining high-frequency components a further SLP-90+ low-pass is added.

The error signal is then fed into a laser lock that amplifies it and has a separate integrated (I) and a proportional (P) regulation signal output with variable gain. These can be used to adjust the frequencies of the lasers we want to stabilise onto each other. Since the Coherent Mephisto laser is very frequency stable with little noise, we decide on regulating only the frequency of the Verdi V10. This is possible through two piezos built into the lasing cavity. One is used for large frequency changes, with which we achieved a mode hop free tuning range of up to 7 GHz through careful adjustments of the laser parameters. With a piezo-capacitance of ~ 450 nF it is rather slow. For fast feedback the other piezo with a capacitance of only 25 nF and a nominal 20 kHz bandwidth is used. We are, however, limited by the bandwidth of the piezo controllers we use to amplify the regulation signals to the required range of 0 to 100 V. We use the I-feedback signal with the slow piezo for large frequency changes and the P-feedback signal for fast changes and noise reduction.

By adjusting the feedback amplitude and bandwidth we lock the down-converted RF frequency $\nu_{\text{RF}} = \delta\nu_{\text{green}} - \nu_{\text{VCO}}$ to the zero-crossing of the error signal at about 380 MHz. By changing the VCO frequency ν_{VCO} , the relative frequency of both lasers $\delta\nu_{\text{green}}$ can be tuned. This is done with a control voltage U_{VCO} , that for the voltage range 0 to 10 V changes the frequency output approximately linear from 10 to 15 GHz. The computer controlled analogue set voltage is discretised in time in 100 μs -steps. For fast changes these control voltage steps lead to jumps in the VCO frequency which could result in a loss of laser frequency lock. To avoid this, we built an active low-pass filter which includes an amplification by a factor of two to match the voltage range. This third order low-pass has a cut-off frequency of ~ 5 kHz and smooths the temporal response to the expected 100 μs voltage changes efficiently. It has the additional advantage that we are able to perform clean sweeps of the superlattice phase ϕ_{SL} to perform smooth adiabatic Landau-Zener transfers, as we will show in the following sections.

There is a mechanical resonance of the lasing cavity at around ~ 400 Hz that leads to frequency jitter of the 532 nm light with about 5 MHz peak-to-peak amplitude. We can reduce it with the fast feedback in the lock, however, we realised this comes at the cost of stability for fast and large frequency changes. The lock was optimised for these ramps, one of which can be seen in figure 6.3 b), where the lasers followed the change in VCO frequency of about 5.5 GHz in 35 ms, translating to a possible ramp speed of ~ 157 MHz/ms. For further tuning of not only the relative, but the absolute frequencies of both lasers we can tune the Mephisto master laser via the crystal temperature over a range of more than 30 GHz and adjust the Verdi, such that locking over the whole VCO controlled range is possible.

6.2 Characterisation of the superlattice

With the control gained over the frequency difference $\delta\nu_{\text{green}}$ of both z -lattice lasers, we can now create a superlattice with tunable phase ϕ_{SL} . Due to the construction of the z -lattices it is not directly possible to calculate the correlation between both of these quantities, i.e. $\phi_{\text{SL}}(\delta\nu_{\text{green}})$, instead this has to be determined experimentally. This is in contrast to retro-reflected superlattices sharing the same beam path, where the distance to the retro-reflecting mirror in combination with $\delta\nu_{\text{green}}$ fixes the superlattice phase [80].

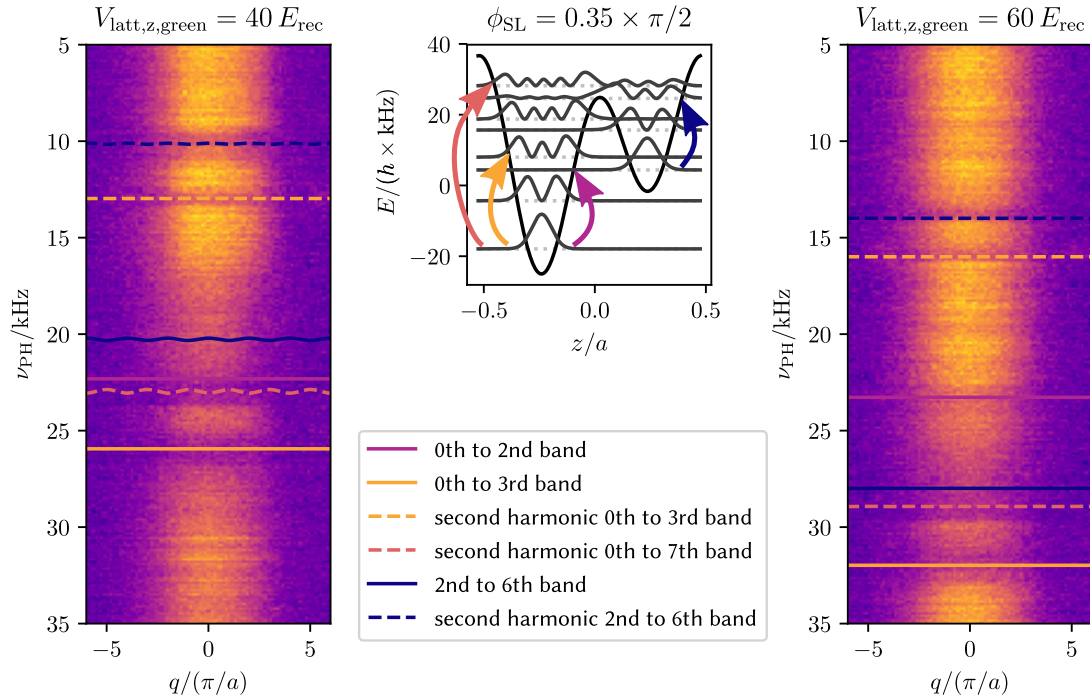


Figure 6.4: Parametric heating of the z -superlattice. By modulating the light intensity of both z -lattice lasers, atoms can transition to higher bands and then leave the trap. Both band-mapped results left and right are at $V_{\text{latt},z,\text{green}} = 100 E_{\text{rec}}$, but differ in green z -lattice depth. By comparing the loss features with numerical simulations, shown in the centre, the superlattice phase ϕ_{SL} is determined. Since at the start the green z -lattice is completely filled, atoms initially are not only in the lowest, zeroth band, but in this case also partially occupy the second excited band. This is important since it also modifies the possible transitions due to overlap and symmetry constraints. While in a monochrome lattice the zeroth to second band are strongly coupled, see figure 4.7, this transition is suppressed in this superlattice configuration, while the transition to the third band is prominent.

Here I will discuss several methods that we used to characterise the superlattice phase. These methods were created and used in that chronological order, always improving on the last one in specific tasks or with a higher final resolution, zooming in on the symmetry point at $\phi_{\text{SL}} = 0$. Additionally we will use some of these methods to determine the inter-layer tunnelling t_{\perp} and the on-site interaction U and compare it to numerical simulations.

6.2.1 Parametric heating of the bi-chromatic lattice

One calibration tool for monochromatic lattices is the parametric heating, where we extract the energy band separation by periodic modulation of the lattice strength, as described in section 4.2.1. These energy differences are then compared with numerical lattice simulations to extract the conversion factor of optical power to lattice depth.

Modulating the superlattice in a similar fashion gives again insights into the band structure. Especially when we first calibrate the lattice depths of both z -lattices individually and are then, with known lattice depths, able to extract the superlattice phase ϕ_{SL} as the only free parameter.

For this both lattice laser intensities are modulated with the same signal source, leading to a periodic change of the whole superlattice potential. By varying the modulation frequency ν_{PH} , we can identify heating resonances that we compare with numerical simulations. As shown in figure 6.4, these resonances are visible over a large range of modulation frequencies, here for two configurations with the same superlattice phase ϕ_{SL} but with different lattice depths. The interpretation of these resonances is, however, not as straight forward as expected, as is illustrated in the centre plot of figure 6.4. For large lattice depths the Bloch waves of the lowest bands are localised on alternating lattice sites. This means that the wave functions of some bands do not overlap, and therefore no transfer can be achieved. In addition to this, the parametric heating requires the same spatial symmetry of both wave functions that are coupled, as discussed in section 4.2.1, making it hard to determine the correct band transition frequencies. Furthermore, for a given configuration initially all lattice sites in z -direction are potentially populated, leading to two sets of resonances, one which does not start from the lowest band in the system.

Apart from that, there are other constraints to this method. The parametric heating method ideally works with a spatially symmetric, periodic contraction and relaxation of the individual site potentials, leading to an overlap of only Bloch bands with the same spatial symmetry. Yet, depending on the superlattice phase ϕ_{SL} , an overall power modulation of the superlattice does not necessarily lead to a spatially symmetric potential modulation. Additionally the superlattice consists of two separate lasers and therefore their power has to be modulated simultaneously, ideally using the same modulation source. This modulation signal, however, has not the same modulation amplitude gain on both laser power controls. Both of these issues lead to a sometimes ambiguous phase determination. The technique also relies on the precise calibration of the individual lattice depths of the green 532 nm and red 1 064 nm laser. Any error in the initial calibration directly distorts the extracted ϕ_{SL} . Also, when working close the symmetry points of $\phi_{\text{SL}} = 0$ or $\pi/2$, small changes in the superlattice phase do not influence the band structure sufficiently for a fine calibration. Therefore we used this method for an initial rough calibration of $\phi_{\text{SL}}(\delta\nu_{\text{green}})$, but switched to more reliable techniques for further evaluation.

6.2.2 Band mapping in a merged vertical lattice

For a more precise phase calibration around the symmetry point $\phi_{\text{SL}} = 0$, we use a technique where we adiabatically merged the separated double-wells along the z -axis into a single site, i.e. reducing the superlattice to a mono-chromatic lattice. During the green z -lattice loading we only populate each second plane, as described previously. In the frozen xy -lattice, we slowly increase the power of the red 1 064 nm lattice forming double-wells along the z -axis. The atoms still cannot tunnel in this double-well, therefore they are in a localised state on one side of the double-well. By slowly reducing the lattice depth of the green 532 nm lattice, we map the state of the atoms in the initially separated wells to the energy states of the red 1 064 nm lattice only. One has to remember that the number of states/bands does not change during this adiabatic process, and therefore the n^{th} band in the superlattice maps to the n^{th} band in the red 1 064 nm lattice. For example if $\phi_{\text{SL}} \neq 0$ and the populated well is in the beginning lower in potential energy than the second one, it is in the lowest band of the double-well and after merging in the lowest band of the red 1 064 nm lattice as well. For the inverted configuration with the atoms in the energetically higher well, they would map to the first excited or an even higher band. The symmetric configuration $\phi_{\text{SL}} = 0$ has to be at the cross-over where both lowest bands are equally populated.

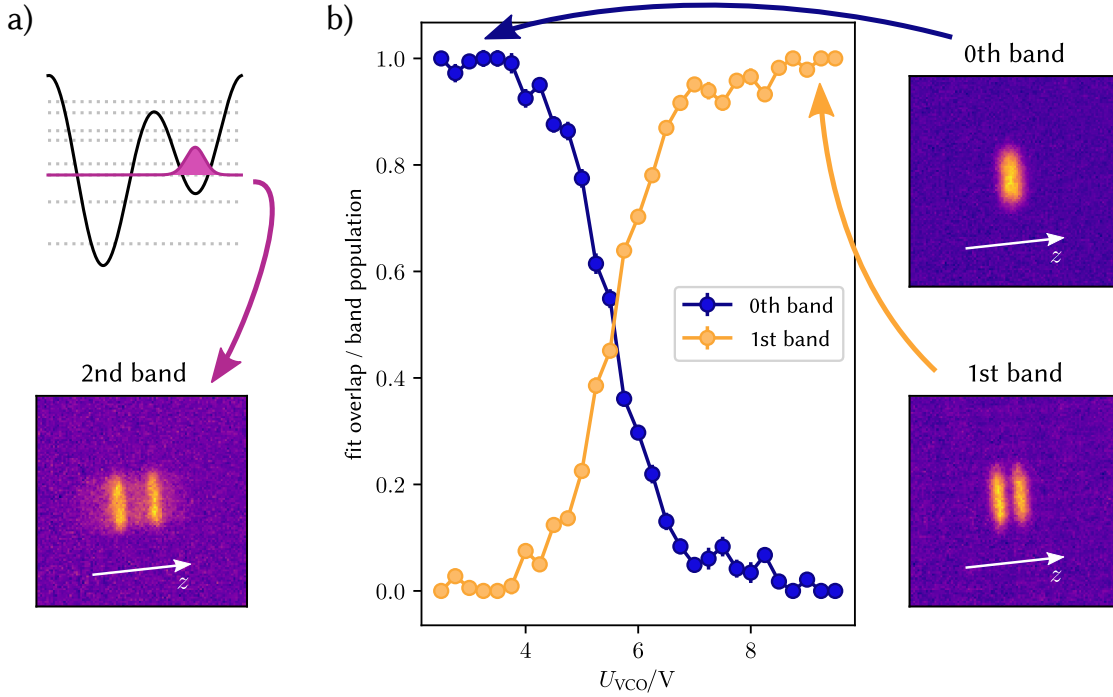


Figure 6.5: Band mapping of a merged superlattice. a) Initially only every second z -layer is populated, here depicted on the right well of a double-well potential. Depending on the superlattice configuration, especially the superlattice phase ϕ_{SL} , they, therefore, potentially occupy not the lowest, but a higher band. By removing the green z -lattice potential we transfer the atoms in the superlattice into a monochromatic lattice. If this process is adiabatic the band populations stays constant (here starting in the second excited band) and can be detected through a band mapping technique, explained in section 4.2.1. b) Close to the symmetric configuration, i.e. $\phi_{\text{SL}} \approx 0$, the atoms occupy either the lowest or the first excited band. By extracting the parameters from the clear limits of the superlattice phase scan range, indicated here with arrows, we can fit a Gaussian (double Gaussian) distribution to get the population of the zeroth (first) band. The crossing of their relative population indicates the symmetric superlattice configuration, where $\phi_{\text{SL}} = 0$.

We then extract the population of the bands via the band mapping technique described in section 4.2.1. The time-of-flight expansion happens here along the z -direction. For the detection we use an imaging path along the y -direction, described in [18, 19, 21, 22], where we have less magnification and spatial resolution compared to the normal z -imaging.

The timing for the lattice power ramps is more critical as well, since the force of gravity quickly distorts the shape of the expanding cloud in TOF. Some measurement results are displayed in figure 6.5, showing merged bands up to the second excited band. There the frequency difference was adjusted manually by tuning the Mephisto crystal temperature over a large range.

To find the exact symmetry point and without manipulating the crystal temperature, we use the superlattice frequency lock described in the beginning of the chapter. We aim to adjust the superlattice phase, such that after merging the atoms are in between the lowest (zeroth) and the first excited band, indicating the symmetric configuration $\phi_{\text{SL}} = 0$. Varying the VCO control voltage U_{VCO} allows us to tune the frequency difference $\delta\nu_{\text{green}}$ over several gigahertz without mode jumps. To extract the populations of the zeroth and the first band in the crossover region, we first integrate

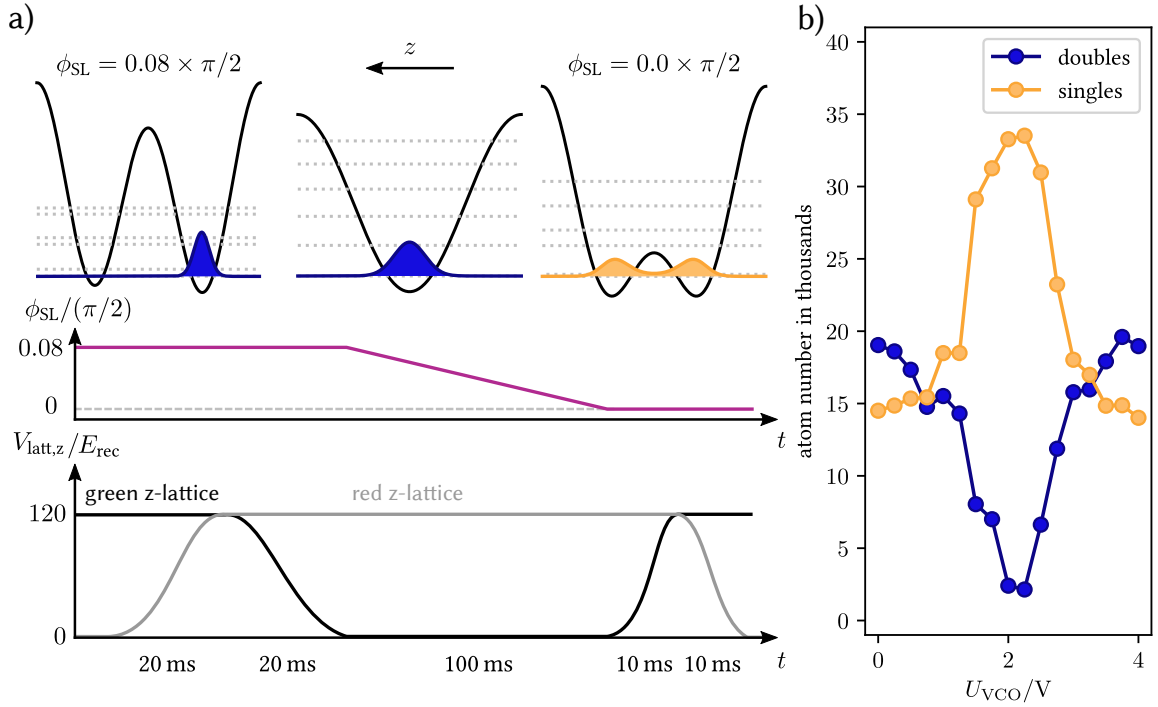


Figure 6.6: Splitting the population of a double-well. a) We merge the superlattice into the red z -lattice with a small phase imbalance, to prepare all atoms in the lowest band. Once the green z -lattice is turned off, the Verdi laser frequency is shifted in 100 ms with the superlattice lock to a different VCO frequency. Depending on the superlattice phase established, the atoms distribute over both lattice sites when the green z -lattice is ramped up again. b) Working with attractive interactions, most atoms will initially form doubles and remain so depending on the potential difference during the second ramp up. For $\phi_{\text{SL}} = 0$, however, these doubles split up into a spin singlet, with one atom in each lattice site. Therefore, we detect this symmetry point by the peak in single occupancies, even for a global atom cloud.

the measured atomic densities along the axis perpendicular to z . Far away from the crossover point, the zeroth band can be approximated by a Gaussian peak due to the limitations of the imaging and the band mapping along gravity. Similarly, the first band consists of a dual Gaussian peak. We extract the curve parameters from a fit to density distributions in both limits, where we can be sure to have only population in either band. We can then use their shape to fit the relative population in the crossover region of both bands as well. There, only the amplitude of the dual Gaussian peak and the single Gaussian peak are free fit parameters measuring the relative band population. The resulting hand-over is seen in figure 6.5 b). The smooth crossing is nicely visible and an exact symmetry point can be seen.

By inverting this method we cross-check the results without time of flight. We first merge the double-well at a superlattice phase where all the atoms are populating the lowest band of the now red 1064 nm z -lattice. Since we work at attractive interactions at about $U/t = -1.8$ before freezing the xy -lattice, most of the sites are occupied with doubles. With the green z -lattice turned off, we now shift the VCO frequency and with it the laser frequency difference $\delta\nu_{\text{green}}$. Slowly increasing the laser power again effectively splits the single-well into a double-well, the direct inverse process of the previous merging. Figure 6.6 a) sketches the sequence used. Since this process is adiabatic

as well and tunnelling in xy -direction still suppressed, we can describe it as a preparation of the ground state in a tilted double-well. Close to the symmetric double-well configuration, where the potential imbalance is $\Delta = 0$, the two-particle ground state transits to form mostly singles in both sites, as shown in figure 2.5. We observe this by scanning the laser frequency difference $\delta\nu_{\text{green}}$, which is shown in figure 6.6 b). The effective reduction of double occupancies in the global cloud by simultaneous increase of singles is a clear signal for the symmetry point and perfectly agrees with the merging measurements. We are, therefore, able to very quickly determine the symmetry point without single plane slicing in less than 15 measurements.

This optimisation required the shift of the absolute Verdi frequency by several tens of gigahertz in total. Therefore, the frequency of the small Mephisto, which creates a superlattice with $\phi_{\text{SL}} \approx \pi/2$ used for the second plane evaporation described in section 4.2.2, has to be shifted as well. Hence, we re-optimised the small Mephisto's frequency and with it the second plane evaporation. To do so, we ramped down the small Mephisto's power during the green z -lattice loading to such a low level that we barely kept some atoms during this evaporation step. Varying the Mephisto frequency we observed a clear maximum in retained atoms during this evaporation step. Since the lattice potential at the sites holding the atoms is deepest at the asymmetric superlattice configuration, we know this maximum indicates the frequency difference $\delta\nu_{\text{green,small}}$ for which $\phi_{\text{SL}}(\delta\nu_{\text{green,small}}) \approx \pi/2$. The observed frequency difference between both Mephisto lasers is $\Delta\nu_{\text{red}} = \nu_{\text{red,small}} - \nu_{\text{red,big}} \approx 28.2$ GHz. The frequency change of a green laser required to go from the $\phi_{\text{SL}} = \pi/2$ configuration to $\phi_{\text{SL}} = 0$ would, therefore, be twice of it, matching the previously stated estimation of ~ 60 GHz.

6.2.3 Second plane removal and phase sweeps

With the method introduced in the previous section, shown in figure 6.6, we are able to create a first kind of bilayer consisting of disconnected double-wells. The measurement in figure 6.6 b) however does not yield any information on the sign of a chemical potential difference between both sides of the double-wells, since we do not observe the population of each site separately. We want to change this by selectively removing the atoms in one of the bilayer planes, which in turn gives us information about the remaining layer population without single-plane slicing. In further steps the removal of each second plane could additionally allow local density measurements with slicing of a single plane with a large frequency separation of ~ 1.280 kHz.

For this we use a similar scheme as for the selective z -lattice loading shown in figure 4.8, where we initially populate only every second z -plane. In contrast to that, after the splitting process, the atoms are in a deep xy -lattice and cannot redistribute. This is necessary to prevent information loss, for example on the double occupancies relative to singles. So after the preparation of a bilayer and the freezing of all motion by increasing the lattice depths we use the small Mephisto laser to again create a superlattice with phase $\phi_{\text{SL}} \approx \pi/2$, lowering the potential at each second z -plane. When ramping down the green z -lattice power, the atoms on the planes not affected by the red z -lattice of the small Mephisto are projected onto higher bands, where tunnelling is not completely suppressed.

It is, however, not sufficient to now turn off the green z -lattice power alone, due to the additional confinement created by the xy -lattices, preventing the atoms from leaving the lattice system. With the fast Feshbach coils we create a strong magnetic field gradient in z -direction, which is used to increase the force pulling the atoms along gravity out of the trapping area. To support this process further, we reduce the frozen xy -lattice depth to $V_{x,y} = 30 E_{\text{rec}}$. At this lattice depth, the in-plane tunnelling rate is only $t/h = 2.0$ Hz, leading to an average tunnelling timescale of 500 ms. By

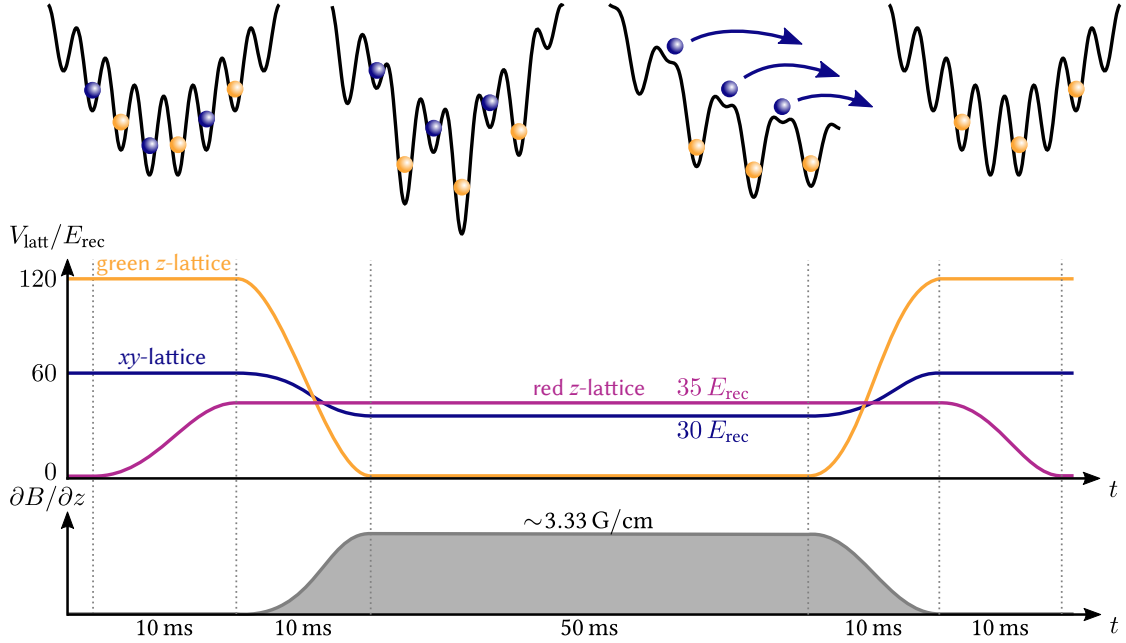


Figure 6.7: Second plane removal in frozen lattice. After a handover from a purely green z -lattice to a superlattice in asymmetric configuration with $\phi_{\text{SL}} = \pi/2$, every second plane has a significantly lower potential. During this and the following steps, tunnelling in xy -direction is completely suppressed. Switching of the green z -lattice power projects the atoms of every second plane, here marked as blue spheres, into high bands in the lattice structure, allowing movement along the z -axis. They, however, cannot leave the trap due to the confining potential created by the xy -lattices. By reducing the xy -lattice power to $30 E_{\text{rec}}$ for 50 ms and additionally applying a magnetic field gradient with the fast Feshbach coils in anti-Helmholtz configuration, these atoms are pulled out of the trap. While these atoms are lost, the rest is retained with an efficiency of more than 95 %.

choosing the time span of the second plane removal step sufficiently low at 50 ms we still assume the atoms are motionally frozen in place. The full removal sequence is shown in figure 6.7. Finally, the infrared z -lattice depth is chosen such that it manages to retain the atoms just from the desired plane, while not also trapping atoms from the plane we want to remove. To adjust this, we choose two VCO control voltages U_{VCO} at both sides of the symmetry phase point and observe the number of doubles and singles retained as a function of the lattice power, finding a suitable value of $V_{z,\text{red}} = 35 E_{\text{rec}}$. Since the superlattice used to initially load every second plane of the z -lattice and the superlattice configuration in the second plane removal have the same phase $\phi_{\text{SL}} \approx \pi/2$, the atoms kept during this removal step are the ones which were in the planes we initially populated.

Double-well preparation through phase sweeps With this technique we are able to follow a method to deterministically populate a single double-well, initially presented in [119] and discussed in detail in [41, 148]. There, they started with a double occupancy on the site with lower potential in a very tilted double-well. Initially the inter-site tunnelling between the sites was low, so this state had near perfect overlap with the ground state of this imbalanced system. By increasing the tunnelling and adiabatically changing the potential imbalance Δ of the double-well, they could

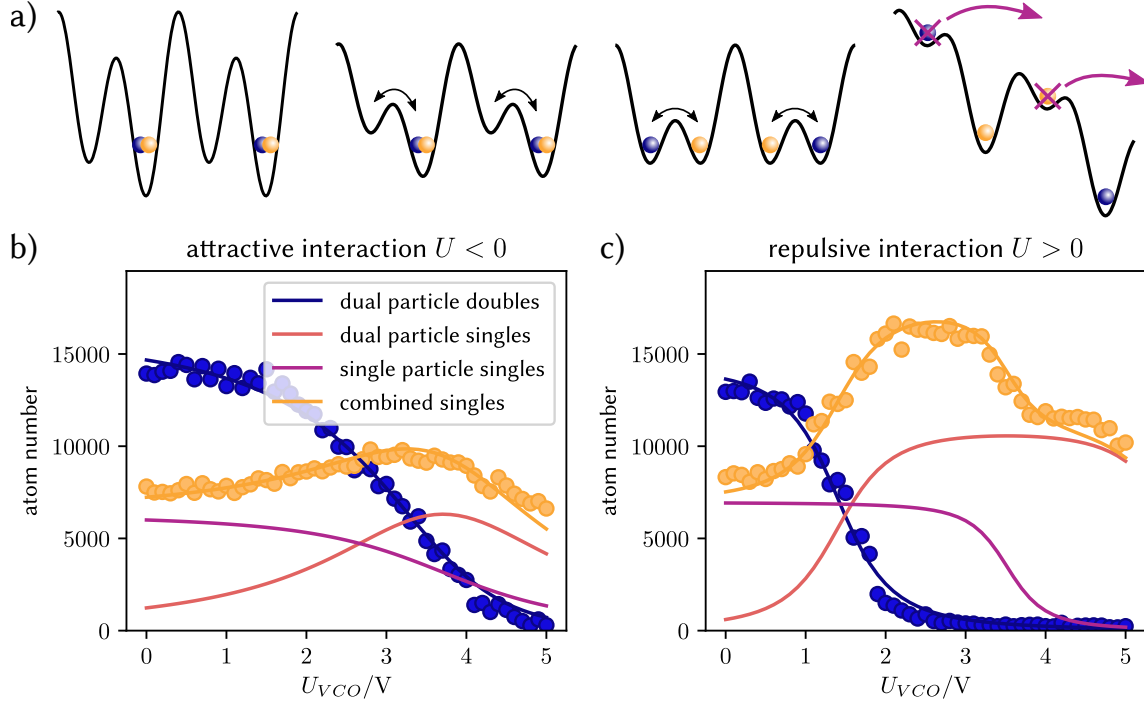


Figure 6.8: Double-well state preparation through a superlattice phase sweep. a) Starting with mostly doubly occupied sites in every second z -plane and a frozen xy -lattice, we hand over to a superlattice close to symmetric configuration with the planes populated by atoms lower in potential than their counterpart. Lowering the barrier in between the double-wells leads to increasing tunnelling and the creation of an array of tilted double-wells with most atoms in the energetic ground state. By adiabatically sweeping the superlattice phase via the lock frequency the atoms stay in the ground state. By freezing and removing every second plane, we measure the ground state occupation probability at the one side of the double-well. b) and c) show the result in singles (doubles) in orange (blue) for such a sweep with varying superlattice phase, which can be translated to a potential imbalance Δ . While b) shows the measurement for attractive interactions at a (simulated) high tunnelling rate of $t_{\perp}/h = 846.3$ Hz, the data in c) was taken with repulsive on-site interaction and a very slow tunnelling rate of $t_{\perp}/h = 115$ Hz. A fit is performed with the two-particle and single particle solution to a tilted double-well with varying Δ , as discussed in section 2.3. Since the energy scale relevant for the physics is Δ/t_{\perp} , the choice of tunnelling amplitude directly influences the scaling of superlattice phase or lock frequency to potential imbalance Δ/t_{\perp} . Close to the symmetry point $\Delta = \phi_{SL} = 0$, here at $U_{VCO} = 3.6(1)$ V, the doubles prominently split up into singles on each site, visible here in the fit contribution shown as red line.

deterministically prepare the ground state of the balanced double-well, where $\Delta = 0$. They then remove the atoms of one well site for detection.

We follow this idea by preparing not a single double-well, but several planes consisting of individual double-wells, where the superlattice phase ϕ_{SL} determines the double-well potential tilt Δ . Figure 6.8 a) sketches the sequence discussed in the following. Initially the lattices are loaded on every second z -plane with attractive interactions and most, but not all atoms form doubles. Increasing the power of the infrared z -lattice one creates the superlattice, consisting of disconnected, tilted double-wells. After decreasing the green z -lattice depth, the barrier between both sites is lowered and tunnelling not prohibited anymore. By adiabatically sweeping the superlattice phase ϕ_{SL} , the atoms are prepared in the ground state of the tilted double-well, with a potential imbalance Δ determined by the final phase reached. After removing every second plane only the atoms in the initially populated sites remain. Since the individual double-wells are not connected, we assume that they are independent and image the whole atom cloud without single-plane resolution, but with singles-doubles separation. By doing so we effectively measure the projection of the ground state Ψ with a single or a double on the site we start with, i.e. either $|\langle \uparrow_{\text{right}} | \Psi \rangle|^2$ or $|\langle \uparrow_{\text{right}} \downarrow_{\text{right}} | \Psi \rangle|^2$. The denomination of left and right can be chosen at free will, in the following I will denote the right site as the one we start from. Here we have to consider that there is a significant part of double-wells with only one atom to start with, so we have to account for the single particle ground state as well as the ground state of two particles with opposing spin.

Figure 6.8 b) shows the measurement results for varying VCO control voltage U_{VCO} . One can clearly observe the gradual transfer of doubles population to the double-well site that gets removed, and which is, therefore, not observed in the measurement. Close to the symmetry point some doubles break up into two singles on each site, seen as a small increase in singles. This shape is mostly defined by the barrier height between both sites, generated with the green z -lattice and determining the horizontal tunnelling rate t_{\perp} and the on site interaction U . It is important to note that both free parameters in the analytical solution of the double-well scale with the tunnelling, Δ/t_{\perp} and U/t_{\perp} . Therefore, any change in t_{\perp} mostly changes the scaling of the x -axis in these plots. This measurement was done at 207.15 G in a $|7\rangle|9\rangle$ mixture, and therefore with attractive interactions. By switching to a $|5\rangle|9\rangle$ mixture via another Landau-Zehner RF sweep we can investigate the behaviour with repulsive interactions as well, as shown in Figure 6.8 c). The tunnelling rate t_{\perp} was numerically calculated for the different barrier heights in each plot. The solid lines in both figures show a combined fit to the solutions of the single-particle and the dual-particle with opposing spin calculations. It determines again the symmetry point where $\phi_{\text{SL}} = 0$, showing no difference to the other two methods already presented. In theory we could extract the interaction strength U or the scaling of U_{VCO} to potential imbalance Δ from this fit by fixing one of the two, but not both at the same time since they are directly scaling with each other. The next two subsections will show how to independently calibrate both and additionally t_{\perp} using different methods.

6.2.4 Induced inter-layer Rabi-oscillations

The three methods introduced before are all capable of determining at which VCO control voltage U_{VCO} the superlattice is in the symmetric configuration $\phi_{\text{SL}} = 0$, meaning where both layers of the bilayer have the same potential $\Delta = 0$. For other parameters like the tunnelling amplitude and the potential imbalance $\Delta(U_{\text{VCO}})$ for $\phi_{\text{SL}} \neq 0$, we relied on numerical calculations. Being able to detect the atom number population of only one side of the double-well, enables another method to

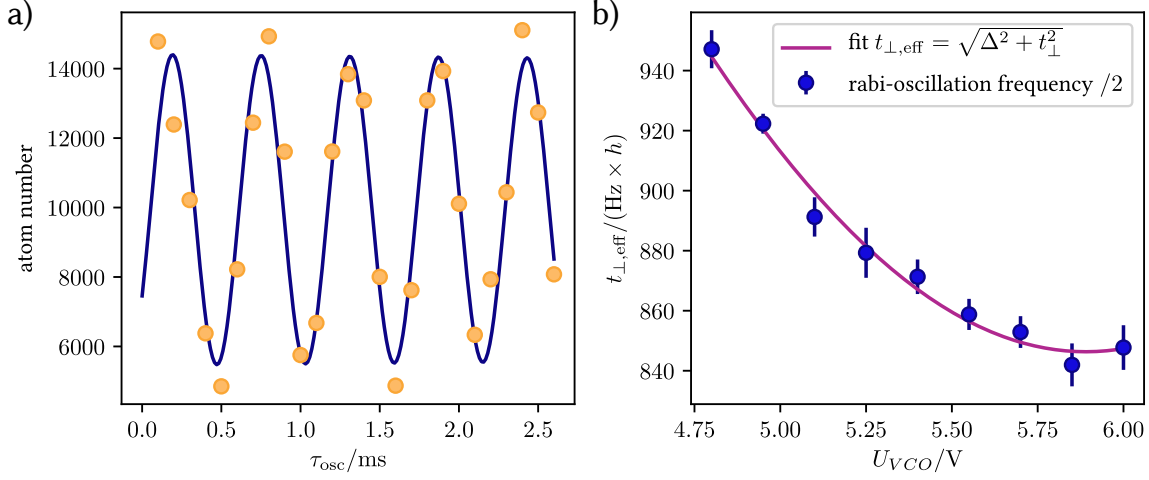


Figure 6.9: Induced Rabi-oscillations to extract t_{\perp} . a) Close to the symmetric configuration, Rabi-oscillations are induced between both lattice sites. After removing the second plane the atom number is detected, here shown as orange points. The oscillation frequency $\nu_{\text{rabi}} = 1.787(15)$ kHz is extracted through a sinusoidal fit. b) As explained in section 2.3 this frequency can be connected to the effective tunnelling amplitude $t_{\perp, \text{eff}}(\Delta) = (\Delta^2 + t_{\perp}^2)^{1/2} = \nu_{\text{rabi}}/2 \times \hbar$, with Δ the potential imbalance between the double-well sites/superlattice layers. By measuring $t_{\perp, \text{eff}}$ and varying the superlattice lock frequency with the VCO, we extract the tunnelling rate t_{\perp} , the VCO voltage U_{VCO} where we obtain the symmetric superlattice phase $\phi_{\text{SL}}(U_{\text{VCO}}) = 0$ and the scaling conversion from VCO voltage to potential imbalance, which in this case is $\Delta/U_{\text{VCO}} = 385(28)$ Hz/V $\times \hbar$. This scaling factor is strongly dependent on the exact z -lattice depths used to create the superlattice.

calibrate both the tunnelling amplitude t and $\Delta(U_{\text{VCO}})$ [41, 119, 148].

Similar to the phase sweep measurement discussed in the previous section, we start again by loading only every second plane, this time, however, with a spin polarised cloud where all atoms are in the $|9\rangle$ state and then freeze out all motion by quickly ramping up the lattice powers. A superlattice with ϕ_{SL} close to the symmetry point is created by increasing the infrared z -lattice, while still suppressing the tunnelling all directions. We then rapidly ramp down the green z -lattice depth from $V_{z, \text{green}} = 110 E_{\text{rec}}$ to a $V_{z, \text{green}}$ between 28 to 13 E_{rec} , where tunnelling is possible again. There the system can be described similar to the coupled state Hamiltonian in equation 3.4 and 2.30, using the dressed states $|\pm\rangle = (|L\rangle \pm |R\rangle)/\sqrt{2}$, where $|L\rangle(|R\rangle)$ is the state with one particle in the left(right) site. These states are separated in energy by the effective tunnelling amplitude $t_{\text{eff}} = (t^2 + \Delta^2)^{1/2}$, see equation 2.31. By ramping down the barrier separating both sites of the double-well in less than 200 μs , the initial state gets projected into the new basis with $|\psi(\tau = 0)\rangle = |R\rangle = (|+\rangle - |-\rangle)/\sqrt{2}$. Since both dressed states are separated in energy by t_{eff} the probability of finding an atom at the right site after the time τ passed is oscillating as well:

$$p_{\text{right}}(\tau) = |\langle R|\psi(\tau)\rangle|^2 = \cos^2(t_{\text{eff}} \times \tau/\hbar). \quad (6.2)$$

In the experiment we measure this by freezing the atomic motion after a time τ_{osc} and then again selectively removing each second plane. By varying τ_{osc} we can extract the effective tunnelling amplitude t_{eff} for different superlattice configurations using the VCO control voltages U_{VCO} and

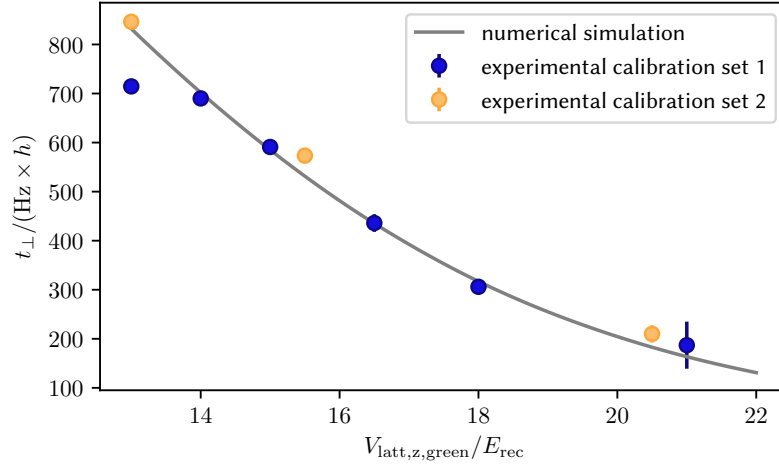


Figure 6.10: Inter-layer tunnelling amplitude t_{\perp} as a function of green lattice depth. Two data sets are shown to check the universality of this calibration and are compared to numerical simulations in a double-well potential. Both sets were taken several days apart but agree well with the numerical simulations. The error bars represent statistical errors and do not include systematic errors, which are assumed to be more prominent at the limits of the calibration range.

adjusting the z -lattice depths, both in green and infrared. In figure 6.9 a) such an oscillation on the detected atom number is depicted, including a damped sinusoidal fit to the data, showing a rather high oscillation frequency of 1.461(22) kHz. For stronger potentials, i.e. higher lattice depths of the green and red z -lattice, the lattice potentials can differ significantly across the xy -space of the atom cloud. This leads to locally varying double-well parameters, with varying barrier heights, wave function overlap, and therefore different tunnelling frequencies. Thus we choose to only evaluate the Rabi-oscillations at the centre of the cloud, where we aim to perform the bilayer experiments. Nevertheless, one has to keep this inhomogeneity in mind, which limits the range where we can use this calibration method to low and intermediate lattice depths.

From a single fitted frequency we cannot yet extract the true tunnelling amplitude, since it reflects an effective tunnelling rate and the potential imbalance Δ is still unknown. By evaluating the oscillations for different superlattice phases with a changing VCO control voltage U_{VCO} , as plotted in figure 6.9 b), we are able to fit the effective tunnelling amplitude $\nu_{\text{eff}} = t_{\text{eff}}/h$ to the data, extracting both t and $\Delta(U_{\text{VCO}})$ for a single configuration of lattice depths. These measurements are, however, very sensitive to the mode stability of the superlattice, in particular the frequency mode of the Verdi which we tune via the laser lock. Additionally, the amplitude of the oscillations is greatly reduced further away from the symmetry phase of the superlattice, so the range where this method works is limited in our experiment. Consequently the fitted parabola width is not as accurate and $\Delta(U_{\text{VCO}})$ can only be determined with some systematic error. At the same time the minimum in oscillation frequency can be extracted well, resulting in a good calibration of t_{\perp} for all superlattice parameters used in further experiments.

As can be seen in figure 6.10, these values agree within $\sim 5\%$ of the numerically calculated values determined by the overlap of the localised wave functions, which will be the estimate on the systematic error of this calibration.

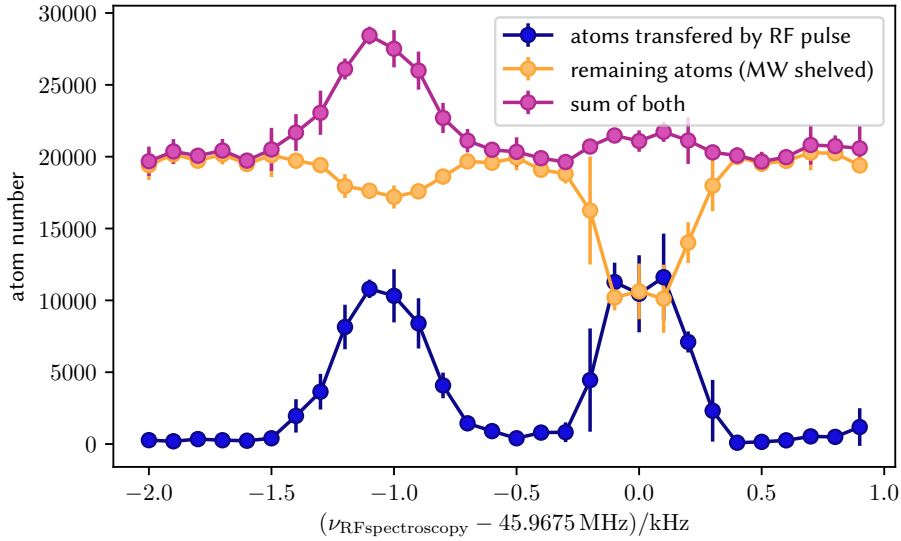


Figure 6.11: On-site interaction U calibration by RF-spectroscopy. In a frozen lattice with $V_{\text{latt},xy} = 60 E_{\text{rec}}$, the atoms are loaded into a superlattice with $\phi_{\text{SL}} \approx 0$ creating slightly tilted double-wells. Atoms transferred with a RF-pulse are then directly measured (blue circles) while the remaining ones (orange circles) are first MW shelved. Double occupancies that are shelved into higher hyperfine states are lost due to spin-changing collisions, allowing us to separate the resonances of doubles, left peak in the sum, with the singles, right peak. Even though tunnelling between the two sites of the double-well is allowed, leading to efficiency loss in the transfers, we can extract the energy difference of the doubles between initial and final interaction shift ΔU . This shift can be correlated with the known scattering length difference Δa , see figure 4.10, from which we can calculate the on-site interaction U of the initial and final state. The on-site interaction also depends on the xy -lattice depth, in this case with $V_{\text{latt},z,\text{red}} = 120 E_{\text{rec}}$ and $V_{\text{latt},z,\text{green}} = 20 E_{\text{rec}}$. For experiments with lower xy -lattice depth and xy -tunnelling enabled, this has to be scaled according to previously created lattice calculations [21, 22].

6.2.5 Interaction strength calibration

The on-site interaction strength U depends on the scattering length $a(B)$ and the spatial integral over the absolute value of the single-particle wave function to the power of four, see equation 3.45. The exact calculation of the interacting, localised wave function and with it the on-site interaction is, however, not trivial. For the monochromatic lattice there are good approximations that were previously used on this experiment to determine U [21, 22], yet they cannot be directly applied to the bilayer.

Here we introduce a method, where the singles-doubles spectroscopy resolving the interaction shift for doubles ΔU is used to determine the interaction U for a certain mixture of hyperfine states. If the z -lattice is orthogonal to the xy -plane, which we assume, the integral of the wave function can be separated into an in-plane part, multiplied with the inter-layer, i.e. double-well, component. Since we know from previous calculations how the in-plane wave function scales with changing xy -lattice depth [21, 22], it is sufficient to calibrate U for a fixed, large xy -lattice depth, where horizontal tunnelling is suppressed, and then subsequently rescale this result to the experimental xy -tunnelling amplitude required. We choose a certain set of z -lattice depths creating a superlattice

with a phase ϕ_{SL} close but not equal to zero. Similar to the initial preparation of the superlattice phase sweep measurement in section 6.2.3, we would like to start in the slightly tilted double-well, containing a still significant amount of double occupancies. There, enough atoms experience the on-site shift, resulting in a good signal, while the localised wave function in z -direction is very close to the one at the symmetric superlattice configuration. By doing RF spectroscopy in this setting, we resolve the difference in the interaction energies ΔU of the initial hyperfine state combination and the one we transfer the atoms to.

We know the Feshbach resonances for K^{40} , see figure 4.10, and with it the scattering length difference Δa between both state combinations. Since $\Delta U \propto \Delta a$, we are able to calculate the interaction strength U for the hyperfine states involved. Such a spectroscopic measurement is shown in figure 6.11, where the atoms were in a superlattice with $V_{\text{latt},z,\text{red}} = 120 E_{\text{rec}}$, $V_{\text{latt},z,\text{green}} = 20 E_{\text{rec}}$, but not allowed to move horizontally with $V_{\text{latt},xy} = 60 E_{\text{rec}}$. At 194.825 G the measured interaction strength difference of $\Delta U/h = 1.07 \text{ kHz}$ corresponds to an interaction strength of $U_{97}/h = 3.66 \text{ kHz}$. For a situation with tunnelling in the xy -plane, for example at $V_{\text{latt},xy} = 6 E_{\text{rec}}$ and an intra-layer tunnelling rate of $t/h = 224 \text{ Hz}$, this has to be scaled down to $U_{97} = 1.21 \text{ kHz} \times h = 5.39 t$ due to the lower confinement in the horizontal direction. Using this to calibrate our numerical simulations we calculate the interaction strength in the relevant parameter space of $V_{\text{latt},z,\text{green}} = 13$ to $28 E_{\text{rec}}$ for a fixed infrared lattice depth of $V_{\text{latt},z,\text{red}} = 120 E_{\text{rec}}$.

6.3 From band insulator to bilayer

Now with the z -superlattice fully under control, we are ready to create a bilayer Hubbard system, as discussed in section 2.5. Through the calibrations done in the previous section we can determine all system parameters of the bilayer Hubbard Hamiltonian of equation 2.39. To reach low temperatures in such a system, we aim to use an entropy cooling scheme [121], where we extract the entropy of a low potential region, filling it nearly exclusively with doubles. Having created such a low entropy two-dimensional band insulator, one can proceed to transform this into a system at half-filling, by adiabatically doubling the lattice site number.

It was proposed in 2011 to use a superlattice to create a low temperature, antiferromagnetic, two-dimensional Hubbard system [149]. It was suggested to freeze the in-plane lattice, then adiabatically transform the single sites into double-wells, effectively splitting the doubles into spin-singlets. In a next step, these singlets would then be connected by unfreezing the lattice again, ideally creating a very low temperature system with large antiferromagnetic ordering. One advantage of this method would be that by creating the singlets an initial magnetic order would have been established already in the first step, even though it was not fully detailed how the singlets would then coherently align with their neighbours. Perhaps and more significantly, no density reordering would be required. It was shown numerically that any particle movement in the lattice to accommodate for chemical potential changes effectively heats the system [98]. In a publication in 2018 it was reported that a state engineering scheme that started with a band insulator and simply doubled the available lattice site number by lowering a potential barrier showed significant heating during the redistribution ramp, increasing the entropy per particle by an order of magnitude [124].

In this work, we use an entropy and quantum state engineering scheme, which does not require density redistribution. Instead of transforming a two-dimensional band insulator to a two-dimensional antiferromagnetic Mott insulator, we separate the band insulator into two coupled

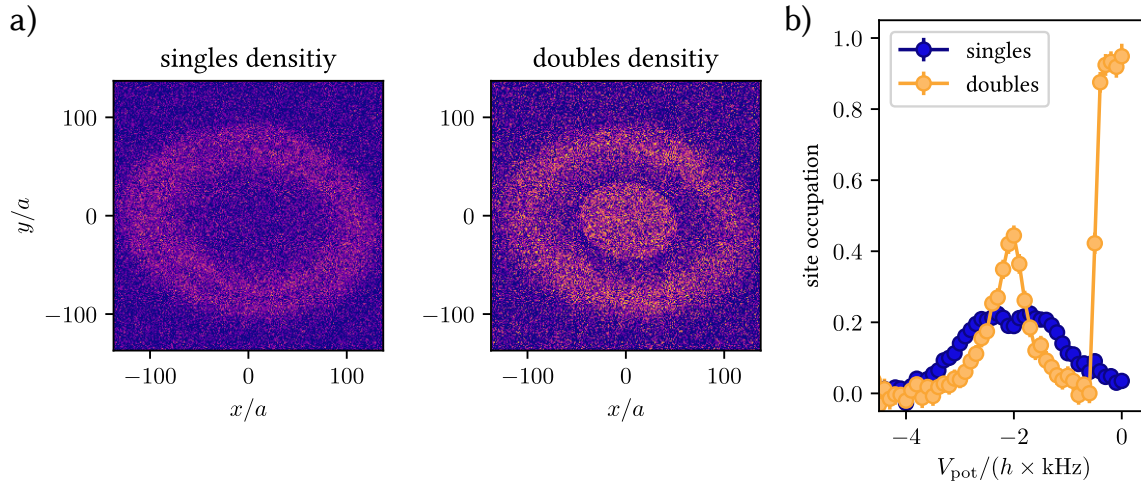


Figure 6.12: Loading a band insulator in a two-dimensional lattice. a) Ten picture average of the local singles and doubles density after loading into the xy -lattice. The SLM is used to modify the local chemical potential, creating a centre region, which is not affected by the SLM light, and an outer region with strongly increased potential with very low atom density. This low-density region acts as an entropy reservoir, to create a low-entropy central band-insulating region, well separated from the outside atoms. b) The averaged densities using the naive chemical potential mapping V_{pot} without the additional SLM potential. If the additional potential is based on the isopotentials of the original potential map, this presentation method still averages again over isopotential regions, even with the SLM potential included. Here visible are two maxima on the singles, indicating half filling, and the (over-)compensation region between $V_{\text{pot}} = 0.5$ to 2.0 kHz.

planes, creating a bilayer. In the following I will discuss the initial creation of the two-dimensional band insulator and two methods on how to melt it into a bilayer system close to half-filling.

6.3.1 Preparing a repulsive single-layer band insulator

As explained in section 4.4 one can create two distinct regions in the atom filled trap \mathcal{A} and \mathcal{B} , where \mathcal{B} stores more entropy per particle, allowing for a lower relative entropy region \mathcal{A} . To employ such a scheme a large difference in entropy per particle is desirable, see figure 4.15, with one choice for \mathcal{A} being a very low chemical potential centre, filled with doubles, with an outside region extracting entropy.

This is done using the spatial light modulator (SLM) and ~ 727 nm light, which is blue detuned for the atoms, locally increasing the chemical potential. We use a similar shape as shown in figure 4.15, which is constructed to compensate the harmonic trapping potential, creating a homogeneous potential ring in an outside region which will act as the entropy reservoir. In the centre region the lowest chemical potential is required, so no potential is added there, and the harmonic trap confinement is unchanged. This has the additional benefit that where the doubles density is highest, light assisted collisions are strongly suppressed due to the lack of blue detuned laser light. The potential shaping light is added during the xy -lattice loading step, to allow an easy density reordering while the atoms are still strongly delocalised and the tunnelling amplitude t is large. Through experimental optimisation we found out that it is best to increase the SLM laser power exponentially, with the xy -lattice beams being ramped in a sine squared shape. While initially assumed that

a flat outside potential, where the SLM light compensates the harmonic confinement would be ideal for entropy extraction, it turns out that by increasing the power to slightly over three times the compensation value we can improve the doubles fraction even more. This could be due to a compression effect in the central cloud at a time where the atoms are already localised. It has the beneficial effect that the potential at the boundary between the centre region and the reservoir on the outside is so large, that these regions are essentially disconnected. To increase the doubles fraction in the centre even further, this loading into a band insulator is done with attractive interactions at a magnetic field of 207.15 G in a $|7\rangle|9\rangle$ mixture. In our system and with $t/h = 224$ Hz this configuration leads to $U/t \approx -1.72$.

After the lattice loading, we hold for further 100 ms to ensure the density equilibrated in the SLM potential before we freeze the in-plane motion by setting the xy -lattice depth to $60 E_{\text{rec}}$. Figure 6.12 shows the density distribution in this frozen state, with 95 % of all sites occupied by doubles. Since we use the original local chemical potential map $V_{\text{pot}}(x, y) = V_{\text{pot}}(\mathbf{r})$ to create the compensation potential, it is very natural to evaluate these density distributions in the same way we did for the equation of state, see figure 4.14. This naively bins the densities in the equipotential regions the system would have without the compensation potential. It also allows for a determination of evaluation regions by the use of chemical potential differences in the unmodified potential. For example, we directly see that the core region was designed to go from the centre potential V_c up to a difference of $V(\mathbf{r}) - V_c = 0.5 \text{ kHz} \times h$. In the experiment, this corresponds to an elliptical area with an extend of about 100 and 80 lattice sites along the x and y -axis. The potential is over-compensated up to the harmonic potential of $V(\mathbf{r}) - V_c = 2 \text{ kHz} \times h$. Both these parameters were used in the experiments in this and the following chapter. At the edge of the centre region $V(\mathbf{r}) - V_c = 0.5 \text{ kHz} \times h$ the doubles and singles density is close to zero. This is useful once we allow horizontal tunnelling again by decreasing the xy -lattice depth, since we can separate both the core and the reservoir region through the use of very steep potential barriers.

Once the xy -lattice is frozen, the potential shaping light can be turned off. Similar to the double-well splitting and the double-well phase sweep calibration the atoms need to be transferred into the infrared z -lattice. This is again done by first ramping up the infrared z -lattice power to $V_{\text{latt},z,\text{red}} = 120 E_{\text{rec}}$ creating a superlattice in z -direction. The phase is chosen such that it is close to the symmetric configuration $\phi_{\text{SL}} \approx 0$, creating tilted double-wells along the z -axis, with all atoms in the planes with lower chemical potential. By ramping down the green z -lattice power both double-well sites merge into one, with all atoms in the lowest energy state of this site. Here the atoms still experience attractive interactions, preventing the occupation of higher energy states during the ramp due to interaction effects. This process of merging the planes is very similar to the one already presented in section 6.2.2.

After this transfer is done, the xy -lattice is ramped down to a chosen value of $V_{\text{latt},xy}$ in between 5 to $7 E_{\text{rec}}$, where horizontal tunnelling is allowed. Since the local trap potential changed significantly, the atoms would immediately start to redistribute, strongly heating the system. To avoid this another pattern is projected with the DMD, especially compensating the trap potential effects of the infrared z -lattice, and with high potential barriers on the edge of the core region. In the following experiments these barriers usually had a height larger than 20 times the tunnelling amplitude t and were tens of sites wide, going from $V(\mathbf{r}) - V_c = 500$ to 700 Hz.

We would like to study the physics of the repulsive bilayer Hubbard model, which requires a change from the attractive loading situation to a repulsive on-site interaction. This can either be done by transferring to a $|5\rangle|9\rangle$ mixture using a Landau-Zener RF sweep or by changing the magnetic

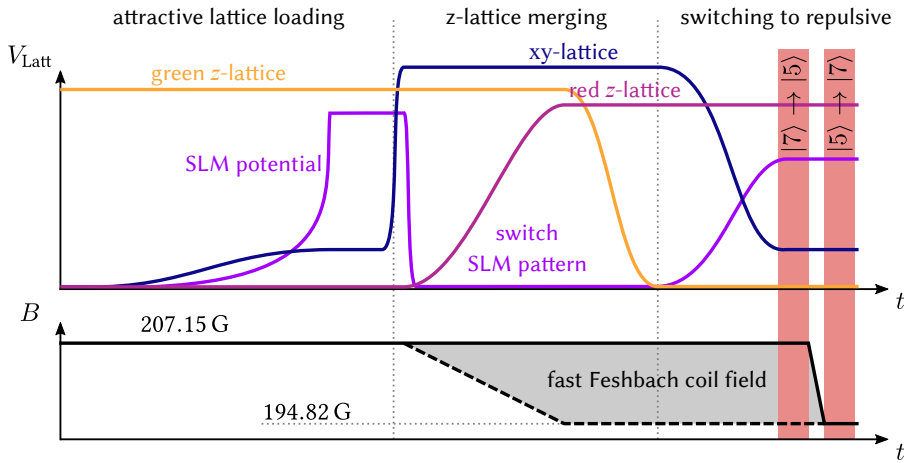


Figure 6.13: Experimental sequence to create a band insulator with repulsive interactions. The initial xy -lattice loading of every second plane is done with a $|9\rangle |7\rangle$ mixture at 207.15 G, leading to attractive on-site interaction. After freezing the motion, the green z -lattice sites get merged into the infrared z -lattice. Following the unfreezing of the xy -lattice the interaction is switched to repulsive by changing the magnetic field and crossing the Feshbach resonance.

field and with it, via the Feshbach resonance, the scattering length, see figure 4.10. We discovered, however, that at the field we are working at $B = 207.15$ G, losses occur in the $|5\rangle |9\rangle$ mixture, probably due to the $|5\rangle |9\rangle$ p-wave resonance at ~ 215 G. Therefore, performing experiments in this configuration is unfavourable and changing the magnetic field a more sensible choice. We decided to perform these experiments at a field of $B = 194.82$ G in a $|7\rangle |9\rangle$ mixture, which enables strong repulsive interactions, while still avoiding the $|7\rangle |7\rangle$ p-wave resonances at ~ 197.7 G. To avoid losses while crossing the Feshbach resonance at 202.13 G, the atoms are transferred shortly in a $|5\rangle |9\rangle$ mixture, and back again once the final field is reached. This field change is ideally very fast, to minimise the time spent in the $|5\rangle |9\rangle$ mixture. While ramping down the field of the slow Feshbach coils, an increased current in the fast Feshbach coils in Helmholtz configuration compensates the loss in magnetic field, effectively staying at $B = \sim 207$ G. Once the atoms are in the $|5\rangle |9\rangle$ mixture, the current in the fast Feshbach coils is reduced to zero in only $600 \mu\text{s}$, followed by a $|5\rangle \rightarrow |7\rangle$ transfer. Due to the change in interaction and the increase in energy for all double occupancies, atoms now can access a larger range of chemical potentials. This means atoms occupy more sites at the slope of the potential barriers separating the core from the outside region. This leads to some redistribution of the atoms in the core region, lowering the central doubles occupation from 95 to 90 %. The full sequence to create this repulsive band insulator, loaded into the infrared z -lattice is shown in figure 6.13.

6.3.2 Phase sweep preparation

In this chapter we already showed how we can use a superlattice phase sweep to prepare the ground state of separated double-wells [119]. This technique should work with a fully connected bilayer system as well, where we start with a large chemical potential difference between the two planes $2\Delta = \mu_2 - \mu_1$ and then ramp the superlattice phase to a balanced chemical potential where $\Delta = 0$.

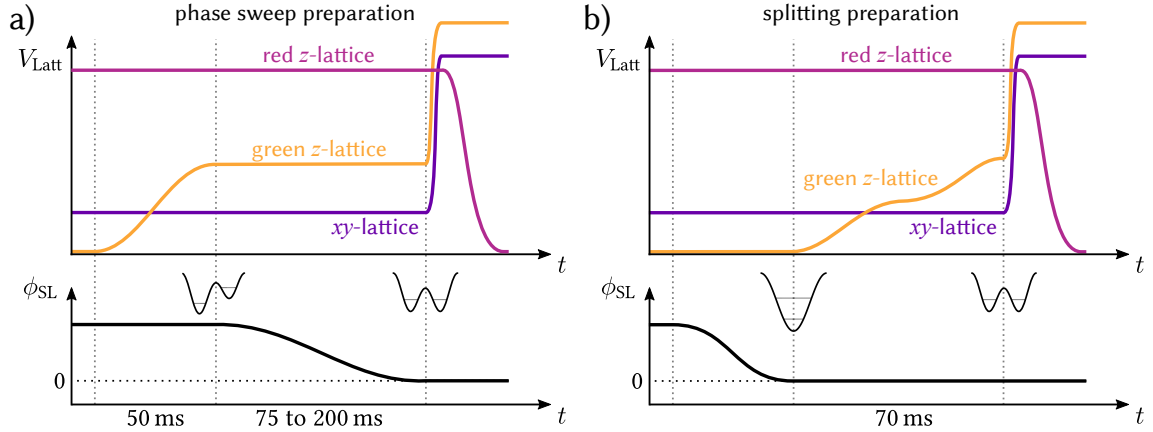


Figure 6.14: Melting the two-dimensional band insulator into a half-filled bilayer system. a) By first ramping up the superlattice with a phase imbalance, we load the atoms into a state very close to the ground state. By adiabatically sweeping the superlattice phase to the symmetric configuration $\phi_{\text{SL}} \rightarrow 0$, we aim to prepare a low entropy state in the balanced bilayer as well. b) By first changing the superlattice phase to $\phi_{\text{SL}} = 0$ and then ramping up the z -lattice, we can avoid having to tune one of the lattice lasers while their light hits the atoms. An intermediate step of $V_{\text{latt}, z, \text{green}} = 9 E_{\text{rec}}$ is used to have equal loading conditions for all following lattice configurations, and therefore inter-layer tunnelling rates t_{\perp} .

Here we assume a homogeneous potential in each layer of the bilayer individually, with the index 1, 2 indicating the two different layers. This intra-layer homogeneous potential can be achieved through the potential shaping light from the SLM.

Starting with the repulsive, two-dimensional band insulator in the infrared z -lattice, the green z -lattice is ramped to the desired value of $V_{\text{latt}, z, \text{green}}$ in between 13 to $28 E_{\text{rec}}$. With this, one creates an imbalanced bilayer system. In contrast to the merging into the infrared lattice process that has happened before, doubles now experience a repulsive on-site interaction, so some atoms might already populate the layer with a higher chemical potential. If the increase of the green lattice depth is slow enough, however, this process is adiabatic and by starting with a band insulator in a single plane, the transformation should create a very low entropy state.

Next, the system has to change to a balanced bilayer system, i.e. $\phi_{\text{SL}} = 0$. A very critical parameter here is the phase ramp speed and with it the total time of the sweep. As shown in figure 6.3 the superlattice offset lock can be shifted half the available lock range in less than 40 ms, which allows us to change from the loading and merging situation to the symmetric superlattice phase $\phi_{\text{SL}} = 0$ in a similar timescale. This helps to prevent long hold times in the lattice, when tunnelling is allowed, and therefore heating occurs. It is important, however, that the ramp is still adiabatic, meaning the imbalanced low entropy state can transform to a balanced low entropy state without increasing the entropy. Therefore, the ramp has to be slow enough relative to all relevant timescales in the system, like the superexchange rate J/h or the coupling between both layers t_{\perp}/h . Still, the exact timescales for equilibration and the many-body dynamics in the bilayer Hubbard model are not known, especially since they involve density redistribution and other complex dynamics during the whole transformation process. Additionally, the change in superlattice phase requires a very large frequency change of the Verdi laser, usually in the range of about 4 GHz. Even though the lock has been optimised in terms of stability it is not optimal to change the frequency of a lattice laser over

that range and with that speed, potentially causing stability issues and amplitude changes, heating up the system during the ramp. Even though we implemented this sequence, shown in figure 6.14 a), and could confirm that it produced the expected balanced density distribution, a different bilayer preparation method was investigated, potentially circumventing some of the stability, timescale and heating issues.

6.3.3 Splitting the band insulator

Another method, shown in figure 6.14 b), is to dynamically split the single layer into a bilayer system, similar to the symmetry point calibration previously discussed. We start again with a two-dimensional band insulator in the infrared z -lattice. Since the green z -lattice is turned off at that moment, changing the Verdi frequency does not impact the atoms. Therefore, after the merging into the infrared z -lattice is complete, the offset lock frequency is tuned to the balanced configuration $\phi_{\text{SL}} \approx 0$. During this time the atoms stay in the band insulator, where they cannot move and experience relatively low heating rates since the number of states is limited due to Pauli blocking. Once the correct frequency is reached, the green lattice depth is increased to the desired configuration, splitting the single plane into two layers. This is done in two time steps, first with a ramp to $V_{\text{latt},z,\text{green}} = 9 E_{\text{rec}}$, then to the final lattice value. Finally the lattice depth of both the horizontal xy -lattices and the green z -lattice is ramped up very quickly to freeze all motion. We discovered experimentally that for $t_{\perp}/h > 500$ Hz, this has to be much lower than the 1 ms usually used to freeze all motion. To suppress density redistribution, especially from doubles separating to singles during the lattice ramp up, the freezing timescale was reduced to 200 μs .

The big advantage of this method is that the control of the lattice laser intensity is much more stable and controllable compared to the frequency and mode control of the Verdi laser. The frequency change required switching from a tilted configuration during lattice merging to the symmetric one creating the bilayer is done without green light on the atoms, reducing possible disturbances and shaking in the potential. Also, no atoms actually have to tunnel to redistribute, since the doubles at the starting plane get continuously split into a bilayer at half-filling. This also ensures excellent initial coupling between the planes, since the doubles start in the lowest harmonic oscillator state along the z -axis. Additionally, we are not limited by the possible superlattice phase ramp speed and can choose any splitting time with only very little constraints, allowing very fast separations. We, therefore, chose to only use this method in the further experimental preparation.

After freezing, the improved z -tomography allows us to resolve all single planes of the completely filled green z -lattice and we can image an individual layer of the bilayer system we prepared. In figure 6.15 a density measurement of one of these layers, resolving singles and doubles is shown.

Having created a bilayer Hubbard system close to half-filling and having calibrated all its system parameters, $t, t_{\perp}, U, \phi_{\text{SL}}, \Delta$, we now continue to examine the physics of this system.

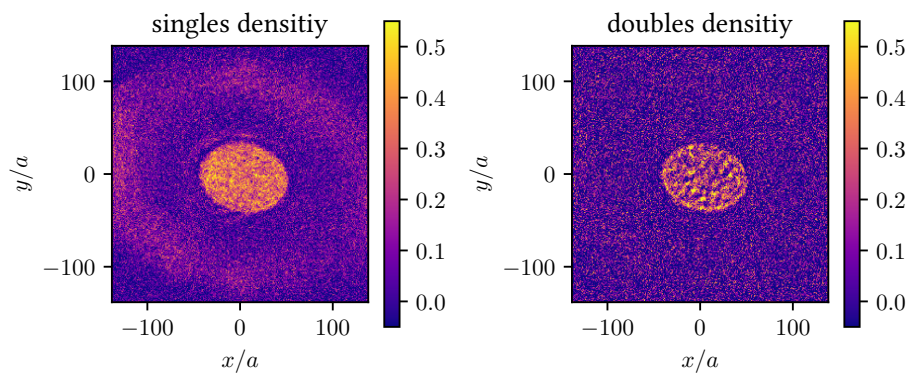


Figure 6.15: Density distribution in a bilayer close to half-filling. The density distribution shown are averaged over 18 pictures of single layer slices, and show the centre region, where the SLM compensates the potential created mostly by the infrared z -lattice. To do so, an additional potential of locally up to $11 \text{ kHz} \times h$ is required. A barrier with $8 \text{ kHz} \times h$ potential height on the outside of the centre region prevents atoms from leaving the centre. It is important to note that apart from the centre and the wall no compensation is applied, and the outside lattice is filled with very hot atoms. The singles density is very homogeneous in the centre region, whereas the doubles density shows local variations. They are more sensitive to potential changes and indicate that the central potential is not perfectly compensated. The issues this raises are discussed in the following chapter. The bilayer Hubbard parameters in this measurement are $t_{\perp}/t = 1.79$ and $U/t = +7.16$ with $t/h = 174 \text{ Hz}$.

Magnetic correlations in a fermionic Hubbard bilayer

Magnetic interactions and order are assumed to be the key ingredients in the superconducting pairing mechanism in high-temperature superconductors [8, 27]. Here, extended, layered Hubbard models and their inter-layer coupling are gaining more and more interest [53, 54, 58–63, 150–152]. In the bilayer Hubbard model, atoms from each site are coupled to five other sites, four in the same layer and one in the perpendicular direction at the opposing layer. In the following these will be called intra- and inter-layer couplings respectively. The relation between both of these can be described by the ratio t_{\perp}/t , where we again used the intra-layer tunnelling amplitude t as a general energy scale for the system. As explained in chapter 2, this coupling in combination with the superexchange mechanism leads to correlations in both directions as well.

In this chapter, I present the correlation measurements of a Hubbard bilayer in our quantum simulator and the methods we used to obtain them. These results were published in [32]. To our knowledge it is the first measurement of both inter- and intra-layer correlations in a bilayer Hubbard model with ultracold atoms, examining a large parameter space of U/t and t_{\perp}/t , additionally performed at very low temperatures of $Tk_B/t \approx 1.2$.

7.1 Intra-layer spin correlations in the bilayer

I will start by presenting the measurement of intra-layer correlations in this section. We make use of correlation measurement techniques that were previously employed in our experiment to measure correlations in the two-dimensional Hubbard model, published in [28, 29]. I will shortly introduce those two techniques before describing their implementation and the results gained from the bilayer Hubbard system.

7.1.1 Magnetisation and spin correlations

When discussing magnetic correlations it is useful to first properly introduce some definitions and measurement values. We start with the local magnetisation operator $\hat{S}_i^{\{x,y,z\}}$, where the superscript

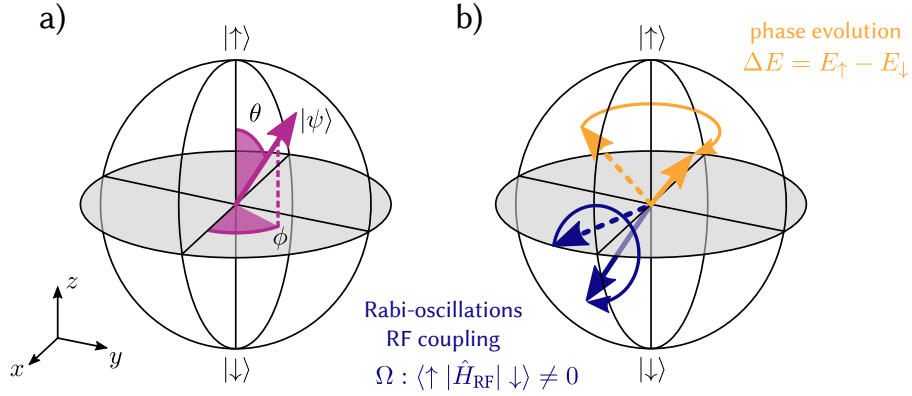


Figure 7.1: Local site magnetisation represented on the Bloch sphere a) The spin superposition of a single atom can be described in the spherical coordinates of the Bloch sphere, see equation 7.2. b) In the experiment, this Bloch vector is manipulated via two different mechanisms. Coupling the two spin states, for example through an RF pulse, leads to a rotation around the x -axis with Rabi-frequency Ω . A difference in energy ΔE for both states of a superposition of $|\uparrow\rangle$ and $|\downarrow\rangle$ induces a phase evolution of the azimuthal angle ϕ . It is to note that due to the Zeeman shift both states are in general non-degenerate since $B \neq 0$, but for a homogeneous magnetic field this rotation around the z -axis affects all spins equally and we only gain a global phase equal for all atoms.

indicates the quantisation axis and i the local site index. In the z -axis it is defined as

$$\hat{S}_i^z = (\hat{n}_{i,\uparrow} - \hat{n}_{i,\downarrow}) / 2 = (\hat{n}_{i,S,\uparrow} - \hat{n}_{i,S,\downarrow}) / 2, \quad (7.1)$$

as the Hubbard model is defined with spin-1/2 particles. Doubly occupied sites and holes do not contribute to the magnetisation, which is why we can rewrite the magnetisation with only the singles operator $\hat{n}_{i,S,\sigma} = \hat{n}_{i,\sigma} - \hat{n}_{i,\uparrow}\hat{n}_{i,\downarrow}$. To describe the wave function of a singly occupied site and with it its magnetisation, it is useful to introduce the Bloch-sphere representation, illustrated in figure 7.1 a), which maps any single spin-1/2 particle state ψ onto a unit sphere with polar coordinates

$$|\psi\rangle = \cos(\theta/2) |\uparrow\rangle + \sin(\theta/2) e^{i\phi} |\downarrow\rangle. \quad (7.2)$$

Measuring the magnetisation in the x - or y -basis would require a change of the measurement basis set. For our experiment this is not possible since we are not working with a real magnetic moment, but a superposition of different hyperfine states. Therefore, we are limited to measuring in the \uparrow, \downarrow -i.e. the z -basis.

It is, however, possible to rotate the state on this Bloch sphere through various methods, see figure 7.1 b). For example, one can manipulate the relative population of spins using RF-coupling to induce Rabi-oscillations, as discussed in section 3.1. These oscillations in the population of the two measurement states (\uparrow, \downarrow) can be described as rotations of the state vector around the x -axis with the angle α . For an RF pulse with constant power and detuning, this angle is proportional to the duration τ of the RF pulse $\alpha(\tau) \propto \tau$. By adjusting τ , pulses with a fixed rotation can be created, for example a pulse with $\alpha = \theta - \theta' = \pi/2$ will transform $|\psi\rangle = |\uparrow\rangle$ to $|\psi'\rangle = (|\uparrow\rangle + i|\downarrow\rangle)/\sqrt{2}$. This

transformation of the state effectively rotates the measurement basis for the magnetisation $\hat{S}_i^{\{x,y,z\}}$, here from the z -basis to the y -basis. In this chapter we will repeatedly make use of these so called $\pi/2$ -pulses, for state preparation and measurement purposes.

Another method to induce a rotation of the Bloch vector is to lift the energy degeneracy of the $|\uparrow\rangle$ and $|\downarrow\rangle$ states (E_\uparrow and E_\downarrow). Through the choice of the two lowest hyperfine states with a significant Zeeman energy splitting, this is given by default in our experiment, see figure 3.1. The state's relative phase will then evolve in time according to the Schrödinger equation:

$$|\psi\rangle(\tau) = c_\uparrow |\uparrow\rangle + c_\downarrow |\downarrow\rangle e^{-i(E_\uparrow - E_\downarrow)\tau/\hbar}. \quad (7.3)$$

As this does not alter the relative probability amplitudes c_\uparrow/c_\downarrow , the relative phase evolution equates to a rotation around the z -axis of the Bloch sphere.

The magnetic or spin correlation of site i with site j is defined as

$$C_{ij}^m = \langle \hat{S}_i^m \hat{S}_j^m \rangle - \langle \hat{S}_i^m \rangle \langle \hat{S}_j^m \rangle, \quad (7.4)$$

where the angled brackets indicate the measurement average over the prepared state with m as a placeholder for the measurement basis x, y or z . Again, it is educational to first understand spin correlations in a two-site, i.e. double-well system with two particles of opposite spin. If we prepare the system with a spin-up particle in the first, and a spin-down particle in the second site, we prepared a classical antiferromagnetic order $|\uparrow, \downarrow\rangle$. However, when using equation 7.4 we see that the z -correlator of this state $C_{12}^z = (1/2 \times -1/2) - (1/2 \times -1/2) = 0$ vanishes. If one examines the spin singlet state $|s\rangle = (|\uparrow, \downarrow\rangle - |\downarrow, \uparrow\rangle)/\sqrt{2}$ we immediately see that both $\langle \hat{S}_{1/2}^z \rangle = 0$. In that case the spin correlations are non-zero with $C_{12}^z = -1/4$.

An important feature we have shown in chapter 5 is that the states of a spin-balanced ($h = 0$) Hubbard system have a spin-SU(2) rotational symmetry. This means that the state is invariant under a rotation of the measurement frame. Therefore, the spin-correlations in a Hubbard system should be independent of the measurement axis as well $C_{ij}^x = C_{ij}^y = C_{ij}^z$ and additionally $\langle \hat{S}_i^z \rangle = 0$. It is useful to keep these differences between a classically prepared and a quantum mechanical antiferromagnetic order in mind.

To measure the local magnetisation one requires information of the singly occupied sites of both spins. In our experiment, we have the capability to measure the local singles densities of both hyperfine states of a single vertical layer. However, our resolution is not sufficient to resolve atoms at the single-site level. The signal we obtain from the point-like source of an atom at site i is described by the *point-spread function* (PSF) $P(\mathbf{r} - \mathbf{r}_i)$, which is normalised to one

$$\int P(\mathbf{r} - \mathbf{r}_i) d^2\mathbf{r} = 1. \quad (7.5)$$

For our discretised pixel space of our measurement basis this is translated to a sum over the integrated pixel values,

$$\sum_l \int_{A_l} P(\mathbf{r} - \mathbf{r}_i) d^2\mathbf{r} = 1, \quad (7.6)$$

where the area of the pixel l is denoted as A_l .

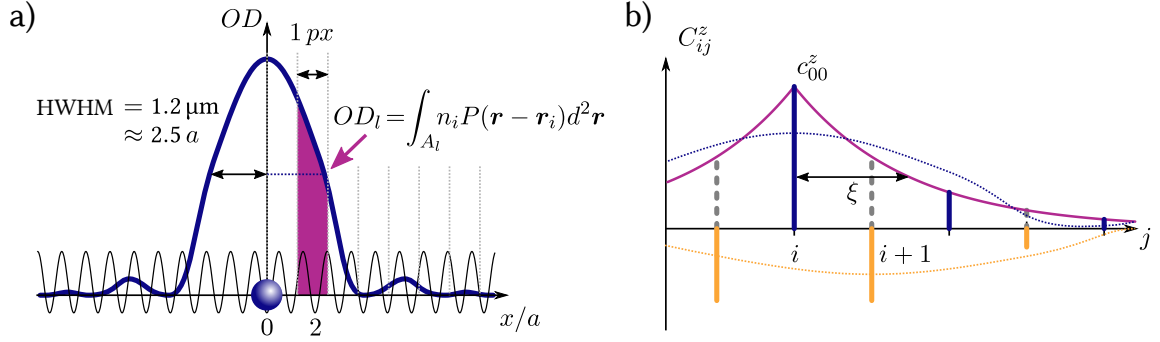


Figure 7.2: Imaging resolution and its limiting effects on detecting spin order. a) The point spread function $P(\mathbf{r})$ smears out the signal of a single atom over a larger, roughly symmetric circle with diameter of five sites (FWHM). The signal we detect at a single camera pixel OD_l thus has contributions from a multitude of occupied sites. This is illustrated in b), where we depict the alternating correlators on one axis from a fixed site i to site j and how their amplitudes are expected to decay exponentially with the correlation length ξ . Detecting the signal of the alternating spins in an antiferromagnetic order is very complex, as the signal of sites i and $i + 1$, displayed with dotted blue and orange lines, overlaps very strongly.

The PSF can usually be described by an Airy-disk, in our case with a radius of $1.25 \mu\text{m}$ (FWHM). With a lattice spacing of $a = 532 \text{ nm}$, this translates to a disk diameter of about 5 sites. The signal of several neighbouring sites with alternating magnetisation is, therefore, mostly washed out, as illustrated in figure 7.2.

7.1.2 Measuring the uniform magnetic structure factor

To overcome the limited resolution and to detect the signal of antiferromagnetic correlations in our two-dimensional system, we developed a technique to measure the uniform spin-structure factor, which was published in [28]. The static spin-structure factor is defined as the discrete Fourier transformation of the spatial spin correlations:

$$S(\mathbf{q}) = \frac{1}{N} \sum_{i,j} e^{-i\mathbf{q}\cdot\mathbf{r}_{ij}} C_{ij}^z, \quad (7.7)$$

with the number of lattice sites N and $\mathbf{r}_{ij} = \mathbf{r}_j - \mathbf{r}_i$ as the distance between sites i and j . For quasi-momentum $\mathbf{q} = 0$ this is simply the averaged sum of all spin correlators of each site in the evaluated region and is then also called the *uniform spin-structure factor*:

$$S(\mathbf{q} = 0) = \frac{1}{N} \sum_{i,j} C_{ij}^z. \quad (7.8)$$

For a completely uncorrelated system where $C_{ij}^z = 0, \forall i \neq j$, the structure factor is given by the *local moment* c_{00}^z , the on-site fluctuation of the magnetisation:

$$c_{00}^z = \frac{1}{N} \sum_i \langle (\hat{S}_i^z)^2 \rangle - \frac{1}{N} \sum_i \langle \hat{S}_i^z \rangle^2. \quad (7.9)$$

In general, the correlator $c_{\delta x \delta y}^z$ indicates the averaged correlations of any sites with a distance of δx and δy in lattice site indices, for example c_{01}^z for nearest-neighbour correlations in y -direction. For antiferromagnetic correlations the sign of the averaged correlators is alternating $c_{\delta x \delta y}^z = |c_{\delta x \delta y}^z|(-1)^{\delta x + \delta y}$.

As previously noted, all states of the spin-balanced Hubbard Hamiltonian have a spin-SU(2) symmetry, meaning their spin orientation and with it the magnetisation can be rotated without changing the state. Assuming this holds for a single site as well, its magnetisation measurement average has to vanish $\langle \hat{S}_i^z \rangle = 0$. We rewrite the first term of equation 7.9 as

$$\langle (\hat{S}_i^z)^2 \rangle = \frac{1}{4} \langle (\hat{n}_{i,\uparrow} - \hat{n}_{i,\downarrow})^2 \rangle \quad (7.10)$$

$$= \frac{1}{4} \langle \hat{n}_{i,\uparrow}^2 - 2\hat{n}_{i,\uparrow}\hat{n}_{i,\downarrow} + \hat{n}_{i,\downarrow}^2 \rangle \quad (7.11)$$

$$= \frac{1}{4} \langle (\hat{n}_{i,\uparrow} - \hat{n}_{i,\uparrow}\hat{n}_{i,\downarrow}) + (\hat{n}_{i,\downarrow} - \hat{n}_{i,\uparrow}\hat{n}_{i,\downarrow}) \rangle \quad (7.12)$$

$$= \frac{1}{4} \langle \hat{n}_{i,S,\uparrow} + \hat{n}_{i,S,\downarrow} \rangle, \quad (7.13)$$

where we used the fact that due to the Pauli principle $\hat{n}_{i,\uparrow}^2 = \hat{n}_{i,\uparrow}$ and applied the definition of singles $\hat{n}_{i,S,\sigma}$. Therefore, the local moment is given by one fourth of the site and measurement averaged singles densities and directly corresponds to the spin-structure factor of an uncorrelated system.

For short-ranged, nearest-neighbour antiferromagnetic correlations $c_{01}^z < 0$, and hence the uniform structure factor value $S(\mathbf{q} = 0)$ is lower than the one for an uncorrelated system $S(\mathbf{q} = 0) < c_{00}^z$. In general we assume a two-fold spatial symmetry about the x - and y -axis $c_{01}^z = c_{10}^z = c_{-10}^z$ and an exponential decay of the absolute correlation values with distance d , such that $|c_{ij}^z| = |c_d^z| \propto e^{-d/\xi}$ with a correlation length ξ , see figure 7.2 b). In a two-dimensional system with $Tk_B/t \approx 1$ we expect only nearest-neighbour correlations, thus detecting a uniform structure factor below the local moment directly implies antiferromagnetic correlations.

In [28] we introduced a method to detect these features, even without the imaging capabilities to resolve single site occupations, which is discussed in detail in [23] and [24]. Here I will present a short summary.

When measuring the local singles density $\rho_\sigma(\mathbf{r})$ of spin σ , we effectively measure the signal of atoms smeared out through the point-spread function (PSF) $P(\mathbf{r})$:

$$\rho_\sigma(\mathbf{r}) = \sum_i P(\mathbf{r} - \mathbf{r}_i) n_{i,S,\sigma}, \quad (7.14)$$

where $n_{i,S,\sigma}$ is the actual singles distribution of one measurement. We then calculate the naive magnetisation $\tilde{S}^z(\mathbf{r})$ by subtracting the measured singles density of the *same* measurement

$$\begin{aligned} \tilde{S}^z(\mathbf{r}) &= [\rho_\uparrow(\mathbf{r}) - \rho_\downarrow(\mathbf{r})] / 2 \\ &= \sum_i P(\mathbf{r} - \mathbf{r}_i) [n_{i,S,\uparrow} - n_{i,S,\downarrow}] / 2 \\ &= \sum_i P(\mathbf{r} - \mathbf{r}_i) S_i^z. \end{aligned} \quad (7.15)$$

If we were to naively calculate magnetic correlations at real space positions \mathbf{r} and $\mathbf{r} + \mathbf{d}$ following equation 7.4, we get

$$\tilde{C}^z(\mathbf{r}, \mathbf{d}) = \langle \tilde{S}^z(\mathbf{r}) \tilde{S}^z(\mathbf{r} + \mathbf{d}) \rangle - \langle \tilde{S}^z(\mathbf{r}) \rangle \langle \tilde{S}^z(\mathbf{r} + \mathbf{d}) \rangle \quad (7.16)$$

$$= \sum_{i,j} P(\mathbf{r} - \mathbf{r}_i) P(\mathbf{r} + \mathbf{d} - \mathbf{r}_j) (\langle S_i^z S_j^z \rangle - \langle S_i^z \rangle \langle S_j^z \rangle) \quad (7.17)$$

$$= \sum_{i,j} P(\mathbf{r} - \mathbf{r}_i) P(\mathbf{r} + \mathbf{d} - \mathbf{r}_j) C_{ij}^z. \quad (7.18)$$

By integrating the naive, smeared-out correlators $\tilde{C}^z(\mathbf{r}, \mathbf{d})$ over a distance $|\mathbf{d}| \leq d_{\max}$ that is much larger than the PSF size and the correlation length ξ , we could get a signal that would potentially be independent of this effect. In our experiment we usually work with $d_{\max}/a = 7$. The equivalent of this integration in real space is a sum over the pixels l in our camera space

$$\tilde{C}_{\text{int}}^z(\mathbf{r}) = \int_{|\mathbf{d}| \leq d_{\max}} \tilde{C}^z(\mathbf{r}, \mathbf{d}) d^2 \mathbf{d} = \sum_{l \forall |\mathbf{r}_l - \mathbf{r}| \leq d_{\max}} \int_{A_l} \tilde{C}^z(\mathbf{r}, \mathbf{d}) d^2 \mathbf{d} \quad (7.19)$$

$$= \sum_{i,j} P(\mathbf{r} - \mathbf{r}_i) C_{ij}^z \underbrace{\sum_{l \forall |\mathbf{r}_l - \mathbf{r}| \leq d_{\max}} \int_{A_l} P(\mathbf{r} + \mathbf{d} - \mathbf{r}_j) d^2 \mathbf{d}}_{\approx 1} \quad (7.20)$$

$$= \sum_{i,j} P(\mathbf{r} - \mathbf{r}_i) C_{ij}^z, \quad (7.21)$$

where in the integral approximation we assumed that only contributions of $|\mathbf{r} - \mathbf{r}_j| \leq d_{\max}$ are relevant and used equation 7.6. We do so by calculating the sum of the auto-correlation functions for each pixel. To make this consistent with the integration shown above, one has to multiply the sum of these auto-correlation functions with the square of the camera pixel size in the experiment frame a_{pixel}^2 .

In our experiment, we are usually interested in the averaged correlations over a certain (pixel) region \mathcal{A} containing N sites:

$$\frac{1}{N} \sum_{l \in \mathcal{A}} \int_{A_l} \tilde{C}_{\text{int}}^z(\mathbf{r}) d^2 \mathbf{r} = \frac{1}{N} \sum_{i,j} C_{ij}^z \underbrace{\sum_{l \in \mathcal{A}} \int_{A_l} P(\mathbf{r} - \mathbf{r}_i) d^2 \mathbf{r}}_{\approx 1} \quad (7.22)$$

$$= \frac{1}{N} \sum_{i,j} C_{ij}^z = S(\mathbf{q} = 0). \quad (7.23)$$

For practical purposes, one usually divides by the number of pixels in the averaging region \mathcal{A} and uses a scaling factor a^2/a_{pixel}^2 that includes the camera pixel size in the experiment frame and the lattice spacing. Therefore, if we only perform pixel-wise summations, beginning with the sum of the auto-correlation functions, a factor of a^2 remains and needs to be included in the final value.

With this summation technique we are now able to directly compute the uniform spin-structure factor $S(\mathbf{q} = 0)$ in a fixed area, for example, in an isopotential region. In [28] this was done for a

large range of chemical potentials, where we could show the antiferromagnetic nature of the low temperature state ($S(\mathbf{q} = 0) < c_{00}^z$) with a maximum of the correlations at half-filling $\mu = 0$.

This technique has some limitations, as it does not allow to resolve individual spin-correlators c_{ij}^z . Additionally, once next-to-nearest neighbours $c_{11}^z > 0$ are included in the correlator sum of the spin-structure factor, they partially cancel the signal of the nearest-neighbour contributions $c_{01}^z < 0$. This is unfortunate, since for long ranging antiferromagnetic order the signal would vanish $S(\mathbf{q} = 0) \rightarrow c_{00}^z$. This renders the technique ill suited for low-temperature thermometry.

7.1.3 Spin-spiral technique and the staggered structure factor

In the previous section we measured the spin-structure factor at quasi-momentum wave vector $\mathbf{q} = 0$. Now we will investigate how the spin-structure factor at $\mathbf{q} \neq 0$ would look like and how to measure it. To gain an understanding of the influence of \mathbf{q} on the magnetic order, we rewrite the correlator sign between sites i and j of an antiferromagnetic ordered system as a phase factor

$$C_{ij}^z = |C_{ij}^z| (-1)^{j_x - i_x} (-1)^{j_y - i_y} = |C_{ij}^z| e^{i\mathbf{r}_{ij} \cdot \mathbf{q}_{\text{afm}}}, \quad (7.24)$$

where i_m, j_m indicate the lattice position on axis m and we define the real space distance vector $\mathbf{r}_{ij} = \mathbf{r}_j - \mathbf{r}_i$. With the lattice index differences $\delta x = j_x - i_x$ and $\delta y = j_y - i_y$ this vector can be directly calculated $\mathbf{r}_{ij} = (\delta x \hat{e}_x + \delta y \hat{e}_y) a_{\text{lattice}}$. Using this in equation 7.24 we get

$$\mathbf{q}_{\text{afm}} = \begin{pmatrix} \pi/a \\ \pi/a \end{pmatrix}, \quad (7.25)$$

which is in both axes half the lattice wave vector $Q = 2\pi/a_{\text{lattice}}$, placing it at the corner of the first Brillouin zone of our reciprocal two-dimensional lattice.

The spin-structure factor at that wave vector is called the *staggered spin-structure factor*:

$$S(\mathbf{q}_{\text{afm}}) = \frac{1}{N} \sum_{i,j} e^{-i\mathbf{q}_{\text{afm}} \cdot \mathbf{r}_{ij}} C_{ij}^z = \frac{1}{N} \sum_{i,j} (-1)^{\delta x + \delta y} C_{ij}^z, \quad (7.26)$$

where the signs of the correlations are effectively inverted on alternating sites. In a system with antiferromagnetic order all individual correlators would then have the same sign in this sum. They would, therefore, all add up, leading to a maximum of the spin-structure factor, in contrast to the minimum at $\mathbf{q} = 0$. For increasing correlation lengths at lower temperatures the staggered structure factor would rise monotonically, making it a great and unique indicator for antiferromagnetic correlations in a system. By comparing this value with numerical simulations it can even act as thermometer for very low temperatures ($T k_B / t < 0.5$), where the density distribution does not change with temperature any more.

In [29] we published a method to coherently manipulate the phase of the correlations and detailed how we applied this to measure correlations in our system. I will present here a short summary of the technique which is explained in detail in [108]. Additionally, results have been discussed as well in [24]. To introduce this method it is useful to first look at how to create a classical chequerboard pattern, starting with a spin polarised, completely filled two-dimensional lattice. The state on each site is represented with a spin-vector on a Bloch sphere, as was done in equation 7.2. Similar to a magnetic moment we are able to manipulate these vectors through rotations around the x -axis with

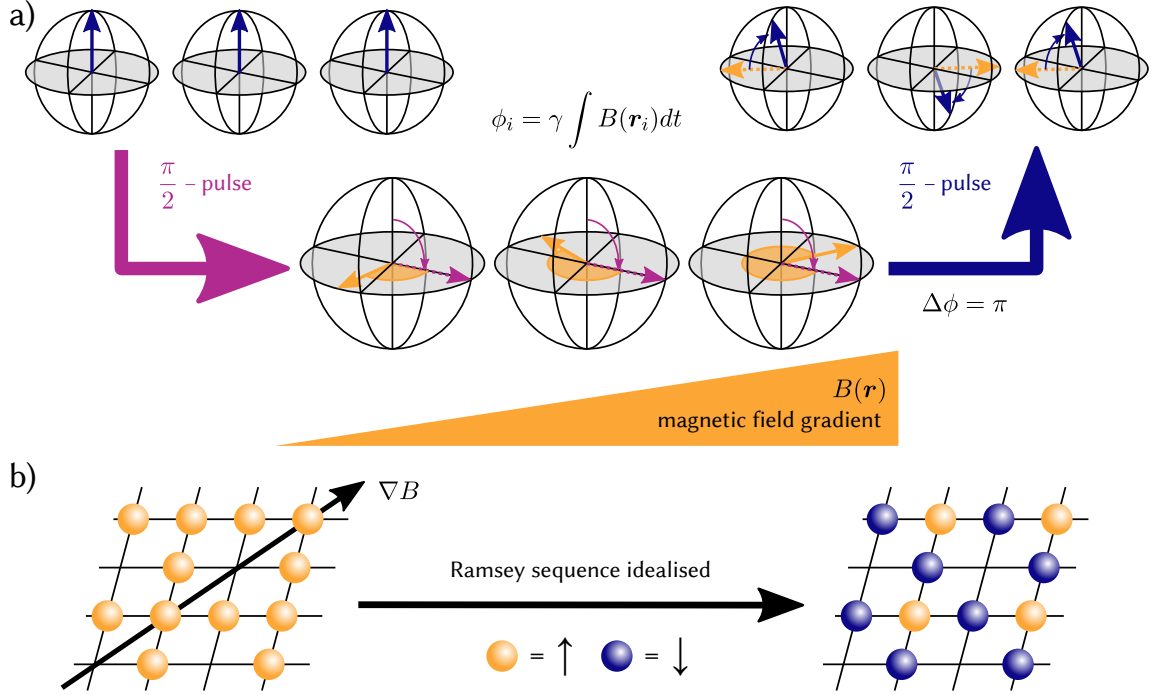


Figure 7.3: Ramsey sequence in a magnetic field gradient a) An array of spin polarised atoms in the $|\uparrow\rangle$ state is rotated into the xy -plane through a $\pi/2$ -pulse as an equal superposition of $(|\uparrow\rangle + i|\downarrow\rangle)/\sqrt{2}$. The magnetic field in the experiment lifts the energetic degeneracy of both spins, leading to a phase evolution of ϕ in the horizontal plane. When applying a magnetic field gradient, the final phase $\phi_i(t_{\text{SP}})$ is now site and time dependent. With the correct parameters we create a phase difference of neighbouring sites $\Delta\phi = \pi$, where each spin is anti-parallel to its neighbour. A second $\pi/2$ -pulse rotates the Bloch vector out of the horizontal plane, while maintaining the anti-parallel spin configuration. b) In a magnetic field gradient along the diagonal of a two-dimensional lattice and with a final projection parallel to z -axis, this Ramsey sequence creates a classical spin chequerboard pattern out of a spin polarised lattice filling.

RF-Pulses and a coherent phase evolution in a magnetic field around the z -axis. Figure 7.3 a) shows a Ramsey-type sequence in a magnetic field gradient. The initially spin polarised atoms, here in $|\uparrow\rangle$ are rotated in the equatorial plane by a $\pi/2$ -pulse: $|\uparrow\rangle \rightarrow |\psi\rangle = (|\uparrow\rangle + i|\downarrow\rangle)/\sqrt{2}$. The magnetic field $B(\mathbf{r}_i)$ at site i lifts the energetic degeneracy of $|\uparrow\rangle = |m_F = -7/2\rangle$ and $|\downarrow\rangle = |m_F = -9/2\rangle$

$$\Delta E_i = E_{i,\uparrow} - E_{i,\downarrow} = \hbar\gamma B(\mathbf{r}_i), \quad (7.27)$$

with the difference of the gyromagnetic ratios for both states $\gamma = \gamma_{\uparrow} - \gamma_{\downarrow}$. Over a time t_{SP} this leads to an evolution of their relative phase $\phi_i = \gamma \int B(\mathbf{r}_i, t) dt$, corresponding to a rotation in the horizontal plane of the Bloch sphere. The phase evolution between two sites i and j is then described with

$$\phi_{ij} = \phi_j - \phi_i = \gamma \int B(\mathbf{r}_j, t) - B(\mathbf{r}_i, t) dt = \gamma \int \nabla B(t) \cdot \mathbf{r}_{ij} dt. \quad (7.28)$$

Perpendicular to the direction of the magnetic field gradient $\nabla B(t)$ the relative phase stays constant.

After an evolution time t_{SP} in the gradient, a second $\pi/2$ -pulse rotates the spin vector out of the horizontal plane again, depending on the absolute phase acquired. If the spin vector is pointing along (opposite to) the y -axis it gets fully rotated to $|\downarrow\rangle$ ($|\uparrow\rangle$). In the direction of the gradient a wave pattern forms, with wave vector $\mathbf{k}_{\text{SP}} = \gamma \int \nabla B(t) dt$, which we obtain by measuring the population of both states. This so called *spin spiral* was previously used in our experiment to measure and then cancel magnetic field gradients [21, 22]. In our case we deliberately create a magnetic field gradient in the xy -plane, with the wave vector pointing along the lattice diagonal, see figure 7.3 b). By choosing the correct evolution time t_{SP} , the created spiral wave vector \mathbf{k}_{SP} is set such that sites directly neighbouring each other gain a relative phase shift of $\phi_{i+1} = \mathbf{k}_{\text{SP}} \cdot \mathbf{r}_{i+1} = \pi$. This means that spin vectors on neighbouring sites are oriented anti-parallel and we can create a classical antiferromagnetic order with $\mathbf{k}_{\text{SP}} = \mathbf{k}_{\text{AFM}}$. It is, however, not SU(2) symmetric and depending on the absolute phase acquired may even be still in a equal superposition of spin-up and down. The exact calibration procedure to get the strength and orientation of the magnetic field gradient ∇B in combination with the required evolution time t_{SP} is described in detail in [108] and can be used to cancel magnetic field gradients in the vertical z -direction as well.

Time evolution of the spin correlators With the spin spiral technique we are able to imprint phase patterns in a classical spin system. Additionally, it also modifies the phase of the quantum mechanical spin correlator C_{ij}^m , as defined in equation 7.4. The evolution of the relative phase of the magnetic correlation between site i and j in a spin spiral like sequence was shown to be

$$\langle \hat{S}_i^z \hat{S}_j^z \rangle \rightarrow \cos(\phi_j - \phi_i) \langle \hat{S}_i^z \hat{S}_j^z \rangle, \quad (7.29)$$

where ϕ_i is the phase picked up by spins at site i and under the strict precondition that the initial state is SU(2) symmetric. The proof of this stated transformation is done by using the Heisenberg picture of operators evolving in time and is shown in [108], together with simulations and limiting conditions. While the technique is not adding a complex phase to the correlators, it is similar to measuring the real part of a phase evolution

$$\langle \hat{S}_i^z \hat{S}_j^z \rangle \rightarrow \text{Re} \left(e^{i\mathbf{k}_{\text{sp}} \cdot \mathbf{r}_{ij}} \right) \langle \hat{S}_i^z \hat{S}_j^z \rangle. \quad (7.30)$$

Since the SU(2) symmetry implies as well that $\langle \hat{S}_i^z \rangle = 0$, the correlators C_{ij}^z evolve exactly the same. Therefore, after having imprinted a spin spiral with quasi-momentum wave vector \mathbf{q}_{sp} the uniform structure factor is transformed such that

$$S(\mathbf{q} = 0) \rightarrow \frac{1}{N} \sum_{i,j} \text{Re} \left(e^{i\mathbf{q}_{\text{sp}} \cdot \mathbf{r}_{ij}} \right) C_{ij}^z = \text{Re} \left(S(\mathbf{q} = -\mathbf{q}_{\text{sp}}) \right), \quad (7.31)$$

or seen inverse, maps $S(\mathbf{q}_{\text{sp}}) \rightarrow S(\mathbf{q} = 0)$, *imprinting* or *unwinding* a spin correlation pattern. By measuring the uniform structure factor after using the spin spiral, we are able to directly measure the real part of the structure factor at \mathbf{q}_{sp} . For example at $\mathbf{q}_{\text{sp}} = \mathbf{q}_{\text{afm}}$ we would measure the staggered structure factor, which is per definition real.

In the magnetic field gradient the correlations in the xy -direction evolve with time, which are then mapped into the z -measurement basis with the second $\pi/2$ -pulse. If this pulse is omitted the correlation in z -direction does not change. The required initial SU(2) symmetry of the measured

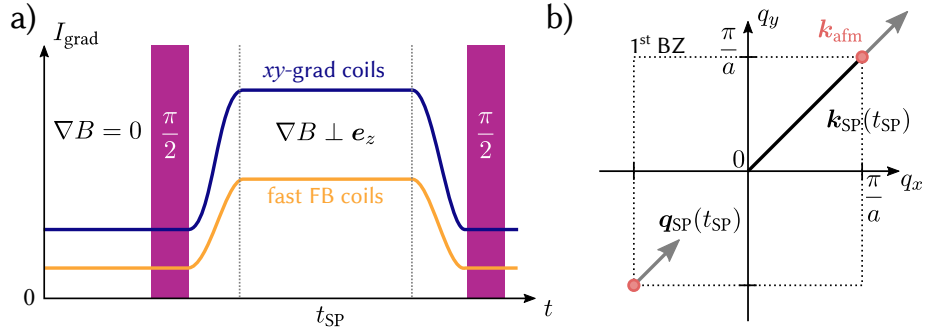


Figure 7.4: Imprinting a wave vector k_{SP} on the spin-structure a) The magnetic field gradient ∇B parallel to the xy -plane required for imprinting a wave vector is created with two small gradient coils, while any z -gradient introduced is cancelled through the fast Feshbach coils. Before the spin spiral all gradients are cancelled using the same coils. For a $SU(2)$ symmetric spin configuration the first $\pi/2$ -pulse is not required. b) Varying the evolution time t_{SP} in the magnetic field gradient we control the length of the imprinted wave vector $|k_{\text{SP}}|$. Having reached the edge of the Brillouin-zone at $k_{\text{SP}} = k_{\text{afm}}$ the vector is folded back to the quasi-momentum q_{SP} . By creating $k_{\text{SP}} = 2k_{\text{afm}}$ this even folds back to $q_{\text{SP}} = 0$, which is used to calibrate the sequence parameters [108].

state implies that cross correlation terms vanish $\langle \hat{S}_i^x \hat{S}_j^z \rangle = \langle \hat{S}_i^y \hat{S}_j^z \rangle = \langle \hat{S}_i^x \hat{S}_j^y \rangle = 0$ [108] and that the initial spin correlations are independent of the measurement direction. This practically means that the initial $\pi/2$ -pulse of the spin spiral is not necessary for the spin-structure factor measurement. Figure 7.4 shows the implementation of such a spin spiral technique in our experimental sequence and the evolution of the quasi momentum $q_{\text{SP}}(t_{\text{SP}})$ we probe in the structure factor $S(q_{\text{SP}})$.

Spin correlations in two-dimensional Hubbard model We published this technique for manipulating spin correlations and several measurements of our two-dimensional Hubbard system in [29]. In light of the following application of this technique to the bilayer, it is insightful to discuss some results here as well.

Figure 7.5 shows the uniform and staggered spin-structure factor averaged over isopotential regions of the chemical potential μ . This measurement was performed in a configuration of $U/t = +8.2$ with $t = 224$ Hz and without any additional potential shaping, for example with the SLM. As expected for an antiferromagnetically correlated system, the uniform structure factor $S(\mathbf{0})$ is consistently lower than the local moment c_{00}^z , which lies below the staggered structure factor $S(q_{\text{afm}})$. For nearest-neighbour correlations only, both structure factors would symmetrically lie around the local moment, since the nearest-neighbour correlator value is inverted. However, one observes an asymmetry of the separation $|S(q_{\text{afm}}) - c_{00}^z| > |c_{00}^z - S(\mathbf{0})|$ close to half-filling $\mu = 0$. This indicates that we have a significant contribution of more than nearest-neighbour correlations, which are not completely inverted at q_{afm} . At half-filling, the staggered structure factor can be calculated down to very low temperatures and since it is monotonic its measured value can be used as a thermometer. In this case it indicates a temperature of $Tk_B/t = 0.63(3)$.

In the same publication we showed how one can use the continuous transformation of the structure factor to extract all individual averaged correlators c_{ij}^z , which is discussed together with other results in [24].

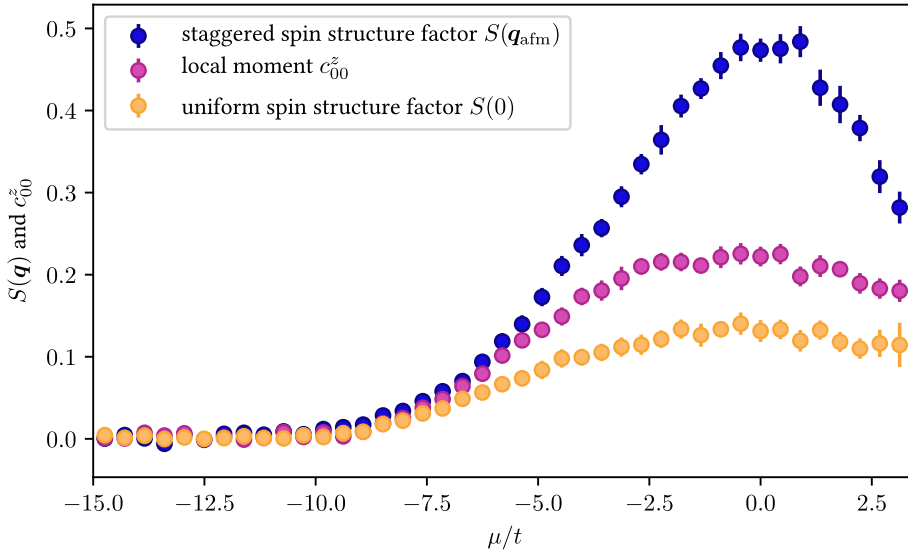


Figure 7.5: Spin-structure factor in the two-dimensional Hubbard model. This graph shows a measurement we published in [29], where we observed spin correlations in a purely two-dimensional system. Its results show no measurement of the bilayer system and only illustrate the technique. Similar to the measurement of the equation of state, we map the spatially resolved data to the chemical potential and average the measured structure factors in isopotential regions. The Hubbard parameters in this measurement were $U/t = 8.2$ with $t/h = 224$ Hz. The signal of the singles peak at half-filling is reflected in the local moment c_{00}^z (pink circles). As expected for antiferromagnetic spin correlations, the uniform structure factor $S(0)$ (orange circles) stays below the local moment, while the staggered structure factor (blue circles), measured with the additional imprinted wave-vector \mathbf{q}_{afm} is always higher than both. Comparison of $S(\mathbf{q}_{\text{afm}})$ at $\mu = 0$ with numerical simulations indicate a system temperature of $k_B T/t = 0.63(3)$.

7.1.4 Observation of intra-layer spin correlations in the bilayer

The spin spiral technique was used initially for a purely two-dimensional Hubbard system. One important requirement for it to work was a spin-balanced atom number population during the initial lattice loading to enable SU(2) symmetry, which needs to be maintained in the frozen lattice up until the spin spiral. Additionally, we need to detect both spin singles of one horizontal plane only.

To measure spin correlations in a bilayer system, the same requirements need to be fulfilled. Especially the single layer detection is challenging, since after the preparation each plane in z -direction is occupied with atoms. One option is to selectively remove every second plane, as described in section 6.2.3, to increase the spectroscopic separation of the planes from ~ 640 Hz to ~ 1.28 kHz. We noticed, however, that this process is slightly spin dependent and introduces a spin-imbalance of about 5% potentially destroying the required SU(2) symmetry. By improving the slicing resolution to less than 500 Hz we are able to resolve even the small separation of the layers, allowing a direct measurement of both spin components of a single layer.

During the preparation and afterwards in the frozen lattice all magnetic field gradients are cancelled to not inadvertently introduce an additional phase shift to the correlators or introduce spin dependency during splitting in the z -direction. Directly after having the motion frozen out by the increased x , y - and z -lattice depth we employ the spin spiral sequence shown in figure 7.4

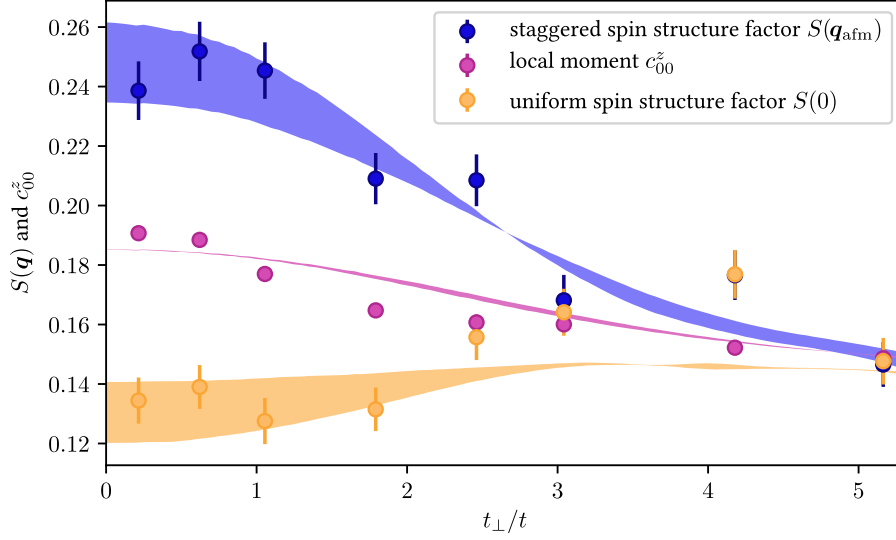


Figure 7.6: Intra-layer spin correlations in a Hubbard bilayer. Both the uniform (orange circles) and staggered (blue circles) spin-structure factors were measured for varying $t_{\perp}/t = 0.22$ to 5.16 with $t = 174$ Hz. The on-site interaction U varies with the inter-layer barrier but is centred around $U/t \approx 7.5$. The shaded regions show the results of a DQMC simulation with doped filling of $n = 0.8$ over a temperature range of $Tk_B/t = 1.0$ to 1.4 . The error-bars indicate the standard deviation from the statistics of the measurement and do not include systematic errors. This measurement was published in [32].

to manipulate the correlator phase. The gradient ∇B and the evolution time t_{sp} are chosen such that $\mathbf{q}_{sp} = \mathbf{q}_{afm}$. By turning the second $\pi/2$ -pulse on and off we measure either the staggered or the uniform spin-structure factor.

As described in chapter 6, a bilayer system is prepared by loading a two-dimensional band insulator and splitting it into two layers. Since the initial band insulator is not completely filled and due to the additional expansion while switching from attractive to repulsive interactions, we have an averaged filling of $n = 0.90$ per site just before the splitting. To account for this we scan the superlattice phase ϕ_{SL} before each measurement to ensure maximal singles density in the layer we observe, leading to a small imbalance in potential between both layers. Additionally, the local chemical potential, shaped by the lattices and the SLM light, is not as homogeneous as we would like, resulting in varying local chemical potential and site filling, as can be seen in the varying doubles fraction in figure 6.15. Averaging the measurement of the uniform and staggered structure factor and the local moment over the whole centre region leads to an effective reduction in signal size, since at half-filling we are centred for all three values at the maximum of a peak and any averaging around this peak will reduce the final value compared to the peak value itself. This issue cannot be compensated by experimental adjustments. We choose to account for it by comparing the experimental data with density doped theoretical DQMC calculations. The doping then simulates the effect of averaging over a range of local chemical potentials.

Figure 7.6 shows the measured uniform (orange circles) and staggered spin-structure factor (blue circles) together with the local moment c_{00}^z (pink circles) in a bilayer over varying $t_{\perp}/t = 0.22(7)$ to $5.16(1)$ and with $t = 174$ Hz. Shaded regions show the results of DQMC simulation with doped

filling of $n = 0.8$ over a temperature range of $Tk_B/t = 1.0$ to 1.4 . All values follow the trend of the DQMC calculations, therefore, we estimate the temperature of the bilayer system we create to $Tk_B/t = 1.2(2)$. Due to the different green z -lattice depths required for the changing inter-layer tunnelling amplitude t_\perp the interaction U changes as well, from $U/t = 8.9(1)$ at the lowest t_\perp value to $U/t = 6.3(1)$ at the highest. This will be visualised in figure 7.13 at the end of this chapter. With the inter-layer tunnelling amplitude getting quite large at $t_\perp/h = 898.5(14)$ Hz one has to keep this timescale in mind and adapt all relevant processes like the freezing of motion through a swift lattice power increase. We observed a strong decrease in double occupancies for large t_\perp when freezing with 1 ms. By lowering this time to $200 \mu\text{s}$ we again had good agreement of singles densities (local moment) and theory simulations.

At low t_\perp we observe significant correlations, visible in the separation of local moment to the uniform and staggered structure factor. Their equal distance to the local moment indicates that we have mostly nearest-neighbour correlations, in contrast to the unequal spacing in figure 7.5. Therefore, we see only short range correlations, and a detailed investigation in the exact correlator distribution is unnecessary. Here we introduce our definition of the *bilayer intra-layer correlations*

$$C_{xy} = 2 [S(\mathbf{q}_{\text{afm}}) - c_{00}^z], \quad (7.32)$$

where we take twice the difference of the staggered structure factor to the local moment to account for the correlations in both layers. For increasing inter-layer coupling, the correlations as defined above decrease drastically, up to a point where there seem to be no intra-layer correlations at all. As discussed in chapter 2.5 this is consistent with a change in the dominant coupling, and therefore the superexchange mediated correlation direction which is directly described by the ratio t_\perp/t . While we can assume that for nearly completely decoupled bilayers at $t_\perp/t \approx 0.22$ the system is described quite well as two weakly coupled, antiferromagnetically ordered Mott insulators this assumption breaks down for $t_\perp/t > 1$. In order to identify this other regime, we need to gain access to the correlations between the plane, the inter-layer correlations.

7.2 Detecting inter-layer singlet pairs

In the extreme case of $t_\perp \gg t$, the bilayer would consist of a two-dimensional grid of weakly connected double-well systems and could thus be understood and described by mostly the physics of double-wells. We will start in this regime and define measures and techniques there, before investigating how these can be extended to the intermediate range of inter-layer tunnelling and further down to $t_\perp < t$.

We begin by defining *inter-layer correlations* C_z similarly to the intra-layer correlators of equation 7.4 and 7.32, this time, however, between the two layers $m = 1, 2$ and averaged over all sites:

$$C_z = -\frac{1}{N} \sum_i \langle \hat{S}_{i1}^z \hat{S}_{i2}^z \rangle - \langle \hat{S}_{i1}^z \rangle \langle \hat{S}_{i2}^z \rangle. \quad (7.33)$$

The minus sign in front assures positive correlation values for antiferromagnetic order similar to the definition of C_{xy} . In this case N is the number of sites in one layer and only half the total number of sites of the whole bilayer. Similar to before we assume that the system we prepare is

naively guessed state	localised double-well basis	spin symmetry
$ d+\rangle$	$\frac{1}{\sqrt{2}}(\uparrow\downarrow, 0\rangle + 0, \uparrow\downarrow\rangle)$	-
$ d-\rangle$	$\frac{1}{\sqrt{2}}(\uparrow\downarrow, 0\rangle - 0, \uparrow\downarrow\rangle)$	-
$ t\rangle$	$\frac{1}{\sqrt{2}}(\uparrow, \downarrow\rangle + \downarrow, \uparrow\rangle)$	+
$ s\rangle$	$\frac{1}{\sqrt{2}}(\uparrow, \downarrow\rangle - \downarrow, \uparrow\rangle)$	-

single site state	on-site interaction \tilde{U}	spin symmetry
$ \uparrow^h \downarrow^h\rangle$	$U/4$	-
$\frac{1}{\sqrt{2}} \left(\uparrow^l \downarrow^h\rangle - \uparrow^h \downarrow^l\rangle \right)$	$U/2$	-
$\frac{1}{\sqrt{2}} \left(\uparrow^l \downarrow^h\rangle + \uparrow^h \downarrow^l\rangle \right)$	$U/2$	+
$ \uparrow^l \downarrow^l\rangle$	U	-

Table 7.1: Spin-symmetry of a half-filled double-well and a dual-band, single-site system. The naively guessed states of the half-filled, spin-balanced double-well introduced in chapter 2 are listed in the upper table. An anti-symmetric spin wave function, like the spin singlet $|s\rangle$, is denoted with a minus. Note that only $|d-\rangle$ and $|t\rangle$ are eigenstates, whereas the energetically lowest and highest ones are a superposition of $|d+\rangle$ and $|s\rangle$. The second table below similarly lists the lowest four eigenstates of a single site but with two harmonic oscillator states available (in a lattice the two lowest bands). We use the notion $|\sigma^m\rangle$ for an atom with spin σ , with m indicating the lower (l) or higher band (h) it is in. Due to the different spatial wave functions, the on-site interaction \tilde{U} varies, with $\tilde{U} = U$ being the on-site interaction for two atoms in the lowest band. This table was inspired by a similar one in [153].

SU(2) symmetric, and therefore $\langle \hat{S}_{im}^z \rangle = 0$.

When investigating a spin-balanced single double-well system ($N = 1$) at half-filling ($n = 1$), we observe that again the spin-singlet $|s\rangle$ would give the maximal interlayer correlation value of $C_z = -\langle s | \hat{S}_{11}^z \hat{S}_{12}^z | s \rangle = 1/4$. In practice however, this value is never reached since the ground state of the double-well has admixtures of a doubles state $|d+\rangle$ as well, which does not contribute to the spin correlations $C_z = -\langle d+ | \hat{S}_{11}^z \hat{S}_{12}^z | d+ \rangle = 0$. Therefore, the correlator value for a spin-balanced system will always be below 0.25 even for very low temperature states.

To detect the spin correlations in between both layers without simultaneously measuring the spin-densities of two layers with both spins at in the same run we use and adapt a technique to measure correlations between two sites, pioneered for bosons in [154] and for fermions in [155]. In the following explanation I summarise and refer for more details to the PhD thesis of Daniel Greif [153]. The method is based on the continuous transformation of a double-well to a single site, similar to the merging procedures introduced in section 6.2.2, this time, however, with both sites potentially occupied and without any potential tilt. To understand this process, we first look at the possible eigenstates of the initial double-well and the final single-site situation.

For a double-well with one spin-up and one spin-down particle we constructed the eigenstates through four orthogonal, *naively guessed*, states see section 2.3 and here again displayed in the upper part of table 7.1. Since we work with fermions, they have to be anti-symmetric to particle exchange, which can either stem from their spatial or spin symmetry. Only one of these states is symmetric under spin exchange, and therefore has an anti-symmetric spatial wave function. In a double-well with strong repulsive interactions relative to the tunnelling amplitude t_\perp between both

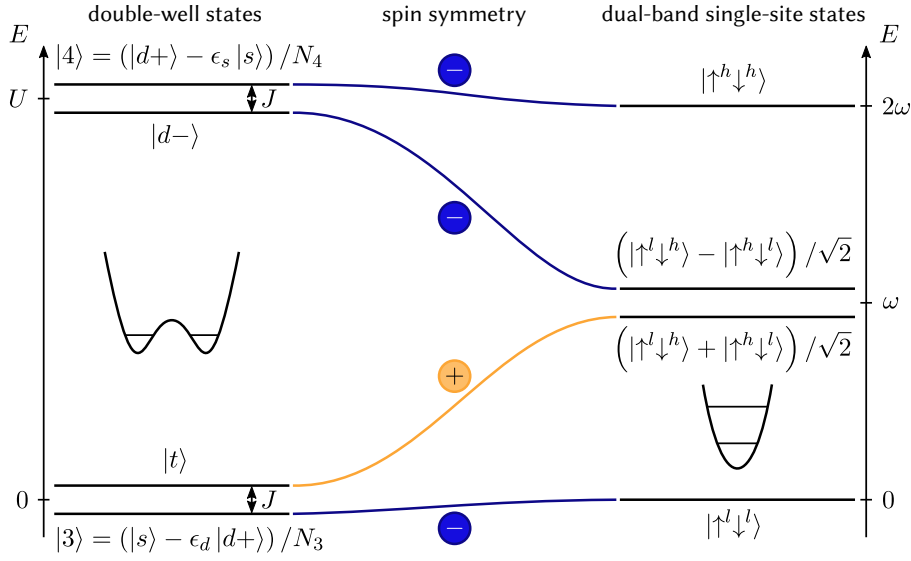


Figure 7.7: Eigenstates of the double-well and the single site connected in merging. Adiabatic merging a double-well into a single site continuously connects the double-well eigenstates on the left with the ones of a single site, maintaining their spatial and spin symmetry. A numerical calculation of this assuming repulsive interaction $U > 0$ was presented in [153], where this figure is adapted from. Note that the energy scales on the far left and right are not in absolute units and are referenced to the lowest energy state. Assuming no high energy excitations are present in the double-well configuration, only $|t\rangle$ and $|3\rangle$ states are present, which have a distinctive spatial and spin symmetry.

sites $U/t_{\perp} \gg 1$, the energetic ground state (denominated $|3\rangle$ in chapter 2) is a superposition of a spin singlet $|s\rangle$ and a small contribution $\epsilon_d(U/t)$ of $|d+\rangle$ and has, therefore, a spatially symmetric wave function. When merging the double-well into a single site, the number of states available has to be conserved, in this case this is only possible by including the next higher harmonic oscillator states. The lower part of table 7.1 lists the eigenstates of the single site including their spin symmetry. It is notable that the on-site interaction of two particles is proportional to $\tilde{U} \propto \int |\psi_1|^2 |\psi_2|^2 dx$, and therefore varies for the different eigenstates. The non-interacting spatial wave function of a particle in an harmonic oscillator can be calculated analytically [156] and was used to obtain the estimated interaction strengths relative to the interaction of two particles in the lowest state U .

In an adiabatic merging process, these states have to continuously transform from the double-well states to the single-site, dual band states. During this process the spatial and spin symmetries have to be maintained. Figure 7.7 sketches the connection of these states and their energy spacing, based on numerical simulations in [153]. The lowest energy states in both situations, i.e. $|3\rangle$ and $|\uparrow^l \downarrow^l\rangle$ have the same spin and spatial symmetry and transform into each other, meaning a spin singlet becomes a double occupancy with both atoms in the lowest band. In contrast to that, one atom of the spin triplet state $|t\rangle$ ends up in the higher band after merging. This is true for other, not spin-balanced triplet states like $|\uparrow, \uparrow\rangle$ and $|\downarrow, \downarrow\rangle$ as well, which is anyway expected due to Pauli-blocking not allowing an identical spin occupying the same state. The two other states in the spin-balanced double-well are separated in energy by $\Delta E \geq U$, and can be considered high energy excitations in our systems with Temperatures $T \approx t \ll U$. Therefore, the doubles fraction in a spin-balanced

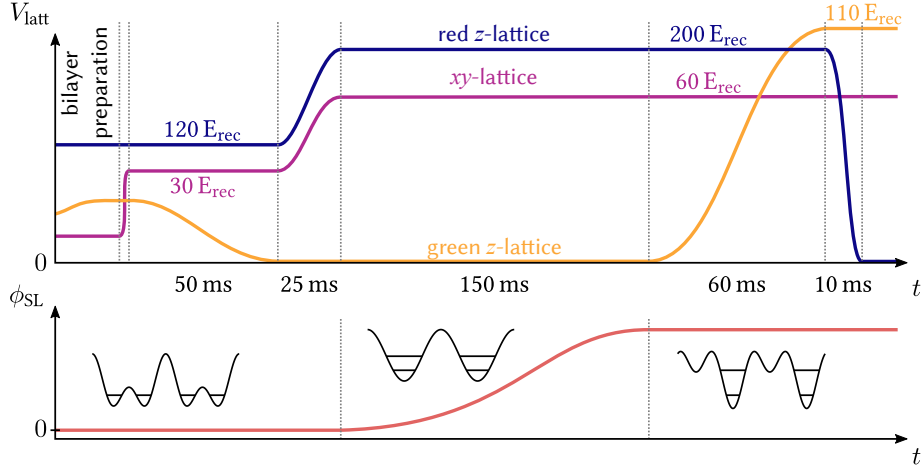


Figure 7.8: Experimental sequence for merging the Hubbard bilayer. After the preparation all sites on inter-layer connections are rapidly separated through an increase in xy -lattice depth before the reduction in green z -lattice depth induces the merging process. Only after a significant shift in the superlattice phase ϕ_{SL} we load the atoms back into the green z -lattice for detection.

double-well at low temperatures most certainly stem from the small doubles admixture $\epsilon_d(U/t)$ of $|d+\rangle$ to the ground state.

To measure the spin-singlet fraction in a bilayer with mostly decoupled double-wells (xy -lattice high during splitting) we adiabatically ramp down the central barrier in the double-well until it is merged into a single site. Then we separate the final states by resolving their on-site interaction shift \tilde{U} . We do so by reducing the green z -lattice power after having created a bilayer of separated double-wells $t_{\perp} \gg t$. Since we prepare the bilayer system by splitting a band insulator, we can assure that each double-well is filled with at maximum two atoms with opposite spin. The critical timescale for this merging is determined by the superexchange J . With a merging time of 50 ms this is done much slower than the relevant timescale of $\tau = J_{\perp}/\hbar = 4t_{\perp}^2/(Uh)$. The measured atom density in the lowest band now directly shows the relative occupation of the ground state $|3\rangle$ of the prepared double-well, which is naturally very high due to our preparation scheme. To get the pure value of spin-singlets in the system, we have to subtract the doubles admixture $\epsilon_d(U/t)$ of $|d+\rangle$ to the ground state. This is obtained by measuring the doubles density of both planes without merging, which we then subtract from the lowest band doubles measured after merging.

When working with a bilayer that is prepared with non-zero intra-layer tunnelling $t > 0$ we first have to separate the bilayer into an array of disconnected double-wells to perform this technique. This is done by ramping up the xy -lattice to $V_{\text{latt},xy} = 30 E_{\text{rec}}$, suppressing any xy -tunnelling, before merging the double-wells into the infrared z -lattice. It projects the atoms of the now separated double-wells into the states shown above. By merging and measuring the lowest band doubles fraction we again obtain the spin-singlet population between both layers. Since now spin correlations can form in both intra- and inter-layer direction we will refer to these spin singlets as inter-layer *dimers* in the bilayer. Here we require that the doubles we detect in the un-merged bilayer and which stem from the superexchange coupling J or J_{\perp} are projected into and are part of the double-well ground state's doubles admixture. Especially for $t_{\perp}/t > 1$ we assume this to be true, since $J \propto t^2$, and therefore $J_{\perp} \gg J$. Additionally one has to consider that we prepare the bilayer by splitting

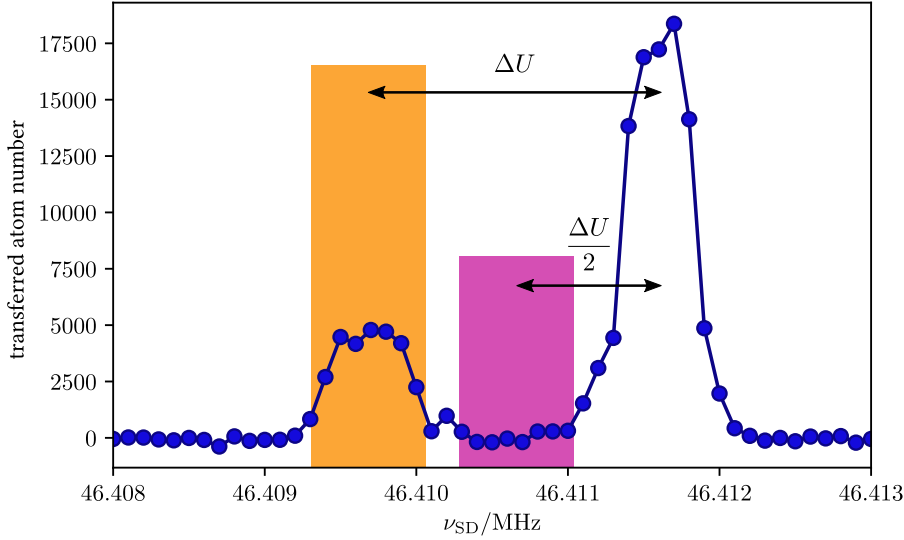


Figure 7.9: Narrow singles-doubles spectroscopy after merging. After merging a prepared Hubbard bilayer with $t_{\perp}/t = 2.51(10)$ one would expect double occupancies in the lowest band and some with one atom in both the lower and upper band. The HS1 used has a pulse width of 500 Hz and we clearly observe the lower band doubles peak at $\Delta\tilde{U} = \Delta U$, here marked by an orange area. We, however, do not observe the doubles with both bands populated at $\Delta\tilde{U} = \Delta U/2$ in the pink area, which indicates that we cannot measure these with our usual detection scheme.

doubles, which should remain at least partly correlated through the tunnelling which is a fully coherent process. Nevertheless we have to test this assumption in the region of $t_{\perp}/t \leq 1$, which we will do at the end of this section.

Figure 7.8 shows the sequence that we used to measure the superexchange induced dimer fraction on the inter-layer links of the bilayer. After the preparation through splitting of a two-dimensional band insulator we separate the system into an array of double-wells by increasing the xy -lattice power. When ramping down the green z -lattice we then merge the double-wells into single sites, resulting in the potential occupation of higher bands. In theory we could detect the double occupancies directly in the infrared z -lattice. The on-site interaction is, however, very sensitive to the wave function, which means that the ΔU we need to resolve with RF spectroscopy is greatly reduced in the infrared lattice compared to our standard detection procedure in the green z -lattice. Thus we will transfer the atoms back into the green z -lattice. This requires that we change the superlattice phase from the symmetric configuration $\Phi_{\text{SL}} \approx 0$ back to a strongly imbalanced one, before we reload the atoms into the green z -lattice by ramping up its power. The required shift in the phase is rather large: with a beat frequency difference to the symmetric configuration of $\Delta\nu_{\text{VCO}} \approx 4$ GHz it is utilising more than 60 % of the available mode-hop free tuning range of the superlattice laser lock. To support this hand-over, the infrared z -lattice depth is increased from $V_{\text{latt},z,\text{red}} = 120 E_{\text{rec}}$ to $200 E_{\text{rec}}$ before the green lattice is ramped up.

Then the standard single plane, singles-doubles detection sequence follows, however, this time with a special focus on the spectroscopy resolving different interaction shifts $\Delta\tilde{U}$ due to different band combinations. To check this separation we prepared a bilayer with interlayer coupling

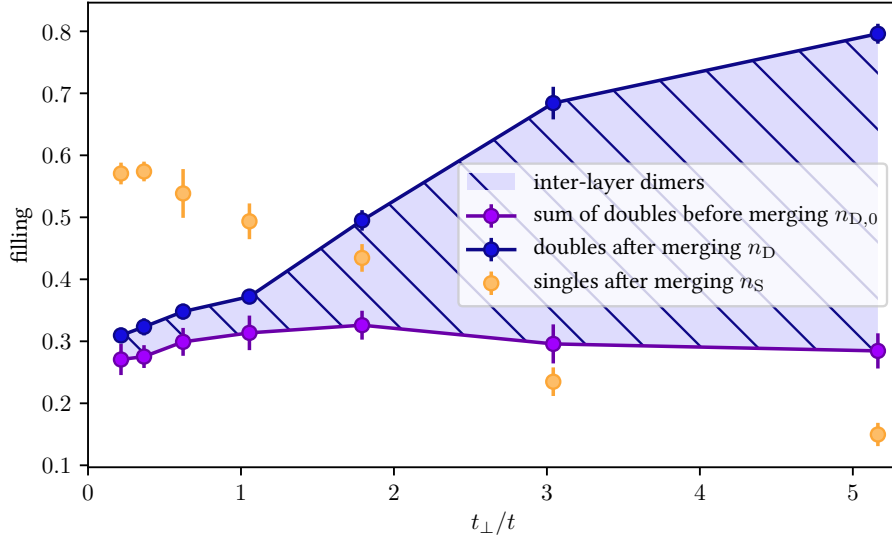


Figure 7.10: Detecting inter-layer dimers after merging. By comparing the average doubles filling (dark blue circles) of one layer after merging with the total doubles we detect in both layers before merging (light blue circles), we measure the average population of dimers along the inter-layer bonds as only these merge into a double we are able to detect. The singles that are measured for low t_{\perp} after merging (orange circles) partially have to stem from sites with two atoms, but in different bands.

$t_{\perp}/t = 2.51(10)$, which should initially already have some inter-layer bonds not occupied by dimers, and therefore higher band population as well. The result of the singles-doubles RF spectroscopy are shown in figure 7.9. The narrow HS1 pulse with a frequency width of 500 Hz allows to resolve the different $\Delta\tilde{U}$ we expect for the merged dimers ($\Delta\tilde{U} = \Delta U$) or spin triplets ($\Delta\tilde{U} = \Delta U/2$). Nonetheless, we do not see any signal in between the singles and doubles peak in this spectroscopy scan. While we can still observe the doubles fraction in the lowest band it is not possible for us to directly assess the population of doubles with one atom in a higher band.

In figure 7.10 the experimental data we took for varying $t_{\perp}/t = 0.22(7)$ to $5.16(1)$ is shown, taken with the same parameters as figure 7.6, most importantly $t/h = 174$ Hz and a range of $U/t = 6.3(1)$ to $8.9(1)$. Plotted are the average site occupation of singles n_S and doubles n_D after merging as well as the summed doubles filling of both layers before merging $n_{D,0}$. The shaded area in between the doubles indicates the excess doubles created in merging singlets along the inter-layer bonds, which increases strongly with rising $t_{\perp} > t$. We define the probability to measure a dimer on one bond as

$$p_{\text{dimer}} = n_D - n_{D,0}. \quad (7.34)$$

It is to note that the total atom number per site after merging is roughly constant as $n = 2 \times n_S + 2 \times n_D \approx 1.8$. For low inter-layer coupling, the summed site occupation probability seems to be larger than one, as we have to assume the singles density is equal for both spins $2 \times n_S + n_D \approx 1.35 > 1$. This indicates that some sites with two atoms, one in the lowest, one in the highest band, are not observed as double occupancies but as singles, as we seemingly cannot

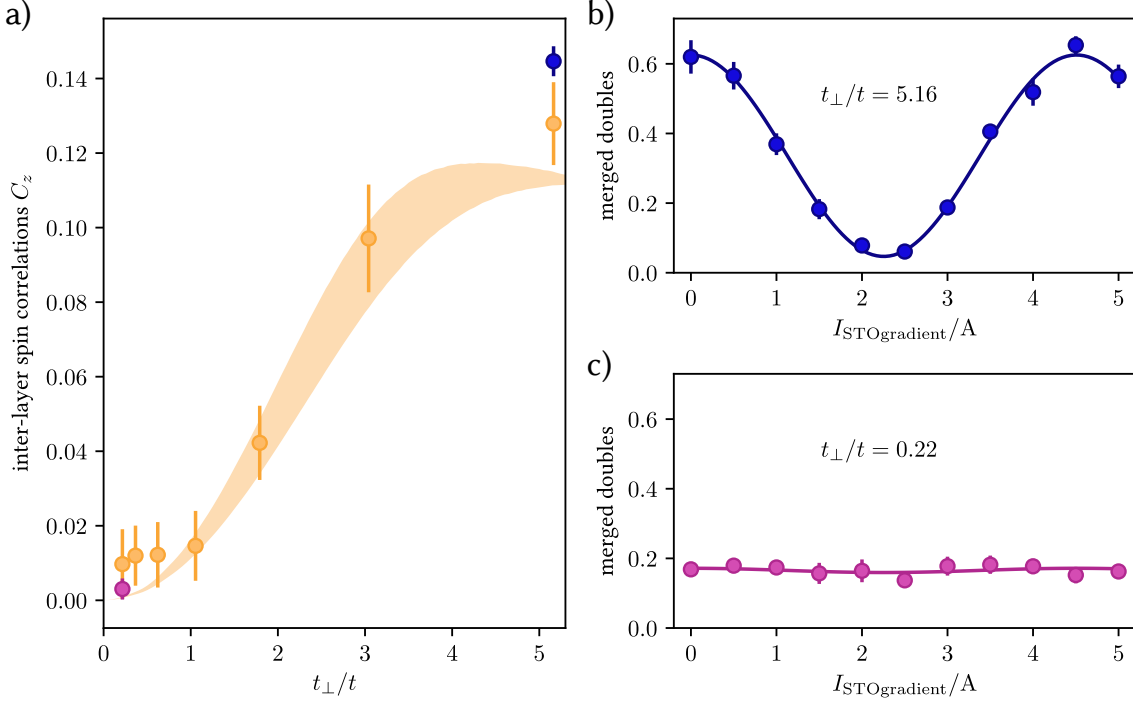


Figure 7.11: Inter-layer spin correlations in a bilayer Hubbard model. a) The inter-layer correlations C_z shown as orange circles are derived from the data presented in figure 7.10. The shaded regions show the results of a DQMC simulation with doped filling of $n = 0.8$ over a temperature range of $Tk_B/t = 1.0$ to 1.4 . The data agrees well with the simulated values. This measurement was published in [32]. To further check our results, especially at $t_{\perp} < t$, we perform singlet-triplet oscillations in a magnetic field gradient along the inter-layer axis similar to [154, 155]. The oscillations displayed in b) were obtained with a prepared bilayer with $t_{\perp} \gg t$ to confirm the validity of the method itself. The peak to peak amplitude represents the amount of singlets induced via superexchange and is comparable in value with the previously used method. c) At $t_{\perp} \ll t$ these oscillations are nearly non-existent, agreeing with our previous data and theory. Random singles on these inter-layer bounds are projected onto both the singlet and triplet state, and are, therefore, generating a significant offset without oscillations. A more detailed measurement of inter-layer singlet-triplet oscillations will be presented and discussed in [157]. The error-bars indicate the standard deviation from the statistics of the measurement and do not include systematic errors.

detect the on-site energy shift of the merged triplet states $\Delta\tilde{U} = \Delta U/2$. With this assumption we can estimate that for the lowest inter-layer tunnelling value approximately 35% of all sites are occupied with a merged triplet state.

With the measured dimer probability at the inter-layer bonds known, we can use the inter-layer spin correlator definition of equation 7.33, which states that a pure spin-singlet/dimer has an inter-layer correlation value $C_z = 1/4$. Therefore, by dividing the probability to measure a dimer by four we get the inter-layer correlator value out of our measurements

$$C_z = \frac{p_{\text{dimer}}}{4} = \frac{n_D - n_{D,0}}{4}. \quad (7.35)$$

The resulting inter-layer correlations for the previous measurement are shown in figure 7.11 a),

with the shaded regions indicating the DQMC simulated values for a bilayer with doped filling of $n = 0.8$ over a temperature range of $Tk_B/t = 1.0$ to 1.4 , exactly the same parameters as for the DQMC theory in figure 7.6. We observe a nice agreement of our measurement data with the values expected from theory, which predicted the strong increase of inter-layer correlations with increased coupling of both layers.

To further check whether this method of detecting dimers by subtracting the initial doubles from the remaining ones is valid for the low inter-layer tunnelling amplitudes $t_\perp \leq t$ as well, we use *singlet-triplet oscillations* [154, 155]. Details of this technique are described again in [153] and I will only introduce its basics here.

After the preparation of the bilayer system, we freeze the motion of the atoms in all directions by ramping up the xy - and the green z -lattice to $V_{\text{latt},xy} = 30 E_{\text{rec}}$ and $V_{\text{latt},z,\text{green}} = 36.3 E_{\text{rec}}$ respectively. Through two RF Landau-Zener swaps we change the hyperfine state of one spin component from $|7\rangle$ to $|3\rangle$. Any doubles will then consist of both $|3\rangle$ and $|9\rangle$ atoms and they get lost out of the trap through spin changing collisions. After having thus removed all doubles, we bring the atoms back to a $|5\rangle$ and $|9\rangle$ mixture with another RF sweep. For two singly occupied sites connected through an inter-layer bond with opposing spin, only two possible states remain, the spin-singlet $|s\rangle = (|\uparrow, \downarrow\rangle - |\downarrow, \uparrow\rangle)/\sqrt{2}$ and the spin-triplet state $|t\rangle = (|\uparrow, \downarrow\rangle + |\downarrow, \uparrow\rangle)/\sqrt{2}$. When these sites get merged, only the atoms in a singlet form a lowest band double that we can detect. However, for low $t_\perp/t < 1$ it might be possible that two spins on these bounds are not correlated and would therefore be projected in an even superposition of singlet and triplet state, for example $|\uparrow, \downarrow\rangle = (|s\rangle + |t\rangle)/\sqrt{2}$ and we need to distinguish these from singlets created by superexchange. To do so we utilise the fact that in a magnetic field gradient along the bond (z -) axis the energetic degeneracy of $|\uparrow, \downarrow\rangle$ and $|\downarrow, \uparrow\rangle$ is lifted. The energetic difference ΔE_{STO} is twice the one calculated in equation 7.27, which was for individual spins only. This means that the singlet and triplet states are not eigenstates any more and will evolve in time. For example two atoms in a spin-singlet configuration at $\tau = 0$ will evolve in time with

$$\psi(\tau) = \left(|\uparrow, \downarrow\rangle - e^{-\frac{i\Delta E_{\text{STO}}\tau}{\hbar}} |\downarrow, \uparrow\rangle \right) / \sqrt{2}. \quad (7.36)$$

After a time $\tau = \pi/(\Delta E_{\text{STO}}/\hbar)$ the time evolution leads to an additional minus sign, changing the singlet to a triplet. With an additional global phase added we can rewrite

$$\psi(\tau) \cdot e^{+\frac{i\Delta E_{\text{STO}}\tau}{2\hbar}} = e^{+\frac{i\Delta E_{\text{STO}}\tau}{2\hbar}} (|s\rangle + |t\rangle) / 2 - e^{-\frac{i\Delta E_{\text{STO}}\tau}{2\hbar}} (|t\rangle - |s\rangle) / 2 \quad (7.37)$$

$$= \cos\left(\frac{\Delta E_{\text{STO}}\tau}{2\hbar}\right) |s\rangle + i \sin\left(\frac{\Delta E_{\text{STO}}\tau}{2\hbar}\right) |t\rangle. \quad (7.38)$$

The atoms initially in a pure singlet state, therefore, transform to a triplet and back again. These are the so called *singlet-triplet oscillations*.

In our experiment we create the magnetic field gradient in z -direction with the fast Feshbach coils in anti-Helmholtz configuration. Instead of varying the evolution time at a constant field, we fix the evolution time to 20 ms and vary the strength of the magnetic field gradient. By merging the sites along the inter-layer bonds we measure the singlet population. This is first done in a configuration where we expect significant dimers, for $t_\perp = 5.16$ with the results shown in figure 7.11 b). The oscillations observed have nearly full contrast, with an amplitude of approximately 0.7. The

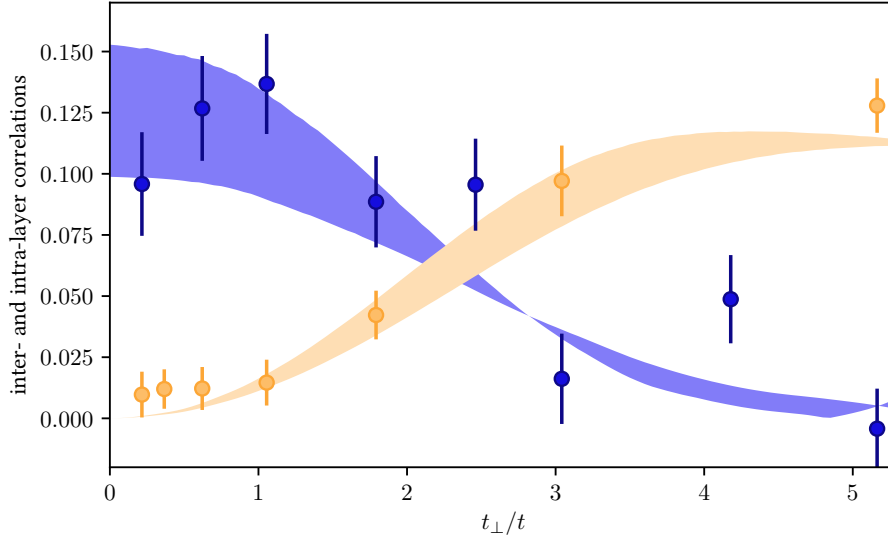


Figure 7.12: Crossover between two competing magnetic orders. By directly comparing the measured inter-layer spin correlations C_z (orange circles) with their intra-layer counterpart C_{xy} (blue circles) one observes indeed a smooth crossover between two correlation regimes, as predicted by the DQMC simulations (shaded areas).

amplitude of the oscillation directly show the amount of singlets created through superexchange, which agrees very well with the value we got from the simple merging procedure with doubles subtraction. This confirms again that for similar parameters the simpler technique works very well.

More interesting is the same measurement for very low inter-layer coupling $t_{\perp} = 0.22$. There we do not expect any correlation induced singlets, but only random projections of two uncorrelated singles into a spin-triplet and a spin-singlet, with an even population of both. This we can actually observe in the data presented in figure 7.11 c), which show no oscillation, only a constant offset. The balanced population of singlets and triplets there does not change during the evolution in the magnetic gradient, similar to a spin rotation of an initially spin-balanced cloud. It therefore agrees with the simpler merging result as well, confirming the validity of this method in our system. Further singlet-triplet oscillation measurements and a more detailed analysis will be shown in the upcoming PhD thesis of my colleague Nicola Wurz [157].

7.3 Competing magnetic orders in the bilayer Hubbard model

Having succeeded in measuring both the intra- and inter-layer correlations of the same initially prepared system, we are finally able to compare their behaviour qualitatively and quantitatively. At first we start with using the correlation metrics defined in the previous sections for the amount of intra-layer C_{xy} and inter-layer C_z correlations. Both are plotted in figure 7.12 relative to their change in t_{\perp}/t with $t/h = 174$ Hz. One clearly observes a smooth crossover between two regimes with different correlation directions. For low inter-layer coupling $t_{\perp} < t$ the system prefers building up intra-layer correlations, which are energetically more favourable due to the stronger in-plane superexchange $J > J_{\perp}$ and the possibility to correlate one spin to four times as many sites compared

to the inter-layer coupling. For an intermediate inter-layer coupling $t_{\perp}/t \approx 2.5$ these advantages for the build up of intra-layer correlations slowly decrease and we enter a regime where the system exhibits correlations in all directions, until with increasing t_{\perp} nearly all atoms form dimers in between both layers.

For a comparison of both correlations it is important to note that the maximal amount of correlations one could detect in both directions can be vastly different, depending on system parameters. In the case of very low temperatures, for example, we would expect an exponential increase in intra-layer correlations C_{xy} relative to Tk_B/t . In contrast to that the inter-layer correlations C_z are limited to the maximal value of one quarter. We can nevertheless define the relative ratio of intra- to inter-layer correlations as

$$R = \frac{C_{xy}}{C_{xy} + C_z}. \quad (7.39)$$

Since we have seen that the maxima of both correlation definitions are roughly similar, it is useful to highlight a central crossing point at $R = 0.5$ where $C_{xy} = C_z$. One has to keep in mind though that we are not cold enough to directly observe the phases pictured in figure 2.12, like the strongly correlated antiferromagnetic (AFM) Mott insulator at low t_{\perp} . They are expected at only much lower temperatures of roughly $Tk_B/t < 0.25$, similar to the two-dimensional Hubbard model. Nevertheless we may interpret the smooth crossover of both regimes, one with a small build-up of AFM order and the other with strongly coupled dimers as precursor to the real underlying phases. Especially for very strong interlayer coupling $t_{\perp}/t \geq 5$ we are rather close to a real band insulator, since there the relevant energy scale is t_{\perp} . For a fixed absolute thermal energy $Tk_B/t \approx 1.2$ we suddenly enter very low relative temperature regimes $Tk_B/t_{\perp} \approx 1.2/5 = 0.24 \ll Tk_B/t$.

Figure 7.13 a) shows this correlation ratio R relative to the inter-layer tunnelling amplitude t_{\perp}/t for three different xy -lattice depths at $V_{\text{latt},xy} = 7, 6$ and $5 E_{\text{rec}}$ resulting in $t/h = 174, 224$ and 290 Hz respectively. This variation of the tunnelling amplitude t allows us to measure the magnetic correlations in the bilayer in three very different parameter configurations, since nearly all relevant quantities in the Hubbard model like U, T and in the case of the bilayer t_{\perp} are scaled with t . Nevertheless the values of R of these three data sets still agree with each other, yielding a comparable result of an equal correlation point $R = 0.5$ at $t_{\perp}/t \approx 2.5$. While the position of this point strongly depends on the definition of the measures for correlation C_{xy} and C_z it shows that the underlying mechanisms creating the low temperature phases are mostly dependent on the ratio t_{\perp}/t for the interaction range investigated. This is especially clear once we look at the same data in a two-dimensional parameter space of U/t and t_{\perp}/t as plotted in figure 7.13 b). Here the colour of the data-points correspond to the respective R . While this is not a true phase diagram, which would only be accessible at low temperatures, it directly maps out two regions that already hint at their underlying phases, namely an AFM Mott insulator at low t_{\perp}/t and a band insulator of dimers at high t_{\perp}/t .

We, therefore, showed experimentally for the first time the competition of the magnetic orders of a Hubbard bilayer system in a quantum simulator with ultra-cold atoms at a low temperature $Tk_B/t \approx 1.2$.

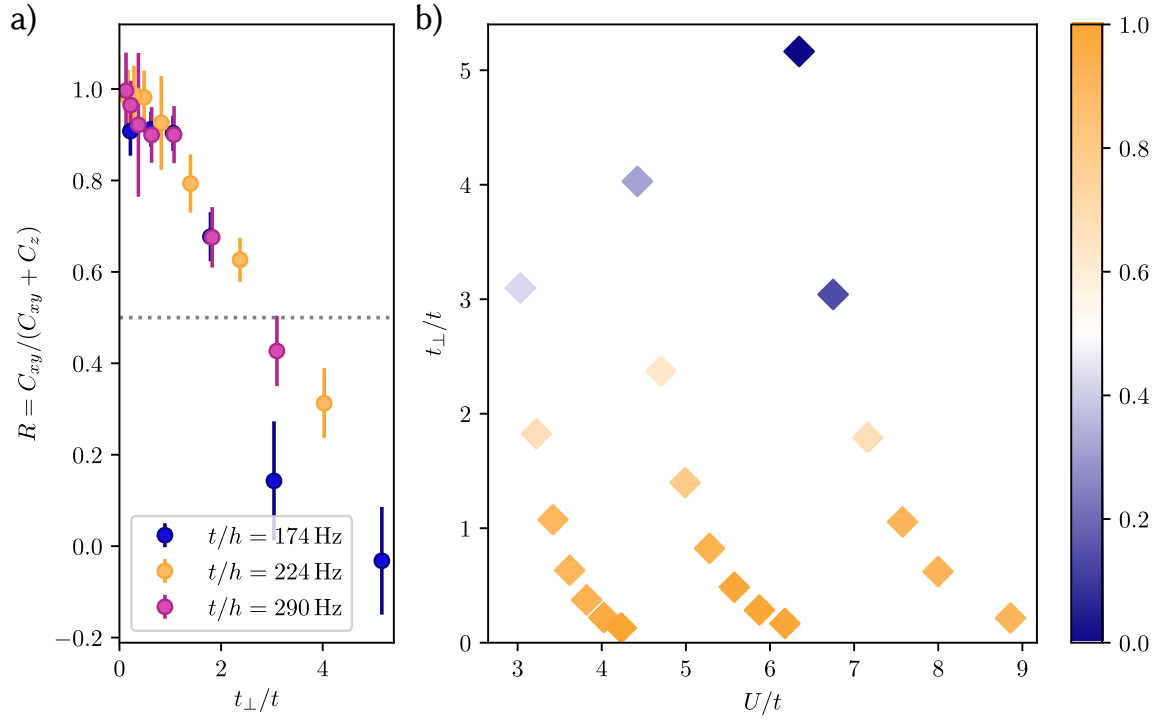


Figure 7.13: Measured correlation ratio in the bilayer Hubbard parameter space. By varying the intra-layer barrier via the xy -lattice depth during splitting, we realise different intra-layer tunnelling rates t/h . This scales the effect of other parameters of the bilayer Hubbard Hamiltonian like t_{\perp} and U such that with this change we simulate three completely different bilayer Hubbard situations. a) Surprisingly this does not change the behaviour of the correlation ratio R with respect to t_{\perp}/t . All three curves indicate a similar point for an equal correlation ratio at $t_{\perp}/t \approx 2.5$. b) Especially when plotting R in the two-dimensional parameter space of t_{\perp}/t and U/t we observe the formation of regions with similar correlation regimes. These regimes are connected to the underlying low temperature phases of the antiferromagnetic Mott insulator (predominantly orange) at low t_{\perp} and the band insulator of dimers (predominantly blue) in the high t_{\perp} regime respectively. The result was as well published in [32].

Conclusion and outlook

In this thesis, I have presented the techniques and the experimental setup that we used to simulate the Hubbard model with ultracold ^{40}K atoms in the two lowest hyperfine states. While summarising previous work, I have also highlighted my contributions in improving the system experimentally.

This allowed, for example, the study of the Hubbard model with attractive on-site interaction. By measuring the singles densities of both spins for imbalanced systems and the singles and doubles densities of doped systems with both repulsive and attractive interaction strengths, we could experimentally verify the particle-hole symmetry we expect from the Hubbard Hamiltonian. This proved the validity of our system as a quantum simulator for said model and might enable other experiments to measure physically relevant variables currently outside their available parameter ranges.

Additionally, I have described how we employed a superlattice to create a bilayer lattice structure and how we adjusted the superlattice phase. Characterising the Hubbard parameters like inter-layer tunnelling and repulsive on-site interaction energy allowed us to simulate the bilayer Hubbard model over a large inter-layer coupling range. We achieved cold system temperatures through an entropy engineering scheme: first a two-dimensional band insulator was created through the use of a spatial light modulator during lattice loading. Then this band insulator was adiabatically split into two layers by carefully manipulating the superlattice phase and the lattice powers. We measured intra-layer magnetic correlations through the spin-structure factor using a spin-spiral technique in combination with a precise layer-selective tomography. Splitting the bilayer into disconnected double-wells and merging those onto a single site allowed us to detect and quantify inter-layer spin correlations. We observed the competition of both correlation directions, depending on the inter-layer tunnelling amplitude, which showed the formation of two regimes with different magnetisation characteristics. For weakly coupled layers intra-layer antiferromagnetic correlations started to form, whereas for very strong inter-layer tunnelling we approached a band-insulator of dimers. This was the first study of the correlation regimes in a Hubbard bilayer using an experimental quantum simulator.

The physics of the bilayer are still rich and show exciting prospects for new experiments. While this thesis was written, we have measured the compressibility of the bilayer by generating a potential tilt with a magnetic field gradient. Through the precise calibration of the magnitude of this potential gradient, the compressibility was quantified. We observed the insulating character of the band-insulator of dimers at large inter-layer tunnelling. This measurement will be presented and discussed

in the upcoming thesis of my colleague Nicola Wurz [157].

There is another interesting question whether there is a critical point for the phase transition of AFM Mott insulator to band insulator at zero temperature. This could be investigated by observing the quantum critical fan of the quantum fluctuations in the phase diagram of the quantum mechanical correlations for varying temperatures, with the inter-layer tunnelling as the assumed order parameter [158].

Lowering the temperature in the bilayer further is required for an increased correlation signal and needed to study long-ranged correlations. Several possible improvements could help in that task. We could reduce the superlattice phase noise by choosing another source for the 532 nm light, which should offer a similar tuning range, but with a lower linewidth than the 5 MHz of the Verdi. Recently, another research group successfully used single-pass frequency-doubled fibre lasers with high power output to perform similar tasks [159].

The potential generated by the spatial light modulator still features a significant spatial variance when compensating the deep global potential formed by the infrared z -lattice laser in the critical bilayer preparation step. Spatially smoothing the potential generated, for example with the iris in the Fourier plane, always leads to a trade-off between the sharpness of the barriers and the reduction in potential variations. Using an extremely broadband light source for the SLM light with very short coherence length could reduce fringes from dust particles and other interferences as well and might be worth considering. Assuming these variations also scale with the magnitude of the potential compensation that is required to create a homogeneous region, one could also try more unconventional methods like dynamically varying the power balance of both interfering arms of the green z -lattice. The resulting strong standing wave component would contribute significantly to compensate the potential of the red z -lattice, and therefore allow a smoother centre region for the bilayer preparation.

An additional way of lowering the temperature would be to improve the entropy cooling scheme. Right now the two-dimensional band insulator is loaded in an attractive interaction regime, with a subsequent switch to repulsive interaction strengths. This lowers the filling in the process, partially due to decompression because of the increase in repulsive energy. By loading repulsively and avoiding the interaction change before the splitting, the sequence would be significantly simplified while potentially improving the filling, i.e. entropy before splitting.

Closer to the original motivation of investigating the emergence of high-temperature superconductivity is the idea of studying a self-doped bilayer, following observations in solid-state physics [160] and promising theoretical simulations [60]. Such a system would still be at half-filling in total, however, with a significant potential difference between both layers. This creates the doping required for superconductivity while still enabling the same entropy cooling scheme used in my thesis.

There are still many open questions for this extended Hubbard model. While it comes indeed, as noted in the introduction, with the cost of additional complexity for theory and experiment, it is worth investigating it further to perhaps someday find the answer to one of the biggest mysteries in solid-state physics, the underlying mechanism of high-temperature superconductivity.

Bibliography

- [1] M. Link, “Exploring non-equilibrium in ultracold fermi gases and machine learning in physics”, PhD thesis (Rheinische Friedrich-Wilhelms-Universität Bonn, 2020).
- [2] Z. E. Musielak and B. Quarles, “The three-body problem”, *Reports on Progress in Physics* **77**, 065901 (2014).
- [3] M. C. Gutzwiller, “Effect of correlation on the ferromagnetism of transition metals”, *Phys. Rev. Lett.* **10**, 159–162 (1963).
- [4] J. Kanamori, “Electron Correlation and Ferromagnetism of Transition Metals”, *Progress of Theoretical Physics* **30**, 275–289 (1963).
- [5] J. Hubbard, “Electron correlations in narrow energy bands”, *Proceedings of the Royal Society of London. Series A. Mathematical and Physical Sciences* **276**, 238–257 (1963).
- [6] J. Hubbard, “Electron correlations in narrow energy bands iii. an improved solution”, *Proceedings of the Royal Society of London. Series A. Mathematical and Physical Sciences* **281**, 401–419 (1964).
- [7] N. F. Mott, “The basis of the electron theory of metals, with special reference to the transition metals”, *Proceedings of the Physical Society. Section A* **62**, 416–422 (1949).
- [8] P. W. Anderson, “The Resonating Valence Bond State in La_2CuO_4 and Superconductivity”, *Science* **235**, 1196–8 (1987).
- [9] E. Y. L. Jr., J. E. Gubernatis, R. T. Scalettar, S. R. White, D. J. Scalapino and R. L. Sugar, “Sign problem in the numerical simulation of many-electron systems”, *Physical Review B* **41** (1990).
- [10] L. Wang, Y. H. Liu, M. Iazzi, M. Troyer and G. Harcos, “Split Orthogonal Group: A Guiding Principle for Sign-Problem-Free Fermionic Simulations”, *Physical Review Letters* **115**, 1–6 (2015).
- [11] I. M. Georgescu, S. Ashhab and F. Nori, “Quantum simulation”, *Reviews of Modern Physics* **86**, 153–185 (2014).
- [12] M. F. Parsons, A. Mazurenko, C. S. Chiu, G. Ji, D. Greif and M. Greiner, “Site-resolved measurement of the spin-correlation function in the fermi-hubbard model”, *Science* **353**, 1253–1256 (2016).
- [13] A. Omran, M. Boll, T. A. Hilker, K. Kleinlein, G. Salomon, I. Bloch and C. Gross, “Microscopic Observation of Pauli Blocking in Degenerate Fermionic Lattice Gases”, *Physical Review Letters* **115**, 1–5 (2015).
- [14] P. T. Brown, D. Mitra, E. Guardado-Sanchez, P. Schauß, S. S. Kondov, E. Khatami, T. Paiva, N. Trivedi, D. A. Huse and W. S. Bakr, “Spin-imbalance in a 2d fermi-hubbard system”, *Science* **14**, 1385–1388 (2017).

- [15] M. Köhl, H. Moritz, T. Stöferle, K. Günter and T. Esslinger, “Fermionic atoms in a three dimensional optical lattice: observing fermi surfaces, dynamics, and interactions”, *Phys. Rev. Lett.* **94**, 080403 (2005).
- [16] L. W. Cheuk, M. A. Nichols, M. Okan, T. Gersdorf, V. V. Ramasesh, W. S. Bakr, T. Lompe and M. W. Zwierlein, “Quantum-gas microscope for fermionic atoms”, *Physical Review Letters* **114**, 1–5 (2015).
- [17] B. Peaudecerf, M. Andia, M. Brown, E. Haller and S. Kuhr, “Microwave preparation of two-dimensional fermionic spin mixtures”, *New Journal of Physics* **21** (2019).
- [18] B. Fröhlich, “A strongly interacting two-dimensional fermi gas”, PhD thesis (University of Cambridge, 2011).
- [19] M. Feld, “Low temperature phases of interacting fermions in two dimensions”, PhD thesis (University of Cambridge, 2011).
- [20] E. Vogt, “Collective modes and polarons in two-dimensional fermi gases”, PhD thesis (University of Cambridge, 2013).
- [21] L. Miller, “Ultracold fermions in two-dimensional optical lattices: quantum simulation of the hubbard model”, PhD thesis (University of Cambridge, 2016).
- [22] E. Cocchi, “Analogue quantum simulation of the two-dimensional hubbard model with ultracold fermions”, PhD thesis (University of Cambridge, 2016).
- [23] J. H. Drewes, “Ultracold quantum gases in three-dimensional optical lattice potentials”, PhD thesis (Rheinische Friedrich-Wilhelms-Universität Bonn, 2020).
- [24] C. F. Chan, “Quantum simulation of strongly-correlated two-dimensional fermions in optical lattices”, PhD thesis (Rheinische Friedrich-Wilhelms-Universität Bonn, 2019).
- [25] M. Qin, C.-M. Chung, H. Shi, E. Vitali, C. Hubig, U. Schollwöck, S. R. White and S. Zhang, “Absence of superconductivity in the pure two-dimensional Hubbard model”, **2**, 39–54 (2019).
- [26] H. C. Jiang and T. P. Devereaux, “Superconductivity in the doped Hubbard model and its interplay with next-nearest hopping t' ”, *Science* **365**, 1424–1428 (2019).
- [27] R. Hott, R. Kleiner, T. Wolf and G. Zwicknagl, “Review on Superconducting Materials”, *digital Encyclopedia of Applied Physics*, 1–55 (2016).
- [28] J. H. Drewes, L. A. Miller, E. Cocchi, C. F. Chan, N. Wurz, M. Gall, D. Pertot, F. Brennecke and M. Köhl, “Antiferromagnetic correlations in two-dimensional fermionic mott-insulating and metallic phases”, *Phys. Rev. Lett.* **118**, 170401 (2017).
- [29] N. Wurz, C. F. Chan, M. Gall, J. H. Drewes, E. Cocchi, L. A. Miller, D. Pertot, F. Brennecke and M. Köhl, “Coherent manipulation of spin correlations in the hubbard model”, *Phys. Rev. A* **97**, 051602 (2018).
- [30] M. Gall, C. F. Chan, N. Wurz and M. Köhl, “Simulating a mott insulator using attractive interaction”, *Phys. Rev. Lett.* **124**, 010403 (2020).
- [31] C. F. Chan, M. Gall, N. Wurz and M. Köhl, “Pair correlations in the attractive hubbard model”, *Phys. Rev. Research* **2**, 023210 (2020).
- [32] M. Gall, N. Wurz, J. Samland, C. F. Chan and M. Köhl, “Competing magnetic orders in a bilayer hubbard model with ultra-cold atoms”, *Nature* (accepted, soon to be published).

-
- [33] R. T. Scalettar, “An Introduction to the Hubbard Hamiltonian”, **6** (2016).
- [34] A. Auerbach, *Interacting electrons and quantum magnetism* (Springer Science & Business Media, 1998).
- [35] M. H. Hettler, A. N. Tahvildar-Zadeh, M. Jarrell, T. Pruschke and H. R. Krishnamurthy, “Nonlocal dynamical correlations of strongly interacting electron systems”, *Phys. Rev. B* **58**, R7475–R7479 (1998).
- [36] A. I. Lichtenstein and M. I. Katsnelson, “Antiferromagnetism and d-wave superconductivity in cuprates: A cluster dynamical mean-field theory”, *Physical Review B - Condensed Matter and Materials Physics* **62**, 9283–R9286 (2000).
- [37] E. Khatami and M. Rigol, “Thermodynamics of strongly interacting fermions in two-dimensional optical lattices”, *Phys. Rev. A* **84**, 053611 (2011).
- [38] S. R. White, D. J. Scalapino, R. L. Sugar, E. Y. Loh, J. E. Gubernatis and R. T. Scalettar, “Numerical study of the two-dimensional Hubbard model”, *Physical Review B* **40**, 506–516 (1989).
- [39] C. N. Varney, C.-R. Lee, Z. J. Bai, S. Chiesa, M. Jarrell and R. T. Scalettar, “Quantum monte carlo study of the two-dimensional fermion hubbard model”, *Phys. Rev. B* **80**, 075116 (2009).
- [40] R. C. Lee, S. Chiesa, C. N. Varney, E. Khatami, Z. Bai, E. F. D’Azevedo, M. Jarrell, T. Maier, S. Y. Savrasov, R. T. Scalettar and K. Tomko, “Quest: quantum electron simulation toolbox”, in (2010).
- [41] A. Bergschneider, “Strong correlations in few-fermion systems”, PhD thesis (Ruperto-Carola University of Heidelberg, 2017).
- [42] S. Trotzky, P. Cheinet, S. Fölling, M. Feld, U. Schnorrberger, A. M. Rey, A. Polkovnikov, E. A. Demler, M. D. Lukin and I. Bloch, “Time-resolved observation and control of superexchange interactions with ultracold atoms in optical lattices”, *Science* **319**, 295–299 (2008).
- [43] E. H. Lieb and F.-Y. Wu, “Absence of mott transition in an exact solution of the short-range, one-band model in one dimension”, in *Exactly solvable models of strongly correlated electrons* (World Scientific, 1994), pp. 9–12.
- [44] A. F. Ho, M. A. Cazalilla and T. Giamarchi, “Quantum simulation of the Hubbard model: The attractive route”, *Physical Review A - Atomic, Molecular, and Optical Physics* **79**, 1–11 (2009).
- [45] V. J. Emery and S. A. Kivelson, “Importance of phase fluctuations in superconductors with small superfluid density”, *Nature* **374**, 434–437 (1995).
- [46] B. Keimer, S. A. Kivelson, M. R. Norman, S. Uchida and J. Zaanen, “From quantum matter to high-temperature superconductivity in copper oxides”, *Nature* **518**, 179–186 (2015).
- [47] L. Tarruell and L. Sanchez-Palencia, “Quantum simulation of the Hubbard model with ultracold fermions in optical lattices”, *Comptes Rendus Physique* **19**, 365–393 (2018).
- [48] T. L. Ho and Q. Zhou, “Obtaining the phase diagram and thermodynamic quantities of bulk systems from the densities of trapped gases”, *Nature Physics* **6**, 131–134 (2010).

- [49] E. Cocchi, L. A. Miller, J. H. Drewes, C. F. Chan, D. Pertot, F. Brennecke and M. Köhl, “Measuring entropy and short-range correlations in the two-dimensional hubbard model”, *Physical Review X* **7**, 1–7 (2017).
- [50] E. Cocchi, L. A. Miller, J. H. Drewes, M. Koschorreck, D. Pertot, F. Brennecke and M. Köhl, “Equation of state of the two-dimensional hubbard model”, *Phys. Rev. Lett.* **116**, 175301 (2016).
- [51] K. Yamazaki, M. Ochi, D. Ogura, K. Kuroki, H. Eisaki, S. Uchida and H. Aoki, “Superconducting mechanism for a new-type cuprate $\text{Ba}_2\text{CuO}_{3+\delta}$ based on a multiorbital lieb lattice model”, 1–19 (2020).
- [52] J. Hutchinson and F. Marsiglio, “Superconducting order parameter symmetry for the extended Hubbard model below T_c ”, 1–9 (2019).
- [53] A. Fuhrmann, D. Heilmann and H. Monien, “From Mott insulator to band insulator: A dynamical mean-field theory study”, *Physical Review B - Condensed Matter and Materials Physics* **73**, 1–6 (2006).
- [54] N. Lanatà, P. Barone and M. Fabrizio, “Superconductivity in the doped bilayer Hubbard model”, *Physical Review B - Condensed Matter and Materials Physics* **80**, 1–9 (2009).
- [55] O. Yuli, I. Asulin, O. Millo, D. Orgad, L. Iomin and G. Koren, “Enhancement of the superconducting transition temperature of $\text{La}_{2-x}\text{Sr}_x\text{CuO}_4$ bilayers: Role of pairing and phase stiffness”, *Physical Review Letters* **101**, 1–4 (2008).
- [56] T. I. Vanhala, J. E. Baarsma, M. O. Heikkinen, M. Troyer, A. Harju and P. Törmä, “Superfluidity and density order in a bilayer extended Hubbard model”, *Physical Review B - Condensed Matter and Materials Physics* **91**, 1–8 (2015).
- [57] K. Matsumoto, D. Ogura and K. Kuroki, “Strongly Enhanced Superconductivity Due to Finite Energy Spin Fluctuations Induced by an Incipient Band: A FLEX Study on the Bilayer Hubbard Model with Vertical and Diagonal Interlayer Hoppings”, *Journal of the Physical Society of Japan* **89**, 044709 (2020).
- [58] R. Rüger, “Implementation of the variational monte carlo method for the hubbard model”, PhD thesis (Master’s thesis, Goethe University Frankfurt, 2013).
- [59] S. S. Kancharla and S. Okamoto, “Band insulator to Mott insulator transition in a bilayer Hubbard model”, *Physical Review B - Condensed Matter and Materials Physics* **75**, 1–4 (2007).
- [60] K. Bouadim, G. G. Batrouni, F. Hébert and R. T. Scalettar, “Magnetic and transport properties of a coupled Hubbard bilayer with electron and hole doping”, *Physical Review B - Condensed Matter and Materials Physics* **77**, 1–7 (2008).
- [61] R. Rüger, L. F. Tocchio, R. Valentí and C. Gros, “The phase diagram of the square lattice bilayer Hubbard model: A variational Monte Carlo study”, *New Journal of Physics* **16** (2014).
- [62] M. Golor, T. Reckling, L. Classen, M. M. Scherer and S. Wessel, “Ground-state phase diagram of the half-filled bilayer Hubbard model”, *Physical Review B - Condensed Matter and Materials Physics* **90**, 1–12 (2014).
- [63] M. Lubasch, V. Murg, U. Schneider, J. I. Cirac and M. C. Bañuls, “Adiabatic preparation of a Heisenberg antiferromagnet using an optical superlattice”, *Physical Review Letters* **107**, 1–5 (2011).

- [64] K. Hida, “Quantum disordered state without frustration in the double layer heisenberg antiferromagnet – dimer expansion and projector monte carlo study –”, *Journal of the Physical Society of Japan* **61**, 1013–1018 (1992).
- [65] A. J. Millis and H. Monien, “Spin Gaps and Spin Dynamics in $\text{La}_{2-x}\text{Sr}_x\text{CuO}_4$ and $\text{YBa}_2\text{Cu}_3\text{O}_{7-\delta}$ ”, *Physical Review Letters* **70**, 1–4 (1993).
- [66] M. Troyer and U. J. Wiese, “Computational complexity and fundamental limitations to fermionic quantum Monte Carlo simulations”, *Physical Review Letters* **94**, 1–4 (2005).
- [67] A. Trabesinger, “Quantum simulation”, *Nature Physics* **8**, 2012 (2012).
- [68] S. Debnath, N. M. Linke, C. Figgatt, K. A. Landsman, K. Wright and C. Monroe, “Demonstration of a small programmable quantum computer with atomic qubits”, *Nature* **536**, 63–66 (2016).
- [69] F. Arute, K. Arya, R. Babbush, D. Bacon, J. C. Bardin, R. Barends, R. Biswas, S. Boixo, F. G. Brandao, D. A. Buell, B. Burkett, Y. Chen, Z. Chen, B. Chiaro, R. Collins, W. Courtney, A. Dunsworth, E. Farhi, B. Foxen, A. Fowler, C. Gidney, M. Giustina, R. Graff, K. Guerin, S. Habegger, M. P. Harrigan, M. J. Hartmann, A. Ho, M. Hoffmann, T. Huang, T. S. Humble, S. V. Isakov, E. Jeffrey, Z. Jiang, D. Kafri, K. Kechedzhi, J. Kelly, P. V. Klimov, S. Knysh, A. Korotkov, F. Kostritsa, D. Landhuis, M. Lindmark, E. Lucero, D. Lyakh, S. Mandrà, J. R. McClean, M. McEwen, A. Megrant, X. Mi, K. Michielsen, M. Mohseni, J. Mutus, O. Naaman, M. Neeley, C. Neill, M. Y. Niu, E. Ostby, A. Petukhov, J. C. Platt, C. Quintana, E. G. Rieffel, P. Roushan, N. C. Rubin, D. Sank, K. J. Satzinger, V. Smelyanskiy, K. J. Sung, M. D. Trevithick, A. Vainsencher, B. Villalonga, T. White, Z. J. Yao, P. Yeh, A. Zalcman, H. Neven and J. M. Martinis, “Quantum supremacy using a programmable superconducting processor”, *Nature* **574**, 505–510 (2019).
- [70] M. Prüfer, P. Kunkel, H. Strobel, S. Lannig, D. Linnemann, C. M. Schmied, J. Berges, T. Gasenzer and M. K. Oberthaler, “Observation of universal dynamics in a spinor Bose gas far from equilibrium”, *Nature* **563**, 217–220 (2018).
- [71] C. A. Regal, M. Greiner and D. S. Jin, “Observation of Resonance Condensation of Fermionic Atom Pairs”, *Physical Review Letters* **92**, 4 (2004).
- [72] M. Greiner, O. Mandel, T. Rom, A. Altmeyer, A. Widera, T. W. Hänsch and I. Bloch, “Quantum phase transition from a superfluid to a Mott insulator in an ultracold gas of atoms”, *Physica B: Condensed Matter* **329-333**, 11–12 (2003).
- [73] D. Jaksch, C. Bruder, J. I. Cirac, C. W. Gardiner and P. Zoller, “Cold bosonic atoms in optical lattices”, *Physical Review Letters* **81**, 3108–3111 (1998).
- [74] T. Tiecke, “Properties of potassium”, University of Amsterdam, The Netherlands, Thesis, 12–14 (2010).
- [75] H. Metcalf and P. Straten, “Laser cooling and trapping springer-verlag”, New York (1999).
- [76] D. A. Steck, *Quantum and atom optics*, available online at <http://steck.us/teaching> (revision 0.12.6, 23 April 2019).
- [77] R. Grimm, M. Weidemüller and Y. Ovchinnikov, “Optical dipole trap for neutral atoms”, *Adv. At. Mol. Opt. Phys.* **42**, 95 (2000).
- [78] N. W. Ashcroft and N. Mermin, *Solid state physics* (Saunders College Publishing, 1976).

- [79] G. H. Wannier, “The structure of electronic excitation levels in insulating crystals”, *Physical Review* **52**, 191–197 (1937).
- [80] J. Bohn, “Tunnelling dynamics of ultracold fermions in a one-dimensional optical superlattice”, MA thesis (University of Cambridge, 2013).
- [81] T. J. Kane and R. L. Byer, “Monolithic, unidirectional single-mode nd: yag ring laser”, *Optics letters* **10**, 65–67 (1985).
- [82] B. Zhou, T. J. Kane, G. J. Dixon and R. L. Byer, “Efficient, frequency-stable laser-diode-pumped nd: yag laser”, *Optics letters* **10**, 62–64 (1985).
- [83] T. Baer, “Large-amplitude fluctuations due to longitudinal mode coupling in diode-pumped intracavity-doubled nd: yag lasers”, *JOSA B* **3**, 1175–1180 (1986).
- [84] B. E. Saleh and M. C. Teich, *Fundamentals of photonics* (John Wiley & Sons, 2007).
- [85] J. Dalibard, “Collisional dynamics of ultra-cold atomic gases”, in *Proceedings of the international school of physics-enrico fermi*, Vol. 321 (1999), p. 14.
- [86] E. Tiesinga, B. J. Verhaar and H. T. C. Stoof, “Threshold and resonance phenomena in ultracold ground-state collisions”, *Phys. Rev. A* **47**, 4114–4122 (1993).
- [87] C. Chin, R. Grimm, P. Julienne and E. Tiesinga, “Feshbach resonances in ultracold gases”, *Reviews of Modern Physics* **82**, 1225 (2010).
- [88] A. J. Moerdijk, B. J. Verhaar and A. Axelsson, “Resonances in ultracold collisions of Li₆, Li₇, and Na₂₃”, *Physical Review A* **51**, 4852–4861 (1995).
- [89] U. Schneider, “Interacting fermionic atoms in optical lattices - a quantum simulator for condensed matter physics”, PhD thesis (Johannes Gutenberg-Universität in Mainz, 2010).
- [90] W. Ketterle, K. B. Davis, M. A. Joffe, A. Martin and D. E. Pritchard, “High densities of cold atoms in a dark spontaneous-force optical trap”, *Phys. Rev. Lett.* **70**, 2253–2256 (1993).
- [91] W. Ketterle and N. Van Druten, “Evaporative cooling of trapped atoms”, in *Advances in atomic, molecular, and optical physics*, Vol. 37 (Elsevier, 1996), pp. 181–236.
- [92] D. M. Stamper-Kurn, H.-J. Miesner, A. P. Chikkatur, S. Inouye, J. Stenger and W. Ketterle, “Reversible formation of a bose-einstein condensate”, *Phys. Rev. Lett.* **81**, 2194–2197 (1998).
- [93] A. G. Truscott, K. E. Strecker, W. I. McAlexander, G. B. Partridge and R. G. Hulet, “Observation of fermi pressure in a gas of trapped atoms”, *Science* **291**, 2570–2572 (2001).
- [94] D. Naik, A. Trenkwalder, C. Kohstall, F. M. Spiegelhalder, M. Zaccanti, G. Hendl, F. Schreck, R. Grimm, T. M. Hanna and P. S. Julienne, “Feshbach resonances in the 6Li- 40K Fermi-Fermi mixture: Elastic versus inelastic interactions”, *European Physical Journal D* **65**, 55–65 (2011).
- [95] M. Greiner, I. Bloch, O. Mandel, T. W. Hänsch and T. Esslinger, “Exploring phase coherence in a 2d lattice of bose-einstein condensates”, *Phys. Rev. Lett.* **87**, 160405 (2001).
- [96] A. Kastberg, W. D. Phillips, S. L. Rolston, R. J. C. Spreeuw and P. S. Jessen, “Adiabatic cooling of cesium to 700 nk in an optical lattice”, *Phys. Rev. Lett.* **74**, 1542–1545 (1995).
- [97] S. Friebe, C. D’Andrea, J. Walz, M. Weitz and T. W. Hänsch, “CO₂-laser optical lattice with cold rubidium atoms”, *Phys. Rev. A* **57**, R20–R23 (1998).

-
- [98] M. Soni, M. Dolfi and M. Troyer, “Density redistribution effects in fermionic optical lattices”, *Phys. Rev. A* **94**, 063404 (2016).
- [99] G. Reinaudi, T. Lahaye, Z. Wang and D. Guéry-Odelin, “Strong saturation absorption imaging of dense clouds of ultracold atoms”, *Opt. Lett.* **32**, 3143–3145 (2007).
- [100] T. Yefsah, R. Desbuquois, L. Chomaz, K. J. Günter and J. Dalibard, “Exploring the thermodynamics of a two-dimensional bose gas”, *Phys. Rev. Lett.* **107**, 130401 (2011).
- [101] M. G. Ries, A. N. Wenz, G. Zürn, L. Bayha, I. Boettcher, D. Kedar, P. A. Murthy, M. Neidig, T. Lompe and S. Jochim, “Observation of pair condensation in the quasi-2d bec-bcs crossover”, *Phys. Rev. Lett.* **114**, 230401 (2015).
- [102] K. Hueck, N. Luick, L. Sobirey, J. Siegl, T. Lompe, H. Moritz, L. W. Clark and C. Chin, “Calibrating high intensity absorption imaging of ultracold atoms”, *Opt. Express* **25**, 8670–8679 (2017).
- [103] A. Ludewig, “Feshbach resonances in ^{40}K ”, PhD thesis (Universiteit van Amsterdam, 2012).
- [104] U. Schneider, “Interacting fermionic atoms in optical lattices - a quantum simulator for condensed matter physics”, PhD thesis (Johannes Gutenberg-Universität in Mainz, 2010).
- [105] C. Regal, “Experimental realization of bcs-bec crossover physics with a fermi gas of atoms”, PhD thesis (University of Colorado, 2005).
- [106] T. Loftus, C. A. Regal, C. Ticknor, J. L. Bohn and D. S. Jin, “Resonant control of elastic collisions in an optically trapped fermi gas of atoms”, *Phys. Rev. Lett.* **88**, 173201 (2002).
- [107] M. Garwood and L. DelaBarre, “The return of the frequency sweep: designing adiabatic pulses for contemporary nmr”, *Journal of Magnetic Resonance* **153**, 155–177 (2001).
- [108] N. Wurz, “Imprinting spin spirals into an ultracold fermi gas”, Master’s Thesis (Rheinische Friedrich-Wilhelms-Universität Bonn, 2016).
- [109] B. Hartmann, “Entwicklung und aufbau einer verbesserten spektroskopietechnik für kalte atome”, Bachelor’s Thesis (Rheinische Friedrich-Wilhelms-Universität Bonn, 2018).
- [110] J. H. Drewes, E. Cocchi, L. A. Miller, C. F. Chan, D. Pertot, F. Brennecke and M. Köhl, “Thermodynamics versus local density fluctuations in the metal–mott-insulator crossover”, *Phys. Rev. Lett.* **117**, 135301 (2016).
- [111] S. Krinner, T. Esslinger and J.-P. Brantut, “Two-terminal transport measurements with cold atoms”, *Journal of Physics: Condensed Matter* **29**, 343003 (2017).
- [112] E. Guardado-Sanchez, A. Morningstar, B. M. Spar, P. T. Brown, D. A. Huse and W. S. Bakr, “Subdiffusion and heat transport in a tilted two-dimensional fermi-hubbard system”, *Phys. Rev. X* **10**, 011042 (2020).
- [113] P. T. Brown, D. Mitra, E. Guardado-Sanchez, R. Nourafkan, A. Reymbaut, C.-D. Hébert, S. Bergeron, A.-M. S. Tremblay, J. Kokalj, D. A. Huse, P. Schauß and W. S. Bakr, “Bad metallic transport in a cold atom fermi-hubbard system”, *Science* **363**, 379–382 (2019).
- [114] M. A. Nichols, L. W. Cheuk, M. Okan, T. R. Hartke, E. Mendez, T. Senthil, E. Khatami, H. Zhang and M. W. Zwierlein, “Spin transport in a mott insulator of ultracold fermions”, *Science* **363**, 383–387 (2019).

- [115] A. L. Gaunt, T. F. Schmidutz, I. Gotlibovych, R. P. Smith and Z. Hadzibabic, “Bose-einstein condensation of atoms in a uniform potential”, *Phys. Rev. Lett.* **110**, 200406 (2013).
- [116] B. Mukherjee, Z. Yan, P. B. Patel, Z. Hadzibabic, T. Yefsah, J. Struck and M. W. Zwierlein, “Homogeneous atomic fermi gases”, *Phys. Rev. Lett.* **118**, 123401 (2017).
- [117] K. Hueck, N. Luick, L. Sobirey, J. Siegl, T. Lompe and H. Moritz, “Two-dimensional homogeneous fermi gases”, *Phys. Rev. Lett.* **120**, 060402 (2018).
- [118] A. M. Kaufman, B. J. Lester and C. A. Regal, “Cooling a single atom in an optical tweezer to its quantum ground state”, *Phys. Rev. X* **2**, 041014 (2012).
- [119] S. Murmann, A. Bergschneider, V. M. Klinkhamer, G. Zürn, T. Lompe and S. Jochim, “Two fermions in a double well: exploring a fundamental building block of the hubbard model”, *Phys. Rev. Lett.* **114**, 080402 (2015).
- [120] D. Barredo, V. Lienhard, S. de Léséleuc, T. Lahaye and A. Browaeys, “Synthetic three-dimensional atomic structures assembled atom by atom”, *Nature* **561**, 79–82 (2018).
- [121] T.-L. Ho and Q. Zhou, *Universal Cooling Scheme for Quantum Simulation*, 2009.
- [122] J.-S. Bernier, C. Kollath, A. Georges, L. De Leo, F. Gerbier, C. Salomon and M. Köhl, “Cooling fermionic atoms in optical lattices by shaping the confinement”, *Phys. Rev. A* **79**, 061601 (2009).
- [123] A. Mazurenko, C. S. Chiu, G. Ji, M. F. Parsons, M. Kanász-nagy, R. Schmidt, F. Grusdt, E. Demler, D. Greif and M. Greiner, “A cold-atom Fermi–Hubbard antiferromagnet”, *Nature Publishing Group* **545**, 462–466 (2017).
- [124] C. S. Chiu, G. Ji, A. Mazurenko, D. Greif and M. Greiner, “Quantum state engineering of a hubbard system with ultracold fermions”, *Phys. Rev. Lett.* **120**, 243201 (2018).
- [125] L. Miller, *Towards engineering entropy distributions in a two-dimensional optical lattice*, First year report, University of Cambridge, 2012.
- [126] C. F. Chan, *Light shaping techniques in exploring strongly-correlated ultracold fermions*, First year report, Rheinische Friedrich-Wilhelms-Universität Bonn, 2016.
- [127] R. Floyd and L. Steinberg, “An Adaptive Algorithm for Spatial Greyscale”, *Proceedings of the Society for Information Display* **17**, 7577 (1976).
- [128] J. Liang, “High-precision laser beam shaping and image projection”, PhD thesis (University of Texas at Austin, 2012).
- [129] J. Weiner, V. S. Bagnato, S. Zilio and P. S. Julienne, “Experiments and theory in cold and ultracold collisions”, *Rev. Mod. Phys.* **71**, 1–85 (1999).
- [130] S. Zhang, “Pseudospin symmetry and new collective modes of the hubbard model”, *Phys. Rev. Lett.* **65**, 120–122 (1990).
- [131] C. V. Yang and S. Zhang, “ SO_4 Symmetry in a hubbard model”, *Modern Physics Letters B* **04**, 759–766 (1990).
- [132] C. N. Yang, “ η Pairing and off-diagonal long-range order in a hubbard model”, *Phys. Rev. Lett.* **63**, 2144–2147 (1989).

-
- [133] D. Mitra, P. T. Brown, E. Guardado-Sanchez, T. Kondov Stanimir S. and Devakul, D. A. Huse, P. Schauß and W. S. Bakr, “Quantum gas microscopy of an attractive fermi–hubbard system”, *Nature Physics* **14**, 173–177 (2018).
- [134] R. Jördens, N. Strohmaier, K. Günter, H. Moritz and T. Esslinger, “A mott insulator of fermionic atoms in an optical lattice”, *Nature* **455**, 204–207 (2008).
- [135] U. Schneider, L. Hackermüller, S. Will, T. Best, I. Bloch, T. A. Costi, R. W. Helmes, D. Rasch and A. Rosch, “Metallic and insulating phases of repulsively interacting fermions in a 3d optical lattice”, *Science* **322**, 1520–1525 (2008).
- [136] L. W. Cheuk, M. A. Nichols, K. R. Lawrence, M. Okan, H. Zhang and M. W. Zwierlein, “Observation of 2d fermionic mott insulators of ^{40}K with single-site resolution”, *Phys. Rev. Lett.* **116**, 235301 (2016).
- [137] D. Greif, M. F. Parsons, A. Mazurenko, C. S. Chiu, S. Blatt, F. Huber, G. Ji and M. Greiner, “Site-resolved imaging of a fermionic mott insulator”, *Science* **351**, 953–957 (2016).
- [138] R. A. Hart, P. M. Duarte, T.-L. Yang, X. Liu, T. Paiva, E. Khatami, R. T. Scalettar, N. Trivedi, D. A. Huse and R. G. Hulet, “Observation of antiferromagnetic correlations in the hubbard model with ultracold atoms”, *Nature* **519**, 211–214 (2015).
- [139] E. Guardado-Sanchez, P. T. Brown, D. Mitra, T. Devakul, D. A. Huse, P. Schauß and W. S. Bakr, “Probing the quench dynamics of antiferromagnetic correlations in a 2d quantum ising spin system”, *Phys. Rev. X* **8**, 021069 (2018).
- [140] M. Boll, T. A. Hilker, G. Salomon, A. Omran, J. Nespolo, L. Pollet, I. Bloch and C. Gross, “Spin- and density-resolved microscopy of antiferromagnetic correlations in fermi-hubbard chains”, *Science* **353**, 1257–1260 (2016).
- [141] T. Esslinger, “Fermi-hubbard physics with atoms in an optical lattice”, *Annual Review of Condensed Matter Physics* **1**, 129–152 (2010).
- [142] G. D. Miller, R. G. Batchko, W. M. Tulloch, D. R. Weise, M. M. Fejer and R. L. Byer, “42%-efficient single-pass cw second-harmonic generation in periodically poled lithium niobate”, *Opt. Lett.* **22**, 1834–1836 (1997).
- [143] *Dxm30af sm ultrafast detector*, TTN143077-S01 Rev. D, manufacturer’s datasheet, Thorlabs Inc. (Aug. 2018).
- [144] *Hmc733lc4b wideband mmic vco w/ buffer amplifier, 10 - 20 ghz*, v04.0514, manufacturer’s datasheet, Analog Devices, Inc. (2014).
- [145] *Hmc264 gaas mmic sub-harmonically pumped mixer, 20 - 32 ghz*, v02.1007, manufacturer’s datasheet, Analog Devices, Inc. (2013).
- [146] U. Schünemann, H. Engler, R. Grimm, M. Weidemüller and M. Zielonkowski, “Simple scheme for tunable frequency offset locking of two lasers”, *Review of Scientific Instruments* **70**, 242–243 (1999).
- [147] *Zfsc-2-1+ coaxial power splitter/combiner*, REV. DM151107 HY/TD/CP/AM151021, manufacturer’s datasheet, Mini-Circuits (Aug. 2018).
- [148] S. Murmann, “Few-particle quantum magnetism with ultracold atoms”, PhD thesis (Ruperto-Carola University of Heidelberg, 2015).

- [149] M. Lubasch, V. Murg, U. Schneider, J. I. Cirac and M.-C. Bañuls, “Adiabatic preparation of a heisenberg antiferromagnet using an optical superlattice”, *Phys. Rev. Lett.* **107**, 165301 (2011).
- [150] R. R. Dos Santos, “Magnetism and pairing in Hubbard bilayers”, *Physical Review B* **51**, 15540–15546 (1995).
- [151] T. A. Maier and D. J. Scalapino, “Pair structure and the pairing interaction in a bilayer Hubbard model for unconventional superconductivity”, *Physical Review B - Condensed Matter and Materials Physics* **84**, 3–6 (2011).
- [152] H. Lee, Y. Z. Zhang, H. O. Jeschke and R. Valentí, “Competition between band and Mott insulators in the bilayer Hubbard model: A dynamical cluster approximation study”, *Physical Review B - Condensed Matter and Materials Physics* **89**, 3–8 (2014).
- [153] D. Greif, “Quantum magnetism with ultracold fermions in an optical lattice”, PhD thesis (ETH Zurich, 2013).
- [154] S. Trotzky, Y.-A. Chen, U. Schnorrberger, P. Cheinet and I. Bloch, “Controlling and detecting spin correlations of ultracold atoms in optical lattices”, *Phys. Rev. Lett.* **105**, 265303 (2010).
- [155] D. Greif, T. Uehlinger, G. Jotzu, L. Tarruell and T. Esslinger, “Short-range quantum magnetism of ultracold fermions in an optical lattice”, *Science* **340**, 1307–1310 (2013).
- [156] C. Cohen-Tannoudji, B. Diu and F. Laloë, *Quantum mechanics*, Translation of Mécanique quantique, Hermann, Paris, 1973 (Wiley, New York, NY, 1977).
- [157] N. Wurz, “Quantum magnetism in the two-dimensional fermi-hubbard model and beyond”, PhD thesis (Rheinische Friedrich-Wilhelms-Universität Bonn, 2021).
- [158] I. Frérot and T. Roscilde, “Reconstructing the quantum critical fan of strongly correlated systems using quantum correlations”, *Nature Communications* **10**, 1–7 (2019).
- [159] J. Koepsell, S. Hirthe, D. Bourgund, P. Sompet, J. Vijayan, G. Salomon, C. Gross and I. Bloch, “Robust bilayer charge pumping for spin- and density-resolved quantum gas microscopy”, *Physical Review Letters* **125** (2020).
- [160] S. Shimizu, H. Mukuda, Y. Kitaoka, A. Iyo, Y. Tanaka, Y. Kodama, K. Tokiwa and T. Watanabe, “Uniform mixing of antiferromagnetism and high-temperature superconductivity in electron-doped layers of four-layered $\text{Ba}_2\text{Ca}_3\text{Cu}_4\text{O}_8\text{F}_2$: A new phenomenon in an electron underdoped regime”, *Physical Review Letters* **98**, 60–63 (2007).
- [161] C. Akcay, P. Parrein and J. P. Rolland, “Estimation of longitudinal resolution in optical coherence imaging”, *Applied Optics* **41**, 5256 (2002).
- [162] E. Cocchi, *A novel optical lattice for ultracold fermions*, First year report, University of Cambridge, 2012.
- [163] B. Anderson, A. Flores, R. Holten and I. Dajani, “Comparison of phase modulation schemes for coherently combined fiber amplifiers”, **23**, 12015–12021 (2015).
- [164] J. B. Coles, B. P. Kuo, N. Alic, S. Moro, C. Bres, J. M. C. Boggio, P. A. Andrekson, M. Karlsson and S. Radic, “Bandwidth-efficient phase modulation techniques for Stimulated Brillouin Scattering suppression in fiber optic parametric amplifiers”, **18**, 3808–3814 (2010).

- [165] B. Anderson, C. Robin, A. Flores and I. Dajani, "Experimental study of sbs suppression via white noise phase modulation", in *Fiber lasers xi: technology, systems, and applications*, Vol. 8961 (International Society for Optics and Photonics, 2014), 89611W.
- [166] A. V. Harish and J. Nilsson, "Optimization of phase modulation with arbitrary waveform generators for optical spectral control and suppression of stimulated Brillouin scattering", (2016).
- [167] *Keysight 346a/b/c noise source*, Operating and Service Manual, Keysight (2014).
- [168] *Pm-0s5-20-pfa-pfa-106*, Test and Calibration Sheet, EOSPACE INC. (2018).
- [169] *Mephisto/mephisto s ultra-narrow linewidth cw dpss laser*, manufacturer's datasheet, Coherent (2013).

Linewidth broadening of the dipole trap laser

In this section I will discuss the construction and characterisation of a new, linewidth broadened laser. During the optical dipole trap evaporation we observed strong losses close to the Feshbach resonance at 202.1 G. As discussed in chapter 4, we assume that they were caused by light assisted collisions, enhanced through the increased interaction strength. We probably hit several of the narrow resonances of this process with the 1 070 nm laser light, since the ytterbium fibre laser (IPG YLM- 20-LP-SC) has a very broad linewidth in the order of 0.5 nm, to avoid the creation of any interference at the position of the atoms. This can occur due to back-reflection from the inner glass cell wall to the atoms (single path distance 12 mm) or in the glass cell wall itself (thickness 4 mm).

The suppression of interference can be described by the visibility of the interference pattern

$$V = \frac{I_{\max} - I_{\min}}{I_{\max} + I_{\min}}, \quad (\text{A.1})$$

where $I_{\max/\min}$ indicates the maximal/minimal measured intensity. The coherence length l_c can then be defined as the full width at half maximum (FWHM) of the self-coherence function, i.e. the visibility of an interference pattern of light split and recombined with a path length difference Δl [161]. The coherence length of the 1 070 nm laser was measured to be as low as $l_c = 0.92(3)$ mm [162], much lower than needed to effectively suppress interference at the trap centre.

To avoid the narrow spectral resonances of the light-assisted collision losses, we would like to have a laser with some frequency tunability and a more narrow spectral width to fit in between resonances. At the same time it has to have sufficiently low coherence length to minimise the creation of an interference pattern during the optical evaporation. The path length of the back reflection inside the glass cell's walls is the smallest length scale relevant with $\Delta l = 2 \times 4 \text{ mm} = 8 \text{ mm}$. This neglects the refractive index of glass $n \approx 1.5$, which would increase this path length even further. For a laser at wavelength λ_0 with a power spectral density distribution shaped as a Gaussian and a FWHM $\Delta\lambda$, the coherence length can be calculated as

$$l_c = \frac{4 \ln 2}{\pi} \frac{\lambda_0^2}{\Delta\lambda}, \quad (\text{A.2})$$

while for a Lorentzian profile this value is reduced by half [161]. To reduce the interference of a $\lambda_0 = 1\,064 \text{ nm}$ laser to at least half of its initial value, we estimate a minimal required linewidth of

$\Delta\lambda = 0.062$ nm for the worst case of a Gaussian profile. This corresponds to a frequency linewidth of approximately $\Delta\nu = 16.6$ GHz. As an additional complication we demand a laser output power of at least 5 W to reach the intensities needed during the optical evaporation.

Since one can use an amplifier to reach the desired output power, getting the wideband source is the main challenge. We did not find any suitable and affordable laser source that could fulfil these requirements. Simple sideband modulation or multimode operation with large mode spacing is also not sufficient, since it only reduces visibility at some interference distances Δl , but shows resurgent interference and coherence depending on the number of the frequency components and their relative spectral separation [163]. A true reduction in coherence length can be achieved by adding phase fluctuations, which are inherently random. There are specially designed electro-optical modulators (EOM) which manipulate the phase of light passing a crystal, which work up to very high modulation frequencies in the microwave regime >10 GHz. By modulating these EOMs with white noise, we might be able to widen the *continuous* power spectral density profile of a laser, leading to a true linewidth increase up to the $\Delta\nu > 16.6$ GHz we need.

Our noise modulation setup is displayed in figure A.1 and uses a very high frequency, fibre-based EOM in travelling-wave configuration, the EOSPACE PM-0S5-20-PFA-PFA-106 with a frequency response range up to more than 20 GHz. As input laser we use about 80 mW Mephisto light at 1 064 nm, since the maximal recommended input power of the crystal is 100 mW. After two fibre-to-fibre couplings and including the insertion loss of the crystal, about 24 mW are then used as seed laser for the Ytterbium fibre amplifier Koheras BOOSTIK HP Y10 10W built by NKT Photonics. Fibre amplifiers like this one struggle with very narrow laser linewidth seed lasers, due to stimulated-Brillouin scattering (SBS) potentially destroying the laser. This effect is, however, reduced when using multiple input frequencies or even linewidth broadened lasers. All literature I found on the topic of laser linewidth broadening was actually related to the construction of high power fibre lasers [163–166]. For my thesis, the most relevant publication used white noise with a cut-off at approximately 500 MHz to broaden the linewidth of a high power fibre amplifier seed laser to reduce stimulated-Brillouin scattering [165]. We would like to do something similar, but with a noise spectrum frequency range nearly two orders of magnitude larger.

To generate the RF noise spectrum we use a HP 346B calibrated noise source (product continued as Agilent/Keysight 346B) with excess noise ratio (ENR) of 15dB up to 18GHz [167]. The ENR defines the increase in noise in a spectral range generated by turning on the device. It is important to note, that the output power spectrum includes higher frequencies as well, however, with lower ENR. The output power of this noise source, integrated over its whole frequency range is only $P_{\text{NS}} = -56(4)$ dBm [167], and therefore has to be amplified before we could use it on the EOM. It was not immediately clear how to theoretically determine the right input power for the modulation to obtain a smooth linewidth broadening. For a single frequency, one specifies the π -voltage V_{π} , which defines the modulation signal's voltage peak-to-peak amplitude required to change the light's phase by π (peak-to-peak as well). The EOM we use is specified to a π -voltage of 2.5 V at 1 GHz [168]. This corresponds to a signal power of ~ 21 dBm on the $50\ \Omega$ RF input of the EOM. Assuming the same *power* is required for our noise signal we would require an amplification of about 75 dB for most of the frequency range of 0 to >18 GHz. We use three Minicircuits ZVA-183X-S+ large bandwidth amplifiers with a specified amplification of ~ 26 dB each over a range of 0.7 to 18 GHz, leading to a naive total power amplification of 78 dB or nearly eight orders of magnitude. Figure A.1 shows the spectrum we could generate in this configuration. By removing one of the three amplifiers and comparing it with the initial spectrum we observe the gain of a single amplifier. Then, turning the

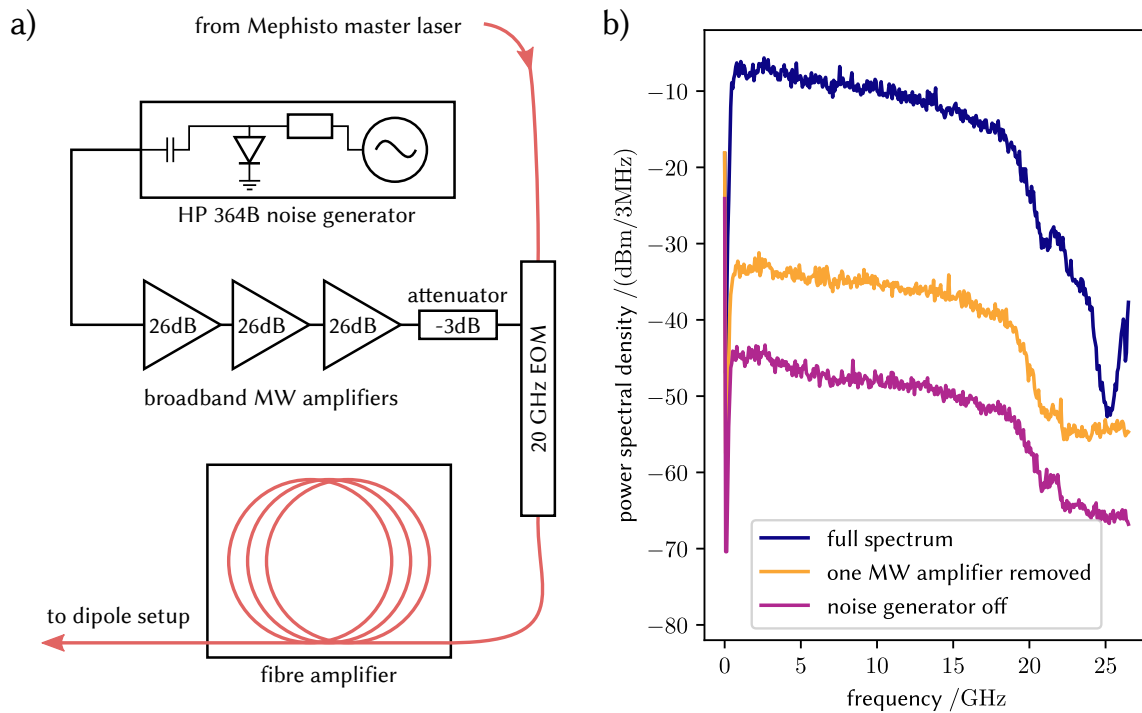


Figure A.1: Linewidth broadening with high frequency noise generation a) The high frequency noise source HP 346B has a power output of only about -56 dBm over its specified frequency range and is amplified by three broadband minicircuits ZVA-183X-S+ MW amplifiers. This signal is then used on a EOM with frequency response of more than 20 GHz. A 3 dB attenuator is added for optimal performance. The phase modulated light is used as a seed laser for a Koheras BOOSTIK HP Y10 fibre amplifier with a maximum output of 10 W, before being sent to a separate optical setup controlling its use in the experiment. In b), the full high frequency signal used for phase modulation is shown in blue. Important to note here is that the noise spectrum is continuous, so the power output for each data point has to be interpreted as the integrated value over the spectrum analyser bandwidth of 3 MHz. By removing one of the amplifiers we obtain the orange signal. The difference to the dark blue signal indicates the expected gain profile over its operating range up to 18 GHz. The excess noise ratio (ENR) of the noise generator can be derived by the difference of the orange signal to the one in pink, which shows the spectrum after the generator has been turned off.

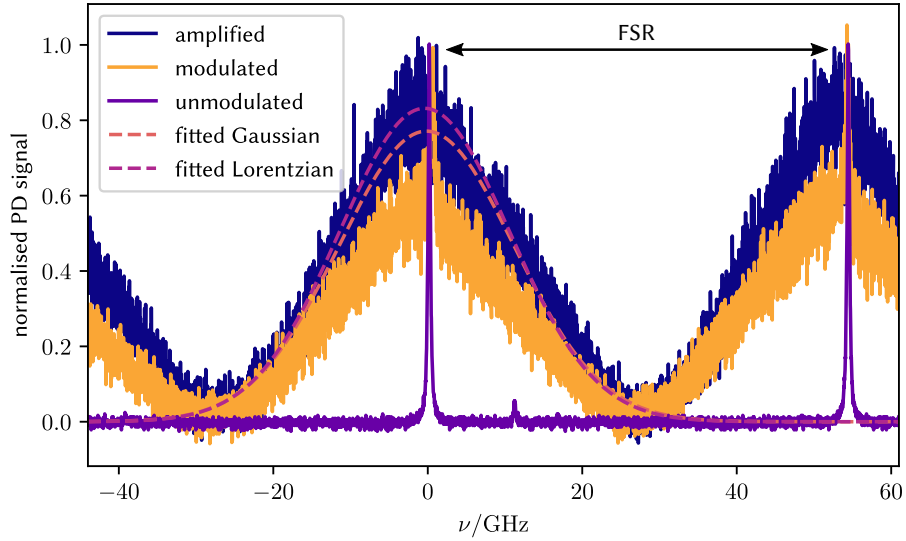


Figure A.2: Noise-broadened optical spectrum The effect of the phase modulation is observed using a Fabry-Pérot interferometer with a free spectral range (FSR) of 54.3(1) GHz. Comparing the unmodulated signal (in pink) to the one obtained after the EOM (in orange) shows the significantly increased spectral width, with some remaining unmodulated carrier. After passing the fibre amplifier this carrier cannot be observed any more (in dark blue) while the rest of the spectrum remains unchanged. All signals were normalised to one to be comparable. The final power spectral density was fitted with a Gaussian and a Lorentzian shape (dashed lines). While both seem to qualitatively fit to the signal well, their calculated coherence length would differ by a factor of two [161].

noise source on and off shows us the excess noise ratio (ENR). While the noise source output extends to higher frequencies as the one specified, the amplifier limits the overall spectrum to ~ 18 GHz. While we assume that we could probably replace the active noise source with a fourth amplifier and a good 50Ω termination at the input port, the noise source offers an in theory more controlled application.

In order to characterise the modulation effect onto the laser light, we built a small optical cavity, consisting of two slightly curved quarter inch mirrors with 98 % reflectivity set on both sides of a 2 mm thick ring piezo stack and glued with epoxy. The free spectral range (FSR) of this Fabry-Pérot interferometer was determined to be 54.3(1) GHz, well suited to measure the spectral widths we expect. Figure A.2 displays the measured power spectrum with this cavity, with (in blue) and without (in orange) the fibre amplifier. The overall shape and width only change slightly, we, however, observe the suppression of the remaining carrier intensity through the fibre amplifier. Fitting a Gaussian profile (red dashed line), we obtain a spectral FWHM of $\delta\nu = 25.5(2)$ GHz or $\delta\lambda = 0.0963(8)$ nm. Fitting a Lorentzian distribution (violet dashed line), would only result in a slightly larger FWHM. By assuming a Gaussian and not a Lorentzian distribution, we potentially overestimate the coherence length to be $l_{c,\text{theo}} = 10.38(8)$ mm, which was calculated using equation A.2.

To measure the actual coherence length we employ a small Michelson interferometer, with one mirror on a translation stage and the resulting interference pattern captured by a CCD camera. The central pattern then is fitted with a two-dimensional Gaussian distribution modulated by a sine to

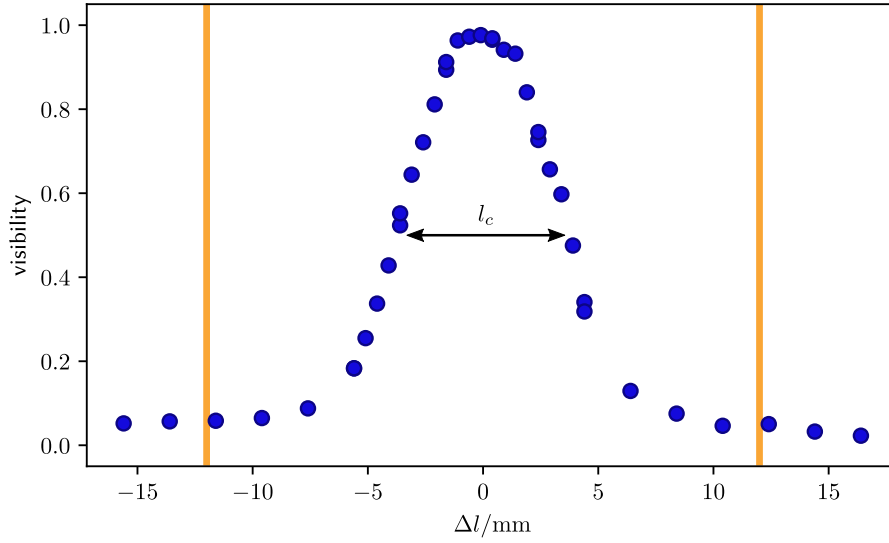


Figure A.3: Coherence length characterisation in a Michelson-interferometer We observe the change in visibility of an interference pattern by varying the position of the mirror in one of the interferometer legs, which in turn alters the optical path length difference Δl . The coherence length, defined as the FWHM of the self coherence pattern is extracted as $l_c = 6.18(9)$ mm. This is more than sufficient to suppress interference from reflections inside the glass walls of the vacuum cell which would occur roughly at the orange bars in the diagram shown.

extract the visibility depending on the path length difference. The results of this measurement are shown in figure A.3 b), from which we extract the coherence length as the FWHM $l_c = 6.18(9)$ mm. This is nearly half the value of the coherence length calculated using equation A.2, where we assumed a Gaussian shaped power spectral density instead of a Lorentzian shaped one. For the latter a factor two would have to be included, bringing the calculation closer to an agreement with the directly measured result. Nevertheless, both would significantly suppress interference of light reflected inside the glass wall, which would occur at the oranges lines drawn in figure A.2, where we assumed a refractive index of $n = 1.5$. Hence we showed how we used the seed light of a Coherent Mephisto

laser with a linewidth of ~ 1 kHz and >1 km coherence length [169] and added phase noise in the microwave frequency range to increase its linewidth to $25.5(2)$ GHz. This linewidth broadening by more than 7 orders of magnitude reduces the coherence length to only $6.18(9)$ mm when it is amplified to 5 W and used as the main dipole trap laser in our optical evaporation stage. This laser configuration suppressed the losses from light assisted collisions significantly, as can be seen in the measurement in figure 4.4.

List of Figures

2.1	The Hubbard model in two dimensions	6
2.2	Single-site limit	8
2.3	Eigenenergies of the balanced double-well	10
2.4	The superexchange	12
2.5	Eigenenergies and ground state composition of the tilted double-well	13
2.6	Superexchange in a tilted double-well	14
2.7	The Hubbard band picture	16
2.8	Phase diagram of the half-filled two-dimensional Hubbard model	17
2.9	High-temperature superconductors and their phase diagram	19
2.10	Equation of state obtained through DQMC calculations	19
2.11	The bilayer Hubbard model	20
2.12	The phase diagram of the half-filled bilayer Hubbard model	22
3.1	The hyperfine states of ^{40}K	24
3.2	Coupled states and state transfer methods	26
3.3	The accordion lattice	29
3.4	Band structure of a one-dimensional lattice	30
3.5	Deriving the Hubbard parameters with Wannier functions	32
3.6	The superlattice and its eigensolutions	33
3.7	Inhomogeneous lattice potentials and the local-density approximation	35
3.8	Feshbach resonances	38
4.1	Magneto-optical trap	42
4.2	Evaporative cooling	43
4.3	Optical evaporation sequence	44
4.4	Field dependent atom loss through light-assisted collisions	46
4.5	Lattice laser configurations	47
4.6	Laser switch for the superlattice phase	49
4.7	Parametric heating	51
4.8	z -superlattice loading sequence	52
4.9	In-situ absorption imaging	54
4.10	Feshbach resonances in ^{40}K and doubles detection	55
4.11	Single plane detection	59
4.12	Sequences for spin-spin or singles-doubles detection	60
4.13	Trap frequency and beam waist calibration	61
4.14	Potential mapping and the equation of state fit	63

4.15	Entropy cooling and potential shaping	65
4.16	SLM optical setup	66
4.17	Errors in the potential pattern generation	67
4.18	Potential shaping laser and wavelength dependent losses	69
4.19	Atom feedback for potential generation	70
5.1	Particle-hole exchange symmetry I	77
5.2	The symmetries of the Hubbard model	78
5.3	Particle-hole exchange symmetry II and its mapping of phases	79
5.4	Preparing the attractive Hubbard model.	80
5.5	Creating a spin-imbalanced system	82
5.6	Post-selective data binning in h	83
5.7	Particle-hole symmetry with varying interactions	85
5.8	Interchanging the chemical potential with the effective Zeeman shift	86
5.9	Simulating a Mott insulator using attractive interactions	87
6.1	Optical setup for frequency doubling and beating	90
6.2	Microwave beat note down-conversion and signal processing	91
6.3	Closed feedback loop of the frequency lock	93
6.4	Parametric heating of the z -superlattice	95
6.5	Band mapping of a merged superlattice	97
6.6	Splitting the population of a double-well	98
6.7	Second plane removal in frozen lattice	100
6.8	Double-well state preparation through a superlattice phase sweep	101
6.9	Induced Rabi-oscillations to extract t_{\perp}	103
6.10	Inter-layer tunnelling amplitude t_{\perp} as a function of green lattice depth	104
6.11	On-site interaction U calibration by RF-spectroscopy	105
6.12	Loading a band insulator in a two-dimensional lattice	107
6.13	Experimental sequence to create a band insulator with repulsive interactions	109
6.14	Melting the two-dimensional band insulator into a half-filled bilayer system	110
6.15	Density distribution in a bilayer close to half-filling	112
7.1	Local site magnetisation represented on the Bloch sphere	114
7.2	Imaging resolution and its limiting effects on detecting spin order	116
7.3	Ramsey sequence in a magnetic field gradient	120
7.4	Imprinting a wave vector k_{SP} on the spin-structure	122
7.5	Spin-structure factors in the two-dimensional Hubbard model	123
7.6	Intra-layer spin correlations in a Hubbard bilayer	124
7.7	Eigenstates of the double-well and the single site connected in merging	127
7.8	Experimental sequence for merging the Hubbard bilayer	128
7.9	Narrow singles-doubles spectroscopy after merging	129
7.10	Detecting inter-layer dimers after merging	130
7.11	Inter-layer spin correlations in a bilayer Hubbard model	131
7.12	Crossover between two competing magnetic orders	133
7.13	Measured correlation ratio in the bilayer Hubbard parameter space	135

A.1	Linewidth broadening with high frequency noise generation	153
A.2	Noise-broadened optical spectrum	154
A.3	Coherence length characterisation in a Michelson-interferometer	155